TU Delft

Delft University of Technology

Mixtures in Motion

High-Velocity DEM Modeling of Blast Furnace Charging

Roeplal, R.N.

DOI
10.4233/uuid:c119e6ad-c14e-4d7c-942f-f78925e24636

Publication date
2025

Document Version
Final published version

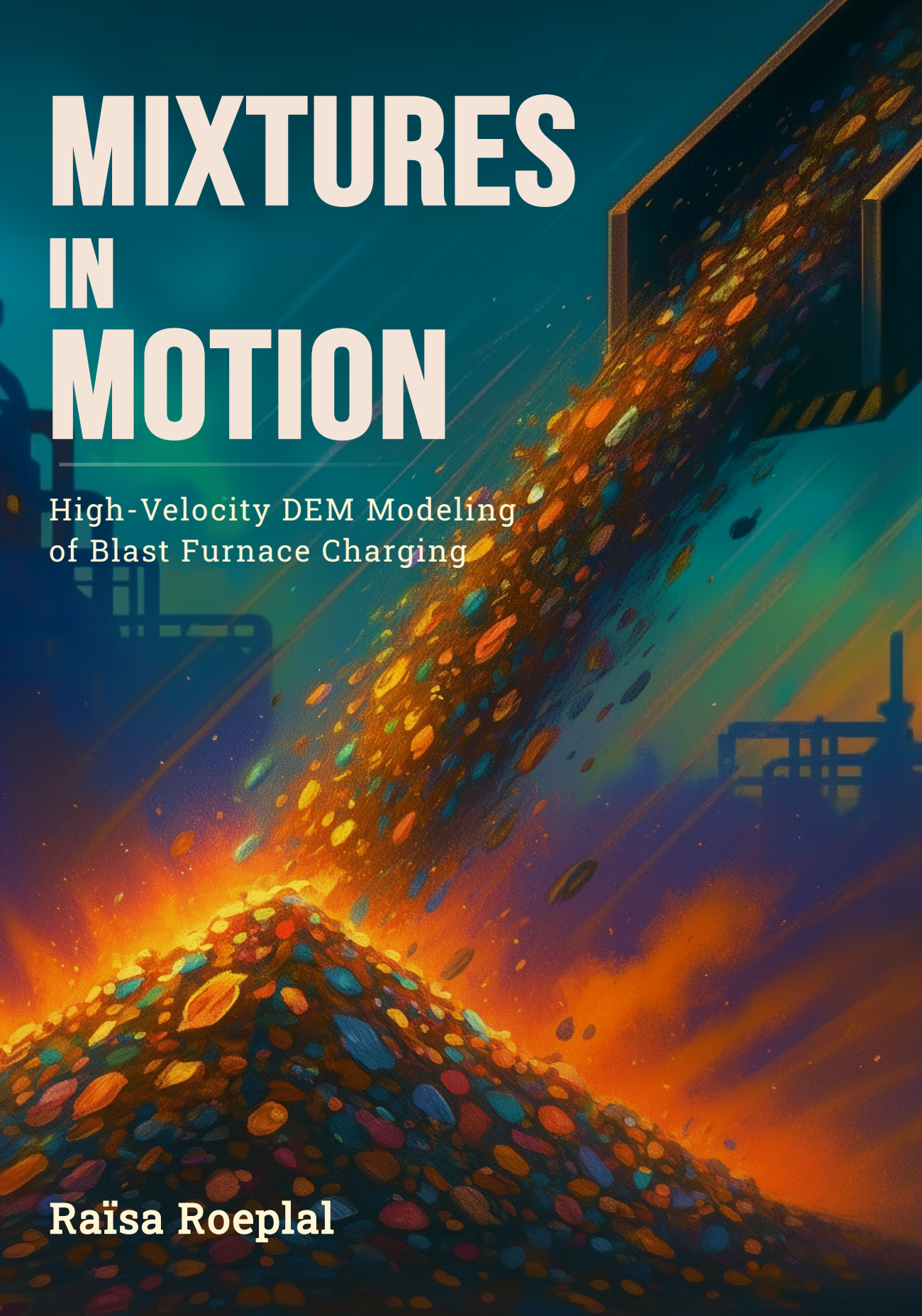
Citation (APA)
Roeplal, R. N. (2025). *Mixtures in Motion: High-Velocity DEM Modeling of Blast Furnace Charging*. [Dissertation (TU Delft), Delft University of Technology]. https://doi.org/10.4233/uuid:c119e6ad-c14e-4d7c-942f-f78925e24636

Important note
To cite this publication, please use the final published version (if applicable).
Please check the document version above.

Copyright
Other than for strictly personal use, it is not permitted to download, forward or distribute the text or part of it, without the consent of the author(s) and/or copyright holder(s), unless the work is under an open content license such as Creative Commons.

Takedown policy
Please contact us and provide details if you believe this document breaches copyrights.
We will remove access to the work immediately and investigate your claim.

This work is downloaded from Delft University of Technology.
For technical reasons the number of authors shown on this cover page is limited to a maximum of 10.


MIXTURES
IN
MOTION
High-Velocity DEM Modeling
of Blast Furnace Charging
Raïsa Roeplal

Mixtures in Motion

High-Velocity DEM Modeling of Blast Furnace Charging

Mixtures in Motion

High-Velocity DEM Modeling of Blast Furnace Charging

Dissertation

for the purpose of obtaining the degree of doctor
at Delft University of Technology,
by authority of the Rector Magnificus prof. dr. ir. T.H.J.J. van der Hagen,
chair of the Board of Doctorates,
to be defended publicly on
Monday, November 10th 2025 at 15.00 o'clock

by

Raïsa Nandeeta ROEPLAL

Master of Science in Mechanical Engineering,
University of Twente, The Netherlands,
born in Paramaribo, Suriname

This dissertation has been approved by
promotor: Prof. dr. ir. D. L. Schott
copromotor: Dr. ir. Y. Pang

Composition of the doctoral committee:

Rector Magnificus,	chairperson
Prof. dr. ir. D. L. Schott,	Delft University of Technology
Dr. ir. Y. Pang,	Delft University of Technology

Independent members:

Prof. dr. ir. J. R. van Ommen,	Delft University of Technology
Dr. N. D. Dogan,	Delft University of Technology
Prof. dr. S. Luding,	University of Twente
Prof. dr. H. Saxén,	Åbo Akademi University
Prof. dr. ir. B. J. Boersma,	Delft University of Technology

The work was carried out as part of the Industrial Dense Granular Flows project, which received funding from the Dutch Research Council (NWO) in the framework of the ENW PPP Fund for the top-sectors and from the Ministry of Economic Affairs in the framework of the “PPS-Toeslagregeling”.





Keywords: Discrete Element Method, Industrial flow, High-velocity, Mixture, Segregation, Calibration
ISBN/EAN: 978-94-6384-856-5 (print)
978-94-6518-155-4 (PDF)

Copyright © 2025 by R. N. Roeplal
Printed by Ridderprint in the Netherlands.
An electronic version of this dissertation is available at:
`http://repository.tudelft.nl/`
Data underlying this dissertation can be accessed via the following DOI:
`10.4121/7e149c70-ad49-4ea1-88c6-8a7c2d494a9f`

To the strong women who came before me,
and made life better with each generation.
I will do the same.

Contents

Summary **xi**

Samenvatting **xv**

Nomenclature **xix**

1 Introduction **1**
1.1 Blast furnace ironmaking . . . 3
1.2 Improving multi-component burden distribution . . . 5
1.3 DEM as a tool for simulating granular flows . . . 7
1.4 Research goal and scope . . . 10
1.5 Research questions and methods . . . 11
1.6 Reading guide . . . 13
1.7 Bibliography . . . 15

2 A Review of DEM-Based Models for Blast Furnace Permeability **17**
2.1 Burden distribution requirements . . . 18
2.2 Overview of DEM models for burden distribution . . . 22
2.3 Performance metrics for segregation . . . 35
2.4 Improvement of burden distribution: effects of design and operational parameters . . . 39
2.5 Conclusions . . . 48
2.6 Bibliography . . . 49

3 A Review of Modeling Strategies in Blast Furnace DEM Simulations **65**
3.1 Basics of DEM . . . 66
3.2 A brief note on large-scale DEM model development . . . 71
3.3 Contact models . . . 76
3.4 Sensitivity analyses for input parameters . . . 78
3.5 Determination of model inputs . . . 85
3.6 Model validation . . . 98
3.7 Large-scale modeling feasibility . . . 100
3.8 Conclusions . . . 103
3.9 Bibliography . . . 104

4 Relevance of Inter-Component Mixture Interaction Parameters 119
4.1 Introduction . . . 120
4.2 Tests and procedures . . . 123
4.3 Results . . . 128
4.4 Conclusions. . . . 140
4.5 Digital supplements . . . 141
4.6 Bibliography . . . 141

5 High-Velocity Experimental Characterization of Material Behavior 145
5.1 Introduction . . . 146
5.2 High-velocity experimental setup design . . . 148
5.3 Test procedure and measurement of KPIs. . . . 152
5.4 Overview of high-velocity experiments . . . 155
5.5 Experimental results and discussion . . . 155
5.6 Conclusions. . . . 159
5.7 Bibliography . . . 160

6 Calibration and Verification of Mixture Model Parameters under High-Velocity Flow Conditions 163
6.1 Introduction . . . 164
6.2 Calibration framework . . . 165
6.3 DEM simulations . . . 170
6.4 Response surface modeling . . . 174
6.5 Multi-objective optimization . . . 178
6.6 Verification . . . 180
6.7 Computational cost considerations . . . 184
6.8 Conclusions. . . . 187
6.9 Bibliography . . . 187

7 Particle Up-Scaling in Industrial Blast Furnace DEM Modeling 191
7.1 Introduction . . . 192
7.2 Ore layer charging: simulation and analysis procedures . . . 194
7.3 Effect of scaling on chute flow and resulting burden packing behavior . . . 199
7.4 Effect of scaling on bunker discharge and resulting burden packing behavior . . . 208
7.5 Conclusions. . . . 215
7.6 Bibliography . . . 216

8 Showcasing the Industrial Blast Furnace Charging Model: Insights from Case Studies **219**
8.1 Brief description of ore layer charging 220
8.2 Simulation and analysis methods 220
8.3 Effect of initial mixture configuration in top bunkers 227
8.4 Effect of burden call level 235
8.5 Effect of chute liner condition 239
8.6 Conclusions 242
8.7 Bibliography 244

9 Conclusions and Recommendations **245**
9.1 Conclusions 245
9.2 Recommendations 247

A Supplementary Data for Chapter 4 **249**

B Measuring Particle Size Distributions **253**

C Hopper Geometry Imperfections: Observations and Modeling **255**
C.1 Hopper construction imperfections 255
C.2 Effect of imperfections on material behavior 258
C.3 Replicating imperfections in hopper geometry 258

D Supplementary Data for Chapter 6 **261**
D.1 Experimental Design Diagrams 261
D.2 DEM simulation results 263

Glossary **267**

Acknowledgments **271**

PhD Portfolio **275**

About the Author **279**

Summary

Despite decades of industrial use, the blast furnace remains, to some extent, a “black box”. Harsh operating conditions and the scale of the process make it difficult to observe how *pellet* and *sinter*, which serve as the main raw material components for molten iron production, are distributed within the layers formed by their *multi-component mixture* during charging. This distribution strongly influences blast furnace permeability, which in turn affects efficiency, energy use, and emissions. Predicting this distribution is challenging due to differences in particle properties and the high-velocity nature of charging, which likely induces *segregation*. As a result, it is unclear whether the burden is deposited uniformly, and if not, how to improve it.

The Discrete Element Method (DEM) offers a powerful tool for addressing this problem. It enables detailed modeling of particle-scale interactions and helps assess how charging strategies influence mixed layer formation. By systematically exploring different operating conditions, DEM supports the development of strategies that promote more uniform distributions and improve furnace performance. This thesis presents a calibrated DEM model of a multi-component mixture used in blast furnace charging, aimed at predicting the distribution for improving the layer permeability.

The work begins by examining the physical mechanisms that affect bed permeability during charging in Chapter 2. Permeability is influenced by component distribution (the spatial arrangement of pellet and sinter), their packing distribution, the overall mass distribution and particle breakage. These are governed by complex processes such as segregation, degradation, flow deviation within the charging system, and the coke-push effect. While prior DEM studies mainly focused on size segregation and flow deviation, less attention has been given to component segregation and degradation, especially in multi-component mixtures. This gap motivated the development of a more comprehensive and realistic modeling approach. The focus was directed toward component and packing distribution, which are key to defining burden structure in the layers.

Given the coarse, free-flowing nature of the materials, the Hertz-Mindlin contact model combined with rolling model C was selected. Modeling a pellet-sinter mixture with these contact models requires calibration of 15 interaction parameters, reflecting the complexity of multi-component systems. A review of existing DEM studies in Chapter 3 revealed several shortcomings of current blast furnace models: reliance on uncalibrated parameters, calibrations based on single key performance indicators (KPIs), use of low-

velocity conditions, and unverified particle up-scaling. These limitations underscored the need for robust calibration supported by experimental data and an evaluation of particle scaling effects.

Determining the full 15-parameter set for modeling the pellet-sinter mixture was challenging due to the large number of interaction parameters. To explore whether the calibration could be simplified, Chapter 4 introduced a pre-calibration step to evaluate the importance of three inter-component parameters: restitution coefficient, sliding friction coefficient, and rolling friction coefficient. Porosity, used as a proxy for packing structure, was selected for its relevance to bed permeability and ease of quantification. Sensitivity analyses showed that all three parameters significantly affected porosity and component distribution. Consequently, all were included in the final calibration. To ensure model reliability, two requirements were defined: (i) calibration must reflect high-velocity flow conditions, and (ii) multiple KPIs must be used to constrain the solution space.

To meet the first requirement, Chapter 5 introduces a novel laboratory setup capable of reproducing high-velocity charging via a 4.7-meter drop height. Systematic piling tests were performed using pellet, sinter, and their 50/50 mixture at various discharge heights. Five KPIs –hopper discharge time, heap mass, heap contour, heap center height, and heap porosity– were selected to characterize material behavior. These KPIs were sensitive to flow velocity and material properties, confirming their relevance for calibration. However, calibrating 15 parameters using only five KPIs remained a challenge.

Chapter 6 addresses this by introducing a step-wise calibration strategy. It began with the separate calibration of pellet and sinter models, followed by calibration of their interaction parameters. In each step, the five KPIs provided sufficient constraints to achieve a unique parameter set. The calibrated model was validated against experimental results at different discharge heights and showed strong agreement, with maximum deviations of only 5.5 percent at the maximum drop height. The model demonstrated reliable predictive performance across a range of velocities.

However, simulating industrial-scale charging with the calibrated model using original particle sizes proved computationally infeasible. To address this, Chapter 7 extends the model to industrial-scale simulations using particle up-scaling. A scaling factor of 2 did not yield practical runtimes, but factors up to 5 preserved key behaviors –layering, segregation, and porosity distribution– when the mass flow rate was adjusted accordingly. While higher scaling reduced flow resolution, particularly along the chute, the final packing structure in the charged layers remained consistent. This confirmed that particle up-scaling is a viable strategy for large-scale simulations, provided it is applied carefully and validated against key performance metrics.

Finally, in Chapter 8, the up-scaled model demonstrated its effectiveness in predicting how different operational conditions influence component distribution and final packing

structure. Through case studies combining various charging scenarios, the model provides insights into potential process improvements and identifies valuable directions for future research.

Samenvatting

Ondanks decennia van industriële toepassing blijft de hoogoven in zekere zin een “black box”. Zware bedrijfsomstandigheden en de schaal van het proces maken het lastig om waar te nemen hoe *pellets* en *sinter* (de belangrijkste grondstofcomponenten voor de productie van vloeibaar ijzer) zich tijdens het beladen van de hoogoven als *multicomponentmengsel* in lagen verdelen. Deze verdeling beïnvloedt sterk de permeabiliteit van de hoogoven, wat op zijn beurt de efficiëntie, het energieverbruik en de emissies bepaalt. Het voorspellen van deze verdeling is uitdagend door verschillen in deeltjeseigenschappen en het hogesnelheidskarakter van de belading, die waarschijnlijk *segregatie* veroorzaken. Daardoor is onduidelijk of het mengsel uniform wordt afgezet en, zo niet, hoe dit kan worden verbeterd.

De Discrete Element Method (DEM) biedt een krachtig hulpmiddel om dit probleem aan te pakken. De methode maakt gedetailleerde modellering van interacties op de deeltjesschaal mogelijk en helpt te beoordelen hoe beladingsstrategieën de vorming van gemengde lagen beïnvloeden. Door systematisch verschillende bedrijfscondities te verkennen, ondersteunt DEM de ontwikkeling van strategieën die uniformere verdelingen bevorderen en de ovenprestatie verbeteren. Dit proefschrift presenteert een gekalibreerd DEM-model van een multicomponentmengsel dat wordt gebruikt bij de hoogovenbelading, met als doel de verdeling te voorspellen ter verbetering van de permeabiliteit.

Het werk begint in Hoofdstuk 2 met een onderzoek naar de fysische mechanismen die de permeabiliteit tijdens het beladen beïnvloeden. De permeabiliteit wordt bepaald door de componentverdeling (de ruimtelijke verdeling van pellets en sinter), hun pakkingverdeling, de totale massaverdeling en deeltjesbreuk. Deze worden gestuurd door complexe processen zoals segregatie, degradatie, stromingsafwijking binnen het beladingssysteem en het “coke-push” effect. Eerdere DEM-studies zich vooral richtten op segregatie als gevolg van verschil in deeltjesgrootte en stromingsafwijking, terwijl er minder aandacht is besteed aan componentsegregatie en degradatie, met name in multicomponentmengsels. Dit tekort in de bestaande benaderingen leidde tot de ontwikkeling van een meer omvattende en realistische modelleringsaanpak. De focus is gericht op component- en pakkingverdeling, die bepalend zijn voor de laagstructuur.

Gegeven het grove, vrij stromende karakter van de materialen is gekozen voor het Hertz–Mindlin-contactmodel in combinatie met rollend model C. Het modelleren van een pellet-sinter-mengsel met deze contactmodellen vereist de kalibratie van 15 inter-

actieparameters, wat de complexiteit van multicomponentsystemen weerspiegelt. Een overzicht van bestaande DEM-studies in Hoofdstuk 3 bracht verschillende tekortkomingen van huidige hoogovenmodellen aan het licht: gebruik van ongekalibreerde parameters, kalibraties gebaseerd op één enkele key performance indicator (KPI), toepassing onder lage-snelheidscondities en niet-gevalideerde deeltjesopschaling. Deze beperkingen benadrukken de noodzaak van robuuste kalibratie, ondersteund door experimentele data, en een evaluatie van de effecten van deeltjesopschaling.

Het bepalen van de volledige set van 15 parameters voor het modelleren van het pellet-sinter-mengsel was uitdagend vanwege het grote aantal interactieparameters. Om te onderzoeken of de kalibratie kon worden vereenvoudigd, introduceert Hoofdstuk 4 een pre-kalibratiestap om het belang te evalueren van drie inter-component parameters: restitutiecoëfficiënt, schuifwrijvingscoëfficiënt en rolwrijvingscoëfficiënt. Porositeit, gebruikt als proxy voor pakkingstructuur, werd gekozen vanwege de relevantie voor permeabiliteit en de eenvoudige kwantificeerbaarheid. Gevoeligheidsanalyses toonden aan dat alle drie parameters de porositeit en componentverdeling significant beïnvloeden. Bijgevolg zijn ze alle drie in de uiteindelijke kalibratie opgenomen. Ter borging van de modelbetrouwbaarheid zijn twee eisen geformuleerd: (i) de kalibratie moet hogesnelheids-stromingscondities weerspiegelen en (ii) meerdere KPIs moeten worden gebruikt om een unieke oplossing te vinden voor de parameterset.

Om aan de eerste eis te voldoen introduceert Hoofdstuk 5 een nieuwe laboratoriumopstelling die hogesnelheidsbelading kan reproduceren via een valhoogte van 4.7 m. Systematische stortproeven zijn uitgevoerd om hoopjes te creëren met pellets, sinter en hun 50/50-mengsel bij verschillende loshoogten. Vijf KPIs (trechterlostijd, hoopmassa, hoopcontour, hooptophoogte en hoopporositeit) zijn geselecteerd om het materiaalgedrag te karakteriseren. Deze KPIs bleken gevoelig voor stroomsnelheid en materiaaleigenschappen, wat hun relevantie voor kalibratie bevestigt. Het bleef echter een uitdaging om 15 parameters te kalibreren met slechts vijf KPIs.

Hoofdstuk 6 pakt dit aan met een stapsgewijze kalibratiestrategie. Eerst zijn de pellet- en sintermodellen afzonderlijk gekalibreerd, gevolgd door de kalibratie van hun interactieparameters. In elke stap boden de vijf KPIs voldoende beperkingen om tot een unieke parameterset te komen. Het gekalibreerde model is gevalideerd aan de hand van experimentele resultaten bij verschillende loshoogten en vertoonde sterke overeenstemming, met maximale afwijkingen van slechts 5.5 % onder de grootste valhoogte. Het model toonde betrouwbare voorspellende prestaties over een breed snelheidsbereik.

Het simuleren van belading op industriële schaal met het gekalibreerde model en oorspronkelijke deeltjesgroottes bleek echter onhaalbaar. Daarom breidt Hoofdstuk 7 het model uit naar simulaties op industriële schaal met behulp van deeltjesopschaling. Een schaalfactor 2 leverde geen praktische rekentijden op, maar factoren tot 5 behielden

kerngedragingen –laagvorming, segregatie en porositeitsverdeling– mits het massadebiet overeenkomstig werd aangepast. Hogere schaalfactoren verminderden wel de stromingsresolutie, met name langs de chute, maar de uiteindelijke pakkingstructuur in de gevormde lagen bleef consistent. Dit bevestigt dat deeltjesopschaling een haalbare strategie is voor grootschalige simulaties, mits zorgvuldig toegepast en gevalideerd.

Tot slot toont Hoofdstuk 8 aan dat het opgeschaalde model effectief voorspelt hoe verschillende operationele condities de componentverdeling en de uiteindelijke pakkingstructuur beïnvloeden. Via casestudies met uiteenlopende laadscenario's biedt het model inzicht in mogelijke procesverbeteringen en identificeert het waardevolle richtingen voor toekomstig onderzoek.

Nomenclature

Acronyms

AoR	Angle of Repose
BF	Blast Furnace
BF-BOF	Blast Furnace–Basic Oxygen Furnace
BLT	Bell-Less Type
BT	Bell-Type
CCC	Concordance Correlation Coefficient
CFD	Computational Fluid Dynamics
DEM	Discrete Element Method
GPU	Graphics Processing Unit
KPI	Key Performance Indicator
LoF	Lack of Fit
RSM	Response Surface Model

Greek symbols

α	Angular acceleration [°/s^2]
β	Bunker opening angle [°]
δ	Contact overlap [m]
γ	Damping coefficient [-]
μ	Friction coefficient [-]
ω	Angular acceleration [°/s]
Φ	Porosity [-]
θ	Orientation [°/s^2]
υ	Poisson's ratio [-]

Roman symbols

a	Acceleration [m/s^2]
d	Diameter [m] / desirability [-]
D	Desirability score [-]
e	Restitution coefficient [-]
E	Young's Modulus [Pa]
F	Force [N]
g	Gravitational acceleration [m/s^2]
G	Shear Modulus [Pa]
H	Discharge height [m]
I	Moment of inertia [kgm^2]
k	Contact stiffness [N/m]
m	Mass [kg]
MSE	Mean squared error [-]
P	Porosity [-]
PI	Porosity Index [-]
R	Particle radius [m]
s	Scaling factor [-]
SI	Segregation Index [-]
t	Time [s]
t_R	Rayleigh time step [s]
T	Torque [Nm]
v	Velocity [m/s]
V	Volume [m^3]
x	Mass fraction [-]
$\vec{r}$	Position vector [-]

Superscripts

c	Elastic
d	Dissipative
n	Normal
P-C	Pellet-coke
P-P	Pellet-pellet
P-S	Pellet-sinter
P-W	Pellet-wall
p-p	Particle-particle
p-w	Particle-wall
ro	Rolling
S-W	Sinter-wall
t	Tangential

Subscripts

b	Bulk
c	Center
C	Coke
d	Discharge
h	Heap
p	Particle
P	Pellet
r	Rolling
R	Rayleigh
s	Sliding
S	Sinter
t	Tracer

1

Introduction

Steel is the most important engineering and construction material worldwide. Given its relatively low production cost in combination with its strength, versatility, and durability, steel is used in nearly all facets of modern society. Steel is also expected to be pivotal in the energy transition, facilitating the construction of renewable energy infrastructure, transmission networks, and storage systems essential for a sustainable future. Since 1970, the worldwide demand for steel has surged more than threefold [1], and in 2024, the World Steel Association recorded a staggering global production of 1,892 million tonnes of crude steel [2]. The increasing demand is expected to grow further in the coming years considering the upcoming energy transition and the role of steel in the construction of green energy systems.

Steel is an alloy of mainly iron and carbon, where the iron content is typically above 97% by weight. The iron required to produce steel is rarely found in its pure form in nature; instead, it exists abundantly in the form of *ores* (usually iron oxides such as magnetite, Fe_3O_4, or hematite, Fe_2O_3) which are mined from various geological deposits around the world. Unprocessed iron ore is typically crushed, ground into powder and subsequently processed to concentrated iron ore powder by removing impurities. As shown in Figure 1.1, the three key stages in crude steel production are raw material preparation, ironmaking, and steelmaking. In the first stage, iron ore powder is agglomerated to produce pellets and sinter (referred to as *iron-bearing materials* or *iron ores*) under high temperature and pressure conditions. Different technologies can be combined in the remaining stages to achieve the same goal: the extraction of iron from iron ores and subsequent refinement to steel. Currently, the blast furnace-basic oxygen furnace (BF-BOF) route is by far the leading technology in this regard, accounting for roughly 70% of global steel production and approximately 90% of primary production [3].

1

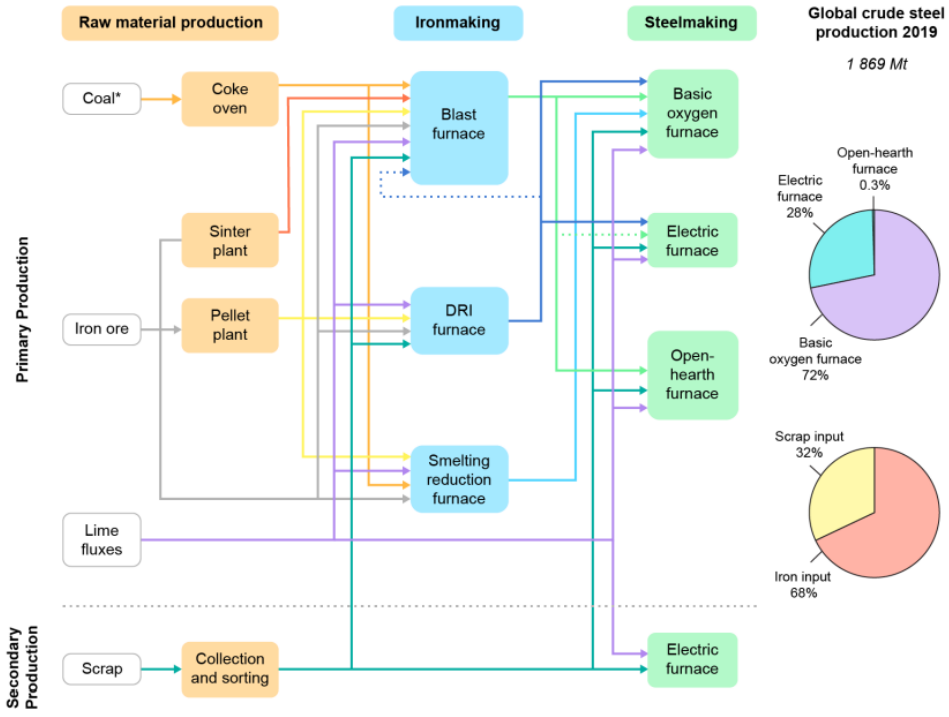


Figure 1.1: Main steel production pathways [3].

1.1 Blast furnace ironmaking

In blast furnace ironmaking, iron is extracted from its ores through the reduction of iron oxides by carbon at high temperatures. The raw materials, collectively referred to as the *burden*†, primarily comprise iron ore and coke, serving as carriers of iron oxides and carbon, respectively. The transportation of these particulate materials from the *stock house*† to the furnace is a granular flow process, where discrete particles are delivered and deposited in a controlled manner, referred to as blast furnace *charging*†. Figure 1.2 presents a schematic of a typical blast furnace and its associated charging system. The blast furnace itself is a large, vertical cylindrical reactor operating continuously under extreme thermal and chemical conditions. Modern furnaces are constructed with working volumes ranging from 3,000 to 5,000 m^3, achieving production rates of up to 12,000 tonnes of hot metal[1] per day. Meeting such high productivity demands a substantial supply of raw materials, typically around 1,570 kg of iron ore and 300 kg of coke per tonne of hot metal produced [4].

In a blast furnace, coke and iron ore are charged in alternating batches from the top, forming stacked *burden layers*† inside the shaft. A rotating chute system directs each batch, controlling both the radial placement and trajectory of the material stream to determine where particles land on the *stock line*† and how the layers are constructed. This spatial arrangement of materials is referred to as the *burden distribution*†. Once charging is complete, hot oxygen-enriched air is injected through tuyeres located near the base of the furnace. The coke combusts near these inlets, generating the heat and carbon monoxide (CO) necessary for the reduction of iron oxides. As CO rises through the descending packed bed, a counter-current flow is established, driving the step-wise reduction reactions essential for ironmaking.

The term *reduction*† refers to the chemical transformation in which iron oxides are "reduced" to metallic iron as they descend through the furnace. Internally, the furnace is divided into distinct zones based on their thermal and chemical environments: the throat (charging zone), the shaft (preheating and indirect reduction), the belly and bosh (intense reduction and softening), and the hearth (melting and collection). As the burden descends through these zones, it experiences progressive heating (see Figure 1.2) and chemical transformation, ultimately enabling the staged reduction of iron oxides into metallic iron. Reduction occurs through two primary mechanisms: *direct reduction*†, where solid carbon reacts with iron oxides at high temperatures near the furnace bottom, and *indirect reduction*†, where CO gas reduces iron oxides in the cooler upper regions. While both mechanisms contribute to overall ironmaking, the majority of the reduction is accomplished through indirect reduction, producing CO_2 as a by-product. Both CO and

[1] Molten iron tapped from the bottom of the furnace as the final product of the ironmaking process.

1

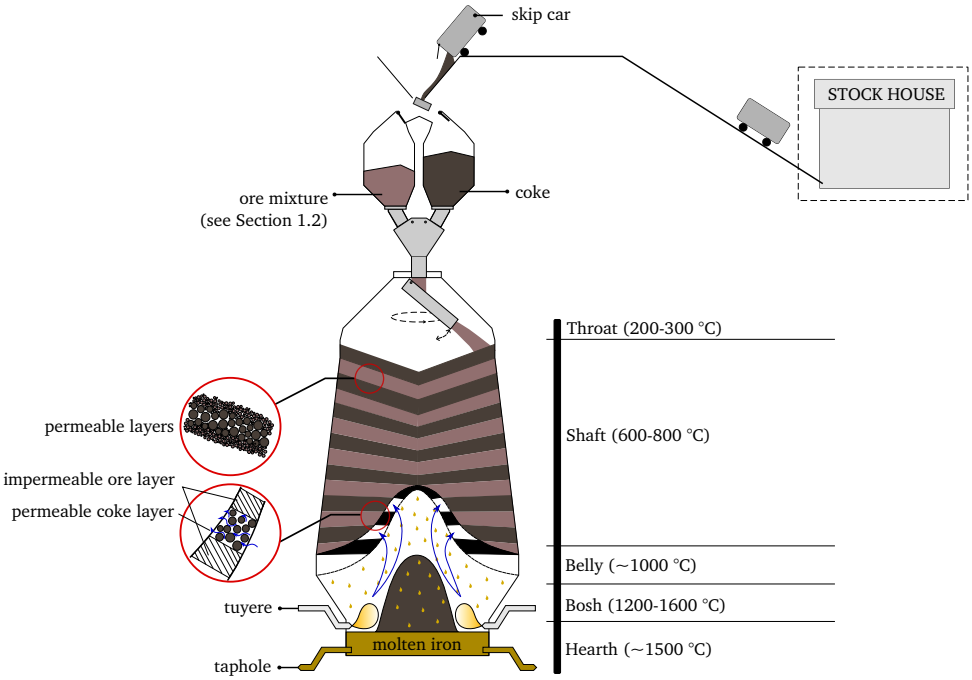


Figure 1.2: Schematic of a blast furnace and charging equipment.

CO_2 exit the furnace through the top gas outlet and are released into the environment.

The efficiency of the reduction process strongly depends on the *permeability*† of the packed bed –that is, the ease with which reduction gas can pass through the interconnected voids between particles. Uniform permeability across the burden layers ensures that each iron ore and coke particle has an equal opportunity to react with the reducing gases, promoting consistent reaction conditions. In contrast, non-uniform permeability disrupts gas flow, leading to regions of incomplete or excessive reaction, increased gas resistance, and upward forces that interfere with burden descent. In severe cases, this can cause erratic descent or even the formation of a hanging burden, jeopardizing furnace stability. Permeability also has a direct impact on coke consumption. Non-uniform gas distribution in the upper and middle zones results in uneven indirect reduction, forcing greater reliance on the more energy-intensive direct reduction pathway, which requires higher temperatures and increased coke usage [5, 6]. Thus, improving bed permeability is critical not only for furnace efficiency but also for reducing carbon emissions associated with the BF-BOF route.

1.2 Improving multi-component burden distribution

The iron ore burden in a blast furnace typically consists of pellets, sinter, and lump ore, with pellets and sinter forming most of the ore burden. These materials are produced and handled separately until they reach the *stock house*†, where they are simultaneously discharged into a *skip car*† (see Figure 1.3). This process generates a *multi-component mixture*†, which is subsequently transferred to the top bunkers feeding the furnace.

As the ore mixture travels from the stock house to the furnace throat, it passes through several handling stages involving chutes, conveyors, and hoppers. Each of these stages presents opportunities for *segregation*†, where particles separate based on differences in size, shape, and/or density [7]. Existing studies on granular flows show that particles may segregate independently according to each property, resulting in distinct phenomena known as size, shape, and density segregation [8]. Segregation has been studied extensively in relatively simple systems, such as hoppers, chutes, and heap formation processes [7], typically focusing on differences in a single particle property. When particles differ across multiple properties simultaneously, the resulting segregation effects can either reinforce or counteract one another, depending on the specific combinations of size, shape, and density.

Predicting segregation of the iron ore mixture during blast furnace charging is complex due to simultaneous differences in particle size, shape, and density, combined with multiple handling stages involving varying flow conditions. Nevertheless, understanding this behavior is critical, as achieving a uniform distribution of particle properties in the deposited ore layers is essential for two main reasons:

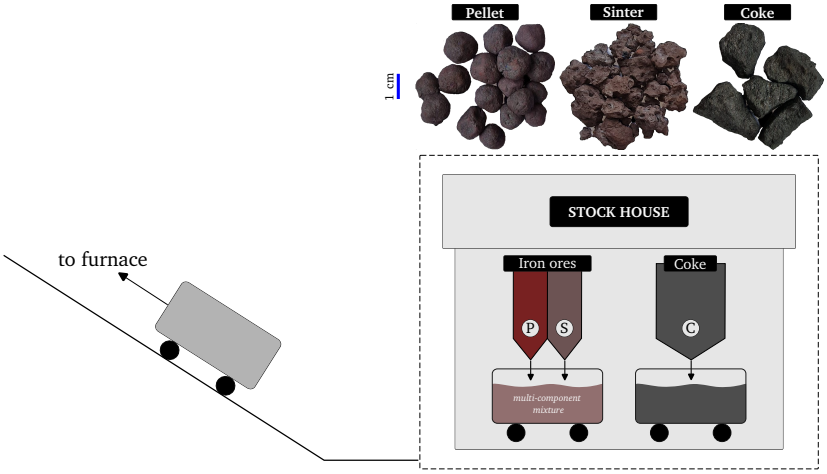


Figure 1.3: Schematic of the stock house illustrating skip-car filling and the resulting multi-component mixture for blast-furnace charging. The iron-ore burden comprises pellets (P) and sinter (S). Separate skip cars transport the iron-ore burden and the coke (C) burden.

- **Uniform packing in the layer**: In general, packing structure –referring to the spatial arrangement of particles and, consequently, the distribution of voids within the packing– depends strongly on the sizes and shapes of the particles [9]. A uniform distribution of different particle sizes and shapes in the ore layer promotes a homogeneous packing, in which void spaces are evenly distributed. This uniformity is essential for maintaining consistent gas flow through the burden. In contrast, uneven packing can lead to localized gas channeling or clogging, ultimately disrupting the desired flow of gases.

- **Uniform chemical (component) distribution in the layer**: Component segregation, driven by differences in particle density, can also compromise chemical uniformity. The different ore types are selected to combine into a slag with optimal melting temperature and viscosity. Component segregation may cause regions enriched in specific materials, leading to sub-optimal slag chemistry, impaired slag drainage, increased viscosity, and blocked gas channels.

Based on these requirements, it is clear that two important aspects –*packing structure*[†] and *component distribution*[†]– directly influence the permeability of the ore layer. Uniform component distribution helps prevent local enrichment of specific materials that could block gas channels, while a uniform packing ensures evenly distributed void spaces for gas flow. Therefore, in evaluating burden formation and its impact on furnace performance,

these two segregation-affected characteristics are key factors governing the permeability of the layer.

While inherent material properties such as size, shape, and density govern the tendency of particles to segregate, the extent of segregation is also strongly influenced by equipment design and operational parameters, including flow rates, drop heights, and chute speeds [8]. Among these factors, operational conditions are the most accessible for adjustment during furnace operation. By carefully controlling flow conditions, it is possible to steer material movement and partially mitigate segregation effects, improving the uniformity of the burden distribution and, ultimately, enhancing furnace performance.

Direct observation of the burden distribution during furnace operation is not feasible due to the extremely high temperatures inside the blast furnace, which prevent the use of conventional measurement or imaging techniques. Even if direct access were possible, accurately measuring segregation would remain challenging [8], particularly at the large industrial scale. As a result, a significant knowledge gap persists in understanding how upstream handling and charging practices influence the burden distribution in the charged layers. Hence, despite its existence for many decades, the blast furnace remains something of a "black box." To address this challenge, virtual experiments and predictive simulations, particularly those using the Discrete Element Method, have become valuable tools. DEM enables detailed modeling of particle interactions and provides insights into how different charging strategies affect segregation and burden distribution. Through systematic exploration of alternative operating conditions, DEM offers a means to develop charging strategies that promote more uniform burden distributions and, ultimately, improve furnace performance.

1.3 DEM as a tool for simulating granular flows

The Discrete Element Method (DEM), introduced by Cundall and Strack [10], provides a framework for simulating granular flows by explicitly computing the forces acting on individual particles and solving Newton's equations of motion via numerical integration. This approach allows for tracking the position, velocity, and rotation of every particle over time. By adjusting material properties, system geometries, and operational parameters, DEM enables the simulation of virtually any granular flow scenario, offering insight into how particles interact with each other and with their environment during handling or processing. DEM is particularly well-suited for analyzing both bulk-scale and particle-scale phenomena, making it a valuable tool for understanding complex industrial processes such as burden distribution in a blast furnace. Through DEM, the influence of operational conditions on flow behavior can be systematically explored, contributing to improved process design and control.

A DEM algorithm consists of three main steps: (1) detecting contacts between particles

and surrounding objects (other particles or walls), (2) calculating the resulting contact forces and torques, and (3) updating particle velocities and displacements by numerically integrating the equations of motion. The computational cost of a DEM simulation is largely governed by the first two steps, as the number of contact detections and force calculations increases rapidly with the number of particles and the complexity of the system geometry. As a result, simulating industrial-scale systems with millions of particles often necessitates the use of high-performance computing resources.

Contact forces are determined using contact laws that are formulated to replicate various physical flow behaviors, such as free-flowing, cohesive, and stress-history-dependent responses [11]. These forces are generally decomposed into a normal and a tangential component, denoted by $\overrightarrow{F^n}$ and $\overrightarrow{F^t}$, respectively. In addition to the contact forces, rotational torques may also be applied to capture particle spin and rolling behavior. As illustrated in Figure 1.4, the contact force and torque models are often conceptualized as combinations of a spring and a damper, where the spring represents the elastic response of the material and the damper accounts for energy dissipation during contact events. The accurate calculation of contact forces and torques requires the specification of several material parameters, including stiffness, coefficient of restitution, friction coefficients, and rolling resistance, among others. These parameters must be carefully selected to ensure that particle-level interactions are realistically translated into macroscopic bulk flow behavior. In many industrial applications, however, the relevant material properties are not directly measurable and may vary significantly across different material types or under varying operating conditions. Consequently, model calibration becomes an essential step in DEM simulations, allowing the adjustment of input parameters to achieve agreement between simulated and observed bulk behaviors.

Calibration involves adjusting model parameters based on laboratory experiments or reference data until the simulated outcomes reproduce observed flow behavior in terms of one or more relevant performance metrics. To ensure meaningful calibration, the flow conditions in the experiments must be consistent with those in the intended application; otherwise, the resulting parameter sets may not be transferable and could compromise the predictive capability of the model [12]. In addition, the calibration procedure must avoid parameter ambiguity, where multiple distinct parameter sets can reproduce similar bulk responses [13]. Avoiding ambiguity is essential to ensure that a unique parameter set is identified that accurately reproduces the targeted flow behavior. This can be facilitated by selecting performance metrics that are sensitive to the calibrated parameters and by employing multiple independent calibration tests where possible. Following calibration, verification and validation must be conducted to confirm that the model correctly solves the governing equations (verification) and accurately represents the physical behavior of the system under the relevant operating conditions (validation).

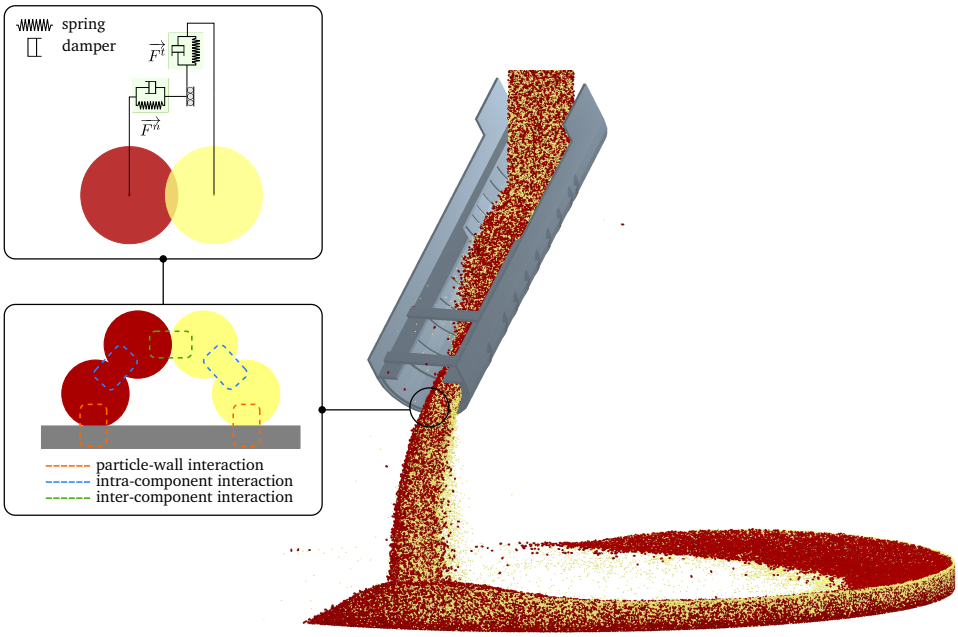


Figure 1.4: Illustration of a binary particle mixture transported through industrial-scale equipment within a DEM simulation, highlighting the different contact interactions that must be accounted for.

1

1.4 Research goal and scope

The application of DEM to simulate blast furnace charging shows considerable promise for elucidating the relationship between operational conditions and burden permeability. Nevertheless, achieving realistic simulations at the industrial scale remains highly challenging due to the inherent complexity of the flow and the large dimensions of the system. As with any modeling effort, a careful balance must be struck between ensuring model reliability and maintaining computational feasibility.

- **Model reliability:** A credible DEM model for blast furnace charging must accurately capture the behavior of a multi-component ore mixture under high-velocity flow conditions. This requires calibration of a relatively large set of interaction parameters; these include the interaction parameters not only between particles of each individual component (*intra-component interactions*[†]) and their respective interactions with equipment surfaces, but also among the different material types within the mixture. However, most existing studies limit their focus to one or two components in isolation, and typically overlook the *inter-component interactions*[†] inherent to realistic mixtures. Furthermore, high-velocity conditions typical of industrial charging are rarely considered during calibration, casting doubt on the reliability of many existing models. Even for single-component systems, the issue of parameter ambiguity –where multiple parameter sets yield similar results– is frequently left unaddressed.
- **Computational feasibility:** A single ore layer in a blast furnace is estimated to contain up to 65 million particles, as will be shown later in this thesis. However, the DelftBlue high-performance computing cluster –used in this research and equipped with state-of-the-art GPU technology– is limited to simulating approximately 32 million particles per GPU [14, 15]. As such, full-scale simulations of blast furnace charging processes remain beyond reach, even with advanced computational resources. To reduce computational load, many studies employ simplified or downscaled system geometries to reduce particle counts. While such strategies improve computational efficiency, they often operate at lower flow velocities and mass flow rates than those encountered in industrial settings, leading to deviations that reduce the physical representativeness and predictive reliability of current models.

Hence, despite substantial research efforts over the past decades, a reliable and validated multi-component DEM model capable of accurately reproducing flow behavior under industrial operating conditions is still lacking. Overcoming the dual challenge of faithfully capturing complex material interactions while managing computational demands is critical to advancing the use of DEM for improving blast furnace charging operations.

Accordingly, the objective of this thesis is

To develop a multi-component DEM model for predicting the component and packing distribution in the top ore layer in an industrial-scale blast furnace.

Referring back to Figure 1.2, the charging system involves multiple handling steps, with raw materials transported through a series of equipment from the stock house to the chute. This thesis focuses on material delivery starting from the top bunkers, as the upstream processes prior to this point are being addressed in a separate research project. Consequently, the segregation history before the top bunkers is not simulated, and an initial burden distribution within the bunkers is assumed. Furthermore, the charging of the coke layer is not included in the model, and the ore mixture is assumed to consist solely of pellets and sinter. Due to the high particle velocities during layer formation, it is assumed that particle motion is unaffected by the gas flow at the top of the furnace. As such, particle-gas interactions, heat exchange phenomena, and associated chemical reactions are not considered in this work. Finally, particles are assumed to be unbreakable, and degradation phenomena during charging are disregarded.

1.5 Research questions and methods

To achieve the objective, the overarching research question guiding this thesis is formulated as follows:

"How can a reliable and computationally feasible multi-component DEM model be developed for predicting the component and packing distribution in the top ore mixture layer in a full-scale industrial blast furnace?"

The following research questions (RQs) are addressed to achieve the objective of this work:

RQ 1. Which phenomena during blast furnace mixture charging affect the bed permeability, and to what extent have they been modeled using DEM?

RQ 2. To what extent are currently developed DEM mixture models of blast furnace charging reliable?

RQ 3. To what extent do inter-component parameters of a pellet-sinter mixture model affect component segregation and packing structure?

RQ 4. How can the behavior of blast furnace materials and their mixtures be experimentally characterized on laboratory scale using relevant performance indicators?

RQ 5. How can a reliable DEM mixture model for blast furnace charging be developed on laboratory scale in terms of the relevant performance indicators?

RQ 6. To what extent can particle up-scaling be applied to make the industrial-scale modeling feasible?

1

The research questions are addressed through a combined experimental-numerical approach, structured into four key phases: (i) literature review, (ii) sensitivity analyses for pre-calibration, (iii) experimental characterization and model calibration, and (iv) particle up-scaling for industrial-scale modeling. Each phase contributes to specific research questions and is reflected in the chapters that follow.

Literature review

A review of the literature was conducted to identify the key phenomena during blast furnace charging that influence bed permeability (RQ 1) and to evaluate the extent to which these phenomena have been modeled using DEM. The review also examines which design and operational conditions have been investigated in relation to permeability, providing insight into which factors can be controlled to improve blast furnace performance. These findings are presented in Chapter 2.

Subsequently, the body of literature was subjected to a further round of review, focusing on how these phenomena have been modeled using DEM. This second review specifically examines the methods employed to ensure model reliability and manage computational feasibility, considering aspects such as calibration practices, particle representation, and system scale (RQ 2). The findings are presented in Chapter 3.

Pre-calibration

Given the relatively large parameter set associated with a pellet-sinter mixture DEM model, a laborious calibration process is anticipated to ensure model reliability. To explore whether this process can be simplified by reducing the number of parameters, a pre-calibration DEM study was conducted to investigate the sensitivity of component segregation and packing structure to inter-component interaction parameters in pellet-sinter mixtures (RQ 3). This step aimed to determine whether pellet-sinter interaction parameters could be neglected during calibration, and the findings are presented in Chapter 4.

Developing a reliable model on laboratory scale – calibration and verification

To characterize the flow behavior of blast furnace materials and their mixtures, experimental tests were carried out at the laboratory scale (RQ 4). These experiments were performed using a novel high-velocity setup designed to replicate blast furnace representative flow conditions and to measure multiple performance indicators using techniques such as video and image analysis, as well as 3D volume scanning. The experimental setup and tests are presented in Chapter 5.

Subsequently, the measured performance indicators were used as calibration targets for the pellet-sinter mixture model calibration (RQ 5). A step-wise calibration strategy was employed, focusing first on the calibration of the individual component models,

followed by the calibration of the mixture model. At each calibration step, response surface modeling combined with multi-objective optimization was used to satisfy the complete set of calibration targets. Verification was performed to ensure that the calibrated model could accurately predict all performance indicators simultaneously. The step-wise mixture calibration procedure and results are presented in Chapter 6.

Developing a feasible model on industrial scale – particle up-scaling
To extend the DEM model to industrial dimensions, particle up-scaling was applied to assess how increasing particle size to reduce computational demands affects the predictive capabilities of the calibrated model (RQ 6) at the real industrial scale. A suitable scaling factor was identified that made simulations feasible at this scale while preserving the flow behavior of the unscaled, calibrated model with respect to component segregation and packing structure. With these results, presented in Chapter 7, the main objective of this thesis is reached.

Model showcasing
Chapter 8 demonstrates the usefulness of the model by applying it to realistic industrial-scale case studies. This application showcases the model's predictive capabilities in terms of segregation and packing distribution, emphasizing its relevance for improving blast furnace operation.

1.6 Reading guide

Figure 1.5 presents an overview of the thesis structure, highlighting the goal of each chapter, the corresponding research questions, and the methods used. Alongside this introduction, as well as the concluding discussion and summary chapters, these form the core framework of the dissertation. For reference, the thesis also includes a list of symbols and a glossary to help identify commonly used symbols and terms. Terms included in the glossary can be recognized throughout the text, as they are italicized and marked with a superscript cross (†).

Figure 1.5: Outline of the dissertation.

1.7 Bibliography

[1] J. Kim, B. K. Sovacool, M. Bazilian, S. Griffiths, J. Lee, M. Yang, and J. Lee. "Decarbonizing the iron and steel industry: A systematic review of sociotechnical systems, technological innovations, and policy options". In: *Energy Research & Social Science* 89 (2022), p. 102565. ISSN: 2214-6296. DOI: 10.1016/j.erss.2022.102565.

[2] worldsteel. *World Steel in Figures - 2024*. 2024. URL: https://worldsteel.org/wp-content/uploads/World-Steel-in-Figures-2024.pdf.

[3] International Energy Agency. *Iron and Steel Technology Roadmap*. 2020. URL: https://www.iea.org/reports/iron-and-steel-technology-roadmap.

[4] M. Geerdes, R. Chaigneau, and O. Lingiardi. *Modern Blast Furnace Ironmaking: An Introduction*. Ed. by Hisko Toxopeus Maarten Geerdes. Fourth. ISBN: 978-1-64368-123-8. IOS Press BV, 2020. ISBN: 978-1-64368-123-8.

[5] H. M. Ahmed, E. A. Mousa, M. Larsson, and N. N. Viswanathan. "Recent Trends in Ironmaking Blast Furnace Technology to Mitigate CO2 Emissions: Top Charging Materials". In: ed. by Pasquale Cavaliere. Springer International Publishing, 2016, pp. 101–124. ISBN: 978-3-319-39529-6. DOI: 10.1007/978-3-319-39529-6_6.

[6] Y. Pan, H. Zuo, J. Wang, Q. Xue, G. Wang, and X. She. "Review on improving gas permeability of blast furnace". In: *Journal of Iron and Steel Research International* 27 (2020), pp. 121–131. ISSN: 2210-3988. DOI: 10.1007/s42243-019-00321-y.

[7] C. A. Kruelle. "Physics of granular matter: Pattern formation and applications". In: *Reviews on Advanced Materials Science* 20 (2009), pp. 113–124.

[8] A. Hadi, R. Roeplal, Y. Pang, and D. Schott. "DEM Modelling of Segregation in Granular Materials: A Review". In: *KONA Powder and Particle Journal* advpub (2023), pp. -. DOI: 10.14356/kona.2024017.

[9] H. Y. Sohn and C. Moreland. "The effect of particle size distribution on packing density". In: *The Canadian Journal of Chemical Engineering* 46 (1968), pp. 162–167. ISSN: 0008-4034. DOI: 10.1002/cjce.5450460305.

[10] P. A. Cundall and O. D. L. Strack. "A discrete numerical model for granular assemblies". In: *Géotechnique* 29 (1979), pp. 47–65. DOI: 10.1680/geot.1979.29.1.47.

[11] J. Rojek. “Contact Modeling in the Discrete Element Method”. In: ed. by Alexander Popp and Peter Wriggers. Springer International Publishing, 2018, pp. 177–228. ISBN: 978-3-319-90155-8. DOI: 10.1007/978-3-319-90155-8_4.

[12] C. J. Coetzee. “Review: Calibration of the Discrete Element Method”. In: *Powder Technology* 310 (Jan. 2017). DOI: 10.1016/j.powtec.2017.01.015.

[13] T. Roessler, C. Richter, A. Katterfeld, and F. Will. “Development of a standard calibration procedure for the DEM parameters of cohesionless bulk materials – part I: Solving the problem of ambiguous parameter combinations”. In: *Powder Technology* 343 (2019), pp. 803–812. DOI: 10.1016/j.powtec.2018.11.034.

[14] S. Cole. *How to select a GPU (Graphics Processing Unit) for EDEM*. 2023. URL: https://community.altair.com/discussion/33296/how-to-select-a-gpu-graphics-processing-unit-for-edem.

[15] Delft High Performance Computing Centre (DHPC). *DelftBlue Supercomputer (Phase 2)*. https://www.tudelft.nl/dhpc/ark:/44463/DelftBluePhase2. 2024.

2

A Review of DEM-Based Models for Blast Furnace Permeability

This chapter reviews the key phenomena that influence burden permeability during blast furnace charging and examines how these have been represented in DEM models. The review has two main aims: first, to clarify the concept of burden permeability, outlining its significance for furnace performance and detailing the physical phenomena that govern it; second, to explore how these phenomena have been modeled and analyzed using DEM, highlighting current practices and areas for further research that also guide the case studies presented later in the thesis.

This chapter is based on:
R. Roeplal, Y. Pang, A. Adema, J. van der Stel, and D. Schott, *Modelling of phenomena affecting blast furnace burden permeability using the Discrete Element Method (DEM) – A review*, Powder Technology, vol. 415, 2023.
and
A. Hadi*, R. Roeplal*, Y. Pang, and D. Schott, *DEM Modelling of Segregation in Granular Materials: A Review*, KONA Powder and Particle Journal, vol. 41, pp. 78–107, 2024. (*joint first authors)

2.1 Burden distribution requirements

The raw materials involved in blast furnace ironmaking are iron ores, coke and hot gas. As shown in Figure 2.1, the furnace can be divided into five main zones based on the thermal and chemical state of the raw materials. The lumpy zone is located at the upper part of the furnace, where the materials remain in their solid form, undergoing minimal change as they are gradually heated while descending. As the particles reach the cohesive zone, the ore particles have melted sufficiently to form a cohesive, impenetrable mass. This zone is characterized by coke slits, which are the primary channels through which gas can still travel upward. In the active coke zone, the temperatures are at their highest, as coke undergoes active combustion, producing the heat required for the reduction of iron ore. The raceway is the region where hot gas is injected into the furnace. The oxygen in the hot blast combusts locally with the coke, generating a turbulent, high-temperature gas flow that rises through the furnace. The hearth is the lowest section of the furnace, where the molten iron and slag are collected. Here, the reduced materials reach their final state as molten iron, which is then tapped from the furnace for further processing.

The ore particles contain iron oxides which need to be reduced to iron by the hot gas, while the coke burden has multiple functions [1, 2]: (1) it fulfills the thermal and chemical requirements for the reduction process; (2) it acts as a carburizer; (3) it ensures adequate drainage of liquid products below the cohesive zone and passage for gas to and throughout the upper portion of the bed. The latter is possible due to the higher *permeability* of the coke bed compared to the ore bed, and the fact that only the coke layers remain permeable in the cohesive zone.

The permeability of a packed bed provides a measure for how well the voids between particles comprising the bed (*i.e.*, the pores) are connected [4]. This generally depends on the bed configuration; *i.e.*, on factors such as the packing fraction, and geometrical features (shapes and sizes) of the particles [5]. In the context of blast furnace productivity, the permeability determines to what extent the ascending gas is in contact with the ores, and therefore how well the reduction-melting process takes place. The literature suggests the following burden distribution guidelines regarding the permeability:

1. In the cohesive zone, there should be a minimum number and size of coke slits to allow adequate gas passage to the upper layers [6–8]. It is also important to have evenly sized coke slits, so that the gas flow is even in radial direction [9].

2. In the lumpy zone:

   (a) There should be a homogeneous packing structure in the ore and coke layers. Packing structure generally refers to the spatial arrangement of particles, influenced by particle morphology (size, shape, surface roughness), orien-

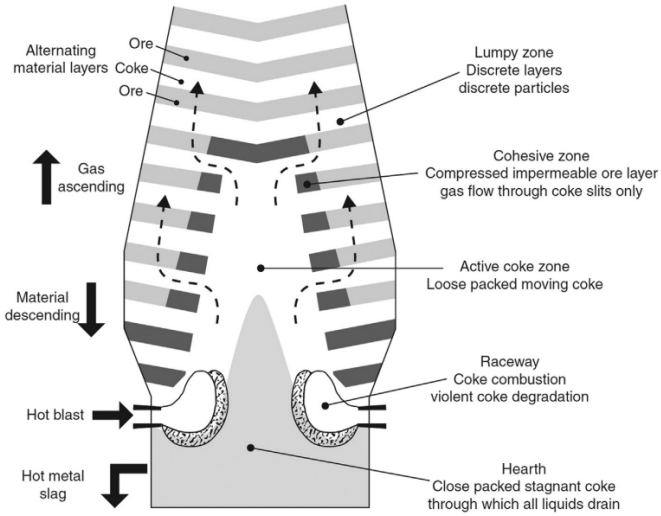


Figure 2.1: The five main zones in a blast furnace; image adopted from [3].

tation (especially for non-spherical particles), and packing formation (*e.g.*, compaction level). This structure determines the void space network, characterized by porosity (fraction of volume occupied by voids), connectivity (whether voids form continuous flow paths or isolated pockets), pore size distribution (range and frequency of void sizes), and tortuosity (degree to which flow paths twist and turn). Together, these factors control gas flow. A uniform packing structure ensures even gas distribution through the ore layer, giving all particles equal access to reducing gases.

(b) The different ore components should be evenly distributed within the mixed ore layer, as their differences in chemical composition are intended to produce a slag with optimal melting temperature and viscosity when combined in the furnace. This ensures efficient slag drainage. If component segregation occurs, sub-optimal slags will form, which in turn negatively impact permeability due to poor slag drainage. The increased viscosity of the slag can block the pores, hindering gas flow. Also, as the ores reach their melting points at different temperatures, an uneven radial and circumferential distribution at the top of the furnace can lead to problems in forming the cohesive zone which plays an important role in gas flow distribution [9].

(c) Each coke layer should have a sufficient and even thickness in radial direction in order to provide adequate gas flow to the subsequent ore layer along the

radius [9–11]. In general, the permeability increases with the coke layer thickness [11]; however, as the steel industry faces increasing pressure to minimize its carbon footprint, the coke layer thickness is minimized as much as possible in modern operation. Pulverized coal is injected with the blast to account for the reduced metallurgical coke rate. To maintain permeability in the cohesive zone, coke is added to the ore burden in the form of small (nut) coke [2].

(d) The ore layers should be as thin as possible to enhance gas–ore contact and have a uniform thickness along the radius [11].

(e) The layers should be nearly horizontal to minimize the effects of variations in repose angles. For instance, in an ore mixture, pellets have a lower angle of repose compared to sinter, which causes pellet particles to roll more easily toward the center of the furnace when the layers are not (nearly) horizontal. Additionally, fine particles tend to accumulate near the point of the stream's impact. If the layers are tilted, fine particles remain concentrated at the impact point, while larger particles roll toward the center. Consequently, tilted layers lead to a less uniform size and component distribution [11].

(f) The amount of fines should be limited, and their even distribution across the layers is essential, as localized concentrations can cause clogging. Increased resistance to gas flow creates an upward force on the burden, hindering its descent. Consequently, localized clogging can lead to irregular burden descent or even burden hanging.

These guidelines aim to diminish spatially separated regions of strong and weak gas flow throughout the packed bed. In practice however, this is not exactly aimed for by blast furnace operators. As shown in Figure 2.2, two basic operation modes are often described in literature [11–14]: central gas flow operation and wall-working operation. The main difference between the two lies in the gas flow distribution. In central gas flow operation, a strong gas flow is achieved in the center while the flow is directed towards the walls in wall-working operation. Other operation modes can also be found in literature such as "double-peak" and "flat" [9], but those are not discussed in this review. The preferential direction of gas flow in different operation modes is achieved by selective deposition of coke, as can be seen in Figure 2.2. Depending on the operation strategy which is aimed for, an "optimal" burden distribution can be defined. However, very little information on the burden distribution requirements corresponding to different operation strategies can be found in literature. According to Liu [9], wall-working operation is not desirable since wall erosion is highest and gas utilization is poor, while central gas flow operation has lowest wall erosion and better gas utilization. The flat operation mode has even better

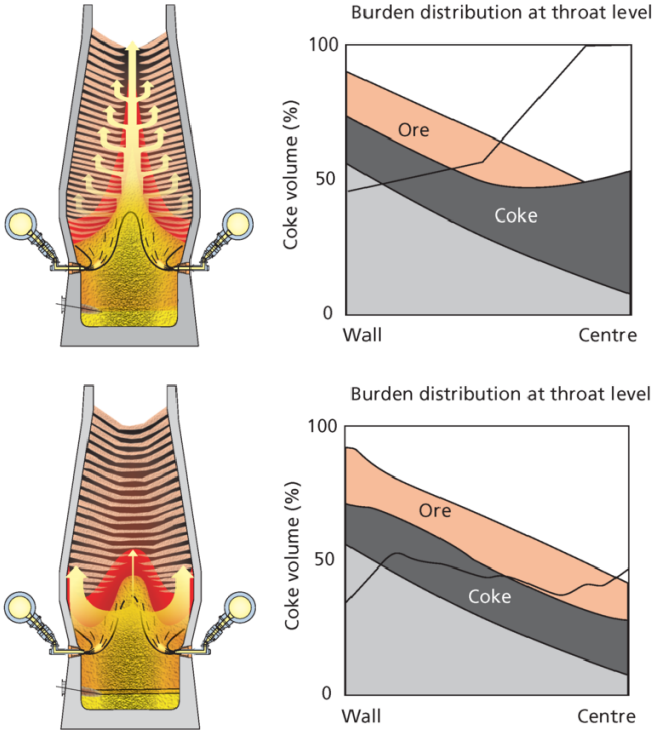


Figure 2.2: Two basic gas flow distribution strategies used in industry (from left to right): (a) central gas flow operation, (b) wall-working operation; images adopted from [11].

gas utilization, but does not offer the same degree of wall protection. Geerdes *et al.* [11] provide a clear set of requirements which, according to them, provides the ideal burden distribution for modern blast furnaces operating under high pulverized coal injection rates: "(1) an ore-free center, (2) nearly horizontal layers of coke and ore burden, (3) some nut coke in the ore burden in the wall area and (4) fines distributed over the radius".

Based on these findings, the following requirements are summarized to maintain good bed permeability and will be discussed in Section 2.2:

1. To achieve a uniform packing structure and composition, the burden should be evenly distributed within each layer. However, due to the use of various charging equipment and the differing physical properties of the materials, **segregation** (Section 2.2.1) can occur during charging, making perfect uniformity in the deposited ore layer unlikely. In addition to charging, segregation may also occur during descent, as the furnace widens gradually toward the bottom, causing the layers to

spread and increasing the potential for further segregation.

2. The generation of fines should be minimized. However, the large scale of the system results in substantial material storage, which imposes high stresses on particles. In addition, high flow velocities during charging and the resulting high-impact collisions during layering further contribute to particle **degradation** (Section 2.2.2). Consequently, particle breakage and fines generation are expected throughout the process. This is especially expected for the coke particles, which are much more prone to breakage than the ores.

3. A uniform mass distribution, both radially and circumferentially, is desirable. However, the so-called **flow deviation phenomenon** (Section 2.2.3) causes an imbalance in the circumferential mass distribution in bell-less top blast furnaces, the predominant design in modern operations. For the coke layer, the **coke-push effect** (Section 2.2.4) causes uneven mass distribution in radial direction.

The following sections review the literature focusing on modeling these phenomena using DEM, and the relevant findings. While the behavior of the coke layer and processes during descent fall outside the scope of this thesis, the review nonetheless includes relevant findings on these topics.

2.2 Overview of DEM models for burden distribution

Table 2.1 summarizes the collected literature (up to 2022) addressing the phenomena affecting permeability, as outlined in Section 2.1. The materials considered in each study are indicated in the table, where a '+' denotes mixtures and a '/' denotes materials considered separately. The table also specifies the portion of the system analyzed and includes notes on particular areas of focus. It is immediately apparent that most DEM modeling efforts have focused on segregation; however, the vast majority of studies address only size segregation within single material components. Mixtures are rarely considered, and when they are, the analysis is limited to particle size uniformity. Component segregation has received little attention, and notably, only Wei *et al.* [15] have investigated porosity distribution –thereby capturing segregation effects indirectly through packing.

Table 2.1: Summary of literature using DEM to model blast furnace material behavior. Abbreviations: P = pellet; S = sinter; L = lump ore; O = ores (used when it is unclear which type of ore); C = coke; n.s. = not specified. System: BLT = bell-less top; BT = bell top. Remarks: [a)] Single/serial-type hopper system, [b)] Parallel-type hopper system.

Source	Materials	System	Note
Segregation			
Mio *et al.*, 2008 [16]	S	Hopper-chute	Size segregation
Mio *et al.*, 2009 [17]	S	BLT charging system[a)] + furnace top	Size segregation
Mio *et al.*, 2010 [18]	S, C	BT charging system	Size segregation
Yu & Saxén, 2010 [19]	P	Hopper	Size segregation
Yu *et al.*, 2011 [20]	P, C	Furnace shaft (simplified)	Size segregation
Mio *et al.*, 2012 [21]	S, C	Delivery system + BLT charging system[b)] + furnace top	Size segregation
Yu & Saxén, 2012 [22]	P, C		
Yu & Saxén, 2013 [23]	P, C	BLT charging system[a)] + furnace top	Burden profiles
Wu *et al.*, 2013 [24]	S	P-W hopper	Size segregation
Yu *et al.*, 2014 [25]	C	P-W hopper	Size segregation
Zhang *et al.*, 2014 [26]	O, C	BLT charging system [b)] + furnace top	Segregation
Liu *et al.*, 2015 [27]	C	BLT charging system [a)] + furnace top	Material behavior during furnace charging
Schott *et al.*, 2016 [28]	P+S+C	Conical hopper	Size segregation
Xu *et al.*, 2017 [29]	C	BLT charging system [b)] + furnace top	Size segregation
Dianyu *et al.*, 2019 [30]	S, O	Blast furnace shaft	Mixed layer formation, porosity distribution
Govender *et al.*, 2019 [31]	S, C	BLT charging system [a)] + furnace top	Size segregation
Kou *et al.*, 2019 [32]	P+S+L	BLT charging system + furnace top	Size segregation
Mio *et al.*, 2019 [33]	S	Hopper-chute	Particle trajectories
Xu *et al.*, 2019 [34]	C	BLT charging system [b)] + furnace top	Size segregation
Chibwe *et al.*, 2020 [35]	P, S	BLT charging system	Segregation
Hong *et al.*, 2020 [36]	P, S, L	BLT charging system + furnace top	Component segregation
Mio *et al.*, 2020 [37]	S, C	BLT charging system + furnace top	Size segregation
Xu *et al.*, 2020 [38]	C	Delivery system + BLT charging system [b)] + furnace top	Size segregation
Wei *et al.*, 2021 [15]	S, C	BLT charging system + furnace top	Porosity distribution
Zhang *et al.*, 2021 [39]	C	P-W hopper	Size segregation
Li *et al.*, 2022 [40]	S, C	BLT charging system [a)] + furnace top	Size segregation
Degradation			
Ueda *et al.*, 2010 [41]	O, C	Blast furnace shaft	Material stresses
Circumferential imbalance			
Narita *et al.*, 2017 [42]	O, C	BLT charging system	
Holmes *et al.*, 2018 [43, 44]	P+S, C	BLT charging system [a)] + furnace top	

Continued on next page

Continued from previous page

Source	Materials	System	Note
Sun *et al.*, 2019 [45]	O	BLT charging system [b] + furnace top	
Holzinger & Schatzl, 2022 [46]	C	BLT charging system [b] + furnace top	
Chen *et al.*, 2022 [47]	P, S	BLT charging system [b] + furnace top	
Coke-push			
Mio *et al.*, 2009 [17]	S, C	BLT charging system[a] + furnace top	
Mitra & Saxén, 2015 [48]	P, C	BLT charging system [b] + furnace top	
Mitra & Saxén, 2016 [49]	P, C	BLT charging system [b] + furnace top	
Kou *et al.*, 2018 [50]	S, C	BLT charging system + furnace top	
Zhou *et al.*, 2021 [51]	P+S+L, C	BLT charging system [a] + furnace top	

2.2.1 Segregation

Segregation, also referred to as reverse mixing or de-mixing, is a phenomenon happening in moving granular materials in which particles with similar properties, *e.g.*, size, density and shape, tend to collect in certain parts of a mixture. Except for a few specific applications in mining and agricultural engineering [52], segregation is generally considered an undesirable occurrence affecting product homogeneity in a negative way. According to Silva *et al.* [53], there are thirteen segregation mechanisms in general. However, some of these mechanisms are either rare or special cases of others. Therefore, past researchers attempted to condense these segregation roots in different ways [54–56]. Williams identified four size-driven mechanisms: trajectory, percolation, vibration-induced rise of coarse particles (Brazil-nut effect), and elutriation [56, 57]. In addition to these size-based mechanisms, the buoyancy mechanism in which the difference in density drives segregation should be considered for multi-component mixtures [58]. Having said that, multiple mechanisms might take place simultaneously, making the prediction of the segregation pattern extremely challenging. For instance, in the case of the mixture of small light and large heavy particles, percolation and buoyancy mechanisms oppose each other and the overall segregation behavior of such a mixture is not known a priori [59]. Furthermore, since segregation only occurs for particles that are in motion –due to either shearing, by means of moving walls (such as in a shear cell or bladed mixer) or as a result of gravitational force (as is the case in hoppers) or vibration– it can be deduced that the formation of segregation patterns depends not only on the properties of the components relative to each other, but also on the system configuration and the degree and type of agitation imposed on the material. Although having knowledge of the mentioned mechanisms can shed light on the segregation behavior of particulate

mixtures, it is necessary to investigate each case independently to determine the dominant segregation mechanism(s).

In blast furnace operations, a burden layer is formed by charging concentric rings, usually starting at the throat periphery and ending at the center. Segregation during charging of these individual rings can pose an impediment to achieving a homogeneous burden distribution within a layer as a whole [60], which might affect the initial permeability distribution [61] and the subsequent redistribution caused by the deformation of burden layers during their descent. Therefore, it is crucial to understand how the burden (which is multi-component in nature when it comes to the ore mixture) segregates during charging and descent, and how this influences the permeability distribution.

Segregation during flow through the charging apparatus

The coke and ore burden are charged into the parallel hoppers either from a conveyor belt or a skip car [11]. In the case of a conveyor belt, some segregation of material can already occur during transportation on the belt due to its bouncing motion as it rolls over idlers. The small particles settle to the bottom of the belt while the coarse particles rest upon them. Going even further upstream, segregation also occurs as materials are discharged from storage onto the belt or into the skip car. Very little research has been done on the occurrence of segregation as the material is handled upstream of the hoppers. Spence [62] undertook a thorough experimental investigation on size segregation within the charging system, which included the entire material transportation from the stock house to the receiving hopper, material hopper, rotating chute and finally the furnace throat. They concluded that the segregation patterns emerging during material hopper discharge can be linked to segregation during filling of the receiving hopper. Another example is the work of Mio *et al.* [37], where a 1/3-scale furnace was used to investigate the distribution of coke and sinter in the throat after charging. In their system, the parallel hoppers received the burden materials from a surge hopper through a belt conveyor, and discharged into a funnel. By measuring the mass fraction of different-sized sinter particles as a function of time discharged from the funnel, they concluded that particle size segregation occurred during charging and discharging at the surge hopper and parallel hoppers since larger sinter particles were discharged later. While these experiments demonstrate that size segregation occurs upstream of the hoppers, and during filling of the hoppers, surprisingly little has been done to model the flowing behavior for this portion of the charging process, especially when it comes to loading and unloading of the skip cars or conveyor belt. Most DEM blast furnace research has been done by modeling the system starting with the parallel hoppers. For example, Zhang *et al.* [39], Wu *et al.* [24] and Xu *et al.* [29] all studied size segregation during hopper charging using a fictitious filling method in their simulations. Since the material being fed to the hoppers was assumed to

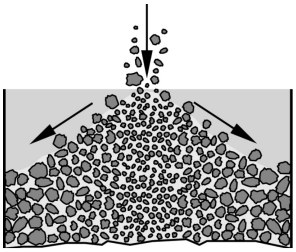


Figure 2.3: Illustration of size segregation during central filling of a vessel; image adopted from [65].

be nonsegregated in these works, the results on size distribution in the hopper may not be representative of the actual operation. Nonetheless, these works have all shown that small particles tend to remain close to the stream impact point while large particles tend to roll away during heaping. The authors all concluded that the size distribution in the hopper changes as a function of the filling position and angle. Size segregation during hopper discharge is dictated by the order in which segregated material groups flow out of the hopper. This depends primarily on the hopper design, but it is generally seen that large particles are discharged later than small particles [21, 24, 26, 29], as illustrated in Figure 2.4a. Since the burden is charged in rings to form a layer, size segregation during hopper filling and subsequent discharge can result in a non-homogeneous size distribution in both circumferential and radial directions.

It should be noted that actual blast furnace operation involves charging of an ore mixture, rather than one material component. As stated in Section 2.1, it is important for the ore layers to have a homogeneous composition. The segregation behavior of ore mixtures during hopper filling and discharge has been studied by Xu *et al.* [63, 64]. Their work is particularly relevant to processes in which the different types of ores are charged to the hopper in batches, rather than as a mixture. The authors investigated how the order of charging ores to the hopper affects the order of discharging and the final component distribution in the throat. They found that the trend of each component's mass fraction from the periphery to the center of the throat followed the mass fraction trend during discharging. This means that component segregation within the ore layer is a direct consequence of the ore mixture's discharging behavior from the hopper.

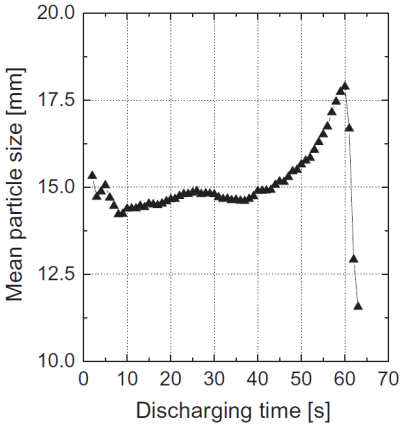
The next part of the charging apparatus which has received much attention is the rotating chute. The chute is the most flexible part of the system, as it can be controlled with respect to tilting angle (the angle between the chute baseline and the vertical center-line of the furnace) and rotating speed, which in turn affects the material flow within the chute itself, as well as the distribution on the stock surface in the throat. Researchers have mainly focused on understanding two main aspects: (1) how the

material segregates as it flows through the chute, and (2) how the bulk flow behavior on the chute affects segregation of the material in the furnace throat. With respect to point (1), several researchers [16, 17, 22, 26] have reported the occurrence of size segregation during chute flow. This is evident from the fact that the stream at the chute outlet has small particles at the inner part of the trajectory and large particles at the outer part. This pattern has been seen in both stationary and rotating chutes at different tilting angles [17]. As the particles flow through the rotating chute, they are subject to a variety of forces including inter-particle forces, particle–chute force, gravitational force, Coriolis force and centrifugal force [26]. The reader is referred to the work of Teng *et al.* [66] for a more in-depth description if these forces. The interplay of these forces determines the bulk behavior of the flow in the chute, specifically how compact/dilute the flow is at the chute outlet. When it comes to point (2), researchers have studied the effect of chute design [32] and operation [36, 50] on the stream width and thickness, and how these factors affect segregation during layer build-up. These aspects are discussed later, in Section 2.4.

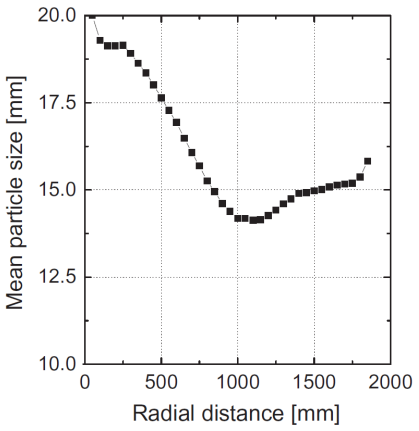
Segregation during layer build-up

Segregation during layer build-up can occur due to different phenomena occurring simultaneously. First of all, when the particles exiting the chute are charged onto the stock surface, segregation due to heaping occurs. Each layer is formed by charging multiple rings, which are essentially heaps of material along the throat circumference. Hence, it is important to understand how the heaping process occurs as the rings are charged in order to understand the burden distribution. Xu *et al.* [67] performed a simple investigation in which a binary mixture of two particle sizes was charged to a 1/15-scale blast furnace throat through a rotating chute. They only charged a single ring of material and found that the larger particles concentrated near the furnace wall while the small particles were near the center. Mio *et al.* [21] simulated the charging behavior of polydisperse sinter through multiple rings in a full-scale furnace. They found that ultimately the average particle size was largest at the furnace center, while the smallest average size was found at around half of the radius (see Figure 2.4b). They later confirmed this radial size distribution through experiments [37]. According to the authors, small particles are relatively immobile after impacting the stock surface and therefore stay in the vicinity of the burden stream's impact point, while large particles are able to roll towards the center during charging of the rings. Therefore, there are more large particles in the center of the furnace. Other researchers [15, 26, 40] provided a similar explanation after observing this accumulation trend in their DEM results. Yu and Saxén [23] also found this trend in their study of pellet charging, but they reported that the degree of segregation was much less compared to sinter due to the relatively narrow size distribution of pellet particles. The focus of these studies has

been on size segregation when charging a single material to the furnace. Investigations of segregation during multi-component mixture charging are scarce. Xu *et al.* [67] extended their aforementioned size segregation study by varying the densities of the large and small particles individually and scrutinizing the effect on segregation. Their results showed that radial size segregation was reduced as the density of small particles increased, while the opposite was true when the density of large particles was increased. In reality, the ore mixture contains three materials (or four, if nut coke is present), each with their own size distributions. Hence, further investigation is required to understand the segregation behavior of blast furnace mixtures during heaping.



(a) Mean particle size in the flow at the outlet of a hopper; image adopted from [21].



(b) Relation between mean sinter particle size and radial distance; image adopted from [21].

Figure 2.4: Comparison of particle size distributions and their relationship with flow characteristics.

Up to this point, the discussion has focused on how radial segregation occurs during layer build-up. Segregation in the vertical direction also arises due to the sieving phenomenon: small ore particles become embedded in the upper part of the coke layer during charging and subsequently travel toward the bottom of the coke layer. This phenomenon results in the formation of a mixed coke-ore layer (see Figure 2.5), which is densely packed and has a lower permeability than the individual coke and ore layers [15]. Several researchers [68–71] have shown experimentally that, depending on the size ratio between particles of the individual layers, this “interface resistance” can have a significant effect on the pressure drop over a stagnant bed. Kajiwara *et al.* [72] performed full-scale experiments of charging ore onto a coke layer and observed both the coke-push phenomenon and the mixed layer formation. Wei *et al.* [15] used DEM to simulate sinter and coke layer formation using a small-scale setup. They charged three alternating layers

of sinter and coke, and studied the effect of segregation and mixed layer formation on the porosity distribution within the entire bed. They found that the porosity varied in both radial and axial directions: a higher porosity was found in the center of the furnace due to the higher average particle size in that region and a lower porosity was found in the bottom layers due to the presence of small particles and the compaction caused by the top layers. In general, the porosity of coke layers was highest while that of the mixed layers was the lowest. Li *et al.* [40] used a full-scale model to investigate both vertical and radial segregation when charging ore onto a layer of coke particles. For simplicity, they used a binary mixture of large and small particles for both materials and investigated the effect of the size ratio (defined as the ratio of small to large particle diameters) of the particles on segregation. Not surprisingly, the radial segregation worsened as the size ratio decreased. As this study was performed at full-scale, the flow conditions were representative of an actual blast furnace; however, the materials were not. Future studies should include more realistic size distributions to study the vertical segregation more accurately.

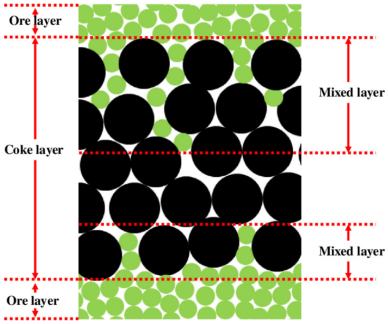


Figure 2.5: Illustration of coke-ore mixed layers; image adopted from [30].

Segregation during burden descent

As the packed bed descends, the coke and ore mixture layers tend to spread out due to the gradual widening of the furnace [73]. Consequently, the voids between particles in each layer become larger and the ore particles are able to further infiltrate underlying coke layers. Hence, the mixed layers formed during charging become thicker, and individual coke and ore layers become thinner. This process has not been studied extensively in a setting representing actual blast furnace operation. Although inter-particle percolation has interested researchers for many years now, most of the work in this field involves analysis of the percolation behavior of only few particles in a simplified setup (*e.g.* a static, relatively small cylindrical packed bed) using idealized materials such as beads.

These analyses have been done both experimentally [74, 75] and numerically [76–80], primarily to gain fundamental understanding of the percolation phenomenon. When it comes to blast furnace materials, only Yu & Saxén [81] attempted to study percolation during burden descent experimentally. The authors developed an experimental setup (see Figure 2.6) which allowed for visual inspection of pellet-coke mixed layer formation due to furnace widening. They developed a DEM counterpart of this setup to study the effect of different model parameters on the extent of percolation. The findings are discussed in the next chapter.

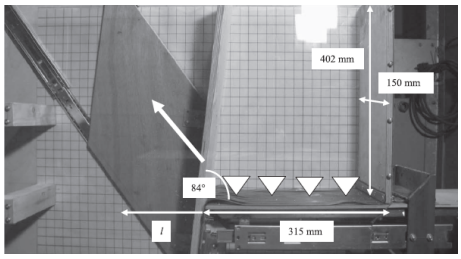


Figure 2.6: Experimental device used to emulate percolation segregation during burden descent; image adopted from [81].

2.2.2 Degradation

Degradation involves the generation of fines and broken particles during transportation and handling. Different types of degradation can occur, depending on the type and magnitude of forces causing degradation [82]. The furnace permeability is directly affected by the proportion of fines in the packed bed. This is true for all burden materials, but perhaps more important for the coke layer which is responsible for gas passage and liquid drainage in lower parts of the furnace. Hence, it is important to quantify degradation of burden materials at each handling stage.

Researchers have performed experiments to investigate degradation of coke [83–86], lump ore [83, 87–89], pellet [90, 91] and sinter [83, 86] using drop tests, impact tests, slow compression tests and tumbling tests. The purpose of these tests is to relate the forces responsible for degradation to the particle size and shape distributions resulting after degradation has occurred. Tavares [92] developed a model to predict the breakage behavior of these materials under different conditions. This model is currently implemented in Altair® EDEM™ and Ansys Rocky™. Despite the possibility of modeling breakage phenomena using DEM, no studies focusing specifically on blast furnace burden breakage modeling have been encountered in the literature. Instead, existing research has used DEM to investigate various aspects related to breakage. For example, Nouchi *et al.* [93] assessed where stresses exceed the compressive stress of coke and therefore could result

in abrasion. Zhang *et al.* [94] determined optimal furnace wall angles based on the stress levels and therefore the expected degree of abrasion occurring for different furnace designs. In these studies, the particles in DEM were modeled as spheres and the breakage mechanism itself was not modeled. Natsui *et al.* [95] used DEM-CFD to determine the effect of coke degradation on the permeability of a coke packed bed. Rather than modeling the degradation process, they assessed how permeability changes after degradation in separate simulations. They initially performed simulations using virgin coke particles. Through tumbler experiments, they could identify the volume of coke fines generated after 50 drum revolutions. Next, they performed simulations of the degraded particle bed by adding a representative amount of fines to a bed of coke particles which had decreased in size, compared to the initial simulation. They examined and compared the distribution of fines and gas velocity in both scenarios, confirming an intuitive expectation: as the number of fines increases, the pressure drop across the bed also rises (indicating a decrease in the bed's permeability). Interestingly, they also discovered that fines lodged between large coke particles can cause these particles to rotate and slip, altering the bed's structure and resulting in markedly different pressure drops, even with the same quantity of fines. Although this study was conducted using very small-scale simulations, it highlights how particle-scale phenomena can significantly influence macroscopic parameters, such as the pressure drop in a packed bed.

2.2.3 Flow deviation phenomenon

Two types of charging systems are often encountered in blast furnace operation: bell top (BT) and bell-less top (BLT). Bell-less systems (serial-type and parallel-type) are typically used in large and new blast furnaces with an improved design providing greater flexibility of charging method and more efficient burden distribution control when compared to bell-type systems [96]. Figure 2.7 illustrates the basic material handling equipment involved in blast furnace charging using serial-type and parallel-type BLT. Compared to the serial-type BLT, the parallel-type requires an additional connection chute (also referred to as the "funnel" or "Y-tube") to direct the material discharged from the bunkers to the rotating chute. Figure 2.8 shows that, unlike in a serial-type BLT, the flow discharged from the bunker is de-centred inside the funnel. This deviation of the material stream's centroid from the center line results in a variation of its collision point on the chute as it rotates [97–100] and this imbalance ultimately causes an uneven circumferential burden distribution in terms of the charged mass flow and the material falling point just above the stock surface.

Xu *et al.* [101] used DEM to investigate the difference in burden distribution when using a serial and parallel-type BLT. They found an even mass distribution in circumferential direction when using a serial-type BLT. For the parallel-type BLT, the mass distribution

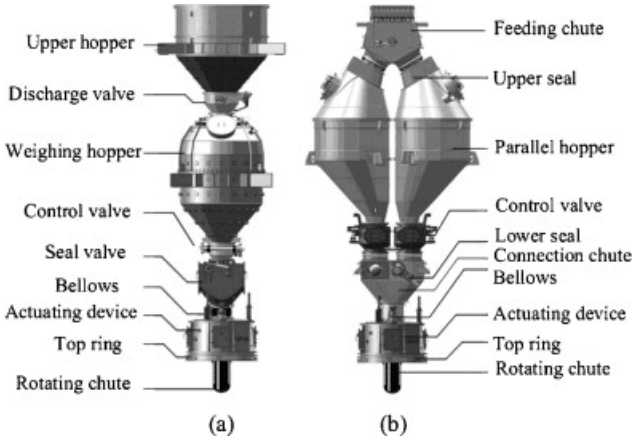


Figure 2.7: Basic material handling equipment in (a) serial-type and (b) parallel-type BLT systems; image adopted from [26].

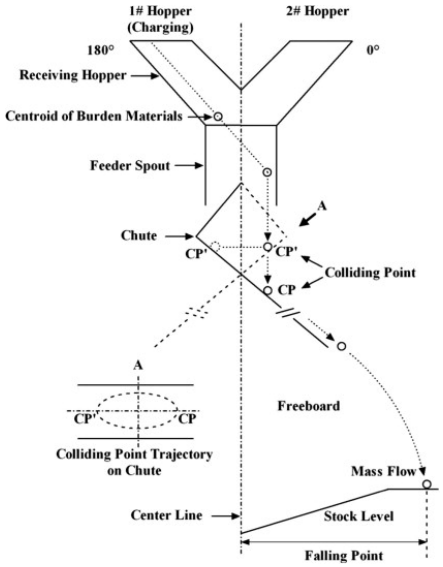


Figure 2.8: Particle flow trajectory in a parallel-type BLT; image adopted from [99].

plot resembled a cosine-like curve, thereby demonstrating the circumferential imbalance. Narita *et al.* [42] performed experiments using a 1/5-scale model of a charging apparatus and confirmed the existence of the circumferential imbalance. Using DEM, they looked at the forces acting on the particles upon entering the chute and claimed that the material is forced to travel along one side of the chute due to its curvature. When the centrifugal force acts in the same direction as the curvature force, then the material discharges at a higher position than when these forces oppose each other. Hence, the authors claimed that this difference in material stream discharge height causes an uneven falling point along the circumference. Using their DEM model, they investigated how the Y-tube design can be adjusted to mitigate the circumferential imbalance. Sun *et al.* [45] used DEM to analyze how the material flow on the chute changes with the collision point. They stated that when the collision point is located higher on the chute, then the flow of material on the chute is relatively sparse. When the striking point is lower, the particles falling down from the funnel tend to accumulate on top of material which already on the chute, making the flow denser. Hence, alternately sparse and dense granular flow exit the chute as it rotates, causing the uneven circumferential mass distribution in the throat. Chen *et al.* [102] used DEM to perform a thorough investigation of how the circumferential imbalance occurs. They claimed that the deflection of particle flow on the chute depends on the interplay between Coriolis force and curvature force, which in turn depends on the collision point on the chute (as summarized in Figure 2.9). Next, they investigated how the mass flow rate and Y-tube design affect the circumferential imbalance. Xu *et al.* [34, 38, 63, 103] investigated how design and operational factors can be adjusted to mitigate the circumferential imbalance. The results of all studies related to equipment and operation design are discussed in Section 2.4.

2.2.4 Coke-push effect

Coke-push occurs when ores are charged onto a layer of relatively light coke particles; this is also referred to as coke layer collapse or gouge formation. The ores “push” the coke particles aside, thereby deforming or shifting the coke layer which ultimately changes the coke-ore distribution, and therefore the permeability [104], in radial direction. Figure 2.10 presents an example illustration of the coke collapse phenomenon. As the top surface of the burden is V-shaped, the coke particles roll down towards the center of the furnace. However, other surface shapes (*e.g.*, “A” or “M” or “W”) are also possible, and the direction in which the coke is shifted depends on the location of impact with respect to the peak [105]. Zulli *et al.* [106] performed experiments using a full-scale furnace model to investigate the coke collapse degree when sinter was charged onto pre-existing coke layers. They found that the radial ore-to-coke distribution was significantly affected by this phenomenon. Ho *et al.* [107] used spheres made of different materials to study gouge

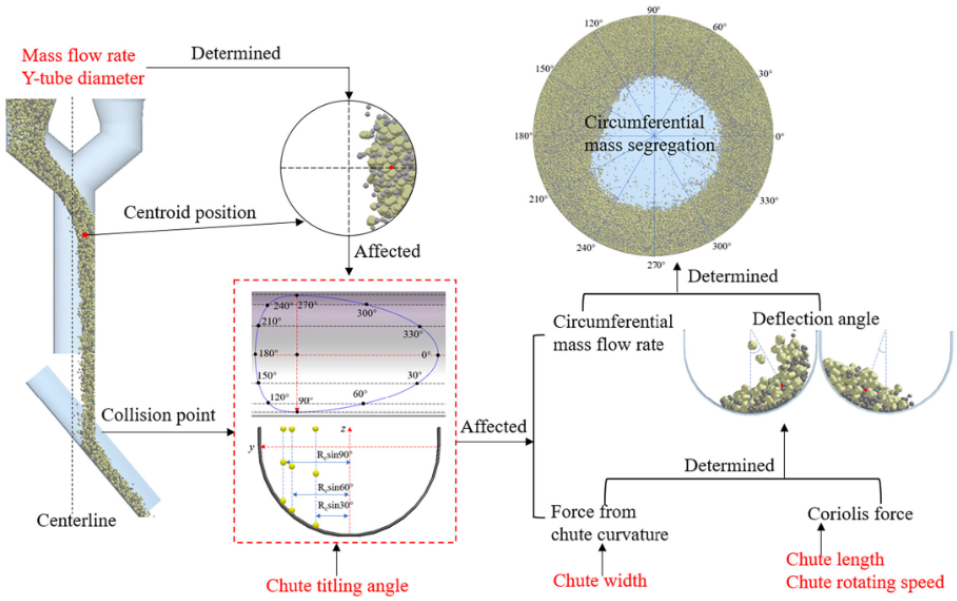


Figure 2.9: Factors affecting circumferential imbalance; image adopted from [102].

formation experimentally in a lab-scale charging setup. They found that the gouge size increases as with the density of the charged material. Mitra and Saxén [48, 49] used DEM to simulate the coke-push effect when charging pellets onto a coke layer using a 1/10-scale blast furnace model, showing that DEM was able to predict this phenomenon. Mio *et al.* [17] simulated sinter charging onto a coke layer using a full-scale model, showing that the coke layer thickness changes significantly in radial direction after coke collapse. Kou *et al.* [50] also used a full-scale model to investigate coke collapse after sinter charging. They found that the severity of coke collapse depends on the chute angle, rotational speed and the amount of sinter being charged. Zhou *et al.* [51] developed a more realistic simulation where pellets, sinter and lump ore were mixed and charged on top of a coke layer in a full-scale furnace model. They investigated the effects of different charging practices such as reverse charging and central coke charging on coke collapse. These aspects are discussed later, in Section 2.4.

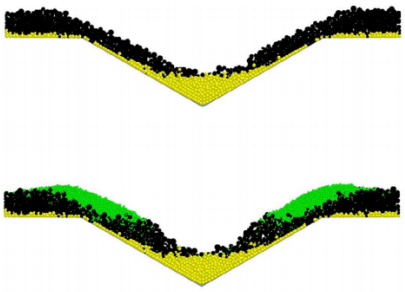


Figure 2.10: Radial burden profiles before (top) and after (bottom) collapse, where yellow, black and green particles represent sinter base, coke and charged sinter, respectively; image adopted from [50].

2.3 Performance metrics for segregation

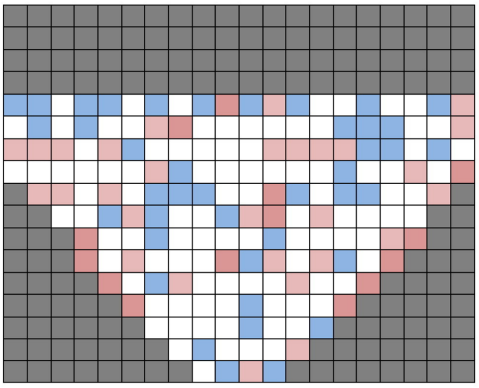
Segregation is a phenomenon of interest not only in blast furnace processes but also in various other systems where mixture uniformity is critical. This section provides an overview of segregation metrics as reported across a broader range of applications in the literature, extending beyond the blast furnace, as discussed in [108].

Since DEM allows tracking the position of each individual particle, it becomes relatively simple to assess the degree of segregation within a system. This can be done in different ways. One approach is to divide the system into subdomains and subsequently determine how different mixture components are distributed in the subdomains by means of plots. Gradient plots are useful for visualizing the distribution of a single mixture component in a system. For example, Xu *et al.* [29] used a gradient plot (see Figure 2.11a) to visualize how small particles within a mixture were distributed after filling a hopper. Since they were dealing with a binary mixture, showing the distribution of one component was sufficient to demonstrate how well the material was mixed in the hopper. When dealing with multi-component mixtures, monitoring only one component's distribution is no longer sufficient and other types of plots can be used. Figure 2.11b shows an example of line plots for monitoring the radial distribution of four different particle sizes in a blast furnace. The method of plots is beneficial as it provides two important insights: (1) whether or not different mixture components are evenly distributed and (2) where the different components are concentrated in case of uneven distribution.

Another method is to use an index which reflects the degree of segregation based on its value. There are generally two types of segregation indices: grid-dependent and grid-independent [109]. In the first type, the system is divided into subdomains similar to the method of plots. The distribution of one mixture component (referred to as the tracer) is evaluated and the segregation index is then determined through statistical analysis of the tracer distribution. If the tracer is distributed evenly, then the material is considered

2

(a)



(b)

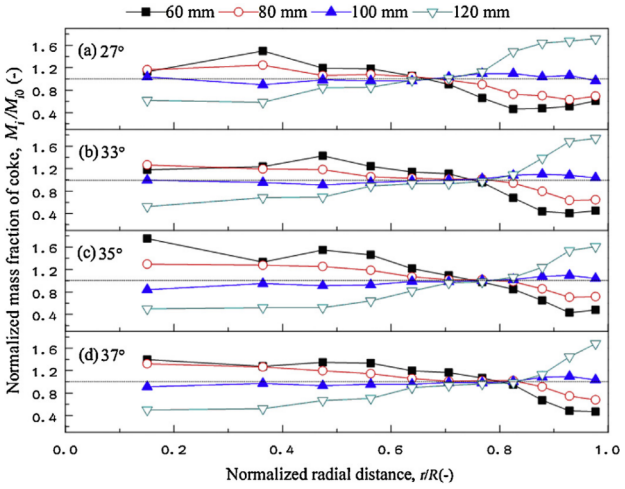


Figure 2.11: (a) Gradient plot for demonstrating how a single component is spatially distributed inside a system (image adopted from [29]) and (b) line plots for different coke sizes, showing how they are distributed inside a blast furnace after being charged using various chute angles (image adopted from [26]).

to be well-mixed and this is reflected by the value of the segregation index. In the second type, the value of the segregation index is determined by considering how the tracer particle is distributed within the system as a whole, rather than in subdomains. The tracer's distribution is generally evaluated on a distance or contact basis, as described by Bhalode and Ierapetritou [109]. The index value reflects how spread out the tracer particles are in the whole system.

The benefit of using an index is that it allows for a quantitative comparison of segregation for different scenarios by means of a single value. This might be more difficult to do with the method of plots, which provides a more qualitative comparison. However, it is generally known that grid-dependent indices depend on the chosen size of the subdomains [110–112] which makes it difficult to judge the degree of segregation based on the index value. For this reason, researchers often investigate how sensitive their segregation predictions are to the grid size. While the grid-independent indices do not have this shortcoming, they are often computationally intensive, especially for industrial applications where millions of particles are involved. Table 2.2 presents a number of frequently unemployed segregation indices, which have grouped by the calculation method (grid-dependent / grid-independent). The equations for calculating the indices are given as well as the range of values which can be assigned to the index. For indices no. 1-8, the concentration of tracer particles is determined in each sub-domain, which can be expressed in terms of the number, mass or volume fraction (y, x or c, respectively). Lastly, the type of segregation index based on the classification according to Bhalode and Ierapetritou [109] is indicated. It is important to note that, as with the method of plots, the single tracer approach is applicable only to binary mixtures. Accordingly, each segregation index indicates whether it is based on a single tracer distribution. For binary mixtures, the single-tracer based segregation indices in Table 2.2 can be used since monitoring one tracer's distribution is sufficient to infer the degree of segregation. For indices which can be applied to multi-component segregation, the reader is referred to the work of Cho *et al.* [110], who studied segregation in a mixer.

2

Table 2.2: Comparison of commonly used segregation indices, categorized by grid-dependence and measurement approach, including their formulations, output ranges, and classification criteria.

Source	Segregation Index	Values (mixed–segregated)	Classification
Grid-dependent			
Panda and Tan [113, 114]	$SI = \sqrt{\frac{\sum_{j=1}^{m}(c_t^j - c_t)^2}{m}}$	0 – (**)	Variance-based / single tracer
Li *et al.* [40]	$SI = \frac{\sum_{j=1}^{m}\left(\frac{N^j}{N}(y_t^j - y_t)\right)^2}{y_t(1-y_t)}$	0 – 1	Variance-based / single tracer
Mantravadi and Tan [115]	$SI = \sqrt{\frac{\sum_{j=1}^{m}\left(\frac{x_t^j}{x_t} - \left(\frac{x_t^j}{x_t}\right)_{\text{avg}}\right)^2}{m-1}}$	0 – (**)	Variance-based / single tracer
	$SI = \frac{\sigma_0^2 - \sigma^2}{\sigma_0^2 - \sigma_r^2}$	1 – 0 (***)	Variance-based / single tracer
Zhang *et al.* [26]	$SI = \sqrt{\frac{\sum_{j=1}^{m}\left(\frac{x_t^j}{x_t} - \left(\frac{x_t^j}{x_t}\right)_{\text{avg}}\right)^2}{m}}$	0 – (**)	Variance-based / single tracer
Zhao *et al.* [116]	$SI = \frac{\left(\frac{\sum_{j=1}^{m} x_{t_1}^j h_j}{\sum_{j=1}^{m} x_{t_2}^j h_j} - 1\right)}{\left(\frac{2x_{t_2} + x_{t_1}}{x_{t_1}} - 1\right)}$	0 – 1	Distance-based / two tracers
Combarros *et al.* [117]	$SI = \sqrt{\frac{\log\sigma_0^2 - \log\sigma^2}{\log\sigma_0^2 - \log\sigma_r^2}}$	1 – 0	Variance-based / single tracer
Grid-independent			
Zhang *et al.* [118]	$SI = \frac{\sigma_0^2 - \sigma^2}{\sigma_0^2 - \sigma_r^2}$	1 – 0	Contact-based
Mandal and Khakhar [119]	$SI = \frac{\text{COM}_{\text{final}} - \text{COM}_{\text{initial}}}{\delta}$	0 – 0.5	Distance-based / single tracer
Chibwe *et al.* [35]	$SI = \frac{\bar{l} - l_{\min}}{l_{ud} - l_{\min}}$	1 – 0	Distance-based / single tracer

Remarks:

(**) For these indices, the maximum value of SI depends on the mixture composition, as the equations contain the variables c_t, y_t, and x_t, which represent the concentration of the tracer in the entire mixture.

(***) In these equations, σ^2, σ_0^2, and σ_r^2 are calculated as follows:

$$\sigma^2 = \frac{\sum_{i=1}^{n}(y_t^i - y_t)^2}{n-1},$$
$$\sigma_0^2 = y_t(1-y_t),$$
$$\sigma_r^2 = \frac{y_t(1-y_t)}{N^i}.$$

2.4 Improvement of burden distribution: effects of design and operational parameters

The design of equipment has a large influence on the burden flow behavior, and therefore the material distribution on the stock surface [24, 38]. Hence, design modification should be considered when exploring the possibilities for enhancing gas-solid interactions in the furnace. However, it is generally more practical to consider how operational conditions can be adjusted, rather than modifying existing equipment design. Operational conditions refer to parameters which can be changed for a given system design. The following discusses how design and operational aspects of different parts of the system can be modified to improve the resulting material distribution, based on findings from blast furnace DEM studies.

2.4.1 Parallel hoppers

As mentioned previously, the hoppers can be loaded using a conveyor or skip cars. The loading method is expected to affect how the burden segregates as it is charged to a Paul-Wurth hopper. Zhang *et al.* [39] investigated the effects of the angle and position of a feeding chute on size segregation during loading of a binary coke mixture to a hopper. The filling procedure in simulations was as follows: pre-mixed particles were generated randomly in a conical feeder bin above the hopper and subsequently discharged through the feeding chute (see Figure 2.12), which replaced the belt charging used in practice. Since the conical feeder bin produced a mass flow upon discharging, the degree of segregation in the hopper after charging was solely the result of segregation during the confined heap formation in the hopper. Parameter studies were performed by adjusting the angle and endpoint of the inclined surface, as shown in Figure 2.12. It was seen that the degree of segregation became less as the filling position was closer to the center of the hopper, and as the filling angle was more vertical.

Wu *et al.* [24] performed a similar analysis for the filling position (either left, center or right, as shown in Figure 2.13), but they considered a ternary mixture of sinter particles and they used a virtual factory rather than a mass flow hopper to generate particles. Their results showed that small particles are generally located near the burden apex, indicating that small particles always tend to accumulate around the striking point during hopper filling. They also concluded that segregation was different for each filling position; but, contrary to the results of Zhang *et al.* [39], it could not clearly be seen that the degree of segregation was less in the case of a centered apex. Xu *et al.* [103] also studied hopper filling, but they simulated the filling process using a feeding belt which resembles the actual hopper filling process. As shown in Figure 2.14, the material discharged from the feeding belt entered a switch chute, which directed the flow to the parallel

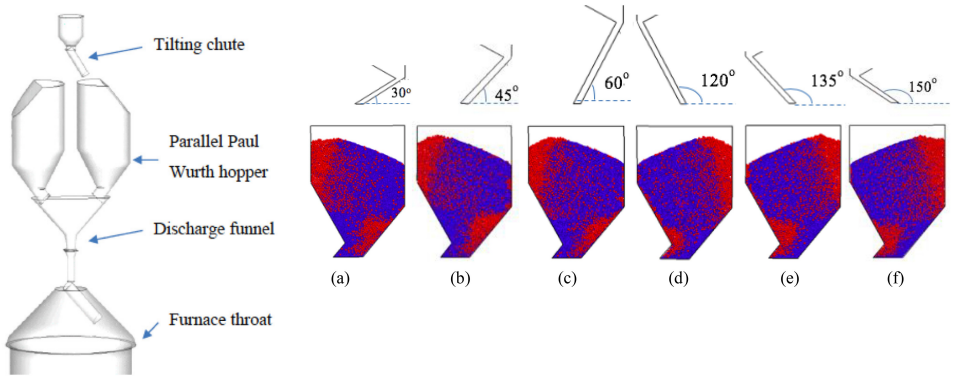


Figure 2.12: Different tilting chute designs for charging the Paul-Wurth (P-W) hopper; images adopted from [39].

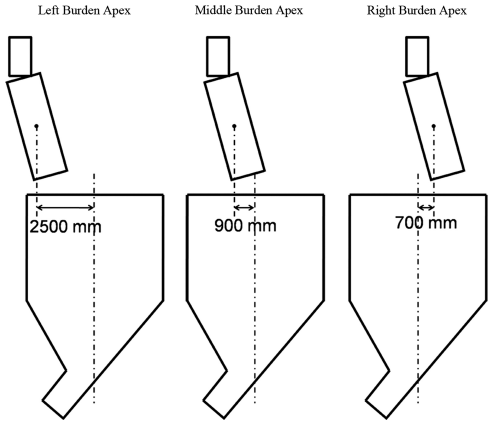


Figure 2.13: Different locations of the charging chute for the P-W hopper; images adopted from [24].

hoppers. They found that when the center line of the feeding belt did not coincide with the symmetry plane of two parallel hoppers, there was a difference in the velocity of the flow to and subsequent burden distribution in the left and right hopper. The burden apex positions were different in the two hoppers, as well as the volume distribution in radial and circumferential directions. The effect on segregation was not investigated.

Segregation during hopper discharge is a result of the sequence of discharge of material. It has been shown that the discharge sequence depends on hopper design and how the material is arranged in the hopper [120]. The former has been shown for example by Wu *et al.* [24]. They scrutinized the effect of hopper outlet slope on size segregation. Keeping in mind that the parallel hoppers should be designed such that the outlet is close

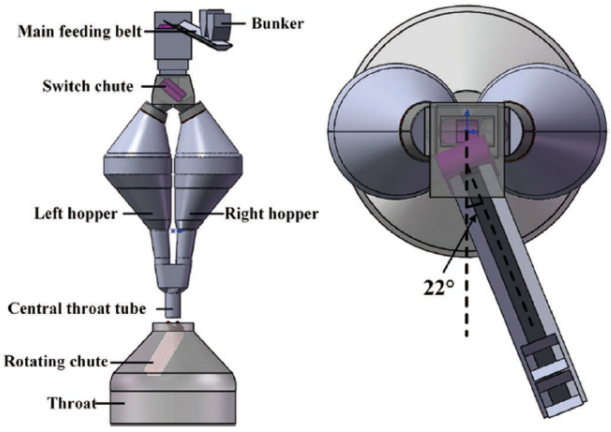


Figure 2.14: Layout of a BLT-charging system with parallel hoppers (left) and the angle between the centerline of the main feeding belt and the symmetry plane of two parallel hoppers; image adopted from [103].

to the furnace center, they considered three hoppers with varying slope outlets but each discharging close to the furnace center (see Figure 2.15). They found that the material discharging sequence was completely different for each design. In fact, for the left outlet hopper the material at the left side was discharged first, while the opposite was true for the right outlet hopper. Moreover, the right outlet hopper had a long outlet pipe which enhanced size segregation. Another design aspect is the hopper outlet size, which was studied by Zhang *et al.* [39]. They described the existence of the so-called "engulfing phenomenon", which involves the formation of a dip in the material during discharge. The dip engulfs large particles in its vicinity so that the discharge composition fluctuates. As the outlet size increases, the moving layers become larger and there is less time for the engulfing mechanism to take place; hence, there is less fluctuation and segregation decreases. When it comes to initial material arrangement, Xu *et al.* [63, 64] scrutinized the discharging behavior of a pellet, sinter and lump ore mixture. In some blast furnace operations, these materials may be charged to the hopper in batches rather than as a mixture. The authors investigated how the charging sequence of the materials to the hopper affects the discharging sequence. They found that particles charged first into the hopper were in fact not discharged first and that different initial arrangements of pellet, sinter and lump ore in the hopper resulted in different (radial and circumferential) burden distributions in the throat. Since each component has a different permeability, the authors pointed out the importance of studying how the initial distribution in the hopper affects the final distribution in the throat.

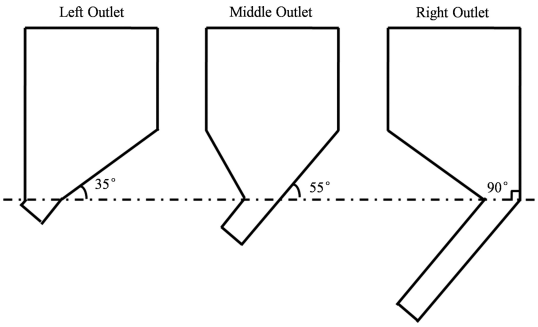


Figure 2.15: Different hopper designs used for analyzing the effect of hopper outlet slope on size segregation during hopper discharge, from left to right: left outlet, center outlet and right outlet; images adopted from [24].

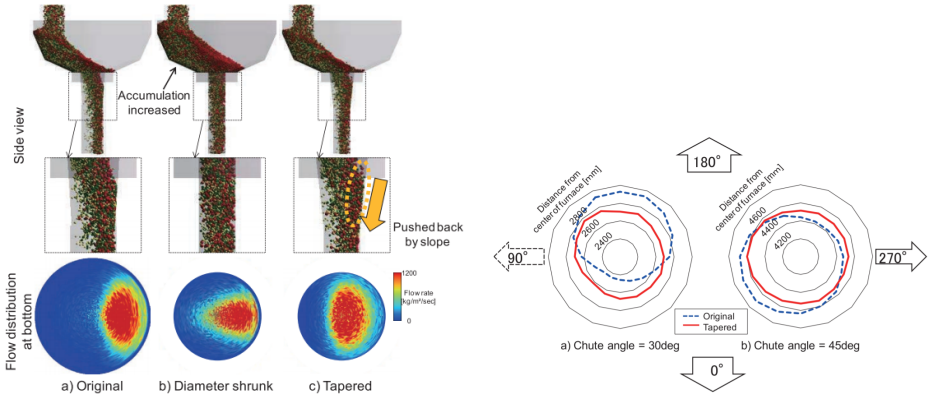
2.4.2 Funnel (Y-tube)

As discussed in Section 2.2.3, the deviation phenomenon occurring in the funnel of a parallel-type BLT charging system eventually leads to a circumferential imbalance of the burden mass in the throat. The burden does not flow through the center of the funnel but rather concentrates either at the right or left side, depending on which hopper is being discharged. Narita *et al.* [42] studied whether the funnel outlet design can be adjusted to produce a more centered burden flow through the funnel outlet, with the aim of mitigating the circumferential imbalance. They considered two adjustments of the funnel outlet, as shown in Figure 2.16a: a smaller outlet diameter compared to the original design, and a tapered outlet rather than a straight pipe. The authors found that particles easily de-center when the original funnel outlet design is used, and that the burden's falling point trajectory depends on the chute tilting angle. Using a smaller funnel outlet was not effective in reducing the imbalance; instead, the burden accumulated inside the funnel. On the other hand, the tapered chute outlet created a "push-back" effect on the de-centered burden stream and, as shown in Figure 2.16b, resulted in a more even circumferential distribution at different chute tilting angles. Chen *et al.* [102] also investigated the effect of funnel outlet diameter and found that increasing the outlet diameter had an adverse effect on the circumferential mass imbalance. Compared with the findings of Narita *et al.* [42], it can be concluded that an optimal outlet diameter exists, for which no accumulation of burden occurs in the Y-tube while the circumferential mass imbalance remains minimal. This topic could be further investigated in future studies.

2.4.3 Rotating chute

Tilting angle, length and rotational speed

The chute's tilting angle, rotational speed and length all affect the magnitude of centrifugal



(a) (b)

Figure 2.16: Effect of funnel outlet shape on: (a) Burden de-centring in the funnel and (b) circumferential particle trajectory; images adopted from [42].

and Coriolis forces acting on the material as it flows through the chute. As the tilting angle and length increase, the particles' residence time on the chute becomes longer and therefore, the particles experience centrifugal and Coriolis forces for longer times. Consequently, the material stream will tend to move along one side of the chute and, according to Hong *et al.* [36], this tendency increases with the chute angle and length. Figure 2.17 illustrates how three performance indicators (stream width, thickness and main striking point *or* MSP) for characterizing the burden distribution *during charging* are defined. Kou *et al.* [32] and Hong *et al.* [36] studied the effect of, among other factors, the chute angle, speed and length on these performance indicators. Despite using the same system, particles, particle sizes, interaction parameters, mass flow rate, amount of material and definitions of performance indicators, Hong *et al.* reported that the stream width increases with the chute angle, while Kou *et al.* reported the opposite. Their results on the effect of chute angle on stream thickness were also not in agreement, while they both stated that the MSP increases with the tilting angle. Zhang *et al.* [26] stated that the stream width increases with the chute angle, thereby forming a heap with a lower peak compared to a heap formed at small tilting angles. They state that large particles can easily roll off this relatively flat heap towards the center of the furnace.

As the centrifugal and Coriolis forces increase with the rotational speed, the material also tends to collect at one side of the chute as the rotational speed increases. Also, the particles at the chute outlet have a higher tangential velocity as the speed increases. Kou *et al.* [50] found that a high tangential velocity of ores is favorable with respect

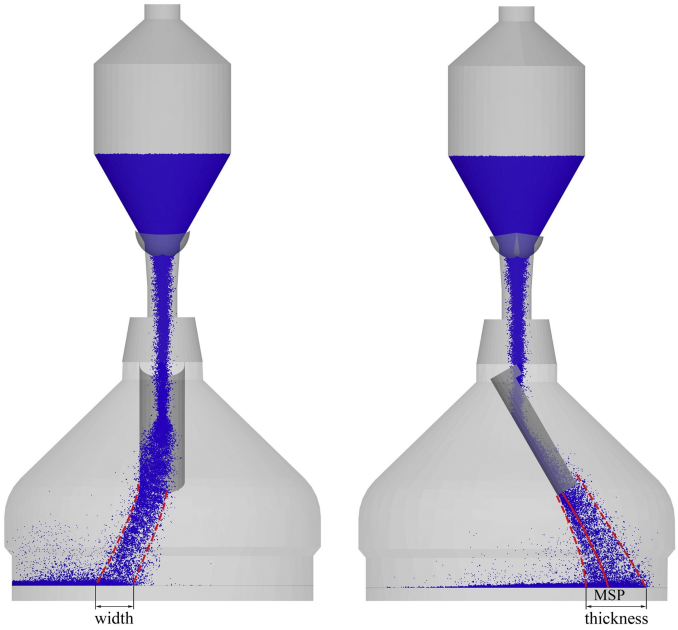


Figure 2.17: Definition of stream width, thickness and main striking point above the burden surface; image adopted from [32].

to coke collapse, since the particles tend to move in tangential direction rather than in radial direction, and therefore the amount of radial coke collapse is reduced for higher rotational speeds.

Cross-section and surface profile

The chute's cross-section shape has a noticeable effect on the motion of particles in the chute and the burden distribution in the furnace throat. Kou *et al.* [32] considered semicircle, trapezoid, and rectangle shaped chutes and found that particles are more "spread out" at the outlet of a rectangular chute when compared to the other two shapes since there is more available space for particles to roll around on the flat rectangular surface. They also found that the MSP is larger for semicircular chutes and successively smaller for trapezoidal and rectangular chutes, and the difference in MSP becomes larger for higher chute angles. Since their study involved a mixture of pellet, sinter and lump ore, they also investigated the effect of chute shape on size segregation in the furnace throat at different chute angles. The authors found that semicircular chutes produce a more uniform radial size distribution at low and middle chute angles while the same is true for trapezoidal chutes at large angles. Xu *et al.* [34] performed a similar study for coke charging, focusing on both radial and circumferential distributions when using a semicircular and rectangular chute

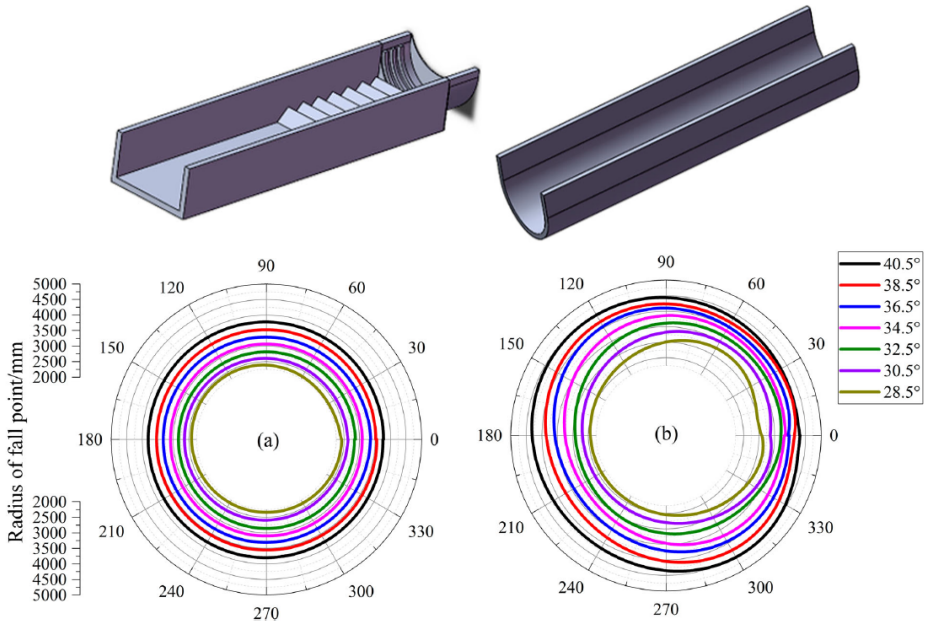


Figure 2.18: Burden falling points distribution at different tilting angles when using rectangular chute (left) and a semicircular chute (right); image adopted from [34].

(see Figure 2.18). They concluded that a rectangular chute outperforms a semicircular chute in different respects when considering the circumferential distribution. First of all, a rectangular chute provides an almost perfectly circular falling point distribution, unlike the semicircular chute. Also, the charged volume distribution is more uniform. However, when it comes to segregation, the semicircular chute provided a slightly lower deviation of burden average diameter distribution. In a later study, Xu *et al.* [121] performed full-scale furnace measurements to compare a semicircular and a rectangular chute across different chute angles (see Figure 2.19). They observed that the rectangular chute yielded a more uniform circumferential falling-point distribution and smaller inner and outer falling-point radii than the semicircular chute, consistent with their earlier DEM results. Notably, in Figure 2.18 the semicircular chute has a fully smooth surface, whereas the rectangular chute features a plated section near the top and a smooth section downstream. Thus, the differences may stem from both shape and surface, and it remains unclear to what extent these factors contributed to their findings.

Holmes *et al.* [44] focused on the effect of chute surface on burden distribution. They considered three semicircular chute designs currently in use by TATA Steel (see Figure 2.20): (i) straight, smooth design (not shown in the figure), (ii) rock-box design,

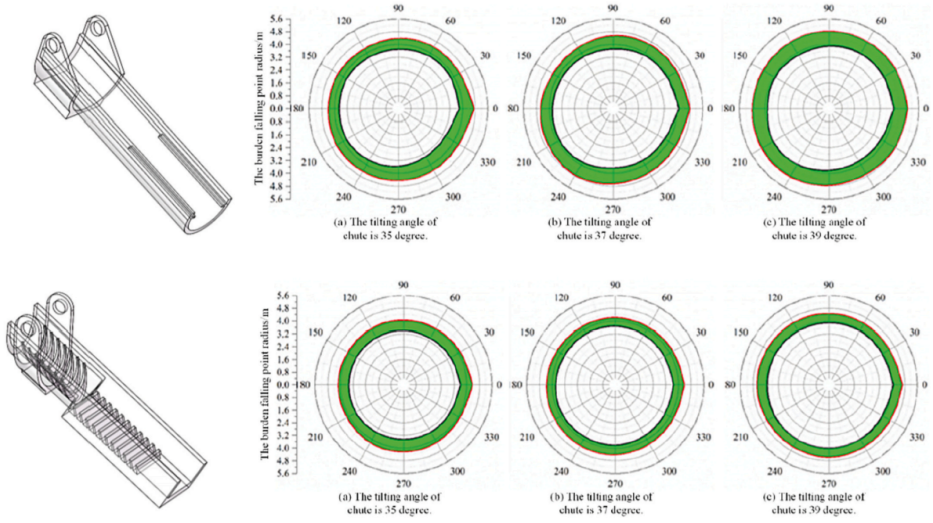


Figure 2.19: Chutes with different cross-section profiles and surface design (left) and the corresponding burden falling point radius distributions; image adopted from [121].

with several open compartments along the chute length, and (iii) hybrid design, which is a combination of the first two. They scrutinized the performance of different chute designs in terms of mass distribution symmetry after charging coke and pellets. Figure 2.21 shows an incomplete ring near the walls for all cases, which is the effect of an underdeveloped flow for a few seconds after starting the charging. Since material tends to accumulate in the rock-box compartments, the burden flows out at a later time for the rock-box chute; therefore, the tail of the outer ring is shorter for the rock-box chute when compared to the other chutes. Also, the rock-box chute appears to provide more scattering of the burden. These two aspects combined result in a better outer ring compared to the other chute designs. Looking at the distribution of the remaining rings, Figure 2.21 also shows that the rock-box design produces a more uniform, symmetrical mass distribution for both coke and pellets when compared to the other designs. The authors stated that the instantaneous chute angle adjustment during ring charging generally results in a sudden unsteady burden delivery until the flow on the chute re-adjusts to the new angle. The authors found that the rock-box design least suffers from this effect due to the its material accumulation capacity. These results indicate that the burden matrix needs to be carefully tuned based on the shape of the chute.

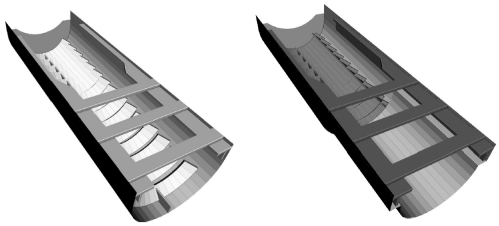


Figure 2.20: Chutes with different surface designs: rock-box (left) and hybrid design (right); image adopted from [44].

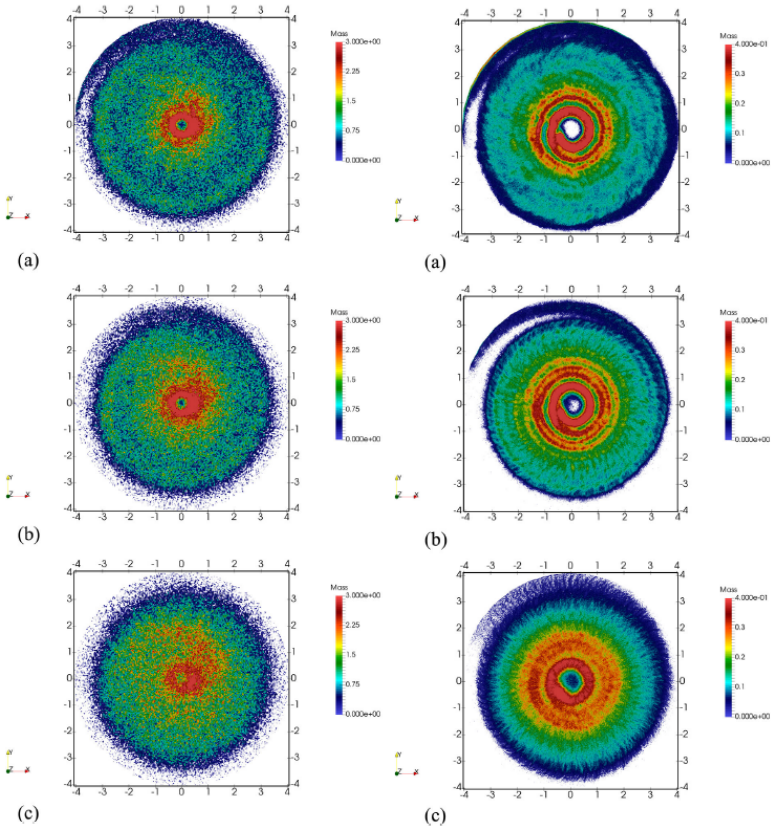
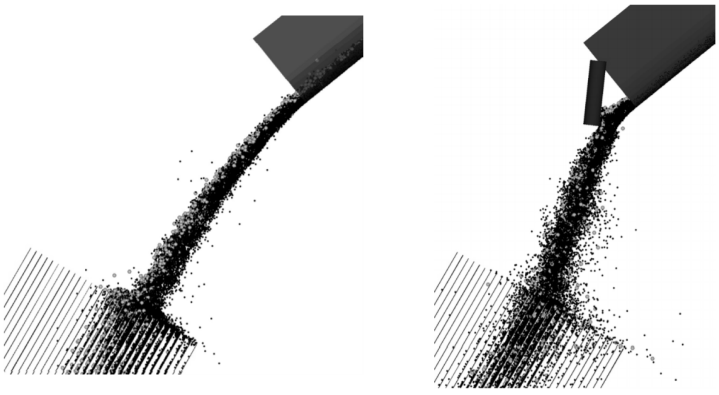


Figure 2.21: Total mass delivery when using different chute designs for coke (left) and pellets (right): (a) straight chute, (b) hybrid chute and (c) rock-box; images adopted from [44].



(a) (b)

Figure 2.22: Snapshots of particle discharging behavior at a chute inclination angle of 45° for (a) no damper and (b) using a damper at the chute outlet; images adopted from [16].

Outlet damper

Mio *et al.* [16] investigated the effect of using a damper on the segregation behavior of sinter particles as they are discharged from a stationary chute. Initially, it was observed that the burden at the chute was clearly segregated. Due to the percolation mechanism, small particles were concentrated at the bottom (along the chute surface) while large particles were at the top. By adding a damper at the chute outlet (see Figure 2.22), the burden stream was agitated which resulted in local mixing of the smaller and larger particles and segregation was reduced since the damper caused particle mixing at the outlet. In their study, Kou *et al.* [32] also briefly discussed the possibility of using a damper. They mentioned that the damper should be designed based on the shape of the chute: for semicircular chutes, the damper should produce a more uniform radial size distribution while it should produce a more aggregated stream for rectangular chutes. However, specific information on how these requirements should be translated to a damper design was not provided.

2.5 Conclusions

This chapter has reviewed recent research on blast furnace burden distribution and control using DEM models. The key conclusions are:

- **Burden distribution involves multiple contributing factors.** With respect to blast furnace permeability, burden distribution encompasses packing, component, and mass distribution. These are affected by segregation, degradation, and flow

deviation within the ore layer, while the coke-push effect additionally influences mass distribution in the coke layer.

- **Charging behavior of multi-component mixtures remains understudied.** Current research has largely focused on developing single-material models. Multi-component mixtures with varying size, shape, and density are rarely considered, despite their relevance to real furnace operation where the burden consists of multiple materials.
- **Permeability has received limited attention.** Although segregation is frequently cited as a factor influencing furnace performance, few studies have explicitly linked it to permeability. Component segregation, in particular, is underexplored. Other phenomena, such as flow deviation and the coke-push effect, have received more focus, while degradation is often limited to stress-based breakage risk estimates. While DEM tools now support breakage modeling, their application to blast furnace systems is still lacking, likely due to computational demands. Breakage modeling is beyond the scope of this work, but its consideration in future studies could contribute to a more complete picture of charging effects on permeability.
- **Charging system models dominate the literature.** Most studies simulate the charging system, or a portion of it, rather than the full material handling path. This is understandable, as material distribution is largely fixed once deposited in the furnace. However, existing models often simplify the process by starting at intermediate equipment such as bins, hoppers, or chutes. Simulating the complete path from the stock house to the furnace would offer a more comprehensive understanding, but such an approach remains computationally demanding. Although beyond the scope of this study, future research is likely to move in this direction.
- **Design changes are studied more than operational strategies.** Many models investigate how geometric or mechanical design modifications can improve material distribution, while operational tuning, which is more practical for existing furnaces, receives less attention.

It is evident that a model is needed which incorporates mixtures of burden components and accounts for the effects of their distribution on bed permeability. Before developing such a model in this work, the next chapter reviews DEM modeling strategies found in blast furnace-related literature. The insights from this review form the basis for the model development presented in this thesis.

2.6 Bibliography

[1] A. Babich and D. Senk. “Coke in the iron and steel industry”. In: ed. by Isabel Suárez-Ruiz, Maria Antonia Diez, and Fernando Rubiera. ISBN: 978-0-08-

102201-6. Woodhead Publishing, 2019, pp. 367–404. ISBN: 978-0-08-102201-6. DOI: 10.1016/B978-0-08-102201-6.00013-3.

[2] D. J. Gavel. “A review on nut coke utilisation in the ironmaking blast furnaces”. In: *Materials Science and Technology* 33 (2017), pp. 381–387. DOI: 10.1080/02670836.2016.1183073.

[3] P. Zulli and P. Goldsworthy. “7 - Value-in-use assessment of metallurgical coals”. In: ed. by Dave Osborne. Second Edition. Vol. 2. Woodhead Publishing, 2023, pp. 203–238. ISBN: 978-0-12-824327-5. DOI: 10.1016/B978-0-12-824327-5.00013-2.

[4] K. M. Graczyk and M. Matyka. “Predicting porosity, permeability, and tortuosity of porous media from images by deep learning”. In: *Scientific Reports* 10 (2020), p. 21488. ISSN: 2045-2322. DOI: 10.1038/s41598-020-78415-x.

[5] W. Xu, K. Zhang, Y. Zhang, and J. Jiang. “Packing Fraction, Tortuosity, and Permeability of Granular-Porous Media With Densely Packed Spheroidal Particles: Monodisperse and Polydisperse Systems”. In: *Water Resources Research* 58 (2022). DOI: 10.1029/2021WR031433.

[6] T. Kon, S. Natsui, S. Matsuhashi, S. Ueda, R. Inoue, and T. Ariyama. “Influence of Cohesive Zone Thickness on Gas Flow in Blast Furnace Analyzed by DEM-CFD Model Considering Low Coke Operation”. In: *steel research international* 84 (2013), pp. 1146–1156. DOI: 10.1002/srin.201300025.

[7] S. Ueda, T. Kon, H. Kurosawa, S. Natsui, T. Ariyama, and H. Nogami. “Influence of Shape of Cohesive Zone on Gas Flow and Permeability in the Blast Furnace Analyzed by DEM-CFD Model”. In: *ISIJ International* 55 (2015), pp. 1232–1236. DOI: 10.2355/isijinternational.55.1232.

[8] M Yakeya, A. Kasai, R. Tadai, and K. Nozawa. “Gas Permeability Improvement Mechanism at the Blast Furnace Cohesive Zone by Mixed Coke Charging in Ore Layer and Effect of Coke Mixing for Different Cohesive Zone Condition on Gas Permeability”. In: *ISIJ International* 60 (2020), pp. 1438–1444. DOI: 10.2355/isijinternational.ISIJINT-2019-699.

[9] Y. Liu. *The Operation of Contemporary Blast Furnaces*. Springer Singapore, 2021. ISBN: 978-981-15-7074-2.

[10] K. Ichikawa, Y. Kashihara, N. Oyama, T. Hirosawa, J. Ishii, M. Sato, and H. Matsuno. “Evaluating Effect of Coke Layer Thickness on Permeability by Pressure Drop Estimation Model”. In: *ISIJ International* 57 (2017), pp. 254–261. DOI: 10.2355/isijinternational.ISIJINT-2016-459.

[11] M. Geerdes, R. Chaigneau, and O. Lingiardi. *Modern Blast Furnace Ironmaking: An Introduction*. Ed. by Hisko Toxopeus Maarten Geerdes. Fourth. ISBN: 978-1-64368-123-8. IOS Press BV, 2020. ISBN: 978-1-64368-123-8.

[12] A. Biswas. *Principles of Blast Furnce Ironmaking: Theory and Practice*. ISBN: 978-0949917089. Cootha Publishing House. ISBN: 978-0949917089.

[13] M. Yoshiyuki, K. Shibata, Y. Yoshida, and R. Ono. “The Principle of Blast Furnace Operational Technology and Centralized Gas Flow by Center Coke Charging”. In: *KOBELCO Technology Review* (Nov. 2005), pp. 12–20.

[14] X. Yu and Y. Shen. “Model Study of Blast Furnace Operation with Central Coke Charging”. In: *Metallurgical and Materials Transactions B* 50 (2019), pp. 2238–2250. ISSN: 1543-1916. DOI: 10.1007/s11663-019-01657-2.

[15] H. Wei, W. Ding, Y. Li, H. Nie, H. Saxén, H. Long, and Y. Yu. “Porosity distribution of moving burden layers in the blast furnace throat”. In: *Granular Matter* 23 (2021). DOI: 10.1007/s10035-020-01080-4.

[16] H. Mio, S. Komatsuki, M. Akashi, A. Shimosaka, Y. Shirakawa, J. Hidaka, M. Kadowaki, S. Matsuzaki, and K. Kunitomo. “Validation of Particle Size Segregation of Sintered Ore during Flowing through Laboratory-scale Chute by Discrete Element Method”. In: *ISIJ International* 48 (2008), pp. 1696–1703. DOI: 10.2355/isijinternational.48.1696.

[17] H. Mio, S. Komatsuki, M. Akashi, A. Shimosaka, Y. Shirakawa, J. Hidaka, M. Kadowaki, S. Matsuzaki, and K. Kunitomo. “Effect of Chute Angle on Charging Behavior of Sintered Ore Particles at Bell-less Type Charging System of Blast Furnace by Discrete Element Method”. In: *ISIJ International* 49 (2009), pp. 479–486. DOI: 10.2355/isijinternational.49.479.

[18] H. Mio, S. Komatsuki, M. Akashi, A. Shimosaka, Y. Shirakawa, J. Hidaka, M. Kadowaki, H. Yokoyama, S. Matsuzaki, and K. Kunitomo. “Analysis of Traveling Behavior of Nut Coke Particles in Bell-type Charging Process of Blast Furnace by Using Discrete Element Method”. In: *ISIJ International* 50 (2010), pp. 1000–1009. DOI: 10.2355/isijinternational.50.1000.

[19] Y. Yu and H. Saxén. “Experimental and DEM study of segregation of ternary size particles in a blast furnace top bunker model”. In: *Chemical Engineering Science* 65 (2010), pp. 5237–5250. DOI: 10.1016/j.ces.2010.06.025.

[20] Y. Yu, A. Westerlund, T. Paananen, and H. Saxén. “Inter-particle Percolation Segregation during Burden Descent in the Blast Furnace”. In: *ISIJ International* 51 (2011), pp. 1050–1056. DOI: 10.2355/isijinternational.51.1050.

[21] H. Mio, M. Kadowaki, S. Matsuzaki, and K. Kunitomo. “Development of particle flow simulator in charging process of blast furnace by discrete element method”. In: *Minerals Engineering* 33 (2012), pp. 27–33. ISSN: 0892-6875. DOI: 10.1016/j.mineng.2012.01.002.

[22] Y. Yu and H. Saxén. “Flow of Pellet and Coke Particles in and from a Fixed Chute”. In: *Ind. Eng. Chem. Res.* 51 (May 2012), pp. 7383–7397. DOI: 10.1021/ie201362n.

[23] Y. Yu and H. Saxén. “Particle Flow and Behavior at Bell-Less Charging of the Blast Furnace”. In: *Steel Research International* 84 (2013), pp. 1018–1033. DOI: 10.1002/srin.201300028.

[24] S. Wu, M. Kou, J. Xu, X. Guo, K. Du, W. Shen, and J. Sun. “DEM simulation of particle size segregation behavior during charging into and discharging from a Paul-Wurth type hopper”. In: *Chemical Engineering Science* 99 (2013), pp. 314–323. DOI: 10.1016/j.ces.2013.06.018.

[25] Y. Yu and H. Saxén. “Segregation behavior of particles in a top hopper of a blast furnace”. In: *Powder Technology* 262 (2014), pp. 233–241. DOI: 10.1016/j.powtec.2014.04.010.

[26] J. Zhang, J. Qiu, H. Guo, S. Ren, H. Sun, G. Wang, and Z. Gao. “Simulation of particle flow in a bell-less type charging system of a blast furnace using the discrete element method”. In: *Particuology* 16 (2014), pp. 167–177. ISSN: 1674-2001. DOI: 10.1016/j.partic.2014.01.003.

[27] S. Liu, Z. Zhou, K. Dong, A. Yu, D. Pinson, and J. Tsalapatis. “Numerical Investigation of Burden Distribution in a Blast Furnace”. In: *steel research international* 86 (2015), pp. 651–661. DOI: 10.1002/srin.201400360.

[28] D. Schott, W. Vreeburg, C. Molhoek, and G. Lodewijks. “Granular Flow to a Blast Iron Ore Furnace: Influence of Particle Size Distribution on Segregation of a Mixture”. In: *Traffic and Granular Flow ’15*. Ed. by Victor L Knoop and Winnie

Daamen. Springer International Publishing, 2016, pp. 621–628-621–628. ISBN: 978-3-319-33482-0. DOI: 10.1007/978-3-319-33482-0_78.

[29] J. Xu, Z. Hu, Y. Xu, D. Wang, L. Wen, and C. Bai. "Transient local segregation grids of binary size particles discharged from a wedge-shaped hopper". In: *Powder Technology* 308 (2017), pp. 273–289. DOI: 10.1016/j.powtec.2016.12.013.

[30] E. Dianyu. "Numerical investigation of mixed layer effect on permeability in a dynamic blast furnace". In: *Engineering Reports* 2 (2020), e12166–e12166. DOI: 10.1002/eng2.12166.

[31] N. Govender, D. N. Wilke, C. Wu, U. Tuzun, and H. Kureck. "A numerical investigation into the effect of angular particle shape on blast furnace burden topography and percolation using a GPU solved discrete element model". In: *Chemical Engineering Science* 204 (2019), pp. 9–26. DOI: 10.1016/j.ces.2019.03.077.

[32] M. Kou, J. Xu, S. Wu, H. Zhou, K. Gu, S. Yao, and B. Wen. "Effect of cross-section shape of rotating chute on particle movement and distribution at the throat of a bell-less top blast furnace". In: *Particuology* 44 (2019), pp. 194–206. ISSN: 1674-2001. DOI: 10.1016/j.partic.2018.07.010.

[33] H. Mio, Y. Narita, S. Matsuzaki, K. Nishioka, and S. Nomura. "Measurement of particle charging trajectory via rotating chute of 1/3-scale blast furnace and its comparing with numerical analysis using Discrete Element Method". In: *Powder Technology* 344 (2019), pp. 797–803. ISSN: 0032-5910. DOI: 10.1016/j.powtec.2018.12.047.

[34] W. Xu, S. Cheng, Q. Niu, and G. Zhao. "Effect of the cross-section shape of rotating chute on particle flow and burden distribution during the charging process of bell-less top blast furnace with two parallel hoppers". In: *Ironmaking & Steelmaking* 46 (2019), pp. 105–112. DOI: 10.1080/03019233.2017.1343412.

[35] D. K. Chibwe, G. M. Evans, E. Doroodchi, B. J. Monaghan, D. J. Pinson, and S. J. Chew. "Charge material distribution behaviour in blast furnace charging system". In: *Powder Technology* 366 (2020), pp. 22–35. ISSN: 0032-5910. DOI: 10.1016/j.powtec.2020.02.048.

[36] Z. Hong, H. Zhou, J. Wu, L. Zhan, Y. Fan, Z. Zhang, S. Wu, H. Xu, L. Wang, and M. Kou. "Effects of Operational Parameters on Particle Movement and Distribution at the Top of a Bell-Less Blast Furnace Based on Discrete Element Method". In: *steel*

research international 92 (Aug. 2020). DOI: https://doi.org/10.1002/srin.202000262.

[37] H. Mio, Y. Narita, K. Nakano, and S. Nomura. "Validation of the Burden Distribution of the 1/3-Scale of a Blast Furnace Simulated by the Discrete Element Method". In: *Processes* 8 (2020). ISSN: 2227-9717. DOI: 10.3390/pr8010006.

[38] W. Xu, S. Cheng, Q. Niu, W. Hu, and J. Bang. "The DEM study of segregation phenomena of burden distribution during the charging process of blast furnace with two parallel hoppers". In: *Ironmaking & Steelmaking* 47 (2020), pp. 337–343. DOI: 10.1080/03019233.2018.1512035.

[39] T. F. Zhang, J. Q. Gan, A. B. Yu, D. Pinson, and Z. Y. Zhou. "Size segregation of granular materials during Paul-Wurth hopper charging and discharging process". In: *Powder Technology* 378 (2021), pp. 497–509. DOI: 10.1016/j.powtec.2020.10.025.

[40] C. X. Li, K. J. Dong, S. D. Liu, G. R. Chandratilleke, Z. Y. Zhou, and Y. S. Shen. "DEM study of particle segregation in the throat region of a blast furnace". In: *Powder Technology* 407 (2022), p. 117660. ISSN: 0032-5910. DOI: 10.1016/j.powtec.2022.117660.

[41] S. Ueda, S. Natsui, Z. Fan, H. Nogami, R. Soda, J. Kano, R. Inoue, and T. Ariyama. "Influences of Physical Properties of Particle in Discrete Element Method on Descending Phenomena and Stress Distribution in Blast Furnace". In: *ISIJ International* 50 (2010), pp. 981–986. DOI: 10.2355/isijinternational.50.981.

[42] Y. Narita, H. Mio, T. Orimoto, and S. Nomura. "DEM Analysis of Particle Trajectory in Circumferential Direction at Bell-less Top". In: *ISIJ International* 57 (2017), pp. 429–434. DOI: 10.2355/isijinternational.ISIJINT-2016-560.

[43] M. Holmes. "A Numerical Simulation of Particulate Distribution of the Blast Furnace Raw Material Burden Through the Paul Wurth Bell-less Top Apparatus". PhD thesis. May 2016. DOI: 10.13140/RG.2.2.22315.85280.

[44] M. A. J. Holmes, D. J. Penney, N. P. Lavery, and S. G. R. Brown. "A numerical investigation assessing the symmetry of burden charging in a blast furnace using different chute designs". In: *Ironmaking & Steelmaking* 45 (2018), pp. 551–559. DOI: 10.1080/03019233.2017.1303893.

[45] C. Sun, J. Xu, Z. Liao, Y. Xu, M. Kou, and L. Wen. “Causes of Particle Trajectory Fluctuation on the Rotating Chute in Circumferential Direction at Bell-less Top with Parallel Type Hoppers”. In: *ISIJ International* 59.9 (2019), pp. 1527–1533. DOI: 10.2355/isijinternational.ISIJINT-2018-862.

[46] G. Holzinger and M. Schatzl. “Effect of chute start angle and hopper change on burden distribution during the charging process of a bell-less top blast furnace with two parallel hoppers”. In: *Powder Technology* 395 (2022), pp. 669–680. ISSN: 0032-5910. DOI: 10.1016/j.powtec.2021.10.005.

[47] J. Chen, H. Zuo, Y. Wang, Q. Xue, and J. Wang. “DEM Simulation of Burden Circumferential Distribution of Blast Furnace With Parallel Hoppers”. In: *Metallurgical and Materials Transactions B* 53 (2022), pp. 3793–3804. ISSN: 1543-1916. DOI: 10.1007/s11663-022-02641-z.

[48] T. Mitra and H. Saxén. “Simulation of Burden Distribution and Charging in an Ironmaking Blast Furnace”. In: *IFAC-PapersOnLine* 48 (2015), pp. 183–188. ISSN: 2405-8963. DOI: 10.1016/j.ifacol.2015.10.100.

[49] T. Mitra and H. Saxén. “Discrete element simulation of charging and mixed layer formation in the ironmaking blast furnace”. In: *Computational Particle Mechanics* 3 (2016), pp. 541–555-541–555. ISSN: 2196-4386. DOI: 10.1007/s40571-015-0084-1.

[50] M. Kou, S. Wu, H. Zhou, Y. Yu, and J. Xu. “Numerical Investigation of Coke Collapse and Size Segregation in the Bell-less Top Blast Furnace”. In: *ISIJ International* 58 (Aug. 2018). DOI: 10.2355/isijinternational.ISIJINT-2018-415.

[51] H. Zhou, J. Wu, Z. Hong, L. P. Wang, S. Wu, M. Kou, G. Wang, and Y. Luo. “Numerical simulation of coke collapse and its optimization during burden charging at the top of bell-less blast furnace”. In: *Powder Technology* 389 (2021), pp. 155–162. DOI: 10.1016/j.powtec.2021.05.033.

[52] J. Zhang, Z. Hu, W. Ge, Y. Zhang, T. Li, and J. Li. “Application of the Discrete Approach to the Simulation of Size Segregation in Granular Chute Flow”. In: *Industrial & Engineering Chemistry Research* 43 (18 Sept. 2004). doi: 10.1021/ie034254f, pp. 5521–5528. ISSN: 0888-5885. DOI: 10.1021/ie034254f.

[53] S. R. De Silva, A. Dyrøy, and G. G. Enstad. “Segregation Mechanisms and Their Quantification Using Segregation Testers”. In: *IUTAM Symposium on Segregation in Granular Flows*. Ed. by Anthony D Rosato and Denis L Blackmore. Kluwer Academic Publishers, 1999, pp. 11–29. DOI: 10.1007/978-94-015-9498-1.

[54] J. W. Carson, T. A. Royal, and D. J. Goodwill. “Understanding and Eliminating Particle Segregation Problems”. In: *Bulk Solids Handling* 6 (1986), pp. 139–144.

[55] P. Tang and V. M. Puri. “Methods for Minimizing Segregation: A Review”. In: *Particulate Science and Technology* 22 (4 2004), pp. 321–337. DOI: 10.1080/02726350490501420.

[56] J. Williams. “Mixing and Segregation in Powders”. In: *Principles of Powder Technology*. Ed. by M. J. Rhodes. John Wiley & Sons, 1991, pp. 71–90. ISBN: 978-0-471-92422-7.

[57] M. Rhodes. *Introduction to Particle Technology*. 2nd. John Wiley & Sons, 2008. ISBN: 9780470014271. DOI: 10.1002/9780470727102.

[58] J. M. Ottino and D. V. Khakhar. “Mixing and Segregation of Granular Materials”. In: *Annual Review of Fluid Mechanics* 32 (2000), pp. 55–91. DOI: 10.1146/annurev.fluid.32.1.55.

[59] N. Jain, J. M. Ottino, and R. M. Lueptow. “Regimes of Segregation and Mixing in Combined Size and Density Granular Systems: An Experimental Study”. In: *Granular Matter* 7 (2005), pp. 69–81. DOI: 10.1007/s10035-005-0198-x.

[60] T. Bhattacharya. “Review Report on Granular Segregation in the Blast Furnace”. In: (Jan. 2008). DOI: 10.13140/RG.2.1.1490.3280.

[61] S. H. Gharat. “Flow and Segregation of Granular Materials during Heap Formation”. In: ed. by Tetsu Mieno, Yasuaki Hayashi, and Kun Xue. IntechOpen, 2020. DOI: 10.5772/intechopen.89650.

[62] A. Spence. “Improving blast furnace burden distribution by stockfeed segregation control”. In: (1996). URL: https://ro.uow.edu.au/theses/2517.

[63] W. Xu, S. Cheng, Q. Niu, W. Hu, and J. Bang. “Investigation on the uneven distribution of different types of ores in the hopper and stock surface during the charging process of blast furnace based on discrete element method”. In: *Metallurgical Research & Technology* 116 (Jan. 2019), p. 314. DOI: 10.1051/metal/2018099.

[64] W. Xu, S. Cheng, and C. Li. “Effect of the charging sequence of iron-bearing burden on burden distribution during the charging process of blast furnace based on discrete element method”. In: *Ironmaking & Steelmaking* 0 (2021), pp. 1–9. DOI: 10.1080/03019233.2021.1976039.

[65] D. Schulze. “Segregation”. In: *Powders and Bulk Solids: Behavior, Characterization, Storage and Flow*. Cham: Springer International Publishing, 2021, pp. 479–537. ISBN: 978-3-030-76720-4.

[66] Z. J. Teng, S. S. Cheng, and G. L. Zhao. “Influence of chute cross section and parameters on burden distribution for blast furnace”. In: *Kang T'ieh/Iron and Steel* 49 (Sept. 2014), 34-37 and 76–37 and 76. DOI: 10.13228/j.boyuan.issn0449-749x.20130577.

[67] Y. Xu, K. Ma, C. Sun, Z. Liao, J. Xu, L. Wen, and C. Bai. “Effect of Density Difference on Particle Segregation Behaviors at Bell-Less Top Blast Furnace with Parallel-Type Hopper”. In: ed. by Jiann-Yang Hwang, Tao Jiang, Mark William Kennedy, Dean Gregurek, Shijie Wang, Baojun Zhao, Onuralp Yücel, Ender Keskinkilic, Jerome P Downey, Zhiwei Peng, and Rafael. Padilla. Springer International Publishing, 2018, pp. 391–399-391–399.

[68] M. Propster and J. Szekely. “The porosity of systems consisting of layers of different particles”. In: *Powder Technology* 17.1 (1977), pp. 123–138. ISSN: 0032-5910. DOI: 10.1016/0032-5910(77)85051-1.

[69] V. Staněk and V. Eckert. “Course of porosity in layered beds of spherical particles”. In: *Archiv für das Eisenhüttenwesen* 50.1 (1979), pp. 19–24. DOI: 10.1002/srin.197904693.

[70] M. Guha, S. Nag, P. Kumar Swamy, and R. Venkat Ramna. “Effect of Interface Resistance on Gas Flow in Blast Furnace”. In: *ISIJ International* 51.11 (2011), pp. 1795–1799. DOI: 10.2355/isijinternational.51.1795.

[71] J. Liu, Q. Xue, X. She, and J. Wang. “Investigation on interface resistance between alternating layers in the upper of blast furnace”. In: *Powder Technology* 246 (2013), pp. 73–81. ISSN: 0032-5910. DOI: 10.1016/j.powtec.2013.05.011.

[72] Y. Kajiwara, T. Jimbo, T. Joko, Y. Aminaga, and T. Inada. “Investigation of Bell-less Charging Based on Full Scale Model Experiments”. In: *Transactions of the Iron and Steel Institute of Japan* 24 (1984), pp. 799–807. DOI: 10.2355/isijinternational1966.24.799.

[73] H. Li, H. Saxén, W. Liu, Z. Zou, and L. Shao. "Model-Based Analysis of Factors Affecting the Burden Layer Structure in the Blast Furnace Shaft". In: *Metals* 9 (2019). DOI: 10.3390/met9091003.

[74] J. Bridgwater, N. W. Sharpe, and D. C. Stocker. "Particle mixing by percolation". In: *Transactions Of The Institution Of Chemical Engineers And The Chemical Engineer* 47.5 (1969).

[75] J. Bridgwater and N. D. Ingram. "Rate of spontaneous inter-particle percolation". In: *Transactions of the Institution of Chemical Engineers and The Chemical Engineer* 49.3 (1971).

[76] F. Lominé and L. Oger. "Transport of small particles through a 3D packing of spheres: experimental and numerical approaches". In: *Journal of Statistical Mechanics: Theory and Experiment* 2006.07 (2006), P07019.

[77] M. Rahman, H. Zhu, A. Yu, and J. Bridgwater. "DEM simulation of particle percolation in a packed bed". In: *Particuology* 6.6 (2008). Simulation and Modeling of Particulate Systems, pp. 475–482. ISSN: 1674-2001. DOI: 10.1016/j.partic.2008.07.016.

[78] H. P. Zhu, M. Rahman, A. B. Yu, J. Bridgwater, and P. Zulli. "Effect of particle properties on particle percolation behaviour in a packed bed". In: *Minerals Engineering* 22 (2009). Special issue: Computational Modelling, pp. 961–969. ISSN: 0892-6875. DOI: 10.1016/j.mineng.2009.03.002.

[79] H. Zhou, S. Wu, M. Kou, Z. Luo, Z. Zou, and Y. Shen. "Analysis of Cohesive Particle Percolation in a Packed Bed Using Discrete Element Method". In: *ISIJ International* 58.1 (2018), pp. 43–51. DOI: 10.2355/isijinternational.ISIJINT-2017-373.

[80] S. M. Arifuzzaman, K. Dong, H. Zhu, and Q. Zeng. "DEM study and machine learning model of particle percolation under vibration". In: *Advanced Powder Technology* 33.5 (2022), p. 103551. ISSN: 0921-8831. DOI: 10.1016/j.apt.2022.103551.

[81] Y. Yu and H. Saxén. "Effect of DEM Parameters on the Simulated Inter-particle Percolation of Pellets into Coke during Burden Descent in the Blast Furnace". In: *ISIJ International* 52 (2012), pp. 788–796. DOI: 10.2355/isijinternational.52.788.

[82] Willem J. Beekman, Gabrie M. H. Meesters, Brian Scarlett, and Todd Becker. "Measurement of Granule Attrition and Fatigue in a Vibrating Box". In: *Particle & Particle Systems Characterization* 19.1 (2002), pp. 5–11.

[83] C. Teo, A. G. Waters, and S. K. Nicol. "Quantification of the breakage of lump materials during handling operations". In: *International Journal of Mineral Processing* 30 (1990), pp. 159–184. DOI: 10.1016/0301-7516(90)90013-0.

[84] R. K. Sahoo and D. Roach. "Effect of different types of impact surface on coal degradation". In: *Chemical Engineering and Processing: Process Intensification* 44.2 (2005). Pneumatic Conveying and Handling of Particulate Solids, pp. 253–261. ISSN: 0255-2701. DOI: 10.1016/j.cep.2004.02.019.

[85] Y. Narita, H. Mio, T. Orimoto, and S. Nomura. "Modelling of Coke Layer Collapse during Ore Charging in Ironmaking Blast Furnace by DEM". In: *EPJ Web of Conferences* 140 (Jan. 2017), p. 2018. DOI: 10.1051/epjconf/201714002018.

[86] R. Carvalho, P. Porto, and L. Tavares. "Modeling breakage and mechanical degradation of steelmaking materials during handling". In: Nov. 2018.

[87] R. Sahoo and D. Roach. "Quantification of the lump coal breakage during handling operation at the gladstone port". In: *Chemical Engineering and Processing: Process Intensification* 44.7 (2005), pp. 797–804. ISSN: 0255-2701. DOI: 10.1016/j.cep.2004.09.004.

[88] L. Marcelo Tavares and R. M. de Carvalho. "Modeling ore degradation during handling using continuum damage mechanics". In: *International Journal of Mineral Processing* 101.1 (2011), pp. 21–27. ISSN: 0301-7516. DOI: 10.1016/j.minpro.2010.07.008.

[89] L. Marcelo Tavares and R. M. de Carvalho. "Modeling ore degradation during handling using continuum damage mechanics". In: *International Journal of Mineral Processing* 112-113 (2012). Special Issue Communition 2009, pp. 1–6. ISSN: 0301-7516. DOI: 10.1016/j.minpro.2010.07.011.

[90] P. P. S. Cavalcanti, H. A. Petit, A. D. Thomazini, R. M. de Carvalho, and L. Marcelo Tavares. "Modeling of degradation by impact of individual iron ore pellets". In: *Powder Technology* 378 (2021), pp. 795–807. ISSN: 0032-5910. DOI: 10.1016/j.powtec.2020.10.037.

[91] H. A. Petit, A. Philippe, A. D. Thomazini, and L. Marcelo Tavares. “Modeling breakage by impact of fragments of fired iron ore pellets”. In: *Powder Technology* 398 (2022), p. 117059. ISSN: 0032-5910. DOI: 10.1016/j.powtec.2021.117059.

[92] L. Marcelo Tavares. “Review and Further Validation of a Practical Single-Particle Breakage Model”. In: *KONA Powder and Particle Journal* 39 (2022), pp. 62–83. DOI: 10.14356/kona.2022012.

[93] T. Nouchi, T. Sato, M. Sato, K. Takeda, and T. Ariyama. “Stress Field and Solid Flow Analysis of Coke Packed Bed in Blast Furnace Based on DEM”. In: *ISIJ International* 45 (2005), pp. 1426–1431. DOI: 10.2355/isijinternational.45.1426.

[94] J. Liang Zhang, Y. X. Chen, Z. Y. Fan, Z. W. Hu, T. J. Yang, and T. Ariyama. “Influence of Profile of Blast Furnace on Motion and Stress of Burden by 3D-DEM”. In: *Journal of Iron and Steel Research International* 18.11 (2011), pp. 1–6. ISSN: 2210-3988. DOI: 10.1016/S1006-706X(11)60108-8.

[95] S. Natsui, A. Hirai, K. Terui, Y. Kashihara, A. Murao, Y. Miki, and H. Nogami. “Impact of high-temperature non-uniform degradation on fines clogging and gas flow in a coke bed”. In: *Chemical Engineering Journal* 427 (2022), p. 131484. ISSN: 1385-8947. DOI: 10.1016/j.cej.2021.131484.

[96] Y. Yu. “Experimental and Discrete Element Simulation Studies of Bell-less Charging of Blast Furnace”. In: *PhD Thesis* (2013).

[97] T. Ren, X. Jin, H. Ben, and C. Yu. “Burden Distribution for Bell-Less Top With Two Parallel Hoppers”. In: *Journal of Iron and Steel Research, International* 13.2 (2006), pp. 14–17. ISSN: 1006-706X. DOI: 10.1016/S1006-706X(06)60035-6.

[98] H. Zhao, M. Zhu, P. Du, S. Taguchi, and H. Wei. “Uneven Distribution of Burden Materials at Blast Furnace Top in Bell-less Top with Parallel Bunkers”. In: *ISIJ International* 52.12 (2012), pp. 2177–2185. DOI: 10.2355/isijinternational.52.2177.

[99] J. Xu, S. Wu, M. Kou, L. Zhang, and X. Yu. “Circumferential burden distribution behaviors at bell-less top blast furnace with parallel type hoppers”. In: *Applied Mathematical Modelling* 35.3 (2011), pp. 1439–1455. ISSN: 0307-904X. DOI: 10.1016/j.apm.2010.09.021.

[100] L. Shi, G. Zhao, M. Li, and X. Ma. “A model for burden distribution and gas flow distribution of bell-less top blast furnace with parallel hoppers”. In: *Applied Mathematical Modelling* 40.23 (2016), pp. 10254–10273. ISSN: 0307-904X. DOI: 10.1016/j.apm.2016.07.024.

[101] Y. Xu, J. Xu, C. Sun, K. Ma, C. Shan, L. Wen, S. Zhang, and C. Bai. “Quantitative comparison of binary particle mass and size segregation between serial and parallel type hoppers of blast furnace bell-less top charging system”. In: *Powder Technology* 328 (2018), pp. 245–255. ISSN: 0032-5910. DOI: 10.1016/j.powtec.2018.01.020.

[102] J. Chen, H. Zuo, H. Zhao, Q. Xue, and J. Wang. “Burden circumferential mass segregation at the blast furnace with parallel hoppers”. In: *Powder Technology* 409 (2022), p. 117845. ISSN: 0032-5910. DOI: 10.1016/j.powtec.2022.117845.

[103] W. Xu, S. Cheng, Q. Niu, and G. Zhao. “Effect of the Main Feeding Belt Position on Burden Distribution during the Charging Process of Bell-less Top Blast Furnace with Two Parallel Hoppers”. In: *ISIJ International* 57 (2017), pp. 1173–1180. DOI: 10.2355/isijinternational.ISIJINT-2017-003.

[104] S. Nag, S. Basu, and A. B. Yu. “A static approach towards coke collapse modelling in blast furnace”. In: *Ironmaking & Steelmaking* 36.7 (2009), pp. 509–514. DOI: 10.1179/174328109X443338.

[105] S. Nag, S. Basu, and T. Bhattacharya. “Modelling of Coke Collapse in Blast Furnace – A Static Approach”. In: *Tata Search (ISSN: 0971-5975)* 1 (Jan. 2007), pp. 105–110.

[106] P. Zulli, W. B. U. Tanzil, J. Monaghan, M. J. McCarthy, and K. L. Hockings. “New Technologies in Blast Furnace Burden Distribution - Physical Modelling”. In: *Chemeca 88: Australia’s Bicentennial International Conference for the Process Industries; Preprints of Papers, 1988, 450-454*. 1988.

[107] C. K. Ho, S. M. Wu, H. P. Zhu, A. B. Yu, and S. T. Tsai. “Experimental and numerical investigations of gouge formation related to blast furnace burden distribution”. In: *Minerals Engineering* 22 (2009), pp. 986–994. DOI: 10.1016/j.mineng.2009.03.004.

[108] A. Hadi, R. Roeplal, Y. Pang, and D. Schott. “DEM Modelling of Segregation in Granular Materials: A Review”. In: *KONA Powder and Particle Journal* advpub (2023), pp. -. DOI: 10.14356/kona.2024017.

[109] P. Bhalode and M. Ierapetritou. “A review of existing mixing indices in solid-based continuous blending operations”. In: *Powder Technology* 373 (2020), pp. 195–209. ISSN: 0032-5910. DOI: 10.1016/j.powtec.2020.06.043.

[110] M. Cho, P. Dutta, and J. Shim. “A non-sampling mixing index for multicomponent mixtures”. In: *Powder Technology* 319 (2017), pp. 434–444. ISSN: 0032-5910. DOI: 10.1016/j.powtec.2017.07.011.

[111] X. Jin, G. R. Chandratilleke, S. Wang, and Y. Shen. “DEM investigation of mixing indices in a ribbon mixer”. In: *Particuology* 60 (2022), pp. 37–47. ISSN: 1674-2001. DOI: 10.1016/j.partic.2021.03.005.

[112] A. Rosato and C. Windows-Yule. *Segregation in Vibrated Granular Systems*. Cited by: 25. 2020, pp. 1–291. DOI: 10.1016/B978-0-12-814199-1.00002-0.

[113] S. Panda and D. S. Tan. “Effect of external factors on segregation of different granular mixtures”. In: *Advanced Powder Technology* 31 (2020), pp. 571–594. ISSN: 0921-8831. DOI: 10.1016/j.apt.2019.11.013.

[114] S. Panda and D. S. Tan. “Study of external factors to minimize segregation of granular particles”. In: *International Journal of Modern Physics C* 31 (10 2020), p. 2050147. DOI: 10.1142/S0129183120501478.

[115] B. Mantravadi and D. S. Tan. “Effect of bend angle on granular size segregation in the chute flow under periodic flow inversion”. In: *Powder Technology* 360 (2020), pp. 177–192. ISSN: 0032-5910. DOI: 10.1016/j.powtec.2019.10.005.

[116] Y. Zhao, S. Yang, L. Zhang, and J. Chew. “DEM study on the discharge characteristics of lognormal particle size distributions from a conical hopper”. In: *AIChE Journal* 64 (4 2018), pp. 1174–1190. DOI: 10.1002/aic.16026.

[117] M. Combarros, H. J. Feise, H. Zetzener, and A. Kwade. “Segregation of particulate solids: Experiments and DEM simulations”. In: *Particuology* 12 (2014). Special issue on conveying and handling of particulate solids – Challenges of discrete element simulation, application and calibration, pp. 25–32. ISSN: 1674-2001. DOI: 10.1016/j.partic.2013.04.005.

[118] T. F. Zhang, J. Q. Gan, D. Pinson, and Z. Y. Zhou. “Size-induced segregation of granular materials during filling a conical hopper”. In: *Powder Technology* 340 (2018), pp. 331–343. ISSN: 0032-5910. DOI: 10.1016/j.powtec.2018.09.031.

[119] S. Mandal and D. Khakhar. “Dense granular flow of mixtures of spheres and dumbbells down a rough inclined plane: Segregation and rheology”. In: *Physics of Fluids* 31 (May 2019), p. 23304. DOI: 10.1063/1.5082355.

[120] T. F. Zhang, J. Q. Gan, A. B. Yu, D. Pinson, and Z. Y. Zhou. “Segregation of granular binary mixtures with large particle size ratios during hopper discharging process”. In: *Powder Technology* 361 (2020), pp. 435–445. ISSN: 0032-5910. DOI: 10.1016/j.powtec.2019.07.010.

[121] W. Xu, S. Cheng, and C. Li. “Experimental study of the segregation of burden distribution during the Charging Process of Bell-less Top Blast Furnace with Two Parallel Hoppers”. In: 2044 (2021), p. 12129. DOI: 10.1088/1742-6596/2044/1/012129.

3

A Review of Modeling Strategies in Blast Furnace DEM Simulations

The previous chapter provided a broad overview of DEM modeling for blast furnace charging. This chapter takes a closer look at how these models have been developed, with the goal of identifying key foundations for building a reliable model. It focuses on methodological choices for material representation in DEM and examines how calibration practices have been applied to ensure that the modeled material behavior aligns with experimental observations. The discussion covers both single-component burden models and how these approaches have been extended to multi-component mixtures. Additionally, strategies used to make large-scale blast furnace simulations computationally feasible are reviewed.

This chapter is based on:
R. Roeplal, Y. Pang, A. Adema, J. van der Stel and D. Schott, *Modelling of phenomena affecting blast furnace burden permeability using the Discrete Element Method (DEM) – A review*, Powder Technology, Volume 415, 2023.

3.1 Basics of DEM

The fundamental principle of the DEM can be summarized as follows: if the forces (F) and torques (T) acting on each particle in the flow are known at each time step of the simulation, then their trajectories can be determined using Newton's second law. In this context, the behavior of each particle i is governed by both the translational and rotational equations of motion, which are given by

$$\sum \overrightarrow{F_i} = m_i \overrightarrow{a_i}(t) = m_i \frac{\mathrm{d}\overrightarrow{v_i}(t)}{\mathrm{d}t} = m_i \frac{\mathrm{d}^2 \overrightarrow{r_i}(t)}{\mathrm{d}t^2} \tag{3.1}$$

$$\sum \overrightarrow{T_i} = I_i \vec{\alpha}_i(t) = I_i \frac{\mathrm{d}\overrightarrow{\omega_i}(t)}{\mathrm{d}t} = I_i \frac{\mathrm{d}^2 \overrightarrow{\theta_i}(t)}{\mathrm{d}t^2} \tag{3.2}$$

where

- m_i and I_i are the mass and moment of inertia of particle i
- $\overrightarrow{a_i}$ and $\overrightarrow{\alpha_i}$ are the acceleration and angular acceleration of particle i
- $\overrightarrow{v_i}$ and $\overrightarrow{\omega_i}$ are the velocity and angular velocity of particle i
- $\overrightarrow{r_i}$ and $\overrightarrow{\theta_i}$ are the position and orientation of particle i

For coarse, free-flowing materials, the total force, $\overrightarrow{F_i}$, consists of gravitational forces and contact forces arising from interactions with surrounding objects j, represented as $\overrightarrow{F_{ij}^c}$. Similarly, the total torque $\overrightarrow{T_i}$ includes contributions from contact torques due to interactions with surrounding objects. At its core, DEM involves computing accelerations from forces and torques using Eq. 3.1 and 3.2, followed by numerical integration to update particle positions at the next time step. This iterative process allows for the prediction of flow behavior over time. A DEM algorithm begins by initializing a set of particles with prescribed initial conditions (such as velocities and positions) and proceeds through three main steps, as shown in Figure 3.1 and summarized below.

3.1.1 Contact detection

Most modern DEM solvers are based on the soft-sphere approach, in which particles are allowed to overlap with surrounding objects upon contact. These objects may include both other particles and walls. Whether a particle is in contact with an object depends on its position within the frame of reference, relative to the positions of its surroundings. A particle is defined in space by its center-of-mass position. By definition, two spherical objects are considered in contact if the distance between their centers is less than the sum of their radii. If this condition is met, the particles overlap and a contact force $\overrightarrow{F_{ij}^c}$ is activated. As shown in Figure 3.2, the normal overlap can be calculated instantaneously from the positions of the overlapping particles at time t by

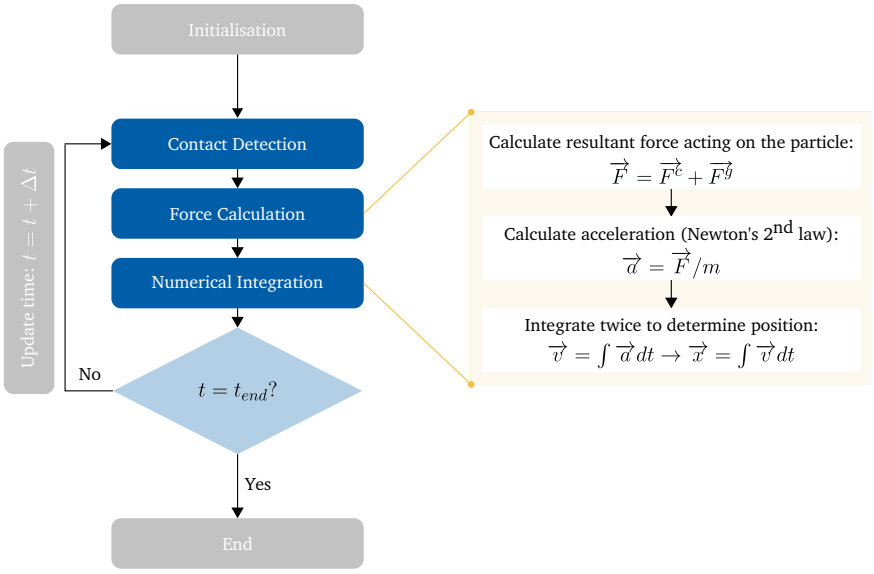


Figure 3.1: Flowchart of the DEM algorithm, showing the steps applied collectively to all particles in the simulation.

$$\delta^n = \left(R_i + R_j\right) - \left(\overrightarrow{r_i} - \overrightarrow{r_j}\right) \cdot \overrightarrow{n_{ij}} \tag{3.3}$$

where

$$\overrightarrow{n_{ij}} = \frac{\overrightarrow{r_i} - \overrightarrow{r_j}}{|\overrightarrow{r_i} - \overrightarrow{r_j}|} \tag{3.4}$$

Consequently, contact detection requires checking the distance between all objects in the system. A particle may be in contact with multiple surrounding objects, and when clumped spheres [1] are used to model non-spherical particles, each individual sphere in the clump is treated separately in the contact detection algorithm. The computed overlaps are stored for use in the subsequent force calculation step. Hence, as the number of objects in the system increases, the computational cost of the simulation rises accordingly with an even steeper increase when using clumped spheres. In addition to requiring more processing time, simulations with more objects and/or clumps also demand greater memory for data storage. Along with the force calculation step, the contact detection typically accounts for around 70-80% of the computational effort in a simulation.

3.1.2 Force and torque calculations using contact models

Once contact between neighboring objects is identified and the overlaps have been stored, the next step is to compute $\sum \overrightarrow{F_i}$ and $\sum \overrightarrow{T_i}$. The challenge lies in accurately determining the contact forces, which require careful consideration of interaction phenomena that depend on the physics of the simulated system. The contact force $\overrightarrow{F_{ij}^c}$ is generally decomposed into its normal and tangential components, denoted as $\overrightarrow{F_{ij}^n}$ and $\overrightarrow{F_{ij}^t}$, respectively. In addition to forces, the total torque at a contact between particles i and j results from $\overrightarrow{F_{ij}^t}$ and additional torque contributions, such as those due to rolling resistance ($\overrightarrow{T_{ij}^r}$). Consequently, Eqs. 3.1 and 3.2 can be reformulated as

$$m_i \frac{\mathrm{d}\overrightarrow{v_i}}{\mathrm{d}t} = m_i \vec{g} + \sum_{j=1}^{N_c} (\overrightarrow{F_{ij}^n} + \overrightarrow{F_{ij}^t}) \tag{3.5}$$

$$I_i \frac{\mathrm{d}\overrightarrow{\omega_i}}{\mathrm{d}t} = \sum_{j=1}^{N_c} (R_i \times \overrightarrow{F_{ij}^t}) + \overrightarrow{T_{ij}^r} \tag{3.6}$$

where R_i is the radius of particle i and N_c is the total number of particles in contact with particle i.

Various models have been developed for computing $\overrightarrow{F_{ij}^n}$, $\overrightarrow{F_{ij}^t}$ and $\overrightarrow{T_{ij}^r}$ based on the physics of the granular system; these are often referred to as "contact models". Contact models typically represent $\overrightarrow{F_{ij}^n}$ and $\overrightarrow{F_{ij}^t}$ using a spring-dashpot system analogy. In this system, the spring with stiffness k models the elastic restorative force, while the dashpot with damping coefficient γ accounts for energy dissipation through damping. Using this analogy, the normal force component $\overrightarrow{F_{ij}^n}$ is modeled as

$$\begin{aligned} \overrightarrow{F_{ij}^n} &= \left(F_{ij}^{e,n} + F_{ij}^{d,n}\right) \overrightarrow{n_{ij}} \\ &= \left(k^n \delta_{ij}^n - \gamma^n v_{ij}^n\right) \overrightarrow{n_{ij}} \end{aligned} \tag{3.7}$$

where $\overrightarrow{v_{ij}^n}$ is the normal velocity at the contact point. Similarly, the same spring-dashpot analogy applies to the tangential force component $\overrightarrow{F_{ij}^t}$. However, in addition to this formulation, the tangential interaction force is constrained by Coulomb's friction law, which limits its magnitude to the product of the normal contact force and the coefficient of friction. Thus, the tangential force component is given by

$$\overrightarrow{F_{ij}^t} = \begin{cases} \left(k^t \delta_{ij}^t - \gamma^t v_{ij}^t\right) \overrightarrow{t_{ij}}, & \text{if } \left|\overrightarrow{F_{ij}^t}\right| \leq \mu_s \left|\overrightarrow{F_{ij}^n}\right|, \\ \mu_s \left|\overrightarrow{F_{ij}^n}\right|, & \text{otherwise.} \end{cases} \tag{3.8}$$

where μ_s is the sliding friction coefficient between i and j. Unlike the normal overlap

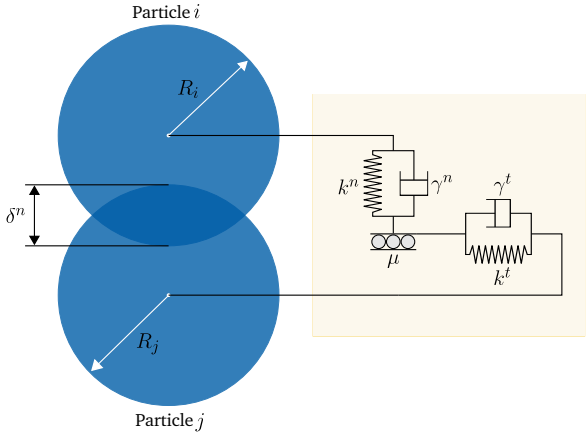


Figure 3.2: Schematic representation of the spring-dashpot interaction force model between two particles i and j in DEM.

δ^n which is calculated directly from the particle positions, the tangential overlap δ^t is accumulated over time based on the relative tangential motion at the contact point. It is determined based on δ^t at the current and previous time steps as

$$\overrightarrow{\delta^t}(t) = O\overrightarrow{\delta^t}(t - \Delta t) + \overrightarrow{v_{ij}^t}\Delta t \tag{3.9}$$

where O is a transformation matrix and $\overrightarrow{v_{ij}^t}$ is the tangential velocity at the contact point (for more details, the interested reader is referred to [2]). The value of $\overrightarrow{\delta^t}(t)$ is truncated to satisfy the yield criterion $\left|\overrightarrow{F_{ij}^t}\right| \leq \mu_s \left|\overrightarrow{F_{ij}^n}\right|$.

Considering the general equations of the force models (given by Eqs. 3.7 and 3.8), δ_{ij}^n, δ_{ij}^t, it is evident that v_{ij}^n, and v_{ij}^t are computed within the DEM algorithm. The remaining parameters (k^n, k^t, γ^n, and γ^t) are specific to the chosen contact model and are typically functions of the particles' material properties.

3.1.3 Numerical integration

After calculating all the forces and torques, the translational and rotational equations of motion for particle i are given by the second-order differential equations:

$$\frac{\mathrm{d}^2\overrightarrow{r_i}(t)}{\mathrm{d}t^2} = \frac{\sum \overrightarrow{F_i}}{m_i} \tag{3.10}$$

$$\frac{\mathrm{d}^2\overrightarrow{q_i}(t)}{\mathrm{d}t^2} = \frac{\sum \overrightarrow{T_i}}{I_i} \tag{3.11}$$

These second-order differential equations can be reduced to two sets of first-order differential equations as follows, with the corresponding initial conditions:

$$\begin{cases} \frac{\mathrm{d}\overrightarrow{v_i}(t)}{\mathrm{d}t} = \overrightarrow{a_i}(t), & \overrightarrow{v_i}(0) = \overrightarrow{v_{0_i}} \\ \frac{\mathrm{d}\overrightarrow{r_i}(t)}{\mathrm{d}t} = \overrightarrow{v_i}(t), & \overrightarrow{r_i}(0) = \overrightarrow{r_{0_i}} \end{cases} \tag{3.12}$$

$$\begin{cases} \frac{\mathrm{d}\overrightarrow{\omega_i}(t)}{\mathrm{d}t} = \overrightarrow{\alpha_i}(t), & \overrightarrow{\omega_i}(0) = \overrightarrow{\omega_{0_i}} \\ \frac{\mathrm{d}\overrightarrow{\theta_i}(t)}{\mathrm{d}t} = \frac{1}{2}\left[0\ \omega_{ix}\ \omega_{iy}\ \omega_{iz}\right]^T \times \theta_i, & \overrightarrow{\theta_i}(0) = \overrightarrow{\theta_{0_i}} \end{cases} \tag{3.13}$$

These sets of first-order ordinary differential equations can be solved using different numerical schemes, as described in detail by Kruggel-Emden *et al.* [3]. For example, the Euler scheme can be used to estimate the particle positions and velocities at the next time step using the known velocities and positions at the current time step. The Euler method is based on a first-order Taylor expansion, where the next value of a function is approximated by using its current value and the rate of change (velocity, acceleration, etc.). Specifically, the positions and velocities at the next time step are given by

$$\begin{cases} \vec{v}(t + \Delta t) = \vec{v}(t) + \vec{a}(t)\Delta t \\ \vec{r}(t + \Delta t) = \vec{r}(t) + \vec{v}(t + \Delta t)\Delta t \end{cases} \tag{3.14}$$

$$\begin{cases} \vec{\omega}(t + \Delta t) = \vec{\omega}(t) + \vec{\alpha}(t)\Delta t \\ \vec{\theta}(t + \Delta t) = \vec{\theta}(t) + \vec{\omega}(t + \Delta t)\Delta t \end{cases} \tag{3.15}$$

For explicit numerical schemes, it is crucial to determine a suitable value for the time step (Δt) to ensure the stability of the integration scheme. Several guidelines for selecting a time step are available in the literature, depending on the contact law. One approach is to use a fraction of the Rayleigh time step, which is based on the propagation speed of shear waves through solid particles. The time step must be small enough to accurately resolve this propagation, and it is governed by the material's stiffness and density. The Rayleigh time step is determined by

$$\Delta t_R = \frac{\pi R_{min}\sqrt{\frac{\rho}{G}}}{0.1631\upsilon + 0.8766} \tag{3.16}$$

where R_{min} is the smallest particle radius in the simulation and ρ, G and υ are the particle density, shear modulus and Poisson's ratio, respectively. In simulations involving mixtures of materials with different properties, Δt_R should be calculated separately for each material and the smallest value should be chosen. It is common to use $\Delta t = [0.2...0.4] \cdot \Delta t_R$ for quasi-static particle simulations.

3.2 A brief note on large-scale DEM model development

As with any model, a DEM model's input parameters must be chosen to ensure that its outputs reflect the real flow behavior. These inputs fall into three categories: (i) morphological parameters (*e.g.*, particle size and shape distributions); (ii) material properties (*e.g.*, density, Poisson's ratio, Young's modulus); and (iii) interaction parameters (*e.g.*, restitution and friction coefficients, which depend on material type, particle shape, and surface roughness). While parameters from categories (ii) and (iii) can theoretically be measured –though often with great difficulty– they are increasingly decoupled from measurable values as simplifications are introduced. Consequently, DEM models require calibration to adjust these parameters so that the model reproduces observed material behavior.

Before calibration, simplifications are often made to reduce computational time, considering the scale of the blast furnace to which the model will be applied. As discussed in Section 3.1, DEM computes particle interactions at each time step via numerical integration; thus, computational efficiency improves by reducing the particle count and increasing the time step. However, the time step depends on the smallest particle size and certain material properties, leading to common practices such as excluding the smallest particles (which otherwise increase both the particle count and time step constraints), using simplified particle size distributions, and adjusting material properties to permit larger time steps. Similarly, non-spherical particles are computationally more expensive to model than spherical particles; therefore, spherical particles are frequently used together with artificially increased rolling friction to approximate the behavior of non-spherical particles while allowing larger time steps. Additionally, the shear modulus is often reduced to further increase the permissible time step.

These modeling choices deliberately simplify reality to achieve computational feasibility for large-scale simulations. Nonetheless, ensuring that the model is not only feasible but also reliable remains essential. Balancing these objectives is an ongoing challenge in DEM model development. Based on insights from the literature [4–8] and accumulated practical experience, the following step-wise procedure is recommended for DEM model development:

1. *Selection of a contact model and fixed input parameters:* Given the variety of contact models available in DEM, the first step is to select a model that appropriately represents the physics of the system and to identify the required input parameters. This list consists of morphological parameters, material parameters, and interaction parameters. Depending on the ease of measurement or availability in the literature, the first two categories are typically determined or measured and fixed, leaving the interaction parameters to be calibrated.

2. *Sensitivity analysis of model inputs:* Input parameters can be determined through direct measurement and/or calibration. Calibration involves iteratively adjusting inputs in simulations until the model reproduces selected experimental responses [5]. To avoid an overly complex calibration process, it is advisable to measure or source less critical parameters from literature while calibrating only those parameters that strongly influence the process. Sensitivity analyses are recommended prior to calibration to identify which parameters require careful adjustment.

3. *Determination of model inputs:* During calibration, it is crucial to select experimental targets that are sensitive to the parameters being calibrated. Since multiple parameters can influence a single target, multiple calibration targets are typically needed to achieve a unique parameter set [6, 7]. Moreover, calibration experiments should reflect the flow conditions of the intended application. Traditionally, calibration is performed through trial-and-error by independently adjusting inputs and comparing simulated outputs to experimental data. However, this approach is inefficient, especially as the number of parameters increases [8], and rarely yields an optimal solution. Recent studies increasingly apply optimization techniques to improve calibration efficiency and accuracy [9–15].

4. *Verification and validation:* Once a parameter set is obtained, verification is necessary to confirm that the parameters remain valid for experiments beyond those used in calibration. It is again important to select validation tests that are sensitive to changes in the calibrated parameters [5]. The final validation step involves applying the calibrated model to the actual (industrial) process and comparing simulation results to operational data.

Table 3.1 provides a structured overview of the main modeling decisions made in previous blast furnace DEM studies. It details the selection of contact models, particle morphology (shape and size distributions), and the scale and type of computational domain employed. These elements directly correspond to the model development steps outlined earlier in this chapter, particularly the selection of the contact model, morphological parameters, and computational setup. By compiling these modeling choices in one place, the table establishes a foundation for the review that follows, where each aspect (such as particle shape approximation, size distribution simplifications, and model scaling) will be evaluated in the context of their impact on model reliability and computational feasibility. This analysis aims to identify current gaps and opportunities for improvement in large-scale DEM model development.

Table 3.1: Details of modeling methods applied in previous studies. Model: specifies the contact model (CM) and rolling model (RM) used; Shape: indicates whether the material component was modeled using "spherical" or "non-spherical" particles, respectively, and the number of non-spherical shapes used to represent a material component is given in parentheses; Size: The first number in the size column denotes how many different sizes were used to model the material component, while the second (parenthesized) number indicates the factor with which particles were enlarged in simulations, when compared to experiments; Computational domain: specifies the scale of the simulated system relative to the true system and the type of computational domain, where Type I = full 3D model, Type II = slot model, Type III = sector model. Abbreviations: HMns = Hertz-Mindlin no-slip, SP = spherical, NSP = non-spherical, m = multiple, PSD = particle size distribution, n.s. = not specified, N/A = not applicable.

Source	**Software**	**Model**	**Pellet**		**Sinter**		**Lump ore**		**Coke**		**Comp. domain**	
		CM / RM	*Shape (no.)*	*Sizes (UF)*	*Shape (no.)*	*Sizes (UF)*	*Shape (no.)*	*Sizes (UF)*	*Shape (no.)*	*Sizes (UF)*	*Scale*	*Type*
[16]	EDEM	HMns / A	SP	3+	–	–	–	–	–	–	n.s.	I
[17]	n.s.	HMns / A	SP	3	–	–	–	–	–	–	1:10	I
[18]	EDEM	HMns / A	SP	PSD	–	–	–	–	–	–	N/A	N/A
[19]	EDEM	HMns / A	SP	1	–	–	–	–	–	–	1:8	I
[20]	n.s.	Voigt / DRF	–	–	SP	3	–	–	–	–	1:3	I
[21]	n.s.	HMns / A	–	–	SP	3 (n.s.)	–	–	–	–	1:10	–
[22]	n.s.	Voigt / DRF	–	–	SP	8	–	–	–	–	1:3	I
[18]	EDEM	HMns / A	–	–	SP	PSD	–	–	–	–	N/A	N/A
[23]	EDEM	HMns / A	–	–	–	–	–	–	NSP (1)	3	n.s.	III
[24]	n.s.	n.s.	–	–	–	–	–	–	SP	PSD (1.5)	1:1	I
[25]	n.s.	n.s.	–	–	–	–	–	–	SP	PSD (1.5)	1:1	I
[26]	n.s.	HMns / A	–	–	–	–	–	–	SP	3	n.s.	I

Continued on next page

Continued from previous page

Source	Software	Model	Pellet		Sinter		Lump ore		Coke		Comp. domain	
		CM / RM	*Shape (no.)*	*Sizes (UF)*	*Shape (no.)*	*Sizes (UF)*	*Shape (no.)*	*Sizes (UF)*	*Shape (no.)*	*Sizes (UF)*	*Scale*	*Type*
[27]	n.s.	Voigt / n.s.	–	–	–	–	–	–	SP	3	n.s.	I
[28]	n.s.	n.s.	–	–	–	–	–	–	SP	PSD	1:1	I
[29]	EDEM	HMns / A	–	–	–	–	–	–	NSP (5)	PSD	1:1	I
[30]	n.s.	HMns / A	–	–	–	–	–	–	SP	2	n.s.	II
[31]	LIGGGHTS	HMns / C	–	–	–	–	–	–	SP	15	n.s.	I
[32]	n.s.	Voigt / DRF	–	–	SP	5	–	–	SP	4	n.s.	I
[33]	n.s.	Voigt / DRF	–	–	SP	5 (3.0)	–	–	–	–	1:1	I
[34, 35]		HMns / A	SP	1 (0.25)	–	–	–	–	SP	3 (0.25)	1:10	I
[36]	n.s.	Voigt / DRF	–	–	SP	5	–	–	SP	3	1:3	I
[35]	EDEM	HMns / A	SP	3	–	–	–	–	NSP (6)	3	n.s.	N/A
[37]	EDEM	HMns / A	SP	2	–	–	–	–	NSP (1)	6	1:10	III
[38]	EDEM	HMns / A	SP	1	–	–	–	–	NSP (5)	3	1:10	III
[39]	n.s.	HMns / A	SP	1	–	–	–	–	SP	1	1:32	II/III
[40]	EDEM	HMns / A	SP	1	–	–	–	–	NSP (5)	3	1:10	III
[41]	EDEM	HMns / n.s.	SP	m	NSP (1)	m	–	–	NSP (1)	m	n.s.	I
[42]	n.s.	Voigt / n.s.	–	–	–	–	–	–	SP	3	n.s.	I

Continued on next page

Continued from previous page

Source	Software	Model	Pellet		Sinter		Lump ore		Coke		Comp. domain	
		CM / RM	*Shape (no.)*	*Sizes (UF)*	*Shape (no.)*	*Sizes (UF)*	*Shape (no.)*	*Sizes (UF)*	*Shape (no.)*	*Sizes (UF)*	*Scale*	*Type*
[43, 44]	in-house code	n.s.	SP	PSD	SP	PSD	–	–	SP	PSD	1:1	I
[45]	n.s.	HMns / A	–	–	SP	3 (2.0)	–	–	SP	3 (2.0)	1:1	I
[46]	LIGGGHTS	Voigt / n.s.	–	–	NSP	1 (0.05)	NSP	1 (0.05)	–	–	1:20	I
[47]	n.s.	HMns / A	SP	1 (2.0)	SP	1 (2.0)	SP	1 (2.0)	–	–	1:1	I
[48]	n.s.	HMns / A	SP	PSD	SP	PSD	SP	PSD	–	–	1:1	I
[49]	LIGGGHTS	HMns / A	SP	1 (2.5)	SP	2 (2.5)	–	–	–	–	1:5.8	I
[50]	n.s.	HMns / A	SP	1 (2.0)	SP	1 (2.0)	SP	1 (2.0)	–	–	1:1	I
[51]	n.s.	Voigt / DRF	–	–	SP	8	–	–	SP	5	1:3	I
[52]	RockyDEM	HMns / A	SP	PSD	SP	PSD	–	–	–	–	1:1	I
[53]	LIGGGHTS	HMns / C	–	–	SP	3	–	–	SP	3	1:10	I/II
[54]	n.s.	HMns / A	SP	1 (2.0)	SP	1 (2.0)	SP	1 (2.0)	SP	3 (2.0)	1:1	I
[55]	EDEM	HMns / A	SP	3 (2.0)	NSP (3)	4 (2.0)	–	–	–	–	1:1	I
[56]	n.s.	HMns / A	–	–	SP	1	–	–	SP	1	1:1	I

3.3 Contact models

Table 3.1 shows that most blast furnace studies have employed the non-linear Hertz–Mindlin no-slip model [57], with fewer adopting the Kelvin–Voigt model [58], to describe the normal and tangential interaction forces between particles as given by Eqs. 3.7 and 3.8. A rolling resistance model is typically applied alongside these forces to account for the bulk friction of real, non-spherical particles represented by idealized or simplified shapes in DEM. Blast furnace modelers have employed different rolling resistance models based on two main approaches. The first and most common method involves a single (uniform) rolling friction coefficient between all particles of a material component. Ai *et al.* [59] summarized four classes of rolling friction models which are commonly used in DEM studies based on this approach: constant resistive torque (Model A), viscous resistive torque (Model B), elastic–plastic spring dashpot torque (Model C) and contact-independent resistive torque (Model D). Rolling models A and C are most often used in DEM simulations [60], although rolling model C performs better than model A in static situations, where model discontinuities may occur [59]. Another approach, originally suggested by Mio *et al.* [20] for modeling sinter behavior, involves a distributed rolling friction coefficient. It was argued that since sinter particles have many different shapes, a unique friction coefficient should be determined to account for each shape. Table 3.1 shows that the distributed rolling friction (DRF) approach has only been utilized within the research group of Mio *et al.* and almost all remaining studies used rolling model A. The choice of rolling model used is obscure, which is interesting given the fact that Ai *et al.* [59] pointed out the difference in performance of the models. Moreover, the fact that model C is only encountered in the studies of Wei *et al.* [53] and Holzinger and Schatzl [31] while it is considered superior to model A [59], is remarkable. A possible explanation for this overwhelming use of model A is its widespread implementation in different software packages at the time of execution. For example, in EDEM, model C became available as a standard rolling model only from version 2021.2. However, this cannot be investigated further as the majority of the studies listed in Table 3.1 do not state which software package was used.

Based on these findings, the Hertz–Mindlin no-slip model combined with rolling model C appears to be a suitable choice for developing a blast furnace charging model. Table 3.2 summarizes the equations and parameters for these models. In summary, a DEM model using these contact models requires the following input parameters:

1. Particle size (R), which can be specified in terms of a particle size distribution (PSD)
2. Particle shape distribution, when non-spherical particles are used
3. Particle density (ρ_p)

Table 3.2: Mathematical relations for the Hertz–Mindlin no-slip contact model and rolling models A–D, applied to interactions between particles i and j.

Hertz-Mindlin no-slip contact model and parameters [61]			
Effective Young's modulus		$E^* = \left(\frac{1-\upsilon_i^2}{E_i} + \frac{1-\upsilon_j^2}{E_j}\right)^{-1}$	(3.17)
Effective shear modulus		$G^* = \left(\frac{2-\upsilon_i}{G_i} + \frac{2-\upsilon_j}{G_j}\right)^{-1}$	(3.18)
Effective radius		$R^* = \left(\frac{1}{R_i} + \frac{1}{R_j}\right)^{-1}$	(3.19)
Effective mass		$m^* = \left(\frac{1}{m_i} + \frac{1}{m_j}\right)^{-1}$	(3.20)
Damping ratio		$\beta = \frac{\ln e}{\sqrt{(\ln e)^2+\pi^2}}$	(3.21)
Normal force	Eq. 3.7, with	$k^n = -\frac{4}{3}E^*\sqrt{R^*\delta^n}$	(3.22)
		$\gamma^n = \sqrt{5}\beta\sqrt{m^*k^n}$	(3.23)
Tangential force	Eq. 3.8, with	$k^t = -8G^*\sqrt{R^*\delta^n}$	(3.24)
		$\gamma^t = 2\sqrt{\frac{5}{6}}\beta\sqrt{m^*k^t}$	(3.25)
Parameters	R, υ, E, G, ρ (via m), e, μ_s (via Eq. 3.8)		
Rolling resistance model and parameters [59]			
Model C		$\begin{cases} T_{ij}^{ro,t+\Delta t} = T_{ij}^{ro,t} + \Delta T_{ij}^{ro} \\ \left\lvert T_{ij}^{ro,t+\Delta t}\right\rvert \le \mu_r R^* F^n \end{cases}$	(3.26)
	with	$\Delta T_{ij}^{ro} = -S^r \Delta\theta_r - C_r \frac{d\theta_r}{dt}$	(3.27)
Parameters	μ_r		

4. Young's (or shear) modulus (E or G) for particle and equipment
5. Poisson's ratio (υ) for particle(s) and equipment
6. Sliding friction coefficient between particles (μ_s^{P-P}) and between particles and equipment (μ_s^{P-W})
7. Restitution coefficient between particles (e^{P-P}) and between particles and equipment (e^{P-W})
8. Rolling friction coefficient between particles (μ_r^{P-P}) and between particles and equipment (μ_r^{P-W})

In this list, items (1) and (2) define the particle morphology, items (3)–(5) specify the material properties, and items (6)–(8) define the interaction parameters required by the contact models. For a single material with fixed properties and morphology, six interaction parameters need to be specified in the DEM model to perform the calculations in Table 3.2: e^{P-P}, e^{P-W}, μ_s^{P-P}, μ_s^{P-W}, μ_r^{P-P}, and μ_r^{P-W}. However, in mixtures of multiple materials, the number of required parameters increases rapidly, as each interaction pair must be defined separately. For a mixture of two materials, three distinct particle–particle interactions must be specified (material 1 with material 1, material 2 with material 2, and material 1 with material 2), along with two separate particle–wall interactions (material 1 with the wall and material 2 with the wall). Consequently, each parameter (e, μ_s, μ_r) must be

specified for all five interaction types, resulting in a total of 15 interaction parameters. For three materials, the number of required parameters increases further to 27. In general, the number of interaction parameters grows quadratically with the number of materials, underscoring the increasing complexity of modeling multi-component mixtures using DEM.

3.4 Sensitivity analyses for input parameters

Sensitivity analyses provide an indication of which input parameters have the biggest impact on the simulation results. These analyses are useful for several reasons. As mentioned previously, one reason is for determining which input parameters are relevant and must therefore be calibrated for a specific application. Also, as blast furnace studies are being performed all around the world with raw materials which may differ in material properties, sensitivity analyses elucidate whether region-dependent custom modeling is required. Finally, it is useful to know whether adjusting certain inputs to speed up simulations still provides accurate results. In order to get insight into these aspects, the results of different studies focusing on such analyses are reviewed in this section.

3.4.1 Effect of morphology

Particle shapes

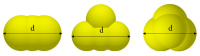
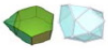
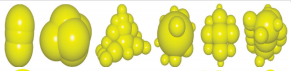
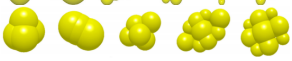
The morphological features of a granular material can be simplified in DEM simulations for computational efficiency. For example, modeling particles as spheres in combination with rolling resistance [4, 60] results in faster simulations when compared to non-spherical particle approximations [62] such as ellipsoids, superquadrics, polyhedrons and clumps (also referred to as clusters, composite spheres or multi-spheres). The simulated flow behavior of irregularly shaped particles can be replicated to some degree by applying rolling resistance to the spherical particles. However, the packing behavior of a non-spherical assembly is different from a non-spherical assembly where interlocking of particles generally allows a higher maximum packing density to be achieved [62, 63]. Hence, the particle shapes which are used to model burden distribution must be carefully considered.

The literature review has shown that pellets are generally modeled as spherical particles due to their nearly spherical shape in reality. Sinter and coke have been modeled as both spherical and non-spherical particles (see Table 3.3) primarily using particle clumps, and using polyhedra in the study of Govender *et al.* [46]. Unlike pellets, coke and sinter particles do not closely resemble spheres and the spherical approximation method must be justified when used, since the particle shape affects important granular phenomena such as segregation and packing characteristics which determine the permeability. Some references state that the spherical approximation method provides suitable results when

the goal is to model flowing behavior rather than packing behavior. Akashi *et al.* [64] investigated the effect of particle shape on the flow and packing behavior of coal particles by using either spheres or clumped spheres in simulations and comparing the results to experiments. The spherical particles had a higher rolling friction coefficient than the clumped spheres; however, it is not clear how the values were determined. They observed that the effect of particle shape on flowing behavior (in terms of mean particle velocity and mean flowing angle) was insignificant, while the bulk density distributions in simulations using spherical particles did not correspond to experiments. Hence, they concluded that the particle shape plays an important role when modeling the packing structure. Mio *et al.* [22], in their study of sinter discharge from a chute, mentioned explicitly that they considered the spherical approximation method to be suitable because trajectories were being studied, rather than packing characteristics. When it comes to studies focusing on segregation, only Yu and Saxén [23] analyzed the effect of particle shape. They considered four different shapes (sphere, triangle, cylinder and hexahedron) for modeling size segregation during charging and discharging of a Paul-Wurth hopper in order to identify which shape showed the best agreement with experimental results. They found that the particle shape is insignificant during the charging process, while the spherical shape provided the best results during the discharging process. Therefore, they concluded that spherical particles are suitable for modeling size segregation of coke during hopper charging and discharging. Mitra and Saxén [38] studied the difference between using spherical and non-spherical coke particles when modeling the coke collapse phenomenon. It was shown that non-spherical particles performed better when considering the heap formation during coke charging. However, some aspects of the formed layers agreed equally well or even better to experimental results when using spherical particles.

It must be noted that the same rolling friction coefficient was applied to both spherical and non-spherical particles in the aforementioned studies. Hence, the models were not calibrated for each individual shape and the comparisons were therefore not objective. Wei *et al.* [68] studied the effect of particle shape (sphere, cone and cylinder) on the porosity distribution of a heap formed by hopper discharge after calibrating the model for each shape. Although these shapes did not resemble blast furnace material shapes, their study pointed out that particle shape plays an important role in the porosity distribution. They later studied packing behavior of pellet [69] and coke [53] in terms of porosity distribution, which is closely linked to permeability. They used spherical particles to model pellet and coke and in both cases and concluded that the porosity distribution obtained from simulations generally matched experimental results. It must be noted, however, that the match in the case of pellets was much better than in the case of coke. Interestingly, the authors attributed differences in results to “systematic errors” and “non-idealities in the experiment” and did not investigate whether non-spherical particles in the simulation

Table 3.3: Shape approximation methods used for modeling sinter and coke particles using DEM according to blast furnace literature. Images adopted from the corresponding citations.

Shape approximation method	**Source**	**Illustration**
Sinter		
Clumped spheres	Schott *et al.* [41]	
	Chakrabarty *et al.* [65]	
	Chen *et al.* [66]	
Polyhedra	Govender *et al.* [46]	
Coke		
Clumped spheres	Yu and Saxén [17]	
	Mitra and Saxén [38, 40]	
	Yu and Saxén [37]	
	Schott *et al.* [41]	
	Chakrabarty *et al.* [29]	
	Bester *et al.* [67]	
Polyhedra	Govender *et al.* [46]	

would provide better results.

Clumps are formed by merging multiple overlapping spheres. The degree of overlap between mutual overlapping spheres and the size of each sphere can be chosen freely so that any arbitrary shape can be generated. While the computational cost increases as more and smaller spheres are used to form a clump, the shape approximation often becomes more accurate. Since actual coke and sinter particles are shape polydisperse [23], the main challenge is to select a representative shape and subsequently approximate the (clumped) shape using a minimum number of spheres which have the largest possible size. Although this an important task for both model accuracy and computational efficiency, the cited studies do not elaborate on the methods which were used to select the representative shapes, and how the clumps were optimized in terms of sphere count and size. It is generally stated that a number of common shapes within a material sample were selected and each shape was generated with equal probability in simulations. Another question which remains is: how many different clump shapes are assumed to be sufficient for representing the material? Yu & Saxén used six highly irregular shapes to model coke in [17], while they assumed only one of those shapes in [37], as shown in Table 3.3. Chakrabarty *et al.* [65] assumed a single shape to model sinter particles, which have high shape dispersity. While it is not clear how this specific shape was selected, they reported a good agreement between simulated and experimental repose angle and bulk density, and concluded that this simple shape was suitable for modeling the bulk behavior of sinter.

The use of other shape approximation methods for blast furnace materials has also been considered. Govender *et al.* [46] investigated the effect of coke and ore particle shape on chute discharge, charged burden topography and charged layer percolation using either polyhedra, which are angular in shape, or spheres in combination with rolling resistance. The size of spheres was equivalent volume of the polyhedra and rolling friction coefficients were determined by matching angle of repose of spherical and polyhedral burden discharged from a chute. The remaining input parameters were identical for both shapes. They concluded that there were significant differences in velocity and mass flow profiles between spheres and polyhedra, which is in contrast to the results of Akashi *et al.* [64]. Inter-layer percolation and packing density were also significantly affected by the particle shape. Hence, the authors concluded that modeling the burden as spherical particles in combination with rolling friction is not sufficient to account for particle shape effects when considering particle velocities, packing topography and permeability. Xia *et al.* [70] studied the effect of using spheres versus different super-ellipsoids to model the flowing and packing behavior of crushed material which, according to the authors, has shape characteristics similar to blast furnace materials. They used a pseudo-2D setup consisting of a hopper and a discharge bin to represent the furnace charging system in a simplified way. They scrutinized the performance of super-ellipsoid

models by comparing the discharged material's macro-scale behavior in simulations to experiments and concluded that while spherical and super-ellipsoid particles were both able to predict the packing height, other aspects such as packing profiles, dynamic repose angle, and flow rate could not be predicted by spheres. Since the micro-scale performance of each model (for example in terms of the packing porosity) was not evaluated by comparison to experiments, it is not clear whether super-ellipsoids are also useful for predicting the packing behavior of materials with large size and shape dispersity.

Particle size distribution

The true particle size distribution can also be simplified in simulations. Small particles are generally avoided since they prolong simulation in two ways: first, according to Eq. 3.16, the numerical time step becomes smaller as the particle size decreases and second, the number of particles required to model the flow increases as the particle size decreases. To increase computational efficiency, the general approach is to adjust particle–to–geometry size ratio such that particles are enlarged; this results in both a larger time step and a reduced number of particles. This can be done by either up-scaling the particle size [71–73] *or* down-scaling the geometry dimensions, or by applying a hybrid scaling approach in which both particle size and geometry dimensions are scaled using individual scaling factors [74, 75]. When scaling the particle size, a distinction is made between coarse-graining and scalping [76]. The first method involves replacing a parcel of unscaled particles by a larger, coarse-grained particle, thereby reducing the number of particles required to simulate the process. In the second method, fines are neglected by "cutting off" the PSD at a certain particle size, which in essence comes down to coarse-graining only the fine particles below the cut-off size [76]. Another scaling technique often used is exact scaling, which involves using the same scaling factor for particles and geometry [77–79]. The aspect of scaling is discussed further in Section 3.7.

Similar to the particle shape, the use of a simplified PSD in simulations requires justification. Table 3.1 shows that only few researchers have modeled burden materials according to their true PSD. The majority of models has been developed using at most three particle sizes. The experimental counterparts of these studies use essentially the same simplified PSD (achieved by sieving); consequently, these models are not representative of actual burden behavior. The number of studies focusing on how the actual PSD can be simplified in simulations, through verification using the actual PSD in experiments, is scarce. Yu and Saxén [17] studied segregation of pellet and coke particles from a fixed chute, where both materials were modeled as a tridisperse mixture of fine, intermediate and coarse particles in simulations. The three particle sizes corresponded to the mean diameter of the size ranges used in the experiments. Unlike pellets, the coke particles were modeled as a combination of six different clumped spheres. To scrutinize the effect

of particle size on the flow behavior in simulations, a test case was performed where the pellets were given the same parameters as the coke particles, except for the size. By comparing the results of this simulation to the original simulation of coke, it was concluded that pellets with the same parameters as coke behave in a similar way as coke with respect to the rotational and translational velocities in the chute. Schott *et al.* [41] investigated whether modeling the true PSD of individual components is required to model the tendency to segregate of a mixture of iron ore pellets, sinter and coke during hopper discharge and subsequent heap formation. It was found that representing each of the materials by its mean particle size (d_{50}) reduces the number of particles and simulation time drastically without compromising the simulation results of the used material models.

3.4.2 Effect of material parameters

Density

The density of an object is defined as the mass per unit volume of the material. Different types of density can be determined based on the volume which is considered in the calculation [80]. For a highly porous material, the true volume (*i.e.*, the volume of the particle which excludes the volume of internal pores, either open or closed) occupied by a solid particle can be significantly lower than the total (encapsulated) volume of the particle. In DEM simulations, particles are modeled as nonporous; hence, the encapsulated density should generally be specified rather than the true (skeletal) density. For non-porous materials, these density values are equal. Section 3.5.1 discusses how both of these values can be measured, and that the skeletal density can be significantly higher than the encapsulated density for porous materials. It is therefore reasonable to question how significant a discrepancy in density value affects the simulation of different phenomena. According to Katterfeld *et al.* [7], the particle density has a negligible effect on the bulk material's flowing behavior while it is strongly related to packing characteristics such as the bulk density and porosity. This was clearly demonstrated in the work of Tripathi *et al.* [18]. The authors used the method of interstitial fluid for measuring pellet and sinter particle density, resulting in a wide range of possible values (see Table 3.4) which could be used as inputs to their material model. In order to assess the effect of this range, they simulated dynamic angle of repose and bulk density tests using the extremes and compared the results to experimental results. They found that the repose angle was not significantly affected by changes between the extremes while the bulk density required an appropriate value within the range to be selected. Ho *et al.* [81] experimentally studied the effect of particle density on coke push by using a simplified charging setup and balls of different densities, where low-density and high-density balls represented coke and ore, respectively. They concluded that the coke push effect becomes more pronounced as the density of the heavy material increases. More specifically, the

gouge size increases as the density increases. The effect of particle density on spontaneous percolation of small particles into a packed bed of larger particles was investigated by Zhou *et al.* [82]. As they expected, there was no considerable effect of the percolating particles' density on their movement through the bed since a tightly packed bed was used in the analysis. The authors hypothesized that there might be a noticeable effect if the packing particles could move after impact with the percolating particles. Yu and Saxén [35] studied the layer expansion process during burden descent. A pellet layer was placed on top of a coke layer, and the percolation of pellets into the coke layer was analyzed for different densities of pellets ($\rho_P = [1000, 2284, 3000]$ kg/m^3) and coke ($\rho_C = [500, 1050, 1500]$ kg/m^3). The value of pellet density had no clear effect on the percolation behavior. On the other hand, the coke density of 1050 kg/m^3 provided the highest degree of percolation. The authors hypothesized that percolation in the case of lowest coke density was obstructed because the heavy pellet particles were able to move the coke particles such that the voids of the coke bed were sealed.

Young's modulus

According to Eq. 3.16, the numerical time step depends on the shear modulus and therefore, by definition, on the Young's modulus. By lowering the value of G (or E), the computational load can be reduced significantly. However, since a lower value of E corresponds to a softer material, it is important to assess to what extent a reduction in E can still provide accurate results [83]. Yu and Saxén [37] lowered the shear modulus of pellets from 10^9 to 10^7 Pa in their simulations of furnace charging and compared their results to a validated model of Okuno *et al.* [84] for predicting mass fraction distribution of a pellet stream. They reported that both values of the shear modulus were in good agreement with the results of Okunu's model. Furthermore, the lowered value of G resulted in only a slight decrease of the total average force on small pellets, while the pellet (average, minimum, maximum and angular) velocities during charging as well as the charged radial burden distribution were practically unaffected. Based on this result, several other researchers [45, 47, 54, 85] adopted the lowered value of 10^7 Pa in their work, applying this value to sinter and lump ore as well. When it comes to segregation, Zhu *et al.* [86] studied the effect of Young's modulus on the percolation of a single particle in a packed bed. They found no significant effect on the percolation behavior when lowering the Young's modulus of the percolating particle. Ueda *et al.* [87] studied how the descending behavior of coke and ore was affected by reducing the Young's moduli for both materials from $5 \cdot 10^9$ to $2 \cdot 10^8$ Pa. They concluded that the layer shapes did not change, while the stress distributions were clearly affected by the hardness reduction.

3.4.3 Effect of interaction parameters

Yu and Saxén [16] studied size segregation of pseudo-tridisperse pellets during discharge of a top bunker (conical) hopper, where pseudo-tridisperse indicates that there were three main size classes of particles with a narrow size distribution. The inter-particle and particle–wall sliding and rolling friction coefficients were varied as $\mu_s, \mu_r = [0.05, 0.5, 0.9]$. It was concluded that the particle–wall friction coefficients affect the degree of segregation while the inter-particle friction coefficients do not. In their sensitivity study for the percolation of pellets into a coke layer during layer expansion, Yu and Saxén [35] also scrutinized the effect of pellet–pellet (P–P) and pellet–coke (P–C) interaction parameters. It was clear that low values of the static friction coefficient ($\mu_s^{P-P} = 0.1$ and $\mu_s^{P-C} = 0.1$) promoted percolation which was expected since a low friction value means low contact resistance between particles. Less percolation occurred at higher static friction values, and there was no noticeable effect when μ_s^{P-P} and μ_s^{P-C} were increased from 0.5 to 0.9. When it comes to the rolling friction coefficient, high values of μ_r^{C-C} resulted in stronger percolation. This can be explained by the fact that coke particles' angular motion increases with rolling friction coefficient, therefore opening up the voids between the particles and allowing pellets to percolate. The values of μ_r^{P-P} and μ_r^{P-C} did not seem to have a noticeable effect on percolation, except that it was improved at very low values ($\mu_r^{P-P} = 0.05$ and $\mu_r^{P-C} = 0.04$). For the restitution coefficient is was found that e^{C-C} had no effect on the pellet percolation, while lower values of e^{P-C} and higher values of e^{P-P} resulted in less percolation. Liu *et al.* [26] modeled the trajectory of material after being discharged from a rotating chute, and its distribution in the furnace throat. It was concluded that inter-particle friction coefficients significantly affected the behavior of material which were in contact with the chute, while the effect on particles which were not in contact with the chute was negligible. When looking at the burden trajectories after being discharged from the chute, the effect of friction coefficients was negligible. However, they had a significant impact on the burden profile in the throat.

3.5 Determination of model inputs

This section reviews the measurement and/or calibration methods used to determine model inputs in blast furnace literature listed in Table 3.1.

3.5.1 Direct measurement

The direct measurement approach has been applied for primarily iron ore pellet and to a far lesser extent for sinter and coke. Table 3.4 lists the test setups used for measuring different input parameters according to blast furnace literature.

Table 3.4: Methods for determining model input parameters from references related to blast furnace literature. Abbreviations: p–p = particle–particle, p–w = particle–wall, n.s. = not specified, N/A = not applicable.

Type	Method (standard, if specified)	Pellet	Sinter	Coke
Particle density, ρ_p (kg/m^3)				
N/A	Gas pycnometer	3948 [88], 3990 [89]	–	–
	Envelope density analyser	3552 [18]	3311 [18]	–
	Water displacement method	3126–3771 [18]	3041–3477 [18]	1021 [67]
	Drainage method	3674 [66]	3199 [66]	–
Young's modulus, E (GPa)				
N/A	Shimadzu autograph universal tester	0.033 [90]	–	–
	Dynamic elastic modulus tester (ASTM E1876–01)	126 [89]	–	–
Shear modulus, G (GPa)				
N/A	Dynamic elastic modulus tester (ASTM E1876–01)	50.9 [89]	–	–
	Impact load cell	0.016 [88]	–	–
Poisson's ratio, υ (-)				
N/A	Dynamic elastic modulus tester (ASTM E1876–01)	0.24 [89]	–	–
Restitution coefficient, e (-)				
p-p	Drop test with glued particle surface	0.42 [89] [91]	0.35 [89]	0.39 [89]
p-w	Drop test with wall surface	0.62 (steel) [89]	0.4 (steel) [89]	0.42 (steel) [89]
Sliding friction coefficient, μ_s (-)				
p-p	Pin-on-disk rotational tribometer	0.49 [88]	–	–
	Tilted table with two glued particle surfaces	0.65 [89]	0.76 [89]	0.87 [89]
	Poured repose angle test i.c.w. Eq. 3.32	0.49 [18]	0.55 [18]	–
p-w	Tilted table with one glued particle surface	0.36 (steel) [89]	0.52 (steel) [89]	–
	Pin-on-disk rotational tribometer	0.5 (steel) [88], 0.71 (rubber) [88]	–	–

Continued on next page

Continued from previous page

Type	Method (standard, if specified)	Pellet	Sinter	Coke
	Inclined surface test	0.19 (glass) [18], 0.38 (acrylic) [18]	0.17 (glass) [18], 0.38 (acrylic) [18]	0.852 (rubber) [67], 0.24 (ceramic) [67]
Rolling friction coefficient, μ_r (-)				
p-p	Particle velocity measurement i.c.w. energy balance equation	0.24 [89]	0.38 [89]	0.46 [89]
	2D Image analysis i.c.w. Eq. 3.33	0.07 [18]	0.20 [18]	–

Remarks:

[a] Determined through simulation with spheres

[b] Determined through simulation with overlapping spheres

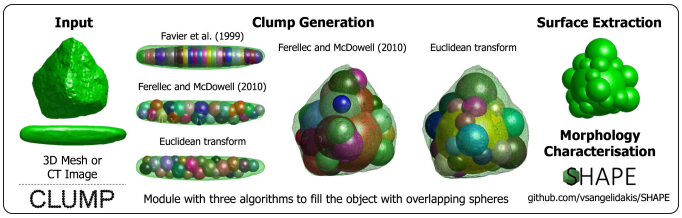


Figure 3.3: The main modules of the CLUMP tool, illustrating how clumped sphere approximations of imaging data are created based on different algorithms. SHAPE can be used as a complementary tool to characterize particle morphology. Image adopted from [94].

Morphology

The particle size and shape distributions are the first to be measured, as calibration is performed for material with a certain morphology. Size distributions are generally measured through sieving, either using a vibration table or manually. The latter was reported to be more practical for iron ore pellets due to the relatively large particle size [2]. Although it is often reported that "pellets are approximately spherical" while "sinter and coke have highly irregular shapes", no blast-furnace publications were found that report the burden's shape distributions. Researchers generally select one or few irregular shapes to represent sinter and coke without stating how the number and type of shape was selected. For future work, a variety of shape descriptors based on 2D and 3D image analysis [92] can be used for particle shape characterization. Angelidakis *et al.* recently developed SHAPE [93] (see Figure 3.3), a MATLAB-based tool which performs morphological characterization of 3D particles obtained from imaging data. They also developed the CLUMP tool [1] for generating clumped particles from the data based on three different algorithms. The user specifies certain requirements of the clump, for example the number of spheres it may be comprised of. Generated clumps can subsequently be imported into different software packages.

Density

Section 3.4.2 discussed how the magnitude of particle density depends on the volume considered in its calculation. Figure 3.4 illustrates the difference between skeletal volume and encapsulated volume which can be measured using a gas pycnometer and encapsulated density analyzer, respectively. A gas pycnometer uses and inert gas to fill a chamber of known volume containing a particle sample. Since the gas is able to penetrate open surface pores, the amount of gas supplied to the chamber, and therefore the true particle volume, can be approximated very closely. This method was used by Barrios *et al.* [88] and Wei *et al.* [89]. An envelope density analyzer uses a granular material with high flowability to achieve a close packing around a particle specimen by compaction

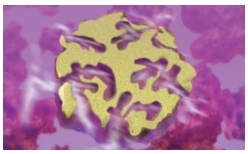
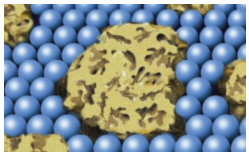



Figure 3.4: Particle volume estimation (from left to right, images adopted from [96]): (a) using a gas pycnometer, (b) using an envelope density analyzer.

using a piston. The packing particles are small enough to adhere closely to the specimen surface; however, they do not enter the open pores. The piston's displacement during compaction allows the encapsulated volume of the specimen to be approximated. Tripathi *et al.* [18] used the GeoPyc 1365TM [95] to determine the envelope density. While encapsulated density meters are relatively fast and easy to use, the main drawback is that such devices are generally limited in the particle size which can be used in the measurement due to the chamber size. Also, particles with very complex shapes (*e.g.* particles with deep concaves such as sinter) might not be suited for this device, as the packing particles may not be able to penetrate surface pores which are small compared to the packing particle size. An alternative is the fluid displacement method, as used by Tripathi *et al.* [18]. They filled a cylindrical container with particles and carefully added water to the brim. By assuming that no water entered the particles' pores, the volume occupied by the particles was determined as the container volume minus the volume of water which was required to fill the container. The envelope density was then determined as the ratio of material mass and volume in the container. To make the estimation more accurate, they excluded the volume of water which entered the pores from the calculation. This was done by measuring the mass of the wet particles and subtracting that value from the mass of the dry particles, which gave the mass (and volume) of water in the pores. This procedure resulted in a wide range of possible values for the envelope density. Chen *et al.* [55] used a similar method, but took measures to prevent water from entering the pores. They sealed the pores by immersing the particles in paraffin before bringing the particles in contact with water. This method is referred to as the "drainage method" and, according to Table 3.4, the measured density values of pellet and sinter were within the wide range of possible values produced by Tripathi *et al.* [18].

Young's modulus, shear modulus and Poisson's ratio

Li *et al.* [90] used a Shimadzu Autograph universal tester to determine the Young's modulus of pellet. Their setup included a piston to apply a vertical (normal) force on a particle until breakage occurs. The force (F^n) and particle indentation (δ^n) were directly obtained from the user interface, and the authors subsequently estimated the Young's

modulus from the Hertz contact law (Eq. 3.7). This was done for pellets varying in size, and average value of all measurements was used. Wei *et al.* [89] used a dynamic elastic modulus tester to measure Young's modulus, Shear modulus and Poisson's ratio of pellet. Rather than accommodating particles directly, this setup requires a rectangular "plate" sample with a minimum size of 3 × 4 × 40 mm. The authors argued that the values of E, G and υ are independent of the material size and shape, and prepared rectangular samples to satisfy the setup requirements. The authors noticed a significant difference between their value of the Young's modulus (1.26×10^{11} Pa) and the value reported by Li *et al.* [90] (3.3×10^{7} Pa) and other values from literature. They mentioned that differences could be attributed to the sample preparation process, which may have enhanced the material strength.

Restitution coefficient

The restitution coefficient is generally determined through a drop test. In some cases, the dropping height (h_d) and rebound height (h_r) are measured using high-speed cameras, as described in [97], and subsequently used to calculated the restitution coefficient as

$$e = \sqrt{\frac{h_r}{h_d}} \tag{3.28}$$

Since this calculation applies to central impact, it is less suitable for irregularly shaped particles. The following equation based on the ratio of rebounding and incoming velocities (v_r and v_i, respectively) has shown to be more appropriate [97]

$$e = \frac{v_r}{v_i} \tag{3.29}$$

A detailed description on how the particle velocity is determined from image analysis is provided by Wei *et al.* [89]. Barrios *et al.* [88] used this approach for measuring the pellet–wall restitution coefficient using steel and rubber surfaces. For the pellet–pellet restitution coefficient, they followed the same method using a packed iron ore surface. Wei *et al.* [89] followed the same method, but instead glued particles to a plate for determining the particle–particle restitution coefficient. In order to reduce the effect of particle shape, they glued the particles such that a "flat" part faced upwards.

Sliding friction coefficient

The most common setup used for determining the sliding friction coefficient involves a surface which is gradually titled until the particle starts to slide [29, 89]. The surface angle (θ_s) on the onset of sliding is then measured, and the friction coefficient is determined as

$$\mu_s = \tan(\theta_s) \tag{3.30}$$

The inclination angle must be increased gradually in order to identify the moment of sliding onset, and the operator should subsequently stop the surface inclination immediately. Another challenge is ensuring that particle rotation is excluded from the measurement. Wei *et al.* [89] did this by using a "particle plate" –which was constructed by gluing multiple particles together– instead of a single particle.

Barrios *et al.* [88] used a pin-on-disc tribometer to measure the particle–wall sliding friction coefficient. Their setup consisted of a rotating disc, covered with the different materials, which is brought in contact with a particle specimen. To determine the particle–particle friction coefficient, the disk surface was covered with ground particle pieces. The setup measures the tangential force (F^t) for different normal forces (F^n), so that the sliding friction coefficient can be calculated as

$$\mu_s^{p-w} = \frac{F^t}{F^n} \tag{3.31}$$

Rolling friction coefficient

The work of Tripathi *et al.* [18] is highlighted here, as they determined pellet and sinter model inputs using primarily the direct measurement approach. The authors first measured pellet and sinter particle density using the fluid displacement method. Next, they estimated the particle–particle sliding friction coefficient from the angle of repose (θ_r) of both materials using

$$\mu_s^{p-p} = \tan\left(\theta_r\right) \tag{3.32}$$

For the particle–particle rolling friction coefficient, they followed the 2D image analysis method of Wensrich [60, 98] which relates rolling friction to particle shape by

$$\mu_r^{p-p} = \frac{< ecc >}{D} \tag{3.33}$$

where $< ecc >$ is the average eccentricity and D is the projected diameter for a given particle image. The remaining material properties (E or G, υ and e) were obtained from literature. Assuming $\mu_r^{p-w} = \mu_r^{p-p}$ and using their estimated value of μ_s^{p-p}, they validated their approach by assigning these values to spherical particles in simulations of dynamic and poured repose angle tests, and comparing the results to experiments. Despite the fact that they used a 2D imaging technique, they reported a good match in both cases and concluded that their method allowed them to avoid a lengthy calibration process. Their work proved that the rolling friction coefficient is not purely a tuning parameter

since it can be determined directly through measurable shape parameters, which is in contrast to other beliefs [9].

3.5.2 Particle-level calibration

Some researchers employed an indirect measurement approach, in which they combined particle measurements with simulations to determine model inputs. The tests and measured values are summarized in Table 3.5. Barrios *et al.* [88] determined the particle–particle rolling friction coefficient using an inclined surface test. In their model, they used directly measured values of the other parameters while varying the value of μ_r. By comparing the simulated angle at which the particles start to roll with experiments, the value of μ_r could be established. Next, they verified whether these single-particle measured values could be used as inputs to a DEM model for mimicking the bulk behavior through comparison of simulations with experiments. Since pellets are not perfectly spherical, they attempted to represent the actual particle shape as much as possible in their simulations by using clumped spheres. For comparison, they also performed simulations using perfectly spherical particles. They concluded that, if pellets are modeled using clumps representing their actual shape, simulations of bulk flow provide realistic results. If pellets are modeled as spheres, the simulated results deviate from experimental results and a reasonable match is only found when the static friction coefficient is tuned. Their work demonstrates that even in the case of nearly-spherical particles, the bulk calibration approach should be applied rather than using parameters from direct measurement when the shape is idealized in simulations.

The research group of Mio *et al.* uses a distribution rolling friction model in combination with spherical particles to account for the actual shape of sinter in simulations, as mentioned earlier. In [20], they briefly described the approach for indirectly measuring the distributed rolling friction coefficient using an inclined surface.

3.5.3 Bulk calibration

Bulk calibration involves experimentally measuring performance indices of the bulk material which are affected by model parameters, and subsequently determining the parameters' values such that the DEM model reproduces the experimental material behavior in terms of the performance indices. Table 3.6 summarizes the tests, calibration targets and values of calibrated parameters found when performing bulk calibration for individual materials and for mixtures in blast furnace literature.

Individual materials

From Table 3.6 it is clear that the calibration process is generally focused on determining inter-particle sliding and rolling friction coefficients. The repose angle is generally used

Table 3.5: Particle-level calibration methods for determining model input parameters from references related to blast furnace literature. Abbreviations: p–p = particle–particle, p–w = particle–wall.

Type	Method	Pellet	Sinter	Coke
Restitution coefficient, e (-)				
p-p	Drop test	0.48 [a)]/0.51[b)] [88]		
p-w	Drop test	0.39 [a)]/0.42[b)] (steel) [88], 0.29[a)]/0.32[b)] (rubber) [88]	–	0.6[b)] (rubber) [67]
Rolling friction coefficient, μ_r (-)				
p-p	Inclined surface test	0.02[b)]/0.21[a)] [88]	variable (Fig. 9)[20]	–
p-w	Inclined surface test	0.01[b)]/0.25[a)] (steel) [88], 0.01[b)]/0.29[a)] (rubber) [88]	variable (Fig. 9)[20]	–

Remarks:
[a)] Determined through simulation with spheres
[b)] Determined through simulation with overlapping spheres

as a calibration target since it is known to be affected by friction coefficients [68, 99–101]. In some studies, the rolling friction coefficient is omitted when complex shapes are used to model irregular particles (*e.g.*, the work of Schott *et al.* [41], Govender *et al.* [46] and Bester *et al.* [67]), so that the calibration procedure is directed towards only the sliding friction coefficient. Others included the rolling friction coefficient since they modeled particles as spheres (*e.g.*, Liu *et al.* [26], Li *et al.* [90] and Chibwe [102]), or even though non-spherical particles were used (*e.g.*, Yu and Saxén [17], Chakrabarty *et al.* [65] and Chen *et al.* [55]).

Several authors [26, 90, 102] have used the repose angle as the sole calibration target, despite calibrating for both rolling and sliding friction coefficients. Not surprisingly, they report multiple possible solution pairs for the friction coefficients. The general approach is to subsequently select a single solution pair somewhat arbitrarily. Li *et al.* [103] are the sole authors who acknowledged that an additional calibration target is required to obtain a unique solution to the calibration problem. They used the angle of repose of a pile formed through hopper discharging and the hopper discharge time as calibration targets. The set of friction coefficients which simultaneously satisfied both targets was then selected.

While the particle shapes used in the works of Chakrabarty *et al.* and Schott *et al.* were very similar, it can be seen that their calibration results for sliding friction are

significantly different, especially for sinter (0.3 and 0.7 according to Schott *et al.* and Chakrabarty *et al.*, respectively). A similar observation holds for (spherical) pellets calibrated through ledge tests. Liu *et al.* and Chibwe *et al.* obtained sliding friction coefficient values of 0.7 and 0.4, respectively. The first possible explanation for these differences lies in the fact that materials used by different researchers are most likely not of the same origin, and the bulk behavior can therefore differ, resulting in different calibration results. Even if materials are the same, differences in the material size distribution which is included in the model and/or experiments may also affect the calibration result. Another possibility is that researchers use different DEM software packages which may have slightly different implementations of the same contact model. These points demonstrate that adopting model parameters from literature should be exercised with caution.

Mixtures

According to Table 3.1, there are several studies in which interactions between different burden materials have been modeled. However, most of these works either mention that the interaction parameters between different material components were obtained from literature, or they completely omit the methods used for determining these parameters [55, 103]. Only few researchers have explicitly reported their methods. Degrassi *et al.* [52], after calibrating the material models of pellet and sinter separately, assumed the average values of the individual sliding friction, rolling friction and restitution coefficients as the pellet–sinter interaction parameters. Their simple approach was only validated qualitatively by performing large-scale hopper filling simulations and visually comparing the material distributions inside the hopper to actual distributions using photographs. Chakrabarty *et al.* [65] took a similar approach to determine pellet–sinter interaction parameters. Using average values, they performed angle of repose experiments using pellet–sinter mixtures of different compositions. The authors reported a good match between simulations and experiments for all compositions and concluded that their method for mixture characterization was simple, yet effective. Schott *et al.* [41] took a different approach to mixture calibration. Instead of assuming the average friction coefficient value for the interaction between mixture components, the authors used a fixed mixture composition (20:10:1 for pellets, sinter and coke on mass basis) and determined the friction coefficient for which the repose angle matched between simulations and experiments. In this way, they determined a sliding friction coefficient of 0.1 between all mixture components. It is not clear how the restitution coefficient between different components was determined and, as mentioned previously, rolling friction was not considered since the particle shape was assumed to be approximated correctly. The obtained pellet–sinter sliding friction coefficient is clearly very different from the value obtained by Chakrabarty

et al. This might be explained by the fact that Schott *et al.* calibrated a mixture consisting of not only pellet and sinter, but also coke.

An important aspect of material model calibration is to include the flow conditions which are expected in the actual application in the calibration test. Considering the sheer size of industrial blast furnaces, the magnitude of flow velocity upon burden surface impact is expected to be in the order of 10 m/s [50]. Hence, models developed for predicating phenomena affecting the burden distribution should be calibrated against high-velocity experimental data. Surprisingly, this aspect has not been taken into account, nor is it even mentioned, in the current blast furnace literature. Another aspect which seems to be ignored completely is taking the stochastic nature of granular material behavior in both virtual and physical experiments into account during calibration, as investigated by Fransen *et al.* [104].

Table 3.6: Bulk calibration methods for determining model particle–particle (p–p) and particle–wall (p–w) parameters found in blast furnace literature. Legend: ρ_p: particle density (kg/m^3), e (-): restitution coefficient, μ_s (-): sliding friction coefficient, μ_r (-): rolling friction coefficient, AoR: angle of repose, n.s. = not specified, N/A = not applicable.

Source	ρ_p	μ_s^{p-p}	μ_r^{p-p}	e^{p-p}	μ_s^{p-w}	μ_r^{p-w}	e^{p-w}	Target / Test
Pellet								
Soda *et al.* [105]	–	0.70	–	–	–	–	–	AoR / Rotating drum test
Mio *et al.* [33]	–	–	–	–	–	–	–	–
Liu *et al.* [26]	–	0.70	0.05	–	–	–	–	AoR / Ledge test
Schott *et al.* [41]	–	0.45	–	–	–	–	–	AoR / Piling test
Mitra and Saxén [40]	–	–	–	–	–	–	–	–
Li *et al.* [90]	–	–	–	–	–	–	–	–
Chibwe *et al.* [49]	–	0.40	0.20	–	–	–	–	AoR / Ledge test
Wei *et al.* [106]	–	0.55	0.20	–	–	–	–	AoR / Lifting funnel test
Chen *et al.* [66]	–	0.40	0.10	–	–	–	–	AoR / Piling test
Sinter								
Liu *et al.* [26][a)]	–	0.70	0.10	–	–	–	–	AoR / Ledge test
Schott *et al.* [41][b)]	–	0.30	–	–	–	–	–	AoR / Piling test
Wei *et al.* [106][a)]	–	0.50	0.30	–	–	–	–	AoR / Lifting funnel test
Chen *et al.* [66][b)]	–	0.60	0.20	–	–	–	–	AoR / Piling test
Coke								
Liu *et al.* [26][a)]	–	0.70	0.10	–	–	–	–	AoR / Ledge test
Schott *et al.* [41][b)]	–	0.20	–	–	–	–	–	AoR / Piling test
Zu *et al.* [107]	–	–	–	–	–	–	–	–
Chibwe *et al.* [49][a)]	–	0.80	0.50	–	–	–	–	AoR / Ledge test
Chakrabarty *et al.* [29][b)]	985	0.55	0.10	0.60	0.90 (steel)	0.20 (steel)	0.40 (steel)	(1) Bulk density / Container test (2) AoR / Ledge test (3) Sliding angle / Inclination test

Continued on next page

Continued from previous page

Source	ρ_p	μ_s^{p-p}	μ_r^{p-p}	e^{p-p}	μ_s^{p-w}	μ_r^{p-w}	e^{p-w}	Target / Test
Bester *et al.* [67][b)]	–	2.00	–	–	–	–	–	AoR / Piling test with chute
Wei *et al.* [106][a)]	–	0.45	0.30	–	–	–	–	AoR / Lifting funnel test
Pellet–Sinter								
Schott *et al.* [41]	N/A	0.10	N/A	n.s.	N/A	N/A	N/A	AoR / Piling test
Degrassi *et al.* [52]	N/A	0.40	0.40	0.30	N/A	N/A	N/A	–
Chakrabarty *et al.* [65]	N/A	0.60	0.07	0.55	N/A	N/A	N/A	–
Pellet–Coke								
Schott *et al.* [41]	N/A	0.10	N/A	n.s.	N/A	N/A	N/A	AoR / Piling test
Sinter–Coke								
Schott *et al.* [41]	N/A	0.10	N/A	n.s.	N/A	N/A	N/A	AoR / Piling test

Remarks:

[a)] Determined through simulation with spheres

[b)] Determined through simulation with overlapping spheres

Note: This distinction is not made for pellets as they are always modeled as spheres in current literature.

3.6 Model validation

The previous subsections showed that blast-furnace DEM modelers often simplify model development; first to reduce computational cost and then to limit calibration effort. While such strategies make large-scale simulations more feasible, over-simplification may compromise accuracy. Validation is therefore a crucial final step to ensure models remain reliable and fit for purpose. In essence, validation assesses whether the chosen modeling methods are adequate for the stated objectives, using carefully selected KPIs that compare numerical results with experimental data. This review indicates that, although many models are reported as acceptable by their authors, validation typically emphasizes burden-flow behavior rather than structural outcomes –even when burden distribution is the primary objective.

In simulations, burden distribution is commonly analyzed using KPIs such as particle trajectories after chute discharge, degree of segregation, radial coke-to-ore ratio, and charged-layer heights. Although these indicators are straightforward to extract in simulations, producing equivalent physical tests and obtaining high-resolution particle data non-destructively is challenging. This section reviews experimental methods reported in the literature that correspond to these simulation KPIs.

Particle trajectories

Mio *et al.* [22] used a relatively large experimental apparatus (1/3-scale model of an actual blast furnace charging system) to observe the behavior and measure the trajectory of sinter which was being discharged from a chute rotating at 13.4 rpm. The particles' trajectories at the chute outlet were captured using high-speed video recording while the flow inside the chute was recorded using pressure-sensitive sheets.

Zhang *et al.* [108] used a laser grid method to measure the stream of burden materials as they were charged into an actual furnace with an inner volume of 3200 m^3. A laser grid was projected as a frame of reference and a video camera was installed in a direction perpendicular to the plane of the laser grid. As the material ejected from the rotating chute cut into the laser grid, an image of the burden trajectory was captured by the video camera and transmitted to a computer. An image processing system was used to extract the burden trajectory data at different chute angles.

Burden profiles

Mitra and Saxén [109] designed a test setup to gain insight into the arising layers of a charging program. The setup was a 1/10-scale model of an industrial bell-less charging system. To mimic the shape of the burden surface in an actual furnace, a conical surface was placed into the throat and a layer of coke particles was glued on the cone. This represented a coke layer with an inclination similar to the angle of

repose of coke. After charging a layer of material, the throat was lowered in order to maintain a constant burden level. A mechanical device was used to determine the layer thickness. By computing the difference between measurements before and after charging, the layer thickness could be approximated. This setup was used to study the charging behavior of pellets on top of a coke layer [38] through both simulations and experiments. When charging pellets on top of the coke layers, the coke collapse effect was observed slightly using the pilot-scale setup. The disadvantage of their measuring technique was that only the layer profile could be mapped, but it could not distinguish where the particles of each layer ended up. Therefore, effects such as coke collapse, which were clearly seen in simulations, were not seen in the experimental layer plots.

Segregation

Segregation has been quantified experimentally using different methods, depending on the type of equipment. For hoppers, the "start-stop" sampling method, originally described by Standish and Kilic [110], has been applied to analyze size segregation during hopper discharge on lab-scale [16, 23] and industrial scale [111]. The hopper is equipped with a sliding plate at the outlet, which is kept closed during the charging process. The sliding plate is removed at various time intervals during discharging, allowing material to be collected intermittently until the hopper is fully discharged. The samples obtained at different discharged mass ratios are measured by a balance below the exit of the hopper. The contents of each sample are then screened and weighed to determine the mass fraction of each particle size as a function of the total discharged mass. Size segregation during hopper filling has also been investigated experimentally. This is more challenging, as the spatial distribution of particles within the hopper must be determined. Standish [112] proceeded to fill the charged hopper with water and subsequently freeze the contents. Then, volume elements from different positions were melted off and dried to analyze the size distribution within the sample.

Size segregation during chute flow occurs due to the kinetic sieving mechanism. The sampling box method, is very popular for observing this effect [17, 20]. As the name suggests, a sampling box with different compartments is placed at the chute outlet, allowing particles to be collected based on their horizontal position. The mass fraction of different sized particles in the compartments is determined, providing an indication of the degree of size segregation.

Segregation during burden descent has been mimicked by Yu and Saxén [35] using a specially designed expansion device. A layer of pellet particles was added on top of a coke layer and the device was slowly expanded, allowing the percolation of pellet into coke layers to be visualized. Although this method did not allow the degree of percolation to be quantified, the bed height at different expansion rates could be mea-

sured and compared to simulations, thereby providing an indication of the model accuracy.

Porosity distributions

The porosity, by definition, is the volume fraction of void space per unit volume of granular material. As this is a property of the internal structure, it is very difficult to quantify experimentally. Wei *et al.* [68, 69] studied porosity distributions of a heap formed during hopper discharge on lab-scale. Measuring beakers were placed under the hopper prior to discharging and the filled beakers were carefully removed after a stable heap was formed. The heap bottom porosity distribution was then determined by adding water from a measuring cup to each particle-filled beaker until the beaker was full. The amount of water required to fill the beaker was read from the measuring cup and this amount was assumed to represent the void volume in the beaker. The same method was used in a more advanced experiment in which a single coke layer was charged to a lab-scale furnace using a rotating chute [53]. The setup contained twelve identical small boxes (with a size of 50 mm $\times$ 100 mm $\times$ 40 mm) nested in a large box which was fixed to the bottom of the throat. The small boxes were dimensioned such that their size was more than 6 times the size of the largest particle and more than 16 times the size of the smallest particle. This allowed the number of particles in each box to be over a hundred; hence it was assumed that the walls did not have an effect on porosity. In general, the authors found general qualitative agreement between simulated and experimental porosity distributions. The simulated porosity profiles were more symmetrical and fairly uniform when compared to the experimental profiles and the authors hypothesized that these differences were caused by systematic errors and non-idealities in the experiments.

3.7 Large-scale modeling feasibility

Given the vast scale of industrial blast furnaces, the computational demands of simulating the entire system are immense, rendering full-scale DEM simulations unfeasible. To reduce the number of particles and make simulations manageable, two primary strategies are typically employed: (i) scaling down the entire geometry to reduce the overall particle count, or (ii) modeling only a representative portion of the geometry, such as a sector or slot, to focus computational resources more efficiently.

3.7.1 Scaling of particles and geometry

As discussed in Section 3.4, a common approach to simulate large-scale systems involves adjusting the particle–to–geometry size ratio, enlarging particles relative to the geometry. This can be done in several ways: by (i) up-scaling particle size while keeping the geometry unchanged, (ii) down-scaling the geometry while maintaining actual particle size, or (iii)

using a combination of both. Each method has limitations. Up-scaling particles reduces flow resolution and may fail to capture size-dependent interactions between material and geometry accurately. Down-scaling geometry can alter flow rates and velocities, leading to deviations from real system behavior. Thus, both approaches must be applied with care.

Table 3.1 shows that scaling is commonly applied in blast furnace simulations. Whether particles or geometry are scaled –or a hybrid method is used– few studies discuss the rationale behind the chosen scaling factor, and verification of whether scaled models accurately replicate industrial-scale phenomena is rare. This is a critical oversight because, according to the principle of similarity, "the behavior of two systems will be similar if the ratio of their linear dimensions, forces, velocities, reactions, etc., is the same" [113]. For studies investigating burden distribution at lab scale, both kinematic (motion) and dynamic (force) similarity with the full-scale system should be maintained. Otherwise, burden energy and momentum at impact with the stock surface will be underestimated in down-scaled models.

For instance, Mitra and Saxén [109] observed only a slight coke collapse when charging pellets onto coke layers in a 1:10-scale pilot setup. However, their large-scale simulations revealed a much stronger coke-push effect, leading to significant burden redistribution. In subsequent work, they investigated coke–ore mixed layer formation using the same setup [38] and hypothesized that mixed layer formation would be less pronounced in an actual blast furnace due to scale effects. Similarly, Narita *et al.* [114] compared mixed layer formation between a 1:10-scale setup and a full-scale blast furnace, finding the phenomenon to be less significant at full scale. By analyzing momentum balance, they identified the coke-to-ore mass ratio as a key scaling factor and demonstrated that reducing coke particle size in experiments helped replicate full-scale mixed layer behavior.

While most studies in Table 3.1 focus on burden distribution during charging, future DEM research may extend to burden descent and gas flow behavior –critical for assessing bed permeability. For such studies, maintaining similarity based on the Froude number is essential, as emphasized in numerous publications [82, 115–119].

3.7.2 Simplifying the computational domain

Instead of a full 3D model (Type I), slot (Type II) or sector (Type III) models can be used, as illustrated in Figure 3.5. These simplified models reduce particle count by simulating only a portion of the geometry. However, walls (front/rear or side walls, as shown in Figures 3.5b and 3.5c) can influence material behavior; thus, they are typically treated as frictionless or periodic boundaries to minimize wall effects. The slot thickness or sector angle must be carefully selected to ensure that the simulated flow behavior remains representative of the full system.

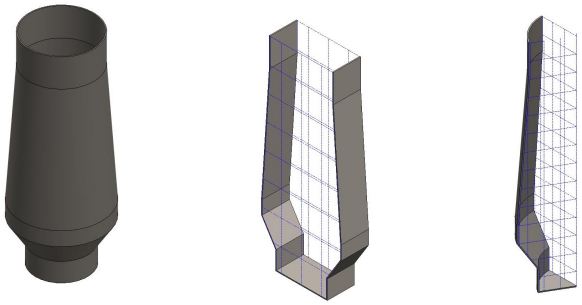


Figure 3.5: Blast furnace computational domains used in simulations (from left to right): (a) full 3D (Type I) model, (b) slot (Type II) model, and (c) sector (Type III). The hatched surfaces indicate the periodic boundaries.

Table 3.1 indicates that simplified computational domains have not been widely used in blast furnace modeling. Yang *et al.* [120] found that sector models are particularly suitable for simulating material behavior in cylindrical systems such as conical hoppers. Later, they compared slot and sector models for simulating solid particle motion in a furnace shaft [39]. Their findings showed that slot models produced different bed characteristics –such as zone sizes and layer shapes– whereas sector models closely matched results from full 3D models. The authors also examined sector angles and reported no significant differences in flow behavior between 30°, 45°, 60°, and 90° angles, ultimately recommending sector models with circumferential boundary conditions for CFD-DEM studies of gas-solid flow in blast furnaces.

Zhang *et al.* [30] employed a slot model with periodic boundaries to investigate size segregation during discharge from a Paul-Wurth hopper. Wei *et al.* [53] developed a DEM model to analyze porosity distribution during bed descent. While their simulation featured a fully 3D charging system, the furnace shaft was simplified using a slot model with periodic boundaries, and particles falling outside the slot during charging were removed. In both studies, the criteria for selecting the slot thickness were not specified.

Currently, what is missing in both scaling and partial domain approaches is a systematic analysis of how these cost-reduction strategies compare to full-scale simulations. Future research should address this research gap to ensure that computational efficiency does not come at the expense of physical accuracy.

3.8 Conclusions

This chapter outlined a step-by-step model development framework based on practices recommended in DEM literature. The review identified several opportunities to improve the reliability of DEM-based blast furnace models, particularly in the area of parameter determination. The key conclusions are summarized below:

- **Particle shape remains a modeling challenge.** Studies using clumped spheres and polyhedra offer conflicting conclusions on whether spherical particles can sufficiently represent material flow and final distribution. A systematic comparison of shape approximation methods is needed, supported by experimental validation. Similar uncertainties exist for particle size distribution choices and their influence on packed bed structure and permeability.
- **The Hertz–Mindlin model with rolling model C is recommended.** This combination of contact models is most commonly used for blast furnace DEM simulations. While modeling a single burden component requires six interaction parameters, mixture models such as pellet–sinter require calibration of up to 15 parameters, highlighting the complexity of multi-component systems.
- **Most models lack systematic parameter calibration.** Interaction parameters are often adopted from literature rather than obtained through direct measurement or calibration. While some studies report bulk calibration for individual components, none systematically determine inter-component parameters for material mixtures.
- **Angle of repose has clear limitations as a calibration target.** Although widely used, it cannot ensure a unique parameter set due to its non-specific nature and is typically measured under low-velocity conditions. More representative calibration experiments are needed, using multiple KPIs under realistic flow conditions.
- **Link between calibration and segregation/packing behavior remains unclear.** It is uncertain whether calibration based on the angle of repose adequately captures local segregation and packing behavior. Future work should identify calibration targets that better reflect localized flow and structural phenomena.
- **Use of KPIs is well established for burden flow but underdeveloped for permeability.** Simulations generally align well with experiments when using KPIs related to material trajectories and distribution. However, KPIs for permeability are rarely defined or measured. Future efforts should establish permeability-specific KPIs and methods for their experimental validation.
- **Feasibility strategies for industrial-scale modeling need validation.** Current approaches for reducing computational cost lack systematic evaluation. Further studies are needed to assess how simplifications affect simulation accuracy compared to full-resolution models.

Based on these findings, it is evident that systematic calibration procedures and scaling approaches are lacking, raising concerns about the reliability and real-world applicability of current models. This gap is apparent for models of individual burden components and becomes even more critical when modeling multi-component mixtures. Given the goal of this thesis, the next chapters will focus on model development for a pellet–sinter mixture. As highlighted earlier, such a mixture requires the definition of 15 distinct interaction parameters –a substantial number. In line with the model development procedure outlined in this chapter, the immediate next step is to perform sensitivity analyses to determine whether certain parameters can be reasonably omitted from the subsequent calibration phase. This chapter showed that the interaction parameters have not been systematically investigated before and will form the basis of the work presented in the next chapter.

3.9 Bibliography

[1] V. Angelidakis, S. Nadimi, M. Otsubo, and S. Utili. “CLUMP: A Code Library to generate Universal Multi-sphere Particles”. In: *SoftwareX* 15 (2021), p. 100735. ISSN: 2352-7110. DOI: 10.1016/j.softx.2021.100735.

[2] S. Lommen. “Virtual prototyping of grabs: Co-simulations of discrete element and rigid body models”. In: (2016). DOI: 10.4233/uuid:418996d9-9b48-4349-823e-b78d8349af25.

[3] H. Kruggel-Emden, M. Sturm, S. Wirtz, and V. Scherer. “Selection of an appropriate time integration scheme for the discrete element method (DEM)”. In: *Computers & Chemical Engineering* 32 (2008), pp. 2263–2279. ISSN: 0098-1354. DOI: 10.1016/j.compchemeng.2007.11.002.

[4] C. J. Coetzee. “Calibration of the discrete element method and the effect of particle shape”. In: *Powder Technology* 297 (2016), pp. 50–70. DOI: 10.1016/j.powtec.2016.04.003.

[5] C. J. Coetzee. “Review: Calibration of the Discrete Element Method”. In: *Powder Technology* 310 (Jan. 2017). DOI: 10.1016/j.powtec.2017.01.015.

[6] T. Roessler, C. Richter, A. Katterfeld, and F. Will. “Development of a standard calibration procedure for the DEM parameters of cohesionless bulk materials – part I: Solving the problem of ambiguous parameter combinations”. In: *Powder Technology* 343 (2019), pp. 803–812. DOI: 10.1016/j.powtec.2018.11.034.

[7] A. Katterfeld, C. J. Coetzee, T. Donohue, J. Fottner, A. Grima, Á. Ramírez-Gómez, D. Ilic, R. Kačianauskas, J. Necas, D. Schott, K. Williams, and J. Zegzulka. "Calibration of DEM Parameters for Cohesionless Bulk Materials under Rapid Flow Conditions and Low Consolidation". In: (July 2019). DOI: 10.13140/RG.2.2.26318.31048/1.

[8] A. Boikov, R. Savelev, V. Payor, and A. Potapov. "Universal Approach for DEM Parameters Calibration of Bulk Materials". In: *Symmetry* 13 (2021). DOI: https://doi.org/10.3390/sym13061088.

[9] L. Benvenuti, C. Kloss, and S. Pirker. "Identification of DEM simulation parameters by Artificial Neural Networks and bulk experiments". In: *Powder Technology* 291 (2016), pp. 456–465. DOI: 10.1016/j.powtec.2016.01.003.

[10] F. Elskamp, H. Kruggel-Emden, M. Hennig, and U. Teipel. "A strategy to determine DEM parameters for spherical and non-spherical particles". In: *Granular Matter* 19 (June 2017). DOI: 10.1007/s10035-017-0710-0.

[11] H. Q. Do, A. M. Aragón, and D. L. Schott. "A calibration framework for discrete element model parameters using genetic algorithms". In: *Advanced Powder Technology* 29 (2018), pp. 1393–1403. DOI: 10.1016/j.apt.2018.03.001.

[12] C. Richter, T. Rößler, G. Kunze, A. Katterfeld, and F. Will. "Development of a standard calibration procedure for the DEM parameters of cohesionless bulk materials – Part II: Efficient optimization-based calibration". In: *Powder Technology* 360 (2020), pp. 967–976. DOI: 10.1016/j.powtec.2019.10.052.

[13] C. Richter and F. Will. "Introducing Metamodel-Based Global Calibration of Material-Specific Simulation Parameters for Discrete Element Method". In: *Minerals* 11 (2021). DOI: 10.3390/min11080848.

[14] M. J. Mohajeri, C. van Rhee, and D. Schott. "Replicating cohesive and stress-history-dependent behavior of bulk solids: Feasibility and definiteness in DEM calibration procedure". In: *Advanced Powder Technology* 32 (2021), pp. 1532–1548. DOI: 10.1016/j.apt.2021.02.044.

[15] M. P. Fransen, M. Langelaar, and D. L. Schott. "Application of DEM-based metamodels in bulk handling equipment design: Methodology and DEM case study". In: *Powder Technology* 393 (2021), pp. 205–218. ISSN: 0032-5910. DOI: 10.1016/j.powtec.2021.07.048.

[16] Y. Yu and H. Saxén. "Experimental and DEM study of segregation of ternary size particles in a blast furnace top bunker model". In: *Chemical Engineering Science* 65 (2010), pp. 5237–5250. DOI: 10.1016/j.ces.2010.06.025.

[17] Y. Yu and H. Saxén. "Flow of Pellet and Coke Particles in and from a Fixed Chute". In: *Ind. Eng. Chem. Res.* 51 (May 2012), pp. 7383–7397. DOI: 10.1021/ie201362n.

[18] A. Tripathi, V. Kumar, A. Agarwal, A. Tripathi, S. Basu, A. Chakrabarty, and S. Nag. "Quantitative DEM simulation of pellet and sinter particles using rolling friction estimated from image analysis". In: *Powder Technology* 380 (2021), pp. 288–302. ISSN: 0032-5910. DOI: 10.1016/j.powtec.2020.11.024.

[19] K. Zhou, Z. Jiang, D. Pan, W. Gui, and J. Huang. "Influence of Charging Parameters on the Burden Flow Velocity and Distribution on the Blast Furnace Chute Based on Discrete Element Method". In: *steel research international* (2021). DOI: 10.1002/srin.202100332.

[20] H. Mio, S. Komatsuki, M. Akashi, A. Shimosaka, Y. Shirakawa, J. Hidaka, M. Kadowaki, S. Matsuzaki, and K. Kunitomo. "Validation of Particle Size Segregation of Sintered Ore during Flowing through Laboratory-scale Chute by Discrete Element Method". In: *ISIJ International* 48 (2008), pp. 1696–1703. DOI: 10.2355/isijinternational.48.1696.

[21] S. Wu, M. Kou, J. Xu, X. Guo, K. Du, W. Shen, and J. Sun. "DEM simulation of particle size segregation behavior during charging into and discharging from a Paul-Wurth type hopper". In: *Chemical Engineering Science* 99 (2013), pp. 314–323. DOI: 10.1016/j.ces.2013.06.018.

[22] H. Mio, Y. Narita, S. Matsuzaki, K. Nishioka, and S. Nomura. "Measurement of particle charging trajectory via rotating chute of 1/3-scale blast furnace and its comparing with numerical analysis using Discrete Element Method". In: *Powder Technology* 344 (2019), pp. 797–803. ISSN: 0032-5910. DOI: 10.1016/j.powtec.2018.12.047.

[23] Y. Yu and H. Saxén. "Segregation behavior of particles in a top hopper of a blast furnace". In: *Powder Technology* 262 (2014), pp. 233–241. DOI: 10.1016/j.powtec.2014.04.010.

[24] J. Xu, Z. Hu, Y. Xu, D. Wang, L. Wen, and C. Bai. "Transient local segregation grids of binary size particles discharged from a wedge-shaped hopper". In: *Powder*

Technology 308 (2017), pp. 273–289. DOI: 10.1016/j.powtec.2016.12.013.

[25] W. Xu, S. Cheng, Q. Niu, and G. Zhao. “Effect of the cross-section shape of rotating chute on particle flow and burden distribution during the charging process of bell-less top blast furnace with two parallel hoppers”. In: *Ironmaking & Steelmaking* 46 (2019), pp. 105–112. DOI: 10.1080/03019233.2017.1343412.

[26] S. Liu, Z. Zhou, K. Dong, A. Yu, D. Pinson, and J. Tsalapatis. “Numerical Investigation of Burden Distribution in a Blast Furnace”. In: *steel research international* 86 (2015), pp. 651–661. DOI: 10.1002/srin.201400360.

[27] Y. Narita, H. Mio, T. Orimoto, and S. Nomura. “DEM Analysis of Particle Trajectory in Circumferential Direction at Bell-less Top”. In: *ISIJ International* 57 (2017), pp. 429–434. DOI: 10.2355/isijinternational.ISIJINT-2016-560.

[28] W. Xu, S. Cheng, Q. Niu, W. Hu, and J. Bang. “The DEM study of segregation phenomena of burden distribution during the charging process of blast furnace with two parallel hoppers”. In: *Ironmaking & Steelmaking* 47 (2020), pp. 337–343. DOI: 10.1080/03019233.2018.1512035.

[29] A. Chakrabarty, S. Basu, S. Nag, U. Ghosh, and M. Patra. “Model Study of Centre Coke Charging in Blast Furnace through DEM Simulations”. In: *ISIJ International* 61 (Mar. 2021), pp. 782–791. DOI: 10.2355/isijinternational.ISIJINT-2020-498.

[30] T. F. Zhang, J. Q. Gan, A. B. Yu, D. Pinson, and Z. Y. Zhou. “Size segregation of granular materials during Paul-Wurth hopper charging and discharging process”. In: *Powder Technology* 378 (2021), pp. 497–509. DOI: 10.1016/j.powtec.2020.10.025.

[31] G. Holzinger and M. Schatzl. “Effect of chute start angle and hopper change on burden distribution during the charging process of a bell-less top blast furnace with two parallel hoppers”. In: *Powder Technology* 395 (2022), pp. 669–680. ISSN: 0032-5910. DOI: 10.1016/j.powtec.2021.10.005.

[32] H. Mio, S. Komatsuki, M. Akashi, A. Shimosaka, Y. Shirakawa, J. Hidaka, M. Kadowaki, S. Matsuzaki, and K. Kunitomo. “Effect of Chute Angle on Charging Behavior of Sintered Ore Particles at Bell-less Type Charging System of Blast Furnace by Discrete Element Method”. In: *ISIJ International* 49 (2009), pp. 479–486. DOI: 10.2355/isijinternational.49.479.

[33] H. Mio, S. Komatsuki, M. Akashi, A. Shimosaka, Y. Shirakawa, J. Hidaka, M. Kadowaki, H. Yokoyama, S. Matsuzaki, and K. Kunitomo. "Analysis of Traveling Behavior of Nut Coke Particles in Bell-type Charging Process of Blast Furnace by Using Discrete Element Method". In: *ISIJ International* 50 (2010), pp. 1000–1009. DOI: 10.2355/isijinternational.50.1000.

[34] Y. Yu, A. Westerlund, T. Paananen, and H. Saxén. "Inter-particle Percolation Segregation during Burden Descent in the Blast Furnace". In: *ISIJ International* 51 (2011), pp. 1050–1056. DOI: 10.2355/isijinternational.51.1050.

[35] Y. Yu and H. Saxén. "Effect of DEM Parameters on the Simulated Inter-particle Percolation of Pellets into Coke during Burden Descent in the Blast Furnace". In: *ISIJ International* 52 (2012), pp. 788–796. DOI: 10.2355/isijinternational.52.788.

[36] H. Mio, M. Kadowaki, S. Matsuzaki, and K. Kunitomo. "Development of particle flow simulator in charging process of blast furnace by discrete element method". In: *Minerals Engineering* 33 (2012), pp. 27–33. ISSN: 0892-6875. DOI: 10.1016/j.mineng.2012.01.002.

[37] Y. Yu and H. Saxén. "Particle Flow and Behavior at Bell-Less Charging of the Blast Furnace". In: *Steel Research International* 84 (2013), pp. 1018–1033. DOI: 10.1002/srin.201300028.

[38] T. Mitra and H. Saxén. "Simulation of Burden Distribution and Charging in an Ironmaking Blast Furnace". In: *IFAC-PapersOnLine* 48 (2015), pp. 183–188. ISSN: 2405-8963. DOI: 10.1016/j.ifacol.2015.10.100.

[39] W. J. Yang, Z. Y. Zhou, and A. B. Yu. "Discrete particle simulation of solid flow in a three-dimensional blast furnace sector model". In: *Chemical Engineering Journal* 278 (2015), pp. 339–352. DOI: 10.1016/j.cej.2014.11.144.

[40] T. Mitra and H. Saxén. "Discrete element simulation of charging and mixed layer formation in the ironmaking blast furnace". In: *Computational Particle Mechanics* 3 (2016), pp. 541–555-541–555. ISSN: 2196-4386. DOI: 10.1007/s40571-015-0084-1.

[41] D. Schott, W. Vreeburg, C. Molhoek, and G. Lodewijks. "Granular Flow to a Blast Iron Ore Furnace: Influence of Particle Size Distribution on Segregation of a Mixture". In: *Traffic and Granular Flow '15*. Ed. by Victor L Knoop and Winnie Daamen. Springer International Publishing, 2016, pp. 621–628-621–628. ISBN: 978-3-319-33482-0. DOI: 10.1007/978-3-319-33482-0_78.

[42] Y. Narita, H. Mio, T. Orimoto, and S. Nomura. “Modelling of Coke Layer Collapse during Ore Charging in Ironmaking Blast Furnace by DEM”. In: *EPJ Web of Conferences* 140 (Jan. 2017), p. 2018. DOI: 10.1051/epjconf/201714002018.

[43] M. Holmes. “A Numerical Simulation of Particulate Distribution of the Blast Furnace Raw Material Burden Through the Paul Wurth Bell-less Top Apparatus”. PhD thesis. May 2016. DOI: 10.13140/RG.2.2.22315.85280.

[44] M. A. J. Holmes, D. J. Penney, N. P. Lavery, and S. G. R. Brown. “A numerical investigation assessing the symmetry of burden charging in a blast furnace using different chute designs”. In: *Ironmaking & Steelmaking* 45 (2018), pp. 551–559. DOI: 10.1080/03019233.2017.1303893.

[45] M. Kou, S. Wu, H. Zhou, Y. Yu, and J. Xu. “Numerical Investigation of Coke Collapse and Size Segregation in the Bell-less Top Blast Furnace”. In: *ISIJ International* 58 (Aug. 2018). DOI: 10.2355/isijinternational.ISIJINT-2018-415.

[46] N. Govender, D. N. Wilke, C. Wu, U. Tuzun, and H. Kureck. “A numerical investigation into the effect of angular particle shape on blast furnace burden topography and percolation using a GPU solved discrete element model”. In: *Chemical Engineering Science* 204 (2019), pp. 9–26. DOI: 10.1016/j.ces.2019.03.077.

[47] M. Kou, J. Xu, S. Wu, H. Zhou, K. Gu, S. Yao, and B. Wen. “Effect of cross-section shape of rotating chute on particle movement and distribution at the throat of a bell-less top blast furnace”. In: *Particuology* 44 (2019), pp. 194–206. ISSN: 1674-2001. DOI: 10.1016/j.partic.2018.07.010.

[48] W. Xu, S. Cheng, Q. Niu, W. Hu, and J. Bang. “Investigation on the uneven distribution of different types of ores in the hopper and stock surface during the charging process of blast furnace based on discrete element method”. In: *Metallurgical Research & Technology* 116 (Jan. 2019), p. 314. DOI: 10.1051/metal/2018099.

[49] D. K. Chibwe, G. M. Evans, E. Doroodchi, B. J. Monaghan, D. J. Pinson, and S. J. Chew. “Charge material distribution behaviour in blast furnace charging system”. In: *Powder Technology* 366 (2020), pp. 22–35. ISSN: 0032-5910. DOI: 10.1016/j.powtec.2020.02.048.

[50] Z. Hong, H. Zhou, J. Wu, L. Zhan, Y. Fan, Z. Zhang, S. Wu, H. Xu, L. Wang, and M. Kou. “Effects of Operational Parameters on Particle Movement and Distribution at the Top of a Bell-Less Blast Furnace Based on Discrete Element Method”. In: *steel*

research international 92 (Aug. 2020). DOI: https://doi.org/10.1002/srin.202000262.

[51] H. Mio, Y. Narita, K. Nakano, and S. Nomura. "Validation of the Burden Distribution of the 1/3-Scale of a Blast Furnace Simulated by the Discrete Element Method". In: *Processes* 8 (2020). ISSN: 2227-9717. DOI: 10.3390/pr8010006.

[52] G. Degrassi, L. Parussini, M. Boscolo, N. Petronelli, and V. Dimastromatteo. "Discrete element simulation of the charge in the hopper of a blast furnace, calibrating the parameters through an optimization algorithm". In: *SN Applied Sciences* 3 (2021), p. 242. ISSN: 2523-3971. DOI: 10.1007/s42452-021-04254-8.

[53] H. Wei, W. Ding, Y. Li, H. Nie, H. Saxén, H. Long, and Y. Yu. "Porosity distribution of moving burden layers in the blast furnace throat". In: *Granular Matter* 23 (2021). DOI: 10.1007/s10035-020-01080-4.

[54] H. Zhou, J. Wu, Z. Hong, L. P. Wang, S. Wu, M. Kou, G. Wang, and Y. Luo. "Numerical simulation of coke collapse and its optimization during burden charging at the top of bell-less blast furnace". In: *Powder Technology* 389 (2021), pp. 155–162. DOI: 10.1016/j.powtec.2021.05.033.

[55] J. Chen, H. Zuo, H. Zhao, Q. Xue, and J. Wang. "Burden circumferential mass segregation at the blast furnace with parallel hoppers". In: *Powder Technology* 409 (2022), p. 117845. ISSN: 0032-5910. DOI: 10.1016/j.powtec.2022.117845.

[56] C. X. Li, K. J. Dong, S. D. Liu, G. R. Chandratilleke, Z. Y. Zhou, and Y. S. Shen. "DEM study of particle segregation in the throat region of a blast furnace". In: *Powder Technology* 407 (2022), p. 117660. ISSN: 0032-5910. DOI: 10.1016/j.powtec.2022.117660.

[57] R. D. Mindlin and H. Deresiewicz. "Elastic Spheres in Contact Under Varying Oblique Forces". In: *Journal of Applied Mechanics* 20 (2021), pp. 327–344. ISSN: 0021-8936. DOI: 10.1115/1.4010702.

[58] P. Flores. "Compliant contact force approach for forward dynamic modeling and analysis of biomechanical systems". In: *Procedia IUTAM* 2 (2011), pp. 58–67-58–67. DOI: 10.1016/j.piutam.2011.04.006.

[59] J. Ai, J. Chen, J. Michael Rotter, and J. Ooi. "Assessment of rolling resistance models in discrete element simulations". In: *Powder Technology* 206 (2011), pp. 269–282. DOI: 10.1016/j.powtec.2010.09.030.

[60] C. M. Wensrich and A. Katterfeld. “Rolling friction as a technique for modelling particle shape in DEM”. In: *Powder Technology* 217 (2012), pp. 409–417. DOI: 10.1016/j.powtec.2011.10.057.

[61] Y. Tsuji, T. Tanaka, and T. Ishida. “Lagrangian numerical simulation of plug flow of cohesionless particles in a horizontal pipe”. In: *Powder Technology* 71 (1992), pp. 239–250. DOI: 10.1016/0032-5910(92)88030-L.

[62] G. Lu, J. R. Third, and C. R. Müller. “Discrete element models for non-spherical particle systems: From theoretical developments to applications”. In: *Chemical Engineering Science* 127 (2015), pp. 425–465. DOI: 10.1016/j.ces.2014.11.050.

[63] Y. Kallus. “The random packing density of nearly spherical particles”. In: *Soft Matter* 12 (Mar. 2016). DOI: 10.1039/C6SM00213G.

[64] M. Akashi, H. Mio, A. Shimosaka, Y. Shirakawa, J. Hidaka, and S. Nomura. “Estimation of Bulk Density Distribution in Particle Charging Process Using Discrete Element Method Considering Particle Shape”. In: *ISIJ International* 48 (2008), pp. 1500–1506. DOI: 10.2355/isijinternational.48.1500.

[65] A. Chakrabarty, R. Biswas, S. Basu, and S. Nag. “Characterisation of binary mixtures of pellets and sinter for DEM simulations”. In: *Advanced Powder Technology* 33 (2022), p. 103358. ISSN: 0921-8831. DOI: 10.1016/j.apt.2021.11.010.

[66] J. Chen, H. Zuo, Y. Wang, Q. Xue, and J. Wang. “DEM Simulation of Burden Circumferential Distribution of Blast Furnace With Parallel Hoppers”. In: *Metallurgical and Materials Transactions B* 53 (2022), pp. 3793–3804. ISSN: 1543-1916. DOI: 10.1007/s11663-022-02641-z.

[67] J. Bester, P. Venter, and M. van Eldik. “Discrete element model calibration for industrial raw material simulations”. In: *MATEC Web Conf.* 347 (2021), p. 00036. DOI: 10.1051/matecconf/202134700036.

[68] H. Wei, X. Tang, Y. Ge, M. Li, H. Saxén, and Y. Yu. “Numerical and experimental studies of the effect of iron ore particle shape on repose angle and porosity of a heap”. In: *Powder Technology* 353 (2019), pp. 526–534. ISSN: 0032-5910. DOI: 10.1016/j.powtec.2019.05.031.

[69] H. Wei, Y. Ge, M. Li, Y. Li, H. Saxén, Z. He, and Y. Yu. “DEM study of the porosity distribution of pellet sandpile formed by ternary size particles”. In: *Powder Technology* 360 (2020), pp. 1337–1347. DOI: 10.1016/j.powtec.2019.11.017.

[70] X. Xia, L. Zhou, H. Ma, C. Xie, and Y. Zhao. “Reliability study of super-ellipsoid DEM in representing the packing structure of blast furnace”. In: *Particuology* 70 (2022), pp. 72–81. ISSN: 1674-2001. DOI: 10.1016/j.partic.2022.01.010.

[71] D. Nasato, C. Goniva, S. Pirker, and C. Kloss. “Coarse Graining for Large-scale DEM Simulations of Particle Flow – An Investigation on Contact and Cohesion Models”. In: *Procedia Engineering* 102 (2015), pp. 1484–1490. DOI: 10.1016/j.proeng.2015.01.282.

[72] S. Lommen, M. J. Mohajeri, G. Lodewijks, and D. Schott. “DEM particle upscaling for large-scale bulk handling equipment and material interaction”. In: *Powder Technology* 352 (2019), pp. 273–282. DOI: 10.1016/j.powtec.2019.04.034.

[73] S. Kanjilal and S. Schneiderbauer. “A revised coarse-graining approach for simulation of highly poly-disperse granular flows”. In: *Powder Technology* 385 (Feb. 2021). DOI: 10.1016/j.powtec.2021.02.015.

[74] D. Schott, S. Lommen, R. van Gils, J. de Lange, M. Kerklaan, O. Dessing, W. Vreugdenhil, and G. Lodewijks. “Scaling of particles and equipment by experiments of an excavation motion”. In: *Powder Technology* 278 (2015), pp. 26–34. DOI: 10.1016/j.powtec.2015.03.012.

[75] M. J. Mohajeri, R. L. J. Helmons, C. van Rhee, and D. L. Schott. “A hybrid particle-geometric scaling approach for elasto-plastic adhesive DEM contact models”. In: *Powder Technology* 369 (2020), pp. 72–87. DOI: 10.1016/j.powtec.2020.05.012.

[76] T. Roessler and A. Katterfeld. “Scaling of the angle of repose test and its influence on the calibration of DEM parameters using upscaled particles”. In: *Powder Technology* 330 (2018), pp. 58–66. DOI: 10.1016/j.powtec.2018.01.044.

[77] T. Pöschel, C. Salueña, and T. Schwager. “Can we scale granular systems?” In: *Powders & Grains 2001* (Jan. 2001), pp. 439–442.

[78] Y. T. Feng, K. Han, D. R. J. Owen, and J. Loughran. “On upscaling of discrete element models: similarity principles”. In: *Engineering Computations* 26 (2009). Ed. by Antonio Munjiza, pp. 599–609. ISSN: 0264-4401. DOI: 10.1108/02644400910975405.

[79] Y. T. Feng and D. R. J. Owen. “Discrete element modelling of large scale particle systems - I: exact scaling laws”. In: *Computational Particle Mechanics* 1 (2014), pp. 159–168-159–168. DOI: 10.1007/s40571-014-0010-y.

[80] “2 - Basic Properties of Building Decorative Materials”. In: ed. by Yan Li and Shuxia Ren. Woodhead Publishing, 2011, pp. 10–24. ISBN: 978-0-85709-257-1. DOI: 10.1533/9780857092588.10.

[81] C. K. Ho, S. M. Wu, H. P. Zhu, A. B. Yu, and S. T. Tsai. “Experimental and numerical investigations of gouge formation related to blast furnace burden distribution”. In: *Minerals Engineering* 22 (2009), pp. 986–994. DOI: 10.1016/j.mineng.2009.03.004.

[82] Z. Y. Zhou, H. P. Zhu, A. B. Yu, B. Wright, and P. Zulli. “Discrete particle simulation of gas–solid flow in a blast furnace”. In: *Computers & Chemical Engineering* 32 (2008), pp. 1760–1772. ISSN: 0098-1354. DOI: 10.1016/j.compchemeng.2007.08.018.

[83] S. Lommen, D. Schott, and G. Lodewijks. “DEM speedup: Stiffness effects on behavior of bulk material”. In: *Particuology* 12 (2014), pp. 107–112. DOI: 10.1016/j.partic.2013.03.006.

[84] Y. Okuno, S. Matsuzaki, K. Kunitomo, M. Isoyama, and Y. Kusano. “Development of a Mathematical Model to Estimate Burden Distribution in Bell-less Type Charging for Blast Furnace”. In: *TETSU TO HAGANE-JOURNAL OF THE IRON AND STEEL INSTITUTE OF JAPAN* 73 (Jan. 1987), pp. 91–98. ISSN: 0021-1575. DOI: 10.2355/tetsutohagane1955.73.1_91.

[85] M. Kou, W. Zeng, Z. Zhang, X. She, T. Zhang, B. Zhao, X. Ma, and H. Zhou. “Central coke charging and its effect on coke collapse at the throat of blast furnace by DEM simulation”. In: *Powder Technology* 408 (2022), p. 117784. ISSN: 0032-5910. DOI: 10.1016/j.powtec.2022.117784.

[86] H. P. Zhu, M. Rahman, A. B. Yu, J. Bridgwater, and P. Zulli. “Effect of particle properties on particle percolation behaviour in a packed bed”. In: *Minerals Engineering* 22 (2009). Special issue: Computational Modelling, pp. 961–969. ISSN: 0892-6875. DOI: 10.1016/j.mineng.2009.03.002.

[87] S. Ueda, S. Natsui, Z. Fan, H. Nogami, R. Soda, J. Kano, R. Inoue, and T. Ariyama. “Influences of Physical Properties of Particle in Discrete Element Method on Descending Phenomena and Stress Distribution in Blast Furnace”. In: *ISIJ International* 50 (2010), pp. 981–986. DOI: 10.2355/isijinternational.50.981.

[88] G. K. P. Barrios, R. M. de Carvalho, A. Kwade, and L. Marcelo Tavares. “Contact parameter estimation for DEM simulation of iron ore pellet handling”. In: *Powder Technology* 248 (2013), pp. 84–93. ISSN: 0032-5910. DOI: 10.1016/j.powtec.2013.01.063.

[89] H. Wei, H. Nie, Y. Li, H. Saxén, Z. He, and Y. Yu. “Measurement and simulation validation of DEM parameters of pellet, sinter and coke particles”. In: *Powder Technology* 364 (2020), pp. 593–603. DOI: 10.1016/j.powtec.2020.01.044.

[90] C. Li, T. Honeyands, D. O’Dea, and R. Moreno-Atanasio. “The angle of repose and size segregation of iron ore granules: DEM analysis and experimental investigation”. In: *Powder Technology* 320 (2017), pp. 257–272. ISSN: 0032-5910. DOI: 10.1016/j.powtec.2017.07.045.

[91] D. Wang, M. Servin, T. Berglund, K. O. Mickelsson, and S. Rönnbäck. “Parametrization and validation of a nonsmooth discrete element method for simulating flows of iron ore green pellets”. In: *Powder Technology* 283 (2015), pp. 475–487. ISSN: 0032-5910. DOI: 10.1016/j.powtec.2015.05.040.

[92] J. Rodriguez, T. Edeskär, and S. Knutsson. “Particle shape quantities and measurement techniques: a review”. In: *The Electronic journal of geotechnical engineering* 18 (2013), pp. 169–198.

[93] V. Angelidakis, S. Nadimi, and S. Utili. “SHape Analyser for Particle Engineering (SHAPE): Seamless characterisation and simplification of particle morphology from imaging data”. In: *Computer Physics Communications* 265 (2021), p. 107983. ISSN: 0010-4655. DOI: 10.1016/j.cpc.2021.107983.

[94] V. Angelidakis, S. Nadimi, M. Otsubo, and S. Utili. “CLUMP: A Code Library to generate Universal Multi-sphere Particles”. In: *SoftwareX* 15 (2021), p. 100735. ISSN: 2352-7110. DOI: 10.1016/j.softx.2021.100735.

[95] Micromeritics. *GeoPyc 1365 – Envelope Density Analyzer*. 2017.

[96] Micromeritics. *Density Analysis*. Brochure. URL: https://www.micromeritics.com/Repository/Files/Density%5C_Brochure.pdf.

[97] T. Li, J. Zhang, and W. Ge. “Simple measurement of restitution coefficient of irregular particles”. In: *China Particuology* 2 (2004), pp. 274–275. ISSN: 1672-2515. DOI: 10.1016/S1672-2515(07)60074-8.

[98] C. M. Wensrich, A. Katterfeld, and D. Sugo. “Characterisation of the effects of particle shape using a normalised contact eccentricity”. In: *Granular Matter* 16 (2014), pp. 327–337-327–337. DOI: 10.1007/s10035-013-0465-1.

[99] Y. C. Zhou, B. H. Xu, A. B. Yu, and P. Zulli. “An experimental and numerical study of the angle of repose of coarse spheres”. In: *Powder Technology* 125.1 (2002), pp. 45–54. ISSN: 0032-5910. DOI: 10.1016/S0032-5910(01)00520-4.

[100] P. Frankowski and M. Morgeneyer. “Calibration and validation of DEM rolling and sliding friction coefficients in angle of repose and shear measurements”. In: *AIP Conference Proceedings* 1542.1 (2013), pp. 851–854. DOI: 10.1063/1.4812065.

[101] H. M. Beakawi Al-Hashemi and O. S. Baghabra Al-Amoudi. “A review on the angle of repose of granular materials”. In: *Powder Technology* 330 (2018), pp. 397–417. ISSN: 0032-5910. DOI: 10.1016/j.powtec.2018.02.003.

[102] D. Chibwe. “Optimised burden delivery for blast furnace operations”. In: (Sept. 2019).

[103] Q. Li, M. Feng, and Z. Zou. “Validation and Calibration Approach for Discrete Element Simulation of Burden Charging in Pre-reduction Shaft Furnace of COREX Process”. In: *ISIJ International* 53 (2013), pp. 1365–1371. DOI: 10.2355/isijinternational.53.1365.

[104] M. P. Fransen, M. Langelaar, and D. L. Schott. “Including stochastics in metamodel-based DEM model calibration”. In: *Powder Technology* 406 (2022), p. 117400. ISSN: 0032-5910. DOI: 10.1016/j.powtec.2022.117400.

[105] R. Soda, A. Sato, J. Kano, E. Kasai, F. Saito, M. Hara, and T. Kawaguchi. “Analysis of Granules Behavior in Continuous Drum Mixer by DEM”. In: *ISIJ International* 49 (2009), pp. 645–649. DOI: 10.2355/isijinternational.49.645.

[106] S. Wei, H. Wei, H. Saxén, and Y. Yu. “Numerical Analysis of the Relationship between Friction Coefficient and Repose Angle of Blast Furnace Raw Materials by Discrete Element Method”. In: *Materials* 15 (Jan. 2022), p. 903. DOI: 10.3390/ma15030903.

[107] E. X. Zu, P. Zhou, and Z. H. Jiang. “Discrete Element Method of Coke Accumulation: Calibration of the Contact Parameter”. In: *IFAC-PapersOnLine* 51.21 (2018). 5th IFAC Workshop on Mining, Mineral and Metal Processing MMM 2018, pp. 241–245. ISSN: 2405-8963. DOI: 10.1016/j.ifacol.2018.09.425.

[108] J. Zhang, J. Qiu, H. Guo, S. Ren, H. Sun, G. Wang, and Z. Gao. “Simulation of particle flow in a bell-less type charging system of a blast furnace using the discrete element method”. In: *Particuology* 16 (2014), pp. 167–177. ISSN: 1674-2001. DOI: 10.1016/j.partic.2014.01.003.

[109] T. Mitra and H. Saxén. “Model for Fast Evaluation of Charging Programs in the Blast Furnace”. In: *Metallurgical and Materials Transactions B* 45 (2014), pp. 2382–2394-2382–2394. ISSN: 1543-1916. DOI: https://doi.org/10.1007/s11663-014-0156-2.

[110] N. Standish and A. Kilic. “Comparison of stop-start and continuous sampling methods of studying segregation of materials discharging from a hopper”. In: *Chemical Engineering Science* 40 (1985), pp. 2152–2153. ISSN: 0009-2509. DOI: 10.1016/0009-2509(85)87036-6.

[111] Y. Kajiwara, T. Jimbo, T. Joko, Y. Aminaga, and T. Inada. “Investigation of Bell-less Charging Based on Full Scale Model Experiments”. In: *Transactions of the Iron and Steel Institute of Japan* 24 (1984), pp. 799–807. DOI: 10.2355/isijinternational1966.24.799.

[112] N. Standish. “Studies of size segregation in filling and emptying a hopper”. In: *Powder Technology* 45 (1985), pp. 43–56. ISSN: 0032-5910. DOI: 10.1016/0032-5910(85)85059-2.

[113] G. S. Gupta, S. Sarkar, A. Chychko, L. D. Teng, M. Nzotta, and S. Seetharaman. “Chapter 3.1 - Process Concept for Scaling-Up and Plant Studies”. In: ed. by Seshadri Seetharaman. Elsevier, 2014, pp. 1100–1144. ISBN: 978-0-08-096988-6. DOI: 10.1016/B978-0-08-096988-6.00040-7.

[114] K. Narita, A. Inaba, I. Kobayashi, O. Kenichi, M. Shimizu, Y. Takeshi, and T. Shinichi. “Study of Ore and Coke Distribution in Blast Furnase Carried out on a Full Size Model”. In: *Tetsu To Hagane-journal of The Iron and Steel Institute of Japan* 65 (1979), pp. 358–367. DOI: 10.2355/isijinternational1966.19.667.

[115] H. Takahashi, M. Tanno, and J. Katayama. “Burden Descending Behaviour with Renewal of Deadman in a Two Dimensional Cold Model of Blast Furnace”. In: *ISIJ International* 36 (1996), pp. 1354–1359. DOI: 10.2355/isijinternational.36.1354.

[116] J. Jimenez, J. Mochón, A. Formoso, and J. Sainz de Ayala. “Burden Distribution Analysis by Digital Image Processing in a Scale Model of a Blast Furnace Shaft”. In: *ISIJ International* 40 (2000), pp. 114–120. DOI: 10.2355/isijinternational.40.114.

[117] Z. Zhou, H. Zhu, A. Yu, B. Wright, D. Pinson, and P. Zulli. “Discrete Particle Simulation of Solid Flow in a Model Blast Furnace”. In: *ISIJ International* 45 (2005), pp. 1828–1837. DOI: 10.2355/isijinternational.45.1828.

[118] B. Wright, P. Zulli, Z. Y. Zhou, and A. B. Yu. “Gas–solid flow in an ironmaking blast furnace - I: Physical modelling”. In: *Powder Technology* 208 (2011), pp. 86–97. ISSN: 0032-5910. DOI: 10.1016/j.powtec.2010.12.006.

[119] J. Xu, N. Wang, M. Chen, Z. Zhou, and P. Wang. “Evaluation of reduction behavior of blast furnace dust particles during in-flight process with experiment aided mathematical modeling”. In: *Applied Mathematical Modelling* 75 (2019), pp. 535–552. ISSN: 0307-904X. DOI: 10.1016/j.apm.2019.05.048.

[120] W. Yang, Z. Zhou, D. Pinson, and A. Yu. “Periodic Boundary Conditions for Discrete Element Method Simulation of Particle Flow in Cylindrical Vessels”. In: *Ind. Eng. Chem. Res.* 53 (May 2014), pp. 8245–8256. DOI: 10.1021/ie404158e.

4

Relevance of Inter-Component Mixture Interaction Parameters

Developing a DEM model for charging iron ore mixtures into the blast furnace requires determining a large set of model parameters. As established in the previous chapter, a systematic calibration of such a model has not yet been performed in blast furnace DEM studies. Calibrating the interaction parameters between all relevant materials makes the process both computationally and experimentally demanding. To reduce this complexity, it is important to identify parameters with negligible influence on the behavior of the ore mixture so they can be excluded from calibration. This chapter addresses this knowledge gap by systematically evaluating the influence of individual parameters on the mixture's behavior.

This chapter is based on:
R. Roeplal, Yusong Pang and Dingena Schott. *Effects of pellet–sinter interaction parameters on component segregation and bed porosity considering flow velocity and mixture composition: A DEM study*, Advanced Powder Technology, Volume 35, Issue 2, 2024.

4.1 Introduction

A DEM model of blast furnace charging can provide valuable insights into the behavior of different burden components during the charging process and the resulting burden distribution within the charged layers, provided that the interactions between particles and their surroundings are defined through contact models and associated model parameters that accurately represent the true material behavior. Chapter 3 demonstrated that the Hertz-Mindlin contact model combined with rolling model C is commonly employed in blast furnace applications to describe particle contacts. Since the blast furnace burden consists of a mixture, interaction parameters must be specified not only for each individual material component but also for interactions between different material components, as well as between the components and the walls. Consequently, applying these models to simulate the charging of a pellet–sinter mixture requires specifying a large number of parameters. As illustrated in Figure 4.1, a total of 15 model parameters must be defined, including restitution coefficient (e), sliding friction coefficient (μ_s), and rolling friction coefficient (μ_r) for each contact pair. Determining this large parameter set poses a significant challenge, as each parameter must be either measured experimentally or calibrated to ensure that the simulated behavior aligns with observed material behavior under realistic blast furnace conditions.

Sensitivity analyses serve as a crucial first step in avoiding an unnecessarily complex calibration process. If certain interaction parameters have little to no impact on the final burden distribution, their precise calibration is unnecessary, significantly reducing the overall effort required. Sensitivity analysis is therefore an essential pre-calibration step. As discussed in Chapter 3, only a limited number of sensitivity studies relevant to the phenomena occurring during blast furnace charging have been reported to date. Yu and Saxén [1] investigated the effect of particle–particle and particle–wall friction coefficients on pellet size segregation during hopper discharge. They found that particle–wall friction influenced segregation behavior, whereas particle–particle friction did not. In a later study [2], they examined pellet–pellet and pellet–coke interactions during percolation of pellets into a coke layer, using a setup which mimics the expansion of layers during burden descent in the blast furnace. Their results indicated that rolling and sliding friction coefficients influenced percolation only at certain levels of their values. While useful, these studies did not explicitly look at the burden charging as only (low-velocity) parts of the system were considered and only pellets were used, rather than an ore mixture. Liu *et al.* [3] analyzed layer formation in a lab-scale charging process involving a hopper, a rotating chute, and a collection container. While this setup introduced higher-velocity flow, it remained below the actual order of magnitude and excluded ore mixtures, focusing only on sinter or coke layers. Their findings revealed that particle–particle rolling and sliding coefficients did not impact flow trajectories after the chute but significantly influenced

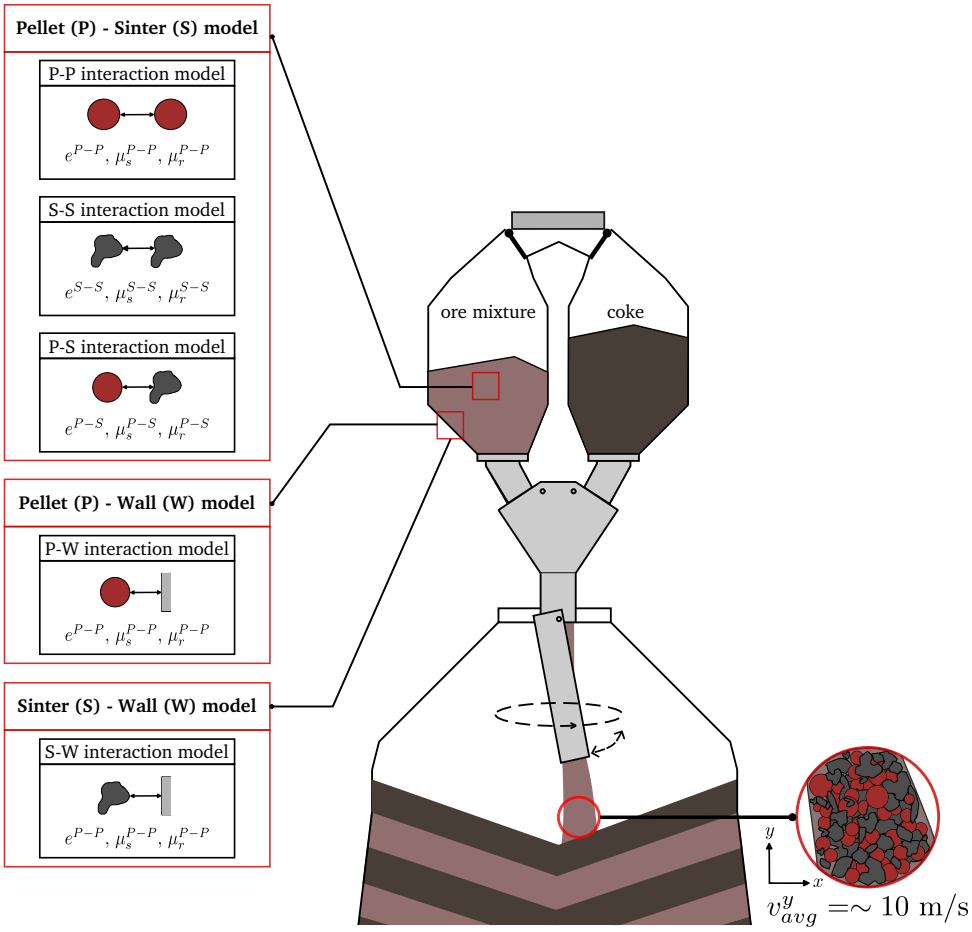


Figure 4.1: Overview of required interaction parameters (restitution coefficient e, sliding friction coefficient μ_s, and rolling friction coefficient μ_r) for modeling blast furnace charging when using the Hertz-Mindlin contact model in combination with rolling model C in DEM simulations.

burden surface profiles. Wei *et al.* [4] conducted a similar study on coke and sinter layer charging, demonstrating that static friction between sinter–sinter, sinter–coke, and coke-coke significantly affected layer shape, radial porosity distribution, and sinter percolation into coke layers. Overall, previous research has examined various key performance indicators (KPIs) of the blast furnace burden, including size segregation of individual materials, material percolation, flow trajectories, and burden layer profiles. However, a key research gap remains: investigating a multi-component ore mixture under representative high-velocity flow conditions, while focusing specifically on permeability-related KPIs.

The objective of this chapter is to investigate the influence of pellet–sinter interaction parameters on component segregation and packing structure. This study represents the first investigation of how interaction parameters between different components affect the behavior of an ore mixture. The findings aim to clarify whether the full set of 15 interaction parameters required for the pellet–sinter model can be reduced, thereby simplifying the calibration process later in this thesis.

The investigation is carried out through sensitivity analyses, using the segregation index and porosity as key performance indicators (KPIs). Porosity, defined as the void fraction within the packed bed, serves as a measure of packing structure. Packing structure, in turn, influences permeability both through the amount of void space and the connectivity between voids. Although porosity does not capture connectivity, a general association exists between higher porosity and higher permeability, and vice versa [5]. Based on this relationship, porosity is used as an indicator of permeability in this study. To facilitate computational efficiency, the packed bed is formed using a simplified setup that enables faster simulation runs while maintaining a representative flow velocity. This velocity corresponds to that encountered at the lowest chute angle in blast furnace operation, where the flow is nearly vertical. Accordingly, the simplified setup consists of a hopper discharging material directly into a container. The effect of flow velocity is examined by varying the discharge height, allowing assessment of the importance of reproducing blast furnace flow conditions in calibration experiments. Additionally, different mixture compositions are considered to ensure relevance across varying ore mixtures in blast furnace practice.

This chapter is organized as follows: Section 4.2 describes the simulation setup and the analysis methods for segregation and packing structure. Section 4.3 details the selection of the time step and demonstrates segregation analysis in different directions. The main and interaction effects of the pellet–sinter interaction parameters on segregation and porosity are then evaluated across a range of flow velocities and mixture compositions to increase the generalizability of the results. Finally, Section 4.4 concludes whether calibration of the pellet–sinter interaction parameters is necessary.

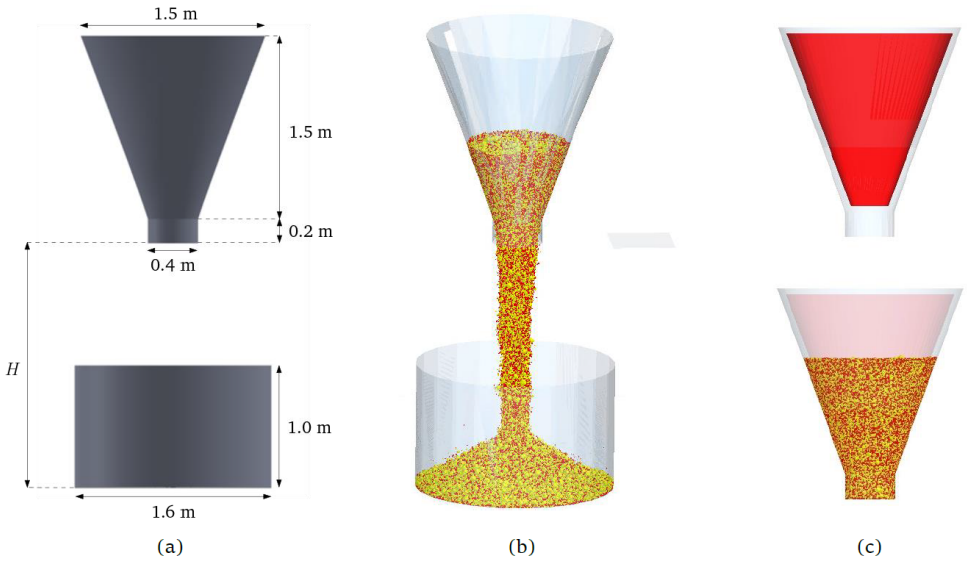


Figure 4.2: (a) Simulation setup and dimensions with varying discharge height (H), (b) Demonstration of mixture discharge and bed formation in the container, (c) Cone-shaped volume used for particle generation at $t = 0$ s (top) and generated mixture right before opening the hopper outlet (bottom).

4.2 Tests and procedures

4.2.1 Simulation setup

Altair® EDEM™ (version 2022.2) was used on the DelftBlue high-performance cluster [6] to run simulations with the described models. The system for this investigation consists of a hopper and a container (see Figure 4.2a), constructed with acrylic walls. The hopper outlet size was selected such that the diameter was 10× the diameter of the largest particle in the system, and the discharge height (H) was varied as discussed in Section 4.3.2. A homogeneous mixture of pellet and sinter was prepared in the hopper, allowing segregation to occur as the mixture was discharged into the container. Figure 4.2b shows a snapshot of the simulation during bed formation. Using a homogeneous mixture in the hopper ensures similar initial conditions for each simulation run.

The simulation procedure was as follows. At $t = 0$ s, the pellet–sinter mixture was generated in the hopper by creating a volume packing with a solid fraction of 40% within the cone-shaped volume shown in Figure 4.2c. In this method, all particles were generated simultaneously inside the cone and allowed to settle. This approach was chosen over continuous particle generation with dynamic factories to minimize segregation during hopper filling. At $t = 2$ s, the hopper outlet was opened, allowing the material to flow into the container and settle.

Table 4.1: Model parameters from Chakrabarty *et al.* [7]. Abbreviations: p–p = particle–particle, p–w = particle–wall.

Parameter (symbol)		Pellet	Sinter	Acrylic (wall)
Particle shape		see Figure 4.3		N/A
Particle size (d_p) / mass percentage		6-9 mm / 5.02% 9-12.5 mm / 68.73% 12.5-16 mm / 26.25%	5-10 mm / 27.97% 10-15 mm / 28.45% 15-20 mm / 29.91% 20-40 mm / 13.67%	N/A
Density (ρ)		3700 kg/m^3	3050 kg/m^3	1200 kg/m^3
Poisson's ratio (υ)		0.25	0.25	0.25
Young's modulus (E)		2.5×10^8 Pa	2.5×10^8 Pa	2.5×10^8 Pa
Restitution coefficient (e)	p–p	0.70	0.40	–
	p–w	0.70	0.40	–
Static friction coefficient (μ_s)	p–p	0.49	0.70	–
	p–w	0.38	0.38	–
Rolling friction coefficient (μ_r)	p–p	0.06	0.08	–
	p–w	0.06	0.08	–
Numerical time step (Δt)		to be determined (section 4.2)		

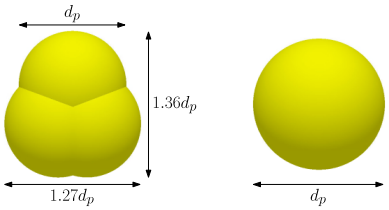


Figure 4.3: Particle shapes used for sinter (left) and pellet (right), with the characteristic dimension d_p provided in Table 4.1. Images adapted from [7].

The (unscaled) particle size distributions and particle shapes for pellet and sinter, and the material properties and interaction parameters for all materials were adopted from the work of Chakrabarty *et al.* [7] (as summarized in Table 4.1 and Figure 4.3) since the authors calibrated the model parameters against experimentally measured values of bulk density (2220.74 ± 27.20 kg/m^3 for pellets and 1826.67 ± 28.37 kg/m^3 for sinter) and repose angle (33.11 ± 1.56 degrees for pellets and 33.23 ± 0.27 degrees for sinter). Since pellet and sinter particles are each represented by a single shape (Figure 4.3) and have multiple sizes, they can be regarded as mono-shaped, poly-sized mixtures. While the particle size ranges from Table 4.1 were specified in [7]; the authors did not elaborate on how the particles were generated. The approach taken in this work is to specify the particle size ranges in EDEM and allow particles within each range to be generated randomly.

Table 4.2: Factors and levels tested. Abbreviation: P-S = pellet–sinter.

Factor (unit)	Low level	Mid level	High level
e^{P-S} (−)	0.1	0.5	0.9
μ_s^{P-S} (−)	0.1	0.5	0.9
μ_r^{P-S} (−)	0.1	0.5	0.9

4.2.2 Time step analysis

Before executing the experiments, a suitable value for the numerical time step (Δt) was determined. It is generally recommended to use a fraction of the Rayleigh time step (Δt_R), determined by Eq. 3.16, which is a function of the material properties and the smallest particle size in the simulation. While the material properties were fixed in the simulations, the size of the smallest particle varied across simulations because particles within each size range were generated randomly. Consequently, the value of Δt_R differed between simulations and was generally on the order of 3×10^{-5} s.

According to the literature, a value between 10–40% of Δt_R is recommended for the time step [8], with the selected value depending on the coordination number and energy in the system [9]. Different values of the numerical time step, ranging from 5% to 40% of Δt_R, were considered to assess the effect on segregation and porosity. Since the flow velocity and impact forces acting on particles during heap formation increased with discharge height, the extreme case of $H = 6$ m was used to determine the time step. For this analysis, equal mass fractions of pellets and sinter were used in the mixture, and the interaction parameters for pellet–sinter were set to $e = \mu_s = \mu_r = 0.5$.

4.2.3 Effects analysis

Independent variables

The restitution coefficient, sliding friction coefficient, and rolling friction coefficient between pellet and sinter are the independent variables (factors). As shown in Table 4.2, each independent variable was tested at three levels, resulting in 27 simulations for a full factorial design. Additionally, each simulation was repeated three times to account for the stochastic nature of the flow.

Dependent variables

The segregation index and bed porosity are the dependent variables (responses). First, the positions and volumes of pellet and sinter particles were extracted at the end of each simulation. These data were then imported into MATLAB for segregation and porosity analyses.

Component segregation

Segregation was quantified using a sampling-based approach [10], as discussed in Chap-

ter 2, in which the particles were divided into a number of sub-domains (samples), and the concentration of one particle type (referred to as the "tracer") was determined in each sample. Taking pellets as the tracer particles, the mass fraction of pellets (x_p) was determined for each sub-domain. The segregation index was defined as [11]

$$SI = \sqrt{\frac{\sum_{i=1}^{N} \left(x_P^i - \overline{x_P}\right)^2}{N-1}} \tag{4.1}$$

where N is the number of sub-domains, ($\overline{x_p}$) is the average mass fraction of all domains, determined by

$$\overline{x_P} = \frac{x_P^1 + \ldots x_P^N}{N} \tag{4.2}$$

and x_P^i is the mass fraction of pellets in the i-th cell determined by

$$x_P^i = \frac{m_P^i}{\left(m_P^i + m_S^i\right)} \tag{4.3}$$

where m_P^i and m_S^i are the masses of pellet and sinter particles in bin i, respectively. As Eq. 4.1 represents the standard deviation of x_p, an SI value of 0.0 indicates a perfectly mixed state, while increasing values correspond to higher degrees of segregation. In order to analyze segregation in different directions, three domain decomposition techniques were considered: radial, vertical, and circumferential. Figure 4.4 illustrates the definition of equal-volume sub-domains for the radial, vertical, and circumferential directions, as well as the numbering of the sub-domains for reference in Section 4.4.

Despite fast computation times, it is well known that the value of a sampling-based segregation index depends on the size (and consequently the number) of the sub-domains used for its calculation [12]. Since this study focuses on investigating the effects of interaction parameters on the segregation index, it is important to assess whether the sample size influences the interpretation of these effects in different directions. Therefore, the sensitivity of the relationships between the factors and the segregation index to the sample size was evaluated using 3, 4, and 5 samples, as presented in Appendix A. The analysis showed that the segregation index in the radial and circumferential directions was unaffected by the number of samples, with three samples being sufficient, whereas four samples were required in the vertical direction. It was also observed that segregation in the circumferential direction was negligible compared to the other two directions, which was expected due to the symmetrical nature of the discharging process in the circumferential direction. Consequently, this investigation focuses solely on segregation in the radial and vertical directions, using three and four samples, respectively.

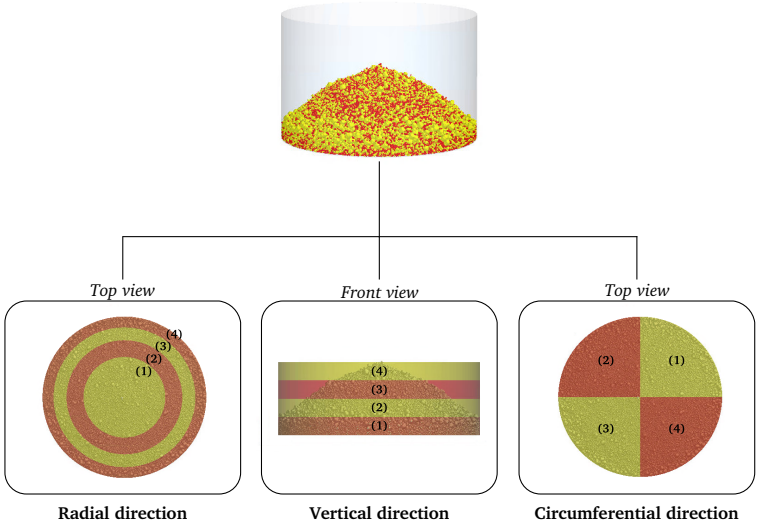


Figure 4.4: Illustration of equal-volume samples in radial, vertical and circumferential directions.

Porosity

The porosity (P) is defined as the volume fraction of pores in the bed and can be directly calculated as

$$P = \frac{V_b - V_p}{V_b} \tag{4.4}$$

where V_p is the total volume of all particles in the bed and V_b is the bed volume. The value of V_p is easily determined in DEM and the value of V_b is approximated by using the *alphaShape* tool in MATLAB, which creates a bounding volume for a set of 3D points (in this case the x, y and z coordinates of all particles).

Control variables

As stated previously, the vertical flow velocity upon striking the stock surface in a blast furnace is in the order of 10 m/s. Nonetheless, blast furnace model calibration is generally done using low-velocity experiments. It is not yet understood how important the flow velocity is with respect to the calibration outcome, *i.e.*, how the calibrated values of model parameters change when using different flow velocities. Similarly, it is not yet understood how the calibrated values of mixture interaction parameters change for different mixture compositions. This is important to understand since the composition is an operational parameter which may change in practice. As a first step, it is investigated to what extent

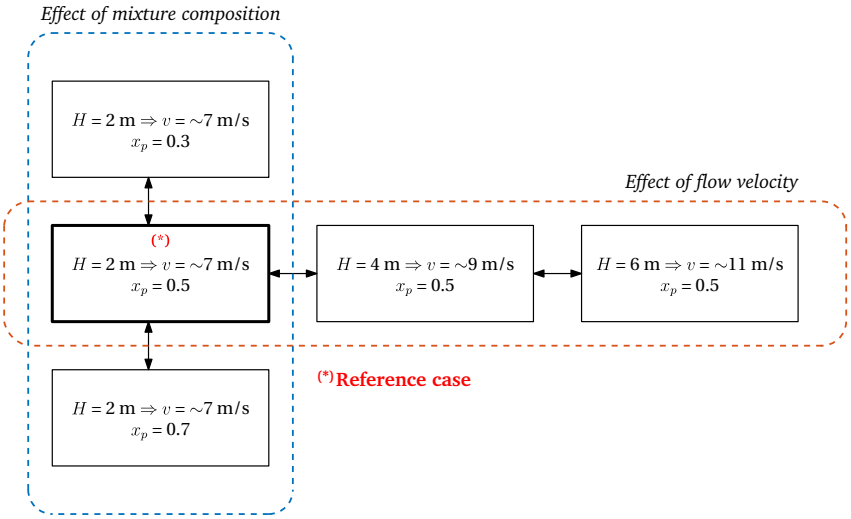


Figure 4.5: Overview of the different cases for which the effects of e^{P-S}, μ_s^{P-S} and μ_r^{P-S} on SI and P are investigated.

the flow velocity and mixture composition affect the sensitivity of SI and P to e^{P-S}, μ_s^{P-S} and μ_r^{P-S}.

The flow velocity during bed formation is varied by using different values of the discharge height H and the composition is varied by adjusting the mass fractions of pellets in the mixture (x_p) which is generated inside the cone-shaped volume of Figure 4.2c. Defining a reference case with $H = 2$ m and $x_p = 0.5$, the study employs a full factorial design over multiple cases (Figure 4.5) to capture the effects of flow velocity and mixture composition.

4.3 Results

4.3.1 Time step determination

Figure 4.6a presents the results of the segregation analysis using four domains in the radial and vertical directions. In the vertical direction, the predicted segregation increases significantly when $\Delta t > 0.1 \cdot \Delta t_R$, while in the radial direction, the segregation decreases slightly beyond this point. Based on these results, a time step of $0.1 \cdot \Delta t_R$ appears suitable. However, Figure 4.6b shows that the predicted bed porosity decreases almost linearly with increasing time step, making the choice of time step with respect to porosity less straightforward.

The effect of the time step on a sub-domain level is further examined by considering the component and porosity distributions in the radial and vertical directions, as shown in

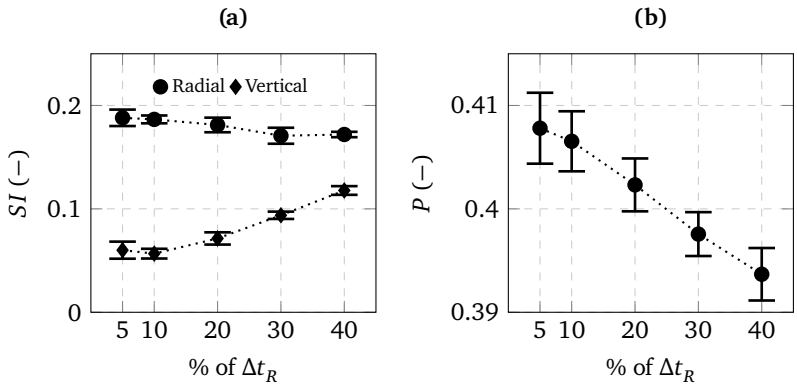


Figure 4.6: Effect of the time step on (a) segregation in radial and vertical directions and (b) overall bed porosity. Error bars indicate the standard deviation based on $n = 6$ repetitions.

Figure 4.7 and Figure 4.8, respectively. Figure 4.7 shows that the mass fraction distribution of pellets and the porosity distribution in the radial direction remain unaffected by the time step until $\Delta t = 0.1 \cdot \Delta t_R$. Although this is less evident in the vertical direction, it can still be observed that the predicted mass fraction distribution changes significantly when $\Delta t > 0.1 \cdot \Delta t_R$, particularly in the bottom layer of the heap. Therefore, $\Delta t = 0.1 \cdot \Delta t_R$ is considered suitable for this study.

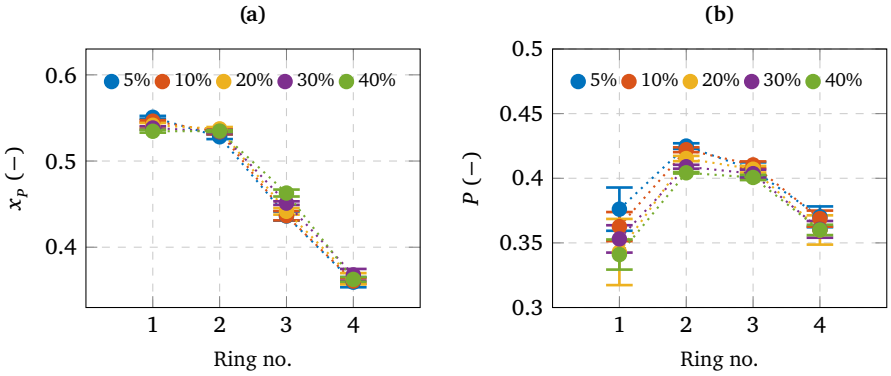


Figure 4.7: Effect of the time step on (a) the mass fraction distribution of pellets and (b) the porosity distribution in radial direction. Error bars indicate the standard deviation based on $n = 6$ repetitions.

4.3.2 Individual factor effects

In this section, the dependence of segregation in the radial and vertical directions, as well as porosity, on pellet–sinter sliding friction, rolling friction, and restitution coefficient is

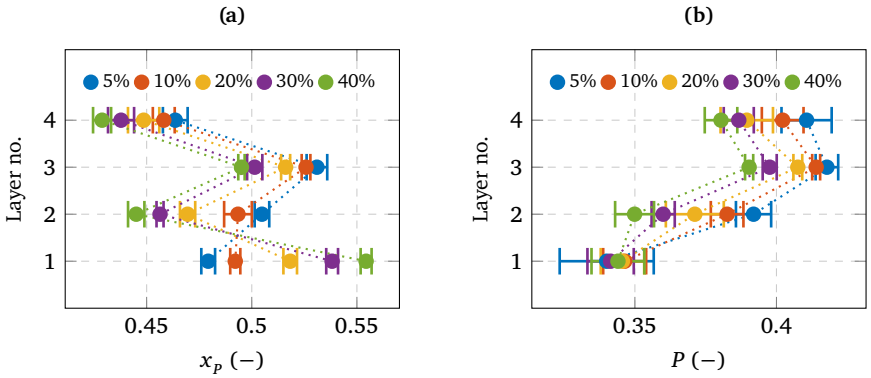


Figure 4.8: Effect of the time step on (a) the mass fraction distribution of pellets and (b) the porosity distribution in vertical direction. Error bars indicate the standard deviation based on $n = 6$ repetitions.

examined under different operational conditions and for different mixture compositions. The results are presented in main effect plots, which facilitate comparison of the relative influence of the independent variables on the dependent variables [13].

Reference case

As an initial step, the effect plots for the reference case, with $H = 2$ m and $x_P = 0.5$, are presented.

Segregation

Figures 4.9a and 4.9b show the main effect plots for e^{P-S}, μ_s^{P-S}, and μ_r^{P-S} on segregation in the radial and vertical directions, respectively. The results show an influence of all three parameters on radial and vertical segregation, with substantially stronger effects observed in the radial direction. This outcome is expected, as particles primarily move vertically during hopper discharge before spreading radially as the container fills. While the SI-value provides an indication of the overall mixing quality within the container, it does not reveal the spatial distribution of the components in cases of uneven mixing. This limitation complicates interpretation of the effects of the interaction parameters solely based on Figures 4.9. To address this, Figure 4.10 presents distribution plots that provide a clearer depiction of how pellet and sinter particles are distributed for different values of e^{P-S}, μ_s^{P-S}, and μ_r^{P-S}.

From the first row in Figure 4.10, it is evident that pellets are primarily concentrated near the center of the heap (rings 1 and 2), with their concentration decreasing sharply towards the container walls. The distribution of pellets becomes more homogeneous as the restitution coefficient decreases and as the friction coefficients increase. From

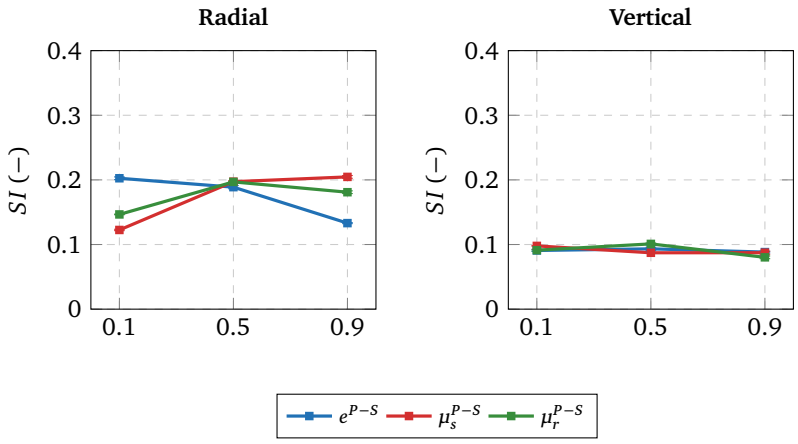


Figure 4.9: Effects of e^{P-S}, μ_s^{P-S}, and μ_r^{P-S} on segregation in radial and vertical directions. Error bars indicate the standard deviation based on $n = 3$ repetitions. Due to the low variability in the measurements, the error bars are not discernible in the plotted data.

the second row in Figure 4.10, showing the vertical pellet distribution, it can be seen that a higher concentration of pellets is present in the bottom layers of the bed when μ_s^{P-S} and μ_r^{P-S} are low. This observation suggests that lower friction values facilitate the percolation of pellets towards the bottom.

Porosity

Figure 4.11 demonstrates a clear effect of all three interaction parameters on bed porosity. The porosity increases, indicating the presence of larger voids in the bed, with higher values of the pellet–sinter sliding friction coefficient (μ_s^{P-S}) and rolling friction coefficient (μ_r^{P-S}). Conversely, the porosity decreases with higher values of the pellet–sinter restitution coefficient (e^{P-S}).

To better understand these effects, the particle contacts during hopper discharge are analyzed. The contacts between different particle types can be directly extracted from EDEM. Figures 4.12a-c illustrate the influence of e^{P-S}, μ_s^{P-S}, and μ_r^{P-S}, respectively, on the number fraction of pellet–pellet, sinter–sinter, and pellet–sinter contacts. In these plots, one parameter is varied from 0.1 to 0.9 while keeping the other two interaction parameters constant at 0.5. Figures 4.12b and 4.12c show that the number of pellet–sinter contacts (N_c) increases with higher values of μ_s^{P-S} and μ_r^{P-S}. This increase can be attributed to the greater contact resistance between pellets and sinters at higher friction values, which limits their relative motion upon contact. Consequently, more pellet and sinter particles remain in contact within the stable heap at higher friction values compared to lower ones. Figure 4.12a reveals that the number of pellet–sinter contacts decreases at higher

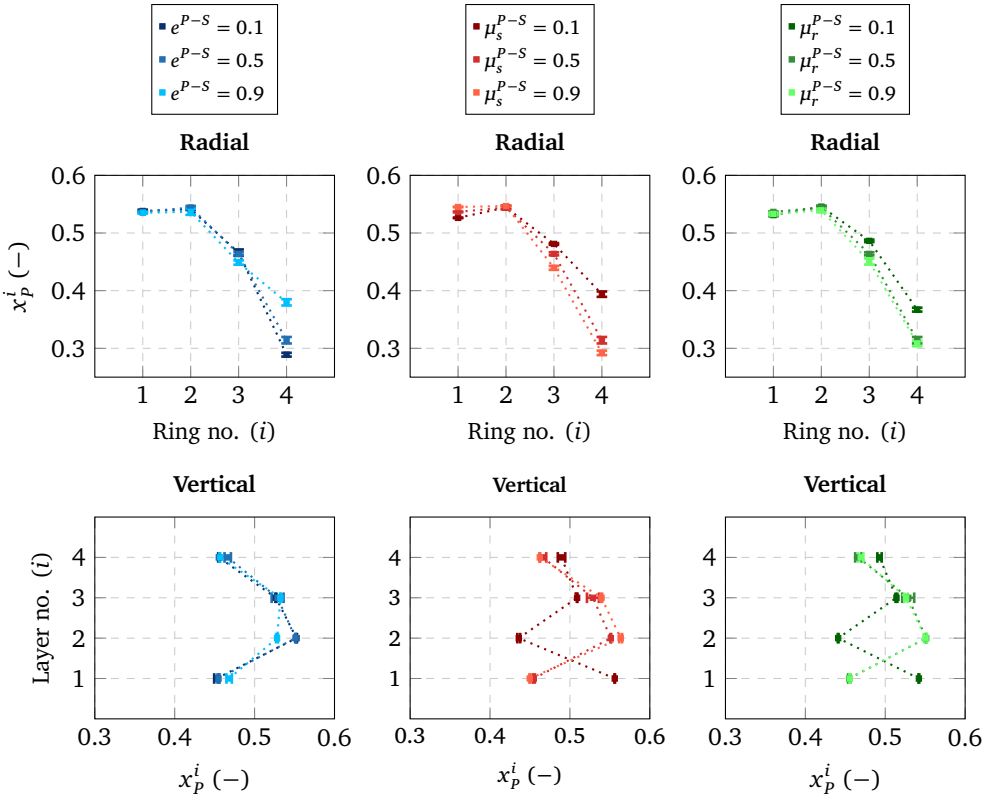


Figure 4.10: Effects of e^{P-S}, μ_s^{P-S}, and μ_r^{P-S} on the pellet distributions in radial (top row) and vertical (bottom row) directions. Results are for the reference case, where $H = 2$ m and $x_P = 0.5$. Error bars indicate the standard deviation based on $n = 3$ repetitions. Due to the low variability in the measurements, the error bars are not discernible in the plotted data.

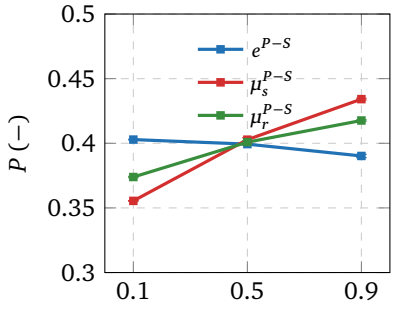


Figure 4.11: Effects of e^{P-S}, μ_s^{P-S}, and μ_r^{P-S} on heap porosity. Error bars indicate the standard deviation based on $n = 3$ repetitions. Due to the low variability in the measurements, the error bars are not discernible in the plotted data.

values of e^{P-S}. This decrease can be explained by the increased mobility of pellet and sinter particles, which tend to move away from each other after collisions when e^{P-S} is high. These results highlight a relationship between particle distribution and overall bed porosity, emphasizing the influence of interaction parameters on the structural properties of the bed.

Effect of flow velocity

Figure 4.13 presents the main effect plots for e^{P-S}, μ_s^{P-S}, and μ_r^{P-S} on segregation and porosity, respectively, for $x_P = 0.5$ at various discharge heights. Figures 4.13a, c, and e show clear effects of e^{P-S}, μ_s^{P-S}, and μ_r^{P-S} on either radial or vertical segregation, or both, across all discharge heights. According to Figures 4.13b, d, and f, similar effects are observed for the porosity. These results indicate that all three interaction parameters must be calibrated for accurate prediction of component segregation and bed permeability, regardless of the flow velocity.

A closer examination reveals that flow velocity does not appear to affect the *trends* in porosity, since the plots in Figure 4.13 are nearly parallel for all three parameters. This observation also applies to segregation in the radial direction, but not to segregation in the vertical direction. Figures 4.13c and 4.13e show that the effects of μ_s^{P-S} and μ_r^{P-S} on vertical segregation change at higher discharge heights. Although the effects of μ_s^{P-S} and μ_r^{P-S} are relatively weak for $H = 2$ m, it is evident that vertical segregation increases for $0.1 < \mu_r^{P-S} < 0.5$ when $H = 2$ m, while the opposite effect occurs for $H = 4$ m and $H = 6$ m. Therefore, the nature of the effect of μ_r^{P-S} on vertical segregation appears to depend on the flow velocity. Another observation is that segregation in the radial direction decreases with increasing discharge height, while segregation in the vertical direction increases with discharge height. In all cases, the effect plots for $H = 4$ m and $H = 6$ m are similar in both trends and values, suggesting the existence of a velocity threshold beyond which no significant effect on vertical segregation is observed.

Effect of mixture composition

Figure 4.14 shows the effects of e^{P-S}, μ_s^{P-S}, and μ_r^{P-S} on segregation and porosity, respectively, for $H = 2$ m when using different mixture compositions. Figures 4.14b, d, and f show that the porosity decreases with a lower mass fraction of pellets (*i.e.*, a higher proportion of sinter particles). Considering particle shape, this result is expected since it is well established in the literature that non-spherical particles generally result in a higher packing density (*i.e.*, lower porosity) than spherical particles with equivalent size distributions [14, 15]. In addition to particle shape, it should be noted that the pellet and sinter particles in this work have different size distributions (as presented in Table 4.1), and the proportion of sinter fines (5–10 mm / 27.97%) is significantly higher than the

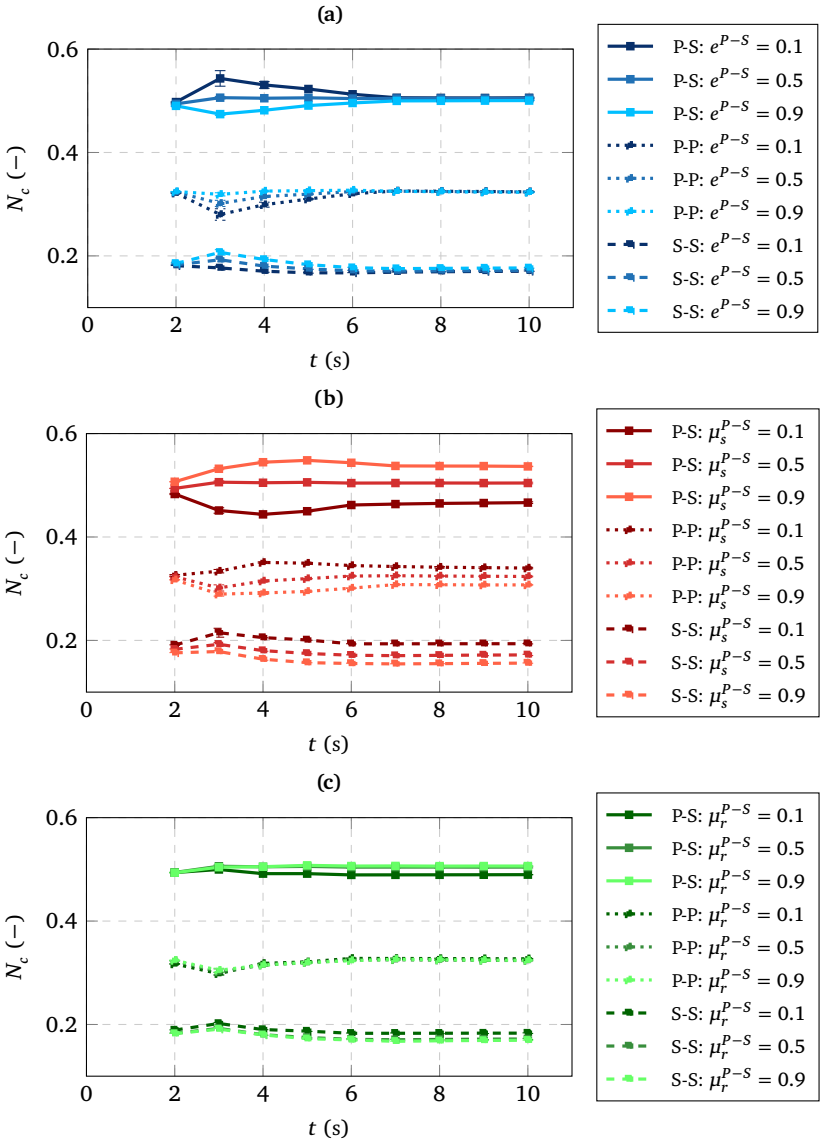


Figure 4.12: Effects of (a) e^{P-S}, (b) μ_s^{P-S}, and (c) μ_r^{P-S} on the fraction of pellet–pellet (P-P), sinter–sinter (S-S) and pellet–sinter (P-S) contacts during hopper discharge.

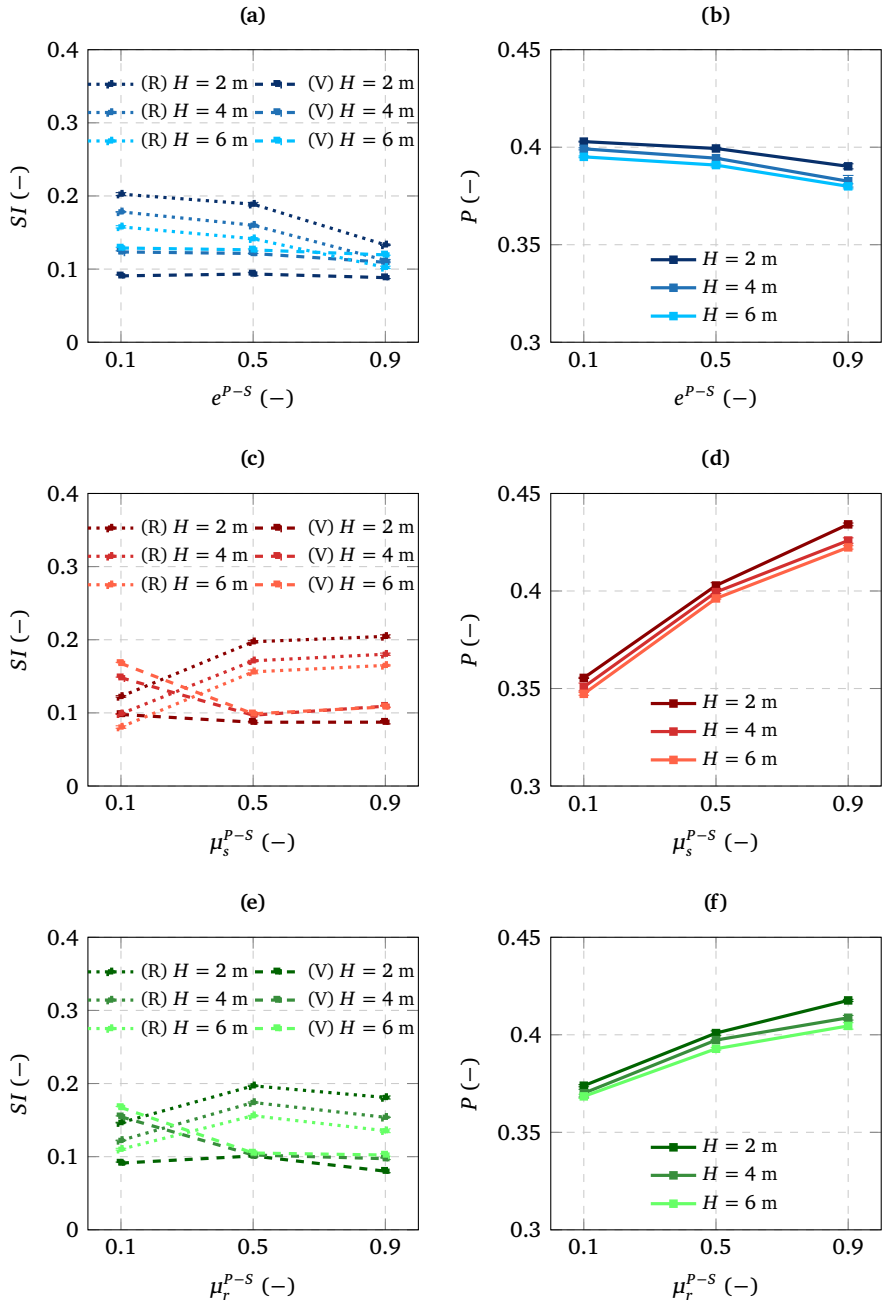


Figure 4.13: Effects of e^{P-S}, μ_s^{P-S} and μ_r^{P-S} on segregation (left column) and porosity (right column) for different discharge heights. Segregation is analyzed in radial (R) and vertical (V) directions. Error bars indicate the standard deviation based on $n = 3$ repetitions. Due to the low variability in the measurements, the error bars are not discernible in the plotted data.

proportion of pellet fines (6–9 mm / 5.02%). The higher fines ratio is also expected to contribute to the increased packing density of sinter.

Based on the segregation values in Figure 4.14, radial segregation increases with decreasing pellet mass fraction, while vertical segregation peaks at $x_P = 0.5$. Mixture composition has little influence on radial trends, which remain consistent across compositions. In contrast, vertical segregation is less pronounced and more sensitive to composition: μ_s^{P-S} and μ_r^{P-S} show similar effects at $x_P = 0.5$ and 0.7, but opposite effects at $x_P = 0.3$, where their influence is also strongest. For e^{P-S}, the segregation index (SI) increases slightly with increasing restitution at $x_P = 0.3$ and 0.7, but the opposite trend appears at $x_P = 0.5$ –though these differences are minimal. Overall, the effects of μ_s^{P-S} and μ_r^{P-S} are more composition-dependent than those of e^{P-S}. Regardless of composition, all three parameters must be calibrated to accurately capture component segregation and bed permeability, due to their clear impact on radial segregation and porosity.

4.3.3 Interaction effects

In this section, interaction plots are used to present how pellet–sinter sliding friction, rolling friction, and restitution coefficient mutually affect segregation in the radial, vertical, and circumferential directions, as well as porosity. An interaction plot between two independent variables is constructed by showing the levels of one independent variable on the x-axis and the dependent variable on the y-axis, with separate lines plotted for each level of the second independent variable. If the individual lines are parallel, no interaction exists between the two independent variables. Conversely, if the lines have different slopes or intersect, some interaction is present, with stronger interaction indicated by greater differences in slope.

In Chapter 3, a summary was provided of which studies in the literature have reported pellet–sinter interaction parameters. By considering the reported values of e^{P-S}, μ_s^{P-S}, and μ_r^{P-S} from these studies, regions of the plots likely applicable to pellet–sinter interactions are indicated using dashed boxes. Thicker dashed lines are used to denote regions where interactions are considered significant based on differences in slopes. For clarity, only the plots for the reference case are shown here; additional plots for other cases are available via [DS1], with figure numbers corresponding to those mentioned in the text.

Figures 4.15 and 4.16 show the interaction plots for the reference case for the radial and vertical segregation index, respectively. In the radial direction, only the interaction between μ_s^{P-S} and μ_r^{P-S} is noteworthy for $\mu_s^{P-S} > 0.5$. In the vertical direction, interaction between μ_s^{P-S} and μ_r^{P-S} is also relevant for $\mu_r^{P-S} < 0.5$. For radial segregation, the results for $H = 4$ m and $H = 6$ m (refer to Figures B1 and B2 in [DS1]) are very similar to the reference case, showing significant interaction between μ_s^{P-S} and μ_r^{P-S} for $\mu_s^{P-S} > 0.5$. This observation also holds for vertical segregation (refer to Figures B1 and B2 in [DS1]);

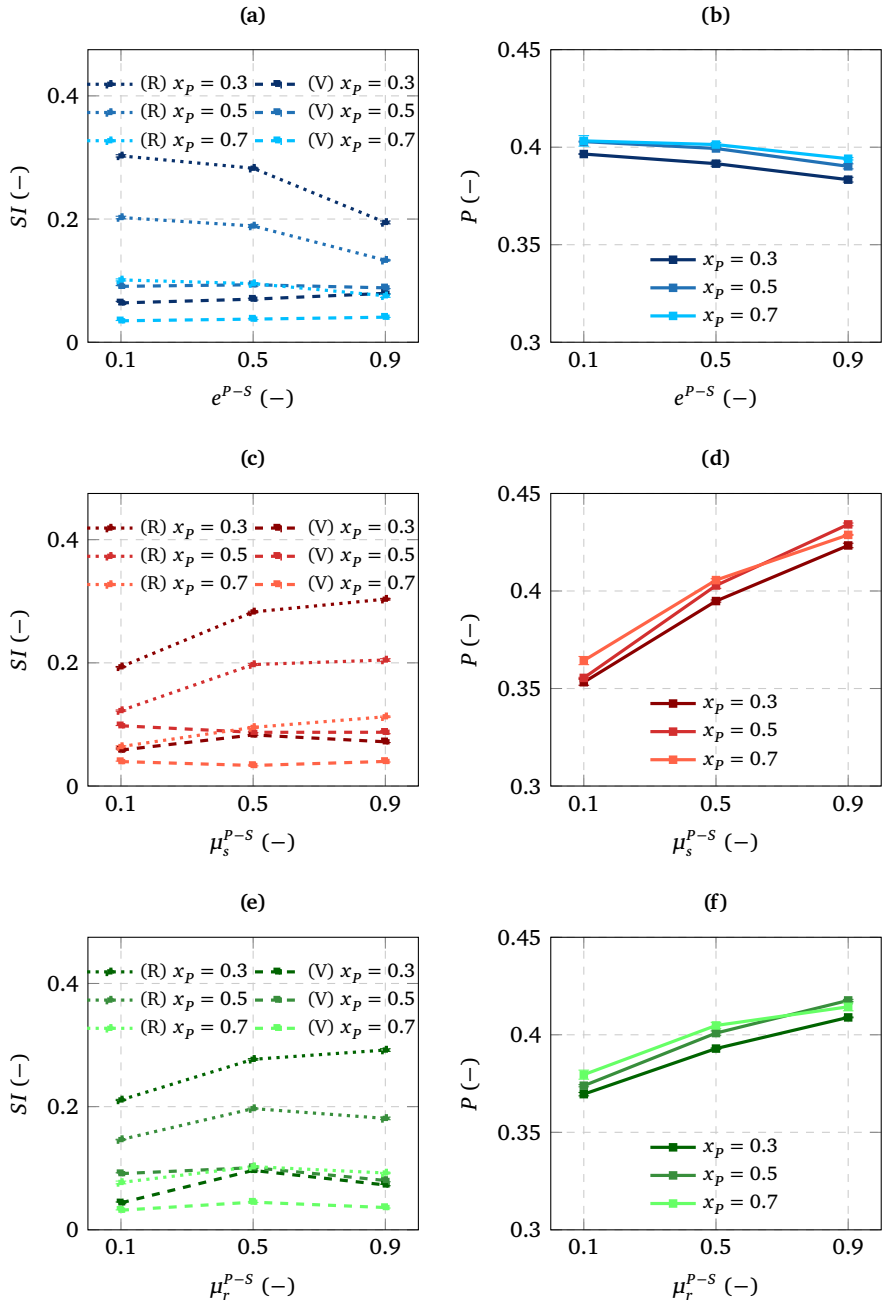


Figure 4.14: Effects of e^{P-S}, μ_s^{P-S} and μ_r^{P-S} on segregation (left column) and porosity (right column) for different mixture compositions. Segregation is analyzed in radial (R) and vertical (V) directions. Error bars indicate the standard deviation based on $n = 3$ repetitions. Due to the low variability in the measurements, the error bars are not discernible in the plotted data.

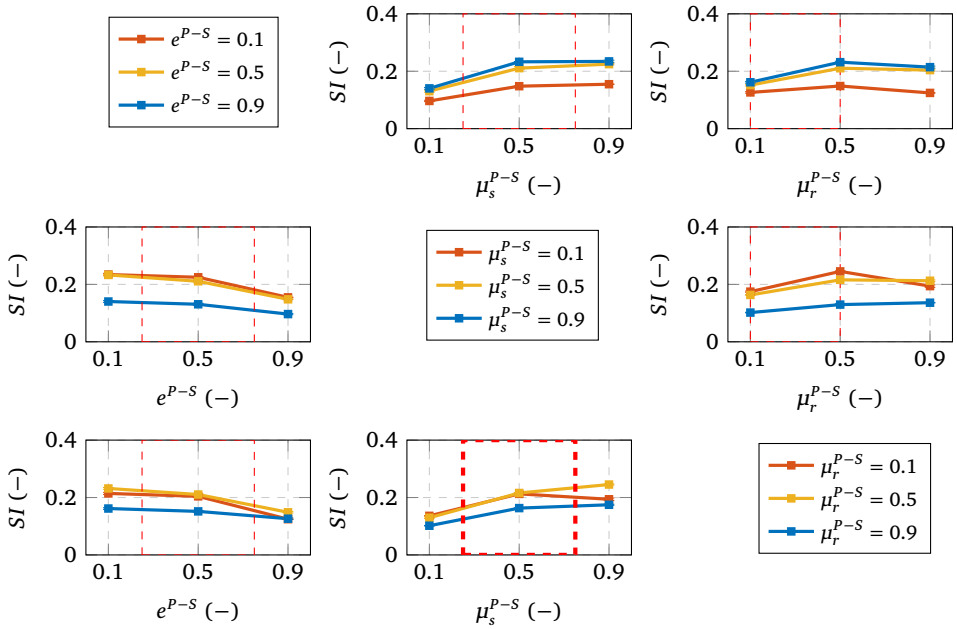


Figure 4.15: Interaction effects of e^{P-S}, μ_s^{P-S} and μ_r^{P-S} on radial segregation for the reference case. Error bars indicate the standard deviation based on $n = 3$ repetitions. Due to the low variability in the measurements, the error bars are not discernible in the plotted data. (Thick) dashed boxes indicate (important) regions of interest.

however, the interactions between μ_s^{P-S} and μ_r^{P-S} are stronger compared to the reference case. The interaction plots for $x_P = 0.3$ and $x_P = 0.7$ in the radial direction are presented in Figures B7 and B8 in [DS1], respectively. Similar to the reference case, interactions between μ_s^{P-S} and μ_r^{P-S} for $\mu_s^{P-S} > 0.5$ are observed for $x_P = 0.7$. Interestingly, no interaction is observed for $x_P = 0.3$. In the vertical direction (refer to Figures B9 and B10 in [DS1]), interactions between μ_s^{P-S} and μ_r^{P-S} are present, similar to the reference case.

Figure 4.17 shows the interaction plots for porosity in the reference case. Similar to the segregation index, weak interactions between μ_s^{P-S} and μ_r^{P-S} are observed. This observation is consistent for other discharge heights (refer to Figures B5 and B6 in [DS1]) and mixture compositions (Figures B11 and B12 in [DS1]).

In Section 4.3.2, it was concluded that e^{P-S}, μ_s^{P-S}, and μ_r^{P-S} each require careful calibration when developing a model for predicting segregation. The results in this section demonstrate that, for all investigated mixture compositions and flow velocities, the effects of μ_s^{P-S} and μ_r^{P-S} on segregation and porosity are interdependent. This finding implies that, once a model has been calibrated, these parameters cannot be adjusted independently. It is sometimes noted in the literature that model parameters are adopted

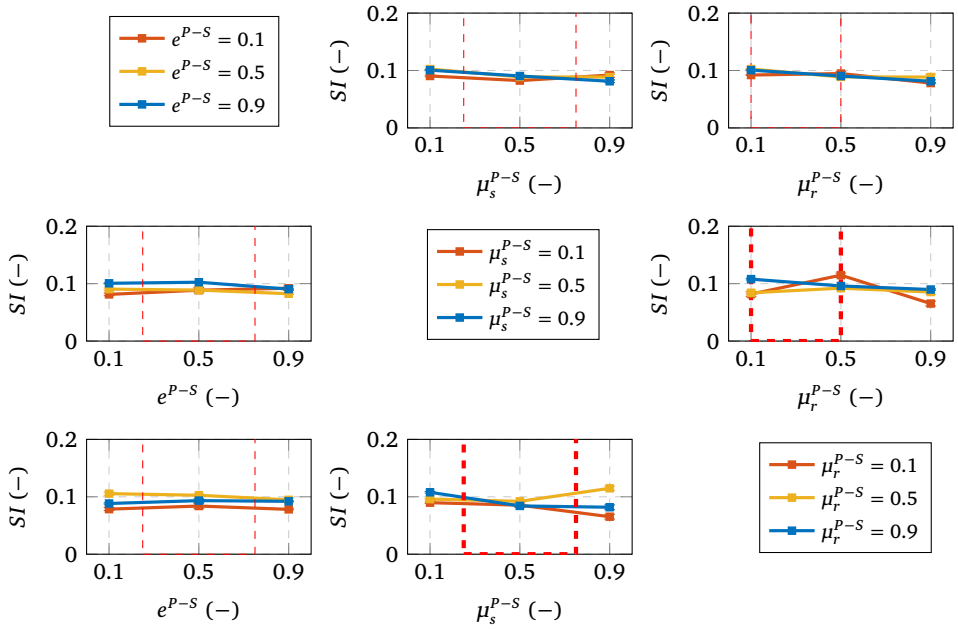


Figure 4.16: Interaction effects of e^{P-S}, μ_s^{P-S} and μ_r^{P-S} on vertical segregation for the reference case. Error bars indicate the standard deviation based on $n = 3$ repetitions. Due to the low variability in the measurements, the error bars are not discernible in the plotted data. (Thick) dashed boxes indicate (important) regions of interest.

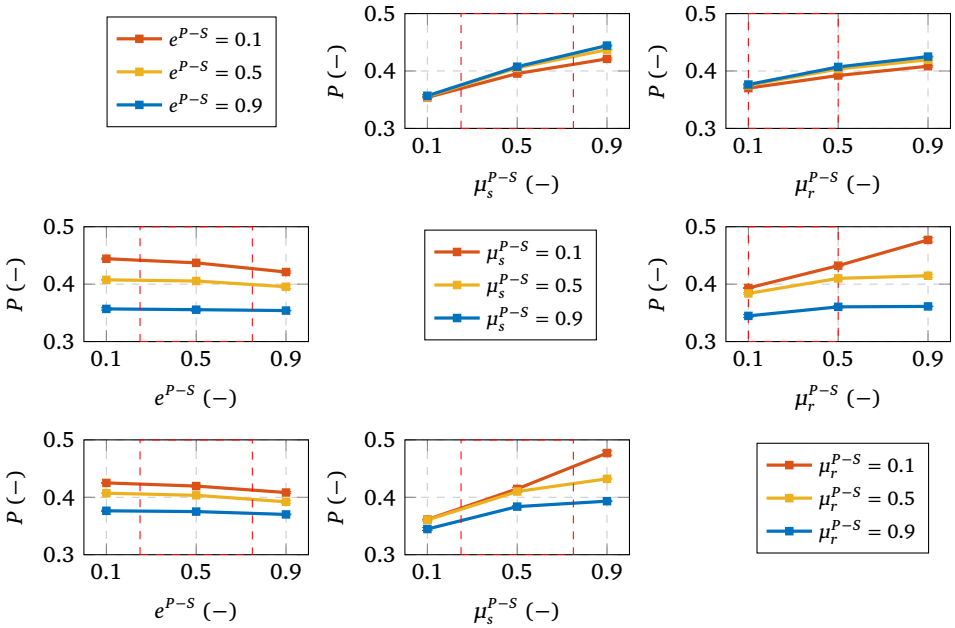


Figure 4.17: Interaction effects of e^{P-S}, μ_s^{P-S} and μ_r^{P-S} on porosity for the reference case. Error bars indicate the standard deviation of the segregation index based on three repetitions. Error bars indicate the standard deviation based on $n = 3$ repetitions. Due to the low variability in the measurements, the error bars are not discernible in the plotted data. (Thick) dashed boxes indicate (important) regions of interest.

from other publications regardless of the particle shapes used; for example, Yu and Saxén [16] modeled coke as non-spherical particles while using the sliding friction coefficient from the work of Mio *et al.* [17], where coke particles were modeled as spheres. By using different shapes, the particle rolling behavior differs and, based on the present findings, the effect of sliding friction on segregation and porosity will also be affected. Therefore, it is recommended to either use models exactly as presented in the literature or re-calibrate them when adjusting the frictional behavior.

4.4 Conclusions

The objective of this chapter was to investigate the influence of pellet–sinter interaction parameters (e^{P-S}, μ_s^{P-S}, and μ_r^{P-S}) on segregation and porosity in a mixture bed formed under representative blast furnace flow conditions. These KPIs are essential, as both segregation and porosity directly affect gas permeability and burden distribution in the furnace. The analysis was conducted across varying mixture compositions and flow velocities to isolate the effects of each interaction parameter. The results demonstrated

that all three parameters had distinct and independent impacts on both segregation and porosity, irrespective of composition or velocity. This highlights the necessity of including each of these parameters in the calibration process. While it is possible that some of the remaining 12 parameters have negligible influence on segregation and packing behavior –and could, in principle, be omitted from calibration– this was not evaluated here. A systematic investigation of their effects would significantly broaden the scope of this study. Accordingly, the complete set of 15 interaction parameters is retained. Reliable DEM modeling of a pellet–sinter mixture requires calibration of this entire set based on multiple KPIs measured under flow conditions representative of the target application. This calls for an experimental setup capable of replicating the high-velocity flow characteristic of blast furnace operation while enabling the measurement of multiple KPIs. The next chapter addresses the design of this calibration setup and the acquisition of the necessary KPI data.

4.5 Digital supplements

This section provides QR codes and links to supplementary digital content related to this chapter.

Table 4.3: Digital resources referenced in this chapter.

ID	Description	QR Code	Short Link
DS1	Repository with additional figures		`http://bit.ly/3GK5uwU`

4.6 Bibliography

[1] Y. Yu and H. Saxén. “Experimental and DEM study of segregation of ternary size particles in a blast furnace top bunker model”. In: *Chemical Engineering Science* 65 (2010), pp. 5237–5250. DOI: 10.1016/j.ces.2010.06.025.

[2] Y. Yu and H. Saxén. “Effect of DEM Parameters on the Simulated Inter-particle Percolation of Pellets into Coke during Burden Descent in the Blast Furnace”. In: *ISIJ International* 52 (2012), pp. 788–796. DOI: 10.2355/isijinternational.52.788.

[3] S. Liu, Z. Zhou, K. Dong, A. Yu, D. Pinson, and J. Tsalapatis. “Numerical Investigation of Burden Distribution in a Blast Furnace”. In: *steel research international* 86 (2015), pp. 651–661. DOI: 10.1002/srin.201400360.

[4] H. Wei, H. Saxén, and Y. Yu. “Numerical Analysis of Factors Affecting the Burden Surface and Porosity Distribution in the Upper Part of the Blast Furnace”. In: *Metals* 13 (2023). ISSN: 2075-4701. DOI: 10.3390/met13020292.

[5] Q. Song. “Effect of Nut Coke on the Performance of the Ironmaking Blast Furnace”. In: (2017).

[6] Delft High Performance Computing Centre (DHPC). *DelftBlue Supercomputer (Phase 2)*. https://www.tudelft.nl/dhpc/ark:/44463/DelftBluePhase2. 2024.

[7] A. Chakrabarty, R. Biswas, S. Basu, and S. Nag. “Characterisation of binary mixtures of pellets and sinter for DEM simulations”. In: *Advanced Powder Technology* 33 (2022), p. 103358. ISSN: 0921-8831. DOI: 10.1016/j.apt.2021.11.010.

[8] J. M. Boac, M. E. Casada, R. G. Maghirang, and J. P. Harner III. “3-D and Quasi-2-D Discrete Element Modeling of Grain Commingling in a Bucket Elevator Boot System”. In: *Transactions of the ASABE* 55 (2012), pp. 659–672. ISSN: 2151-0032. DOI: 10.13031/2013.41367.

[9] Altair EDEM. *EDEM Simulator Settings*.

[10] P. Bhalode and M. Ierapetritou. “A review of existing mixing indices in solid-based continuous blending operations”. In: *Powder Technology* 373 (2020), pp. 195–209. ISSN: 0032-5910. DOI: 10.1016/j.powtec.2020.06.043.

[11] H. Li and J. J. McCarthy. “Cohesive particle mixing and segregation under shear”. In: *Powder Technology* 164 (2006), pp. 58–64. ISSN: 0032-5910. DOI: 10.1016/j.powtec.2005.12.018.

[12] M. Cho, P. Dutta, and J. Shim. “A non-sampling mixing index for multicomponent mixtures”. In: *Powder Technology* 319 (2017), pp. 434–444. ISSN: 0032-5910. DOI: 10.1016/j.powtec.2017.07.011.

[13] J. Antony. “4 - A Systematic Methodology for Design of Experiments”. In: ed. by Jiju Antony. Second Edition. Elsevier, 2014, pp. 33–50. ISBN: 978-0-08-099417-8. DOI: 10.1016/B978-0-08-099417-8.00004-3.

[14] H. Wei, X. Tang, Y. Ge, M. Li, H. Saxén, and Y. Yu. “Numerical and experimental studies of the effect of iron ore particle shape on repose angle and porosity of a heap”. In: *Powder Technology* 353 (2019), pp. 526–534. ISSN: 0032-5910. DOI: 10.1016/j.powtec.2019.05.031.

[15] J. von Seckendorff and O. Hinrichsen. “Review on the structure of random packed-beds”. In: *The Canadian Journal of Chemical Engineering* 99 (2021), S703–S733. DOI: 10.1002/cjce.23959.

[16] Y. Yu and H. Saxén. “Flow of Pellet and Coke Particles in and from a Fixed Chute”. In: *Ind. Eng. Chem. Res.* 51 (May 2012), pp. 7383–7397. DOI: 10.1021/ie201362n.

[17] H. Mio, S. Komatsuki, M. Akashi, A. Shimosaka, Y. Shirakawa, J. Hidaka, M. Kadowaki, S. Matsuzaki, and K. Kunitomo. “Effect of Chute Angle on Charging Behavior of Sintered Ore Particles at Bell-less Type Charging System of Blast Furnace by Discrete Element Method”. In: *ISIJ International* 49 (2009), pp. 479–486. DOI: 10.2355/isijinternational.49.479.

5

High-Velocity Experimental Characterization of Material Behavior

In DEM calibration, model parameters must be determined such that simulations accurately reproduce observed material behavior based on measurable performance indicators. To ensure a reliable DEM model, these indicators should be measured under flow conditions relevant to the intended application, and multiple indicators are needed to constrain multiple parameters and obtain a unique, representative parameter set. Flow velocities at the stock surface of a blast furnace can reach up to 10 m/s during charging, and as shown in the previous chapter, the pellet–sinter mixture model parameters significantly influence material behavior at this velocity. Therefore, calibrating a DEM model for blast furnace pellet–sinter mixture charging requires multiple performance indicators measured under high-velocity flow conditions. This chapter presents the development of a calibration test enabling the measurement of multiple KPIs at blast furnace-representative flow velocities. The experimental setup, a novel piling test, differs from earlier studies by allowing significantly greater discharge heights –up to 4.665 m– compared to the previously reported maximum of approximately 0.4 m.

This chapter is based on:
R. Roeplal, Yusong Pang and Dingena Schott. *Towards Realistic DEM Modeling of Blast Furnace Mixture Charging: Calibration and Verification of Model Parameters under High-Velocity Flow Conditions* (under review).

5.1 Introduction

A DEM model's parameter values can be determined through direct measurement and/or bulk calibration. The latter involves adjusting model parameters by comparing simulation outputs to experimental or benchmark data, ensuring that the simulated bulk behavior closely matches observed physical behavior under similar conditions. The experimentally observed bulk behavior is quantified using one or more key performance indicators (KPIs) related to the material's flow and packing characteristics. It is well known that the following should be adhered to when using the bulk calibration approach:

- The flow conditions in the experiment should match those in the target application [1]. This includes replicating relevant flow velocities, confinement effects, stress states, and boundary interactions to ensure that the calibration reflects the actual operational conditions of the system being modeled. If the calibration experiments are conducted under flow conditions that deviate significantly from the target application, the resulting parameter set may not accurately capture the material behavior, leading to poor predictive performance in simulations.
- At least N KPIs should be used to uniquely determine N model parameters [1]. Using fewer KPIs than the number of unknown parameters generally results in a non-unique solution, implying that multiple sets of parameter values could yield identical KPI outcomes. This ambiguity hinders the ability to generalize the model, as the same KPIs may be achieved with different parameter sets that may perform differently under new conditions.

In Chapter 3, it was demonstrated that these two fundamental principles have not been sufficiently addressed in the existing blast furnace-related literature. Table 5.1 provides an overview of previous studies where bulk calibration has been used to determine one or more model parameters. It is clear that the angle of repose (AoR) is commonly employed as the sole calibration target, regardless of the number of model parameters being adjusted. The AoR has been measured using two types of tests: the ledge test and the piling test, as shown in Figure 5.1. In the ledge test, material is placed inside a box with a hinged door and a ledge on one side. When the door is opened, the material flows out and forms a stable heap against the ledge. In the piling test, material is discharged centrally from a hopper or container into another container below, forming a heap.

Among these tests, the piling test resembles stockpiling, a process that occurs as material is deposited on the stock surface. However, due to the scale of the experimental setups listed in Table 5.1, the flow velocities achieved in these tests are considerably lower than those expected at the blast furnace stock surface (~ 10 m/s). The maximum reported discharge height in the piling tests is $H = 0.4$ m, which, based on a free-fall calculation, corresponds to an estimated flow velocity of approximately 3 m/s. Consequently, the AoR

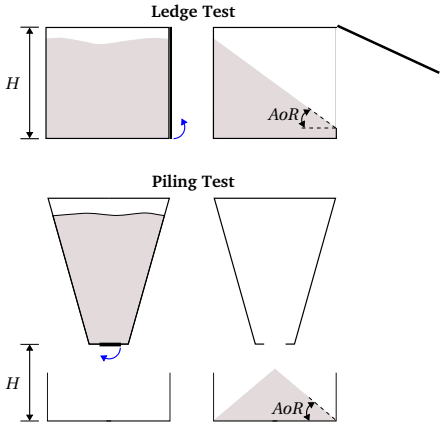


Figure 5.1: Common tests used for measuring the angle of repose (AoR) in blast furnace literature. The characteristic dimension H for each test is listed in Table 5.1.

Table 5.1: Summary of previous studies on DEM model parameter calibration for blast furnace charging using pellet or sinter. Abbreviations: N_{KPI} = number of KPIs used for calibration, N_c = number of parameters to be calibrated, n.s. = not specified.

Source	Material	$N_{\text{KPI}} \geq N_c$?	Test / KPI	Dimension H
Liu *et al.* [2]	Pellet/Sinter	No	Ledge test / AoR	0.3 m
Schott *et al.* [3]	Pellet/Sinter	Yes	Piling test / AoR	0.2 m
Li *et al.* [4]	Pellet	No	Piling test / AoR	0.2 m
Chibwe [5]	Pellet/Sinter	No	Ledge test / AoR	n.s.
Wei *et al.* [6]	Pellet/Sinter	No	Piling test / AoR	0.15 m
Chen *et al.* [7]	Pellet/Sinter	No	Piling test / AoR	0.4 m
Chakrabarty *et al.* [8]	Pellet/Sinter	No	Ledge test / AoR	0.4 m

values measured under these low-velocity conditions are unlikely to accurately represent the actual flow behavior during blast furnace charging. Furthermore, previous studies listed in Table 5.1 have focused on calibrating either pellet or sinter models individually, with no research dedicated to calibrating a pellet–sinter mixture model. This highlights a major gap in the calibration of blast furnace material models, even for individual materials. Specifically, there is a need for calibration experiments that replicate the high-velocity flow conditions characteristic of blast furnace charging while incorporating multiple KPIs to ensure a well-constrained and physically meaningful determination of model parameters.

This chapter has two main objectives. The first is to develop a calibration test that meets both of the previously outlined requirements, ensuring that calibration occurs under conditions representative of blast furnace flow while avoiding ambiguity. The second is to measure KPIs that vary with flow velocity. This is crucial because the model will be calibrated for the high-velocity flow regime ($v \approx 10$ m/s) in the next chapter, and the KPI

values must correspond to this flow condition.

The chapter is structured as follows: Section 5.2 describes the experimental setup for conducting a piling test under representative blast furnace flow conditions. Section 5.3 details the KPIs measured and the methods used for their assessment after each test. Section 5.4 presents the experimental plan, while Section 5.5 discusses the experimental results and the relevance of the measured KPIs for calibration.

5.2 High-velocity experimental setup design

In industrial blast furnaces, the flow from the hoppers to the stock surface is influenced by the chute angle, which can be as low as 11°. At this angle, the chute is nearly vertical, resulting in minimal interaction between the material and the chute, and the flow is almost directly discharged onto the stock surface. This configuration also yields the highest flow velocity in the y-direction ($\sim$ 10 m/s) and, as mentioned previously, resembles a piling test. Therefore, a calibration setup was designed to achieve these flow conditions, as illustrated in Figure 5.2. This high-velocity stockpiling test involves hopper discharge followed by heap formation. The setup features an adjustable discharge height H, which can reach a maximum of $H = 4.665$ m in the lab, enabling control over the flow velocity. At this maximum discharge height, the flow velocity reaches 9.6 m/s, closely matching the velocity expected at the blast furnace stock level during charging. This makes the setup well-suited for calibrating the high-velocity flow conditions expected in the blast furnace.

The experimental setup is shown in Figure 5.3, with its primary components outlined below; key elements are italicized for easy identification in the figure. To contain dust generated during high-velocity discharge tests, the setup is enclosed within a laboratory *enclosure*, which is connected to a dust extraction system (not shown in Figure 5.3) to remove airborne particles from the test area. The *hopper* is mounted to an *overhead crane*, enabling it to be positioned above the *container* at adjustable discharge heights H. It is constructed by stacking and bolting multiple sections together, with its key dimensions shown in Figure 5.4. This segmented construction introduced geometric imperfections at the joints and welds, as detailed in Appendix C.1. The hopper's outlet valve (not shown in Figure 5.4) is remotely controlled to open once the hopper is positioned at the desired height H. For stability, a *hopper guide* is attached to the hopper to restrict lateral movement. This guide fits securely into a wooden *reference frame* fixed to the enclosure, ensuring that the hopper moves only vertically above the container.

The container is equipped with a *heap formation arrangement*, as shown in Figure 5.5. The purpose of the heap formation arrangement is to facilitate the formation of a stable heap. It features a *collection plate* with side ledges that guide heap formation as material is discharged from the hopper. The plate is positioned atop a *bench scale* which measures and

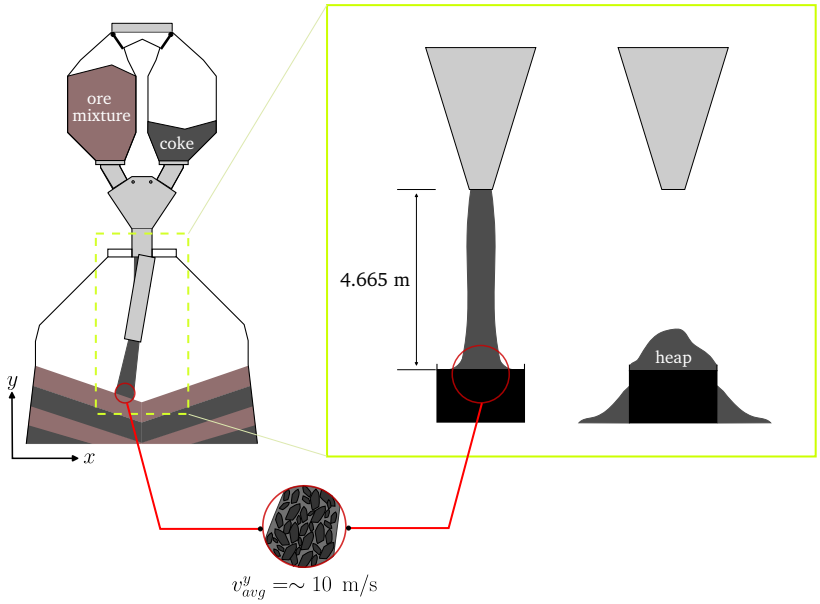


Figure 5.2: Schematic illustration of the lab-scale experimental setup designed to replicate real blast furnace flow conditions.

records the mass on the collection plate, and is equipped with a display. *Framed windows* are installed above the collection plate to confine the heap at the front and back, while any material spilling from the sides is collected in the container. The window frames are constructed from wood, the panes are made of acrylic, and all other structural components are fabricated from steel.

Considering the dimensions of the collection plate and window frames, the setup accommodates heaps with a base dimension of 0.5 m $\times$ 0.3 m. Figure 5.6 shows photographs of a heap after experiments with sinter. The left photograph was taken at the end of the first test, where it was observed that excess material accumulated at the left and right sides of the container, resting against the bench scale and interfering with the mass measurements. To address this, a wooden protective frame was added around the bench scale, as seen in the right photograph, to prevent contact with the material. Additionally, the setup was painted green to facilitate post-processing, as will be described in the next section.

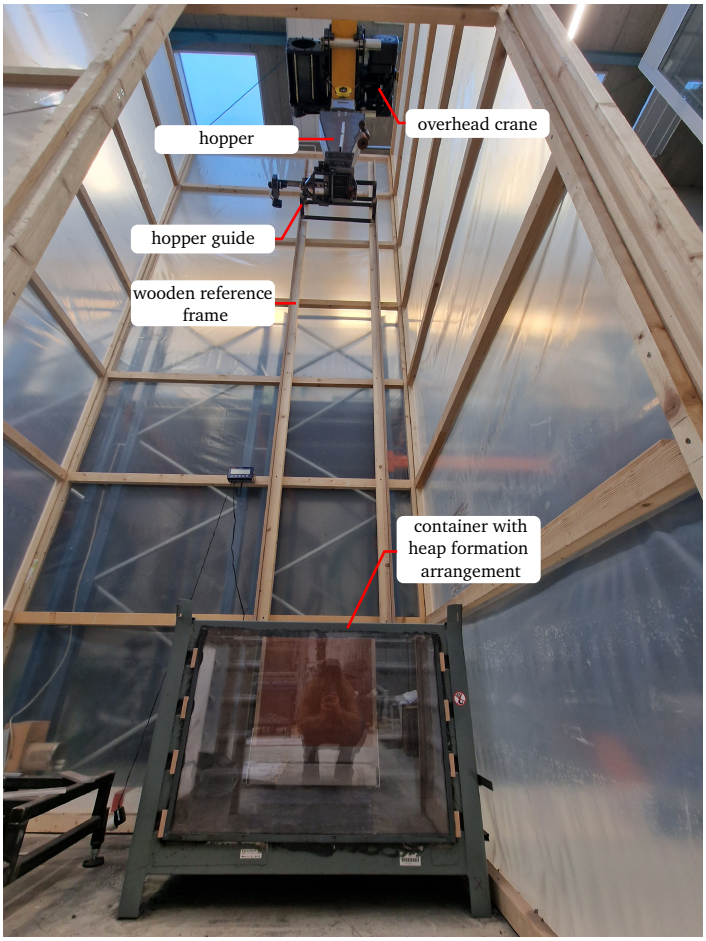


Figure 5.3: Photograph of the experimental setup, highlighting its main components. The setup is housed within an enclosure designed to contain dust generated during experiments. While the enclosure can be fully closed, the door is open in this image for visibility. The dust removal system, connected to a cyclone on the left side of the enclosure, is not visible in the photograph.

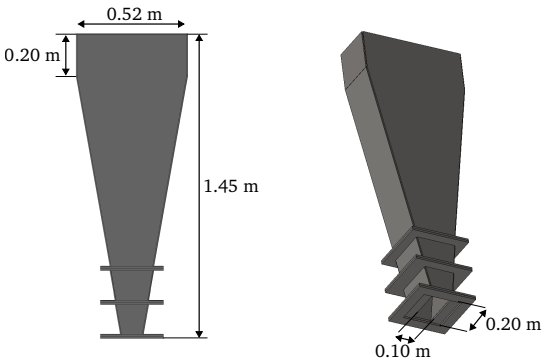


Figure 5.4: Drawing illustrating the hopper dimensions.

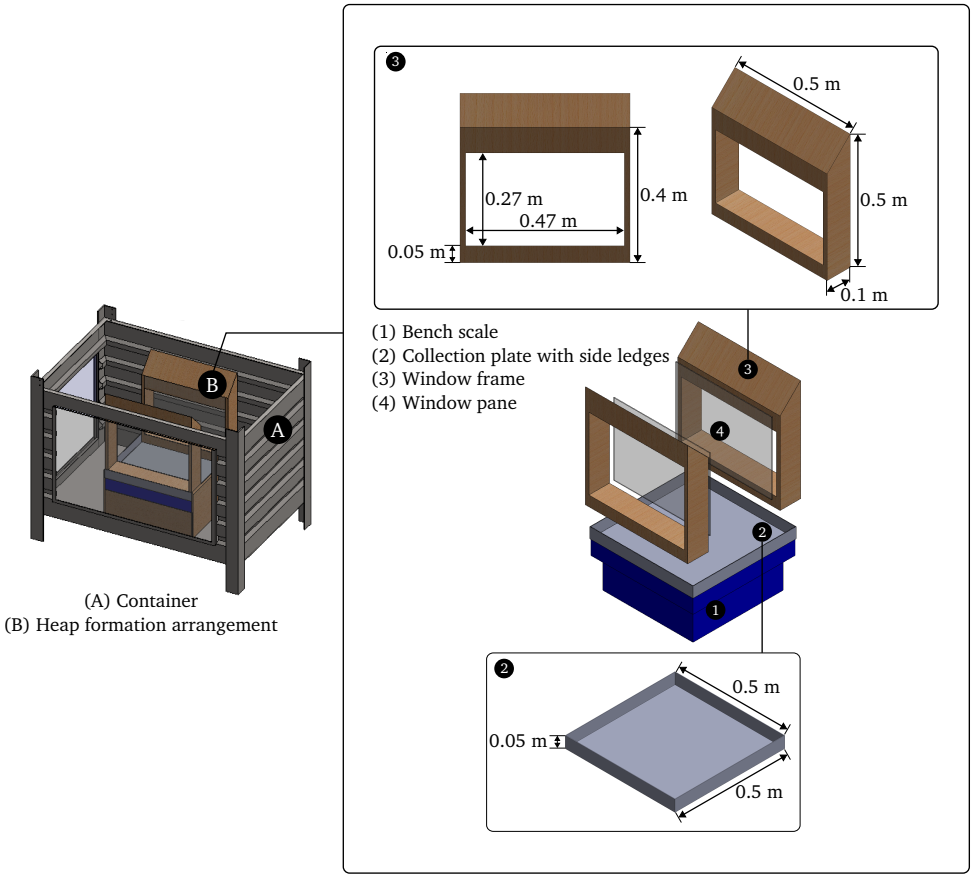


Figure 5.5: Illustration of the container with the heap formation arrangement, detailing its components and corresponding dimensions.



Figure 5.6: Photographs of the heap formed in an experiment with sinter. The image on the right shows the setup after installing wooden protective plates around the bench scale and after applying a green background, which enhances image analysis by providing clear contrast, making the heap more distinguishable from its surroundings.

5.3 Test procedure and measurement of KPIs

At the start of each test, the hopper is filled with material, and a GoPro Hero12 is mounted onto the hopper to capture the material flow during discharge. The hopper is then lifted to a height H using a crane, where H represents the vertical distance between the collection plate and the hopper outlet, measured using a laser distance meter. Once positioned at the desired height, the hopper is securely clamped to a wooden reference frame to ensure stability. After completing the setup, the GoPro is remotely activated to record at 240 FPS, and the hopper outlet is opened remotely. The material discharges onto the collection plate, forming a heap. The recording is stopped once the discharge is complete. Following each test, five KPIs are extracted to quantify material flow and packing behavior:

1. **Hopper discharge time** (t_d, KPI 1)
   The total discharge time is determined through frame-by-frame video analysis using Wondershare Filmora. The start of discharge is identified as the moment the hopper outlet valve begins to move, while the end of discharge is marked when the last particle completely exits the hopper. The discharge time is then calculated as the time difference between these two events. A visual demonstration of this procedure is provided in Figure 5.7.

2. **Heap mass** (m_h, KPI 2)
   The final mass of the heap is directly read from the bench scale display.

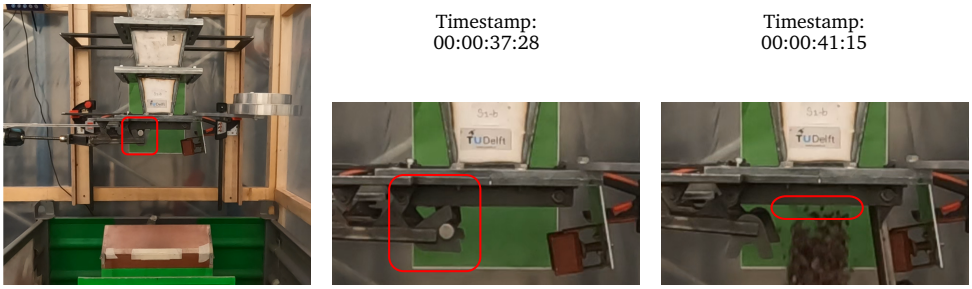


Figure 5.7: Snapshots extracted from WONDERSHARE FILMORA, illustrating the method used to determine the discharge time. Left: the hopper valve is fully closed, just before opening begins; Middle: the hopper valve has just started to open, with the valve barely visible at the indicated timestamp; Right: the timestamp corresponding to the moment the last particle fully exits the hopper outlet. Timestamps are shown in the format HH:MM:SS:MS. The discharge time is calculated by subtracting the initial timestamp from the final timestamp.

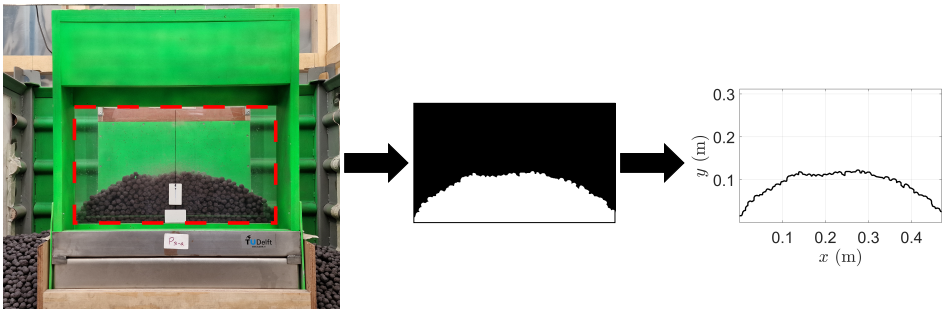


Figure 5.8: Illustration of how the heap contour is extracted at the end of an experiment. The example shown is from a pellet experiment, with the same methods applied to sinter and mixture experiments.

3. **2D heap contour**$^{(*)}$ (KPI 3)

   A front-view photograph of the heap is taken and processed in MATLAB, as shown in Figure 5.8. The heap contour is extracted by converting the RGB image to a binary format, a process facilitated by the distinct contrast between the nearly uniform color of the heap particles and the green background. Initially, the extracted contour is represented in pixel coordinates. However, only the red-dashed portion of the photograph in Figure 5.8 is analyzed, as the windowpane obstructs the left and right edges (each 0.015 m wide). Consequently, only the central 0.47 m of the heap is considered. To convert the contour from pixels to physical dimensions, the x- and y-coordinates are scaled by a factor of $0.47/N_p$, where N_p is the number of pixels in x-direction.

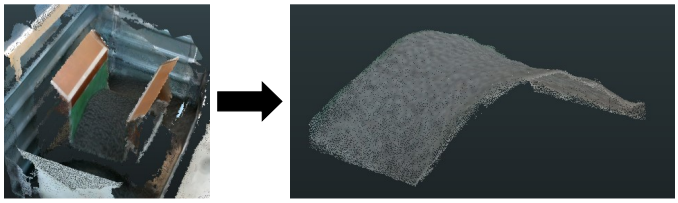


Figure 5.9: Illustration of how the heap volume is extracted at the end of an experiment. The example shown is from a pellet experiment, with the same methods applied to sinter and mixture experiments.

4. **Heap center height** (H_c, KPI 4)
   After converting the heap contour to meter units, the center height H_c is determined in MATLAB. The center height represents the y-coordinate corresponding to $x = 0.25$ m. Since the heap contour is defined by discrete data points, interpolation is used to estimate the precise height at $x = 0.25$ m.

5. **Heap porosity** (ϕ_h, KPI 5)
   A handheld INTEL® REALSENSE™ 3D scanner captures the top surface of the heap, as shown in Figure 5.9. The heap volume V_h is computed by determining the volume between the captured surface and the collecting plate. The bulk density ρ_h is then calculated as

$$\rho_h = \frac{m_h}{V_h} \tag{5.1}$$

   For the pellet and sinter experiments, the heap porosity is then calculated as

$$\phi_h = 1 - \frac{\rho_h}{\rho_p} \tag{5.2}$$

   where ρ_p is the particle density which is measured for pellet and sinter as described in Appendix B.

(*)**Note**: Traditionally, the heap shape is characterized using the *AoR*, but this metric becomes less reliable at the high discharge velocities used in this work, leading to flattened heap tops as will be shown later in Section 5.5. Determining the *AoR* is straightforward for heaps with a distinct peak; however, the flattening of heap tops becomes more pronounced with increasing discharge height, introducing subjectivity in measuring the angle. Therefore, the entire heap contour is used as a KPI, providing a more comprehensive and reliable alternative to the *AoR*.

5.4 Overview of high-velocity experiments

Since the goal is to identify velocity-dependent KPIs, experiments are conducted at different discharge heights.

$$H = [1 \quad 3 \quad 4.665] \text{ m}$$

These heights correspond to flow velocities at the collection plate, estimated using free-fall calculations, of

$$v = [4.4 \quad 7.7 \quad 9.6] \text{ m/s}$$

Experiments were conducted using pellet, sinter, and a 50/50 mass mixture of pellet and sinter. For each test, the hopper was filled to a fixed level, resulting in masses of 176.4 kg for pellet, 150 kg for sinter, and 160 kg for the mixture. Due to time constraints, experiments with pellet and sinter were performed at all three heights, whereas tests with the pellet–sinter mixture were conducted only at $H = 4.665$ m. Each test case with pellet was repeated three times, while tests with sinter and the mixture were repeated five times.

5.5 Experimental results and discussion

Table 5.2 presents the measured hopper discharge times for pellets, sinter, and the pellet–sinter mixture. On average, pellets take the longest to discharge; however, the sinter exhibits a relatively large standard deviation in discharge time. This variability is likely due to interactions between the highly non-spherical sinter particles and the hopper walls, which are not perfectly smooth because of welds and edges resulting from its imperfect construction, as detailed in Appendix C.1. Figure 5.10 illustrates this with a photograph taken at the end of a sinter charging test, showing sinter particles stuck at the outlet, where their sharp edges latch onto the outlet edges.

Figure 5.11a displays the heap mass m_h formed on the bench scale for pellets, sinter, and their mixture at different discharge heights H. For both pellets and sinter, m_h decreases

Table 5.2: Measured values of the hopper discharge time (t_d) for experiments with pellet, sinter and the pellet–sinter mixture (50/50). Results are presented as mean values with associated standard deviations, based on n experiments for each case: $n = 10$ for sinter experiments, $n = 5$ for pellet and mixture experiments.

Material	Mass in hopper (kg)	t_d (s)
Pellet	176.4	5.24 ± 0.28
Sinter	150.0	4.62 ± 1.00
Mixture	160.0	4.40 ± 0.31



Figure 5.10: Photograph taken at the end of a sinter charging experiment, showing accumulated sinter particles at the hopper outlet.

as H increases, which aligns with expectations: higher discharge heights result in greater impact velocities, leading to increased particle rebound and material loss. This effect is also reflected in Figure 5.12, where the heap peak becomes progressively flatter with increasing H, a trend observed for both pellet and sinter heaps.

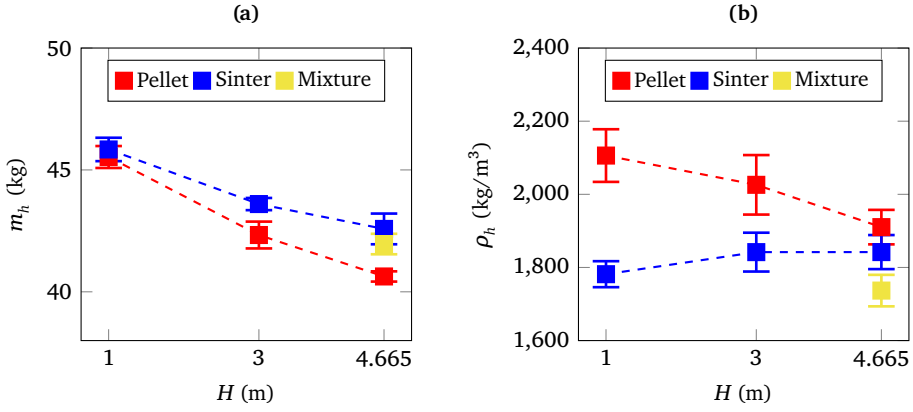


Figure 5.11: Measured values of (a) the heap mass (m_h) and (b) the heap bulk density (ρ_h) for all experiments, with different discharge heights (H). Error bars represent standard deviations based on n experiments for each case: $n = 3$ for pellet experiments, $n = 5$ for sinter and mixture experiments.

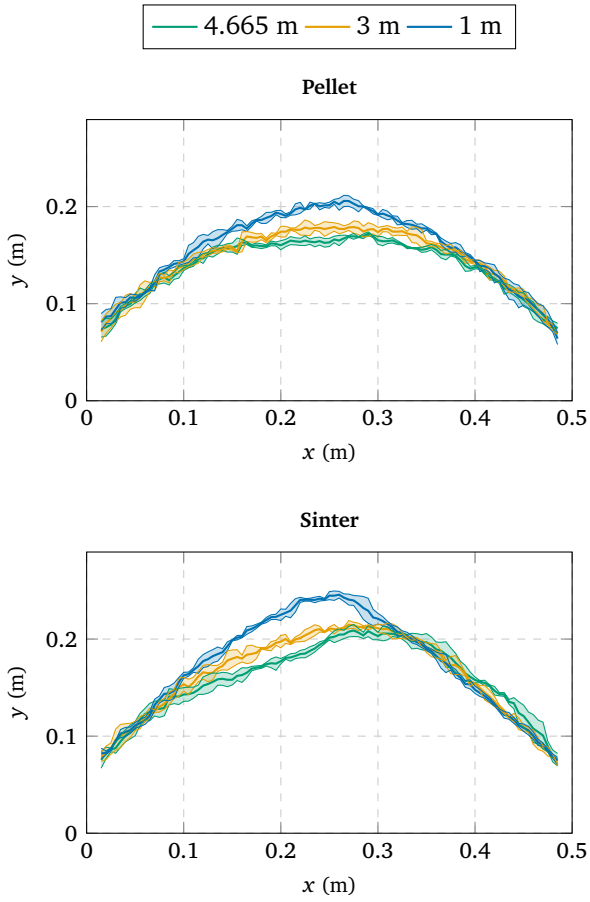


Figure 5.12: Comparison of heap profiles at different heights for pellet and sinter. Shaded areas represent the standard deviation with $n = 3$ for experiments with pellet and $n = 5$ for experiments with sinter.

Table 5.3: Measured values of the heap center height (H_c, in cm) for all experiments, with different discharge heights (H). Results are presented as mean values with associated standard deviations, based on n experiments for each case: $n = 3$ for pellet experiments, $n = 5$ for sinter and mixture experiments.

Material	$H = 1$ **m**	$H = 3$ **m**	$H = 4.665$ **m**
Pellet	20.15 ± 0.31	17.79 ± 0.58	16.31 ± 0.42
Sinter	24.26 ± 0.43	20.88 ± 0.66	19.88 ± 0.45
Mixture	N/A	N/A	17.86 ± 0.54

Table 5.4: Measured values of the heap porosity (ϕ_h) for all experiments, with different discharge heights (H). Results are presented as mean values with associated standard deviations, based on n experiments for each case: $n = 3$ for pellet experiments, $n = 5$ for sinter and mixture experiments.

Material	$H = 1$ **m**	$H = 3$ **m**	$H = 4.665$ **m**
Pellet	0.42 ± 0.02	0.44 ± 0.02	0.47 ± 0.01
Sinter	0.48 ± 0.01	0.47 ± 0.02	0.47 ± 0.01

At all discharge heights, the sinter heap consistently retains a greater mass than the pellet heap. Since sinter particles have a lower density (see Appendix B), this implies that the sinter heap also occupies a larger volume. This is confirmed by Figure 5.12, which compares the heap contours of the materials at different H values. The observed difference is likely due to the spherical shape of the pellets, which promotes rolling and reduces their tendency to form stable heaps compared to sinter particles under the same flow conditions. The heap mass and contour of the mixture fall between those of the pellet and sinter heaps, exhibiting intermediate characteristics that align with its composition. The center heights of the heaps, extracted from these profiles, are summarized in Table 5.3.

Figure 5.11b shows the bulk density values of pellet, sinter, and the pellet–sinter mixture. The sinter heap consistently exhibits a lower bulk density compared to the pellet heap, which can be attributed to the irregular shapes of the sinter particles. As the discharge height increases, the bulk density of the sinter heap increases, indicating a denser packing, while the opposite trend is observed for the pellet heap. This is also reflected in Table 5.4, which shows that the porosity of the sinter heap decreases with increasing H while the opposite is true for the pellet heap.

Revisiting the heap shapes at different values of H (Figure 5.12), it is evident that the sinter heap becomes increasingly asymmetric with higher discharge heights. Heap asymmetry is not observed at $H = 1$ m but becomes clearly visible at $H = 3$ m and is even more pronounced at $H = 4.665$ m. This observation is discussed in detail in Appendix C.1 and C.2, where it was hypothesized that the asymmetry in flow –and consequently in heap formation– is caused by imperfections in the hopper. Flipping the hopper resulted in a mirrored heap shape, providing further support for this hypothesis. The increasing asymmetry at larger discharge heights is likely due to the greater falling distance, whereby

any asymmetry present at the chute outlet becomes more pronounced as the material travels farther. This effect was not observed in the experiments with pellets, which is likely due to the reduced interaction between the smoother, spherical pellet particles and the imperfect hopper walls. In contrast, the irregular shape and sharp edges of the sinter particles make them more prone to interacting with the welds and edges present in the hopper, as detailed in Appendix C.1. Figure 5.10 further illustrates evidence of these interactions.

It was also observed that the heap peak becomes progressively flatter as H increases, a trend present in both pellet and sinter heaps. If the AoR were used as a KPI, accurately measuring it at higher H would become increasingly challenging due to this flattening effect. Since the flattened region must be excluded when determining the AoR, selecting the exclusion zone introduces a degree of subjectivity. Even minor variations in the chosen contour region could result in significantly different AoR values, reducing its reliability as a KPI. Another noteworthy observation is that the sinter heap becomes more asymmetric as H increases. Although the overall heap shape changes with H, the left and right heap angles remain relatively constant before flattening occurs. This implies that similar AoR values can correspond to visibly different heap contours, meaning that important differences in heap shape –caused by variations in flow conditions– are not captured by the AoR. This suggests that the AoR measured in a piling test is not highly sensitive to flow velocity, indicating that it may not effectively distinguish between different flow regimes or serve as a reliable calibration target for a specific regime.

5.6 Conclusions

The objective of this chapter was twofold: (i) to develop a calibration test enabling the measurement of multiple KPIs at flow velocities representative of those in a blast furnace, and (ii) to measure KPIs that are velocity-dependent. To achieve this, an experimental piling test setup was designed and constructed –a widely used approach in DEM calibration and blast furnace research. This setup distinguishes itself from previous configurations by its larger scale, particularly in discharge height and pile size. While earlier studies reported maximum discharge heights of approximately 0.4 m, the present setup allows for significantly greater heights, reaching up to 4.665 m. The key conclusions are:

- **Hopper imperfections influence discharge behavior.** Manufacturing flaws such as welds and surface edges on the hopper interior caused asymmetric piling, particularly for sinter. These geometric imperfections must be included in the DEM hopper model to ensure accurate replication of experimental behavior during calibration.
- **Five KPIs were identified as velocity-sensitive calibration targets across different materials.** Experiments using pellet, sinter, and their 50/50 mixture demonstrated

that hopper discharge time, heap mass, heap shape, heap center height, and heap porosity (via bulk density) were all found to vary with flow velocity. This confirms their relevance as velocity-dependent indicators for use in model calibration under realistic flow conditions. In contrast, the angle of repose was shown to be velocity-invariant in this setup and is therefore unsuitable as a calibration target.

In the next chapter, the five velocity-dependent KPIs will be used as calibration targets for the pellet, sinter, and mixture models at the highest flow velocity ($H = 4.665$ m). Given that only five calibration targets are available for a model with 15 parameters, a stepwise calibration strategy combined with multi-objective optimization will be employed to obtain a unique solution. The calibrated models will then be evaluated for their ability to capture the KPIs at other flow velocities.

5.7 Bibliography

[1] T. Roessler, C. Richter, A. Katterfeld, and F. Will. “Development of a standard calibration procedure for the DEM parameters of cohesionless bulk materials – part I: Solving the problem of ambiguous parameter combinations”. In: *Powder Technology* 343 (2019), pp. 803–812. DOI: 10.1016/j.powtec.2018.11.034.

[2] S. Liu, Z. Zhou, K. Dong, A. Yu, D. Pinson, and J. Tsalapatis. “Numerical Investigation of Burden Distribution in a Blast Furnace”. In: *steel research international* 86 (2015), pp. 651–661. DOI: 10.1002/srin.201400360.

[3] D. Schott, W. Vreeburg, C. Molhoek, and G. Lodewijks. “Granular Flow to a Blast Iron Ore Furnace: Influence of Particle Size Distribution on Segregation of a Mixture”. In: *Traffic and Granular Flow ’15*. Ed. by Victor L Knoop and Winnie Daamen. Springer International Publishing, 2016, pp. 621–628-621–628. ISBN: 978-3-319-33482-0. DOI: 10.1007/978-3-319-33482-0_78.

[4] C. Li, T. Honeyands, D. O’Dea, and R. Moreno-Atanasio. “The angle of repose and size segregation of iron ore granules: DEM analysis and experimental investigation”. In: *Powder Technology* 320 (2017), pp. 257–272. ISSN: 0032-5910. DOI: 10.1016/j.powtec.2017.07.045.

[5] D. Chibwe. “Optimised burden delivery for blast furnace operations”. In: (Sept. 2019).

[6] S. Wei, H. Wei, H. Saxén, and Y. Yu. “Numerical Analysis of the Relationship between Friction Coefficient and Repose Angle of Blast Furnace Raw Materials by Discrete Element Method”. In: *Materials* 15 (Jan. 2022), p. 903. DOI: 10.3390/ma15030903.

[7] J. Chen, H. Zuo, H. Zhao, Q. Xue, and J. Wang. “Burden circumferential mass segregation at the blast furnace with parallel hoppers”. In: *Powder Technology* 409 (2022), p. 117845. ISSN: 0032-5910. DOI: 10.1016/j.powtec.2022.117845.

[8] A. Chakrabarty, R. Biswas, S. Basu, and S. Nag. “Characterisation of binary mixtures of pellets and sinter for DEM simulations”. In: *Advanced Powder Technology* 33 (2022), p. 103358. ISSN: 0921-8831. DOI: 10.1016/j.apt.2021.11.010.

6

Calibration and Verification of Mixture Model Parameters under High-Velocity Flow Conditions

Building on the calibration experiments presented in the previous chapter, this chapter focuses on calibrating the pellet–sinter mixture model using data obtained at the highest flow velocity, representative of blast furnace charging conditions. Five KPIs, measured under these conditions, are used as calibration targets to capture the flow and packing behavior of the mixture. Given the challenge of calibrating a 15-parameter model using only five calibration targets, a step-wise calibration strategy combined with multi-objective optimization is employed to determine a unique and physically meaningful parameter set. For the first time in blast furnace-related DEM calibration, this approach results in a reliable model that accurately captures iron ore mixture behavior at blast furnace velocities. The calibrated model is subsequently verified, demonstrating its ability to reproduce flow behavior not only at the calibration velocity but also across a range of flow velocities.

This chapter is based on:
R. Roeplal, Yusong Pang and Dingena Schott. *Towards Realistic DEM Modeling of Blast Furnace Mixture Charging: Calibration and Verification of Model Parameters under High-Velocity Flow Conditions* (under review).

6.1 Introduction

The DEM has become a valuable tool for simulating the blast furnace charging process and offers significant potential for improving understanding of burden distribution during charging. DEM relies on contact models to predict interactions between particles, material types, and furnace walls. A key challenge in developing a *reliable* DEM model lies in determining the numerous model parameters, particularly when modeling material mixtures, as is required for blast furnace applications. The accuracy of DEM predictions is highly dependent on these parameters, which must be determined to ensure that model outputs align with real-world behavior.

Chapter 3 established that DEM models for blast furnace charging are typically developed using the Hertz-Mindlin contact model in combination with rolling model C. These models have proven effective for simulating coarse, free-flowing blast furnace materials. Together, they require the specification of the static friction coefficient (μ_s), rolling friction coefficient (μ_r), and restitution coefficient (e) for each interaction. Consequently, as illustrated in Figure 6.1, developing a DEM model for a pellet–sinter mixture based on these contact models necessitates specifying 15 parameters to characterize all material interactions. Given the size of this parameter set, Chapter 4 investigated whether the number of parameters to be calibrated could be reduced by examining the influence of the three pellet–sinter interaction parameters on segregation and packing behavior at high velocity. The analysis demonstrated that all three interaction parameters significantly affect mixture behavior and must therefore be included in the calibration. Consequently, calibration of the full 15-parameter set is necessary to develop a reliable pellet–sinter DEM model. In this context, a reliable model refers to a DEM model calibrated to produce a unique parameter set capable of accurately predicting key performance indicators (KPIs) under flow conditions representative of blast furnace charging. To meet the requirement of representative flow conditions, Chapter 5 introduced a novel experimental setup that enables the measurement of multiple KPIs at flow velocities equivalent to those in the blast furnace. This experimental setup successfully provided five measurable KPIs under relevant flow conditions –more than reported in any previous blast furnace-related calibration study. Nevertheless, with 15 model parameters and only five calibration targets, the challenge of achieving a unique solution for the full parameter set remains.

The objective of this chapter is to systematically *calibrate the pellet–sinter mixture model*, ensuring a *unique solution* for the large set of model parameters. This challenge is addressed through a step-wise calibration strategy, initially calibrating the parameters of the individual pellet and sinter models at the highest velocity before calibrating the pellet–sinter interaction parameters.

This chapter is structured as follows. Section 6.2 introduces the step-wise calibration strategy and outlines the calibration workflow. Details of the DEM simulations, including

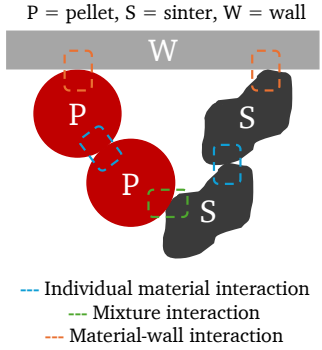


Figure 6.1: Overview of the interactions in a DEM simulation involving a binary mixture of pellets and sinter particles.

the simulation setup and the extraction of KPIs, are provided in Section 6.3. The response surface modeling of the KPIs is presented in Section 6.4. Section 6.5 describes the multi-objective optimization approach used to determine the parameter values that best match the experimentally measured KPIs from the previous chapter, followed by the calibration results. Model verification, including an evaluation of the calibration across different flow velocities, is discussed in Section 6.6. Finally, Section 6.7 explores the extent to which the numerical time step can be increased to accelerate simulations with the calibrated model.

6.2 Calibration framework

6.2.1 Calibration and verification strategy

Referring to Figure 6.1, it is evident that a pellet–sinter mixture model requires calibration of 15 parameters, as each interaction is defined by μ_s, μ_r, and e. Standard calibration practice dictates that at least one KPI is needed per parameter; therefore, direct calibration of the full mixture model would require a minimum of 15 KPIs, whereas only 5 are available from the experiments presented in the previous chapter. To address this challenge, a step-wise calibration approach is proposed, as illustrated in Figure 6.2. The idea is to start by calibrating the complete set of interaction parameters associated with the pellet and sinter models, *i.e.*, the particle–particle (P–P / S–S) *and* particle–wall (P–W / S–W) interaction parameters. Once calibrated, their values remain fixed and are used as inputs for the second calibration step, in which the pellet–sinter interaction parameters in the mixture model are calibrated. Since the pellet and sinter models each require 5 interaction parameters, the majority of parameters (12 out of 15) are determined during the first calibration step. By decomposing the calibration process in this way, the number of required KPIs for a unique solution is significantly reduced, from 15 to 6, thereby

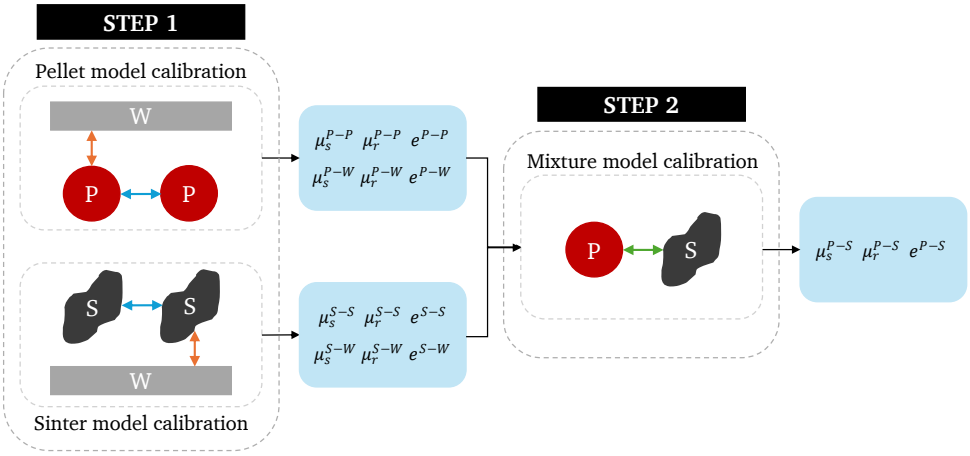


Figure 6.2: Step-wise strategy for calibrating a pellet–sinter mixture model. Abbreviations: P = pellet; S = sinter; W = wall; μ_s = sliding friction coefficient; μ_r = rolling friction coefficient; e = restitution coefficient.

6

simplifying the overall calibration procedure.

In the previous chapter, a high-velocity piling test (schematically shown in Figure 6.3) was used as the calibration experiment. Recall that this setup was specifically designed to enable the simultaneous measurement of multiple KPIs in a single test while achieving different flow velocities by varying the discharge height H. Experiments were performed at $H = [1\ \ 3\ \ 4.665]$ m, resulting in estimated flow velocities at the plate of approximately $v = [4.4\ \ 7.7\ \ 9.6]$ m/s, based on a free-fall calculation. The highest velocity condition ($v = 9.6$ m/s) is particularly relevant for calibrating DEM models for blast furnace charging, as it closely matches the maximum vertical flow velocity when material reaches the stockpile during charging. The data obtained from the other configurations leave room for verification of the calibration results.

Table 6.1 presents a summary of the experiments, listing the materials tested at each discharge height. The highest flow velocity of 9.6 m/s, achieved at $H = 4.665$ m, closely matches the velocity observed at the blast furnace stock level during charging [1]. Thus, the models are calibrated at this configuration. After calibrating the pellet and sinter models, an initial verification is conducted at $H = 4.665$ m to confirm the calibration outcome. The calibrated models are then further tested at $H = 1$ m and $H = 3$ m to evaluate whether re-calibration is needed at different flow velocities. Due to time constraints, the verification at $H = 1$ m and $H = 3$ m is performed only for the pellet and sinter models.

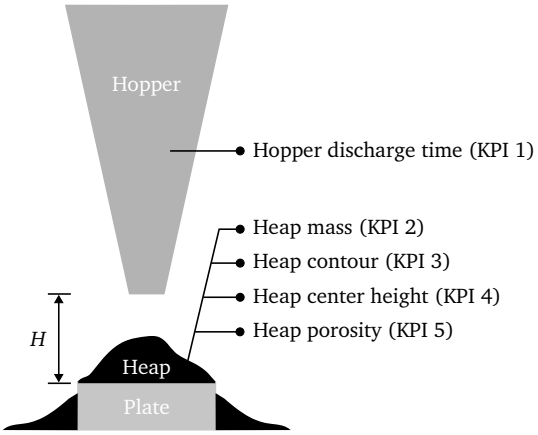


Figure 6.3: Simplified representation of the KPIs measured in Chapter 5, which will serve as calibration targets in the current chapter.

Table 6.1: Experimental setup configurations for tests with pellet, sinter, and the pellet–sinter mixture (50/50). Differences in configurations are based on the discharge height and, consequently, the flow velocity achieved at the plate.

Material	**Configuration**		
	$H = 1$ m $v =\sim 4.4$ m/s	$H = 3$ m $v =\sim 7.7$ m/s	$H = 4.665$ m $v =\sim 9.6$ m/s
Pellet	verification	verification	calibration + verification
Sinter	verification	verification	calibration + verification
Mixture	–	–	calibration + verification

6.2.2 Calibration parameters and targets

Recall the five KPIs experimentally measured in the previous chapter (schematically shown in Figure 6.3), which characterize material flow and packing behavior:

- KPI 1: the hopper discharge time (t_d)
- KPI 2: the heap mass (m_h)
- KPI 3: the 2D heap shape (front view)
- KPI 4: the heap center height (H_c)
- KPI 5: the heap porosity (ϕ_h)

While the ideal KPI for calibrating a high-velocity DEM model designed to predict mixture segregation would be the segregation index, this approach would require a larger experimental setup with significantly more material, increasing complexity and time. Therefore, calibration is performed using the five KPIs listed above, supported by prior studies [2–6] showing that calibration based on bulk flow behavior is an adequate basis for reliable segregation models.

Despite the use of these five KPIs, the calibration process faces the challenge of an underdetermined system, as the pellet and sinter models each include six parameters. To resolve this, the particle–wall restitution coefficient in the pellet and sinter models (e^{P-W} and e^{S-W}, respectively) is fixed based on values reported in the literature, reducing the parameter space to five adjustable variables per model. This approach ensures that the remaining parameters can be effectively calibrated using the available KPIs, providing a systematic and reliable foundation for model development.

6.2.3 Calibration workflow

Following the step-wise strategy outlined in Figure 6.2, the calibration process is conducted separately for the pellet, sinter, and mixture models. The workflow presented in Figure 6.4 details the steps involved in this process, which are applied to each model individually. The core idea behind this approach is that, by predicting KPI behavior across the entire parameter space, it becomes possible to identify parameter values that best match the experimentally measured KPIs in the DEM simulation. This is achieved by minimizing the discrepancy between simulated and measured KPI values, effectively framing the calibration as an optimization problem.

The “Lab Testing” step in Figure 6.4 refers to the experiments described in the previous chapter. The remaining steps –ranging from DEM modeling to Response Surface Modeling, Multi-Objective Optimization, and Verification– are the focus of this chapter, with each step presented in the following sections.

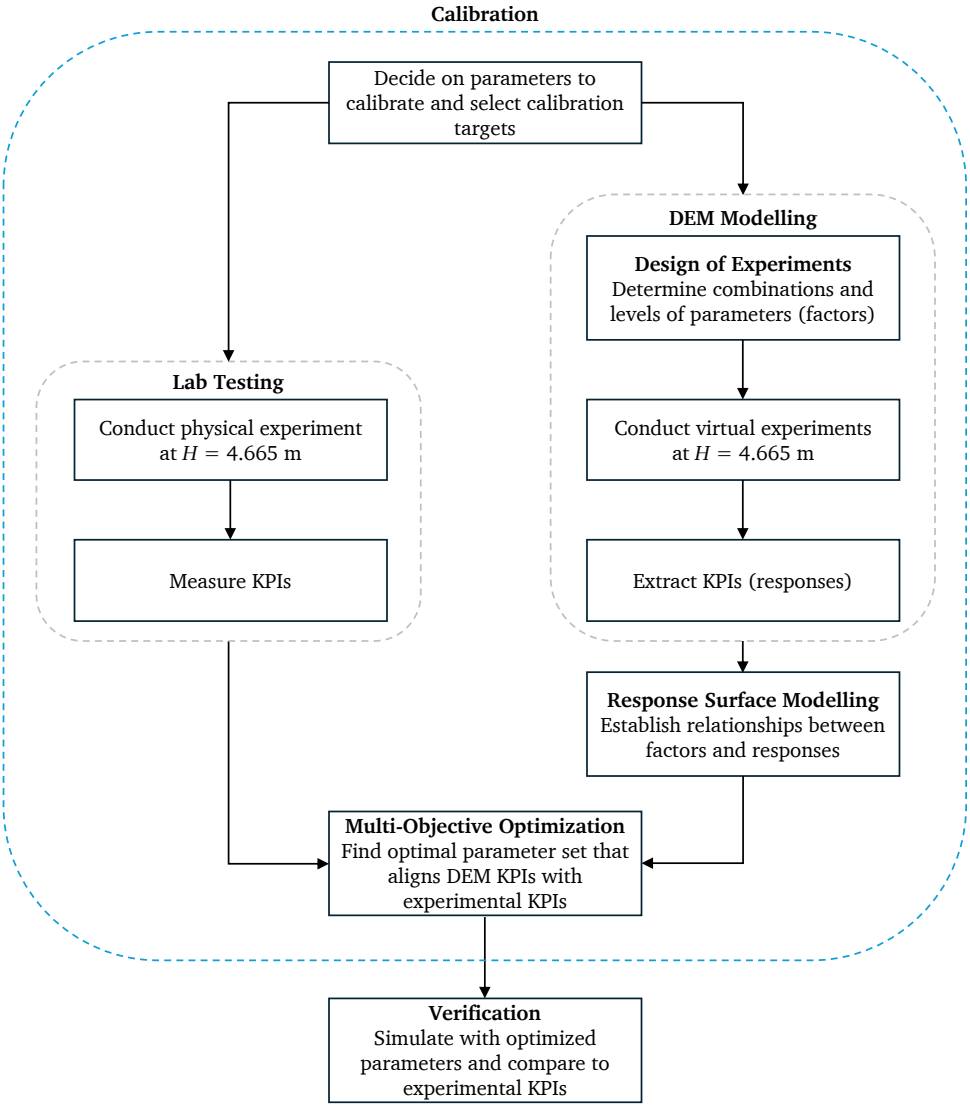


Figure 6.4: Steps involved in the calibration and verification of DEM models.

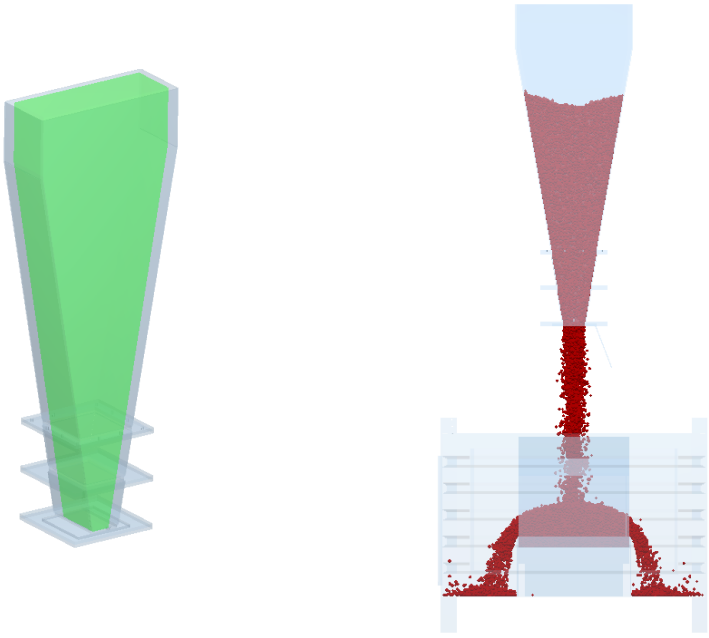
6.3 DEM simulations

6.3.1 Simulation setup

The physical experiments are replicated in a virtual environment using ALTAIR® EDEM™ (version 2023) on the DelftBlue high-performance cluster [7] with a single GPU (NVIDIA Tesla V100S-PCIE-32GB). As discussed in the previous chapter and detailed in Appendix C, the experimental setup exhibited manufacturing imperfections that were found to influence heap formation, particularly in the case of sinter. These imperfections refer specifically to welds and edges along the inner surface of the hopper. Appendix C.3 demonstrates that the heap shape –used as a KPI in this chapter– is directly affected by these imperfections, particularly the edges. Therefore, the imperfections were incorporated into the CAD model of the hopper in SOLIDWORKS. The model dimensions are consistent with the experimental setup, and all structural components are represented as steel. Consequently, the pellet/sinter experiments involved two material types: pellet (P)/sinter (S) particles and steel walls (W), while experiments with the mixture include all three materials. The interactions between these materials are described using the Hertz-Mindlin (no-slip) contact model with an elastic-plastic spring-dashpot rolling friction model (model C). Detailed descriptions of the contact models are available in Chapter 3 and the input parameters used in this study are summarized in Table 6.2.

The particle densities and size distributions for pellet and sinter were measured using 3D scanning, as described in Appendix B. The particle size distributions are presented in Figure 6.6a, expressed in terms of the equivalent spherical diameter. The particle shapes used in the simulations are shown in Figure 6.6b. Since pellets are nearly spherical in reality, they are modeled as spheres. For sinter, four randomly selected particles were scanned, and their shapes were approximated using clumps by fitting spheres to the corresponding STL files. The Young's moduli and Poisson's ratio of all materials are taken from literature, as well as the particle–wall restitution coefficients between pellet and steel. Numerical integration is performed using the Euler scheme with a time step set to 10% of the Rayleigh time step (Δt_R), which is $\Delta t_R = 9.2 \times 10^{-5}$ s for simulations with pellet and $\Delta t_R = 1.8 \times 10^{-5}$ s for simulations with sinter and the mixture.

Each simulation consists of two main parts: the filling of the hopper and the discharging of the material into the container. A virtual volume (see Figure 6.5a) is used for generating particles using a dynamic factory. The simulation procedure is as follows. At $t = 0$ s, the factory starts generating the required amount of material. In the mixture simulations, two factories are connected to the virtual domain, each producing half of the total mixture mass. At $t = 3$ s, the hopper outlet is opened, allowing the material to flow (as seen in Figure 6.5b), and the simulation ends at $t = 15$ s, once all the material has settled in the container.

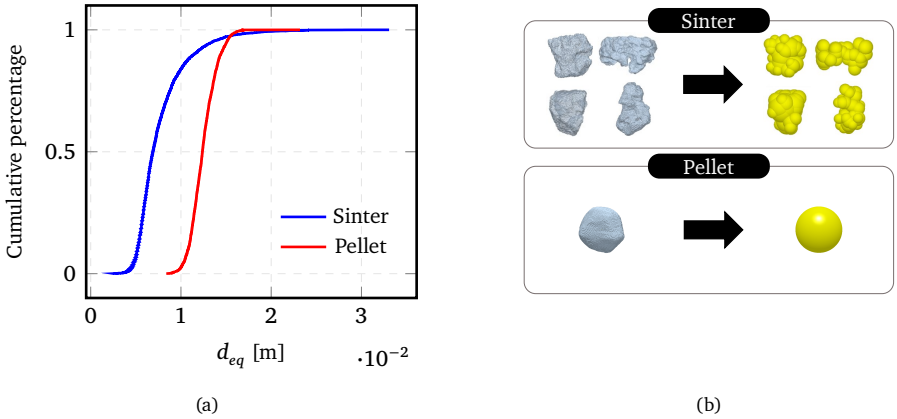


(a) (b)

Figure 6.5: Schematic of the pellet simulation setup: (a) virtual volume used to generate the required quantity of material within the hopper; (b) hopper discharging onto the bench-scale apparatus.

Table 6.2: Hertz-Mindlin model parameters used in this work. Abbreviations: P = pellet, S = sinter, W = wall, N/A = not applicable, t.b.d. = to be determined.

Parameter (symbol)		**Pellet (P)**	**Sinter (S)**	**Steel wall (W)**
Particle size distribution		see Figure 6.6a		N/A
Particle shape		see Figure 6.6b		N/A
Density (ρ) [kg/m^3]		3602	3449	7800 [8]
Poisson's ratio (υ)		0.25 [9]	0.25 [9]	0.30 [8]
Young's modulus (E) [Pa]		2.5×10^8 [9]	2.5×10^8 [9]	5.2×10^{11}
Restitution coefficient (e)	P	t.b.d.	t.b.d.	0.64 [8]
	S	t.b.d.	t.b.d.	0.40 [8]
Static friction coefficient (μ_s)	P	t.b.d.	t.b.d.	t.b.d.
	S	t.b.d.	t.b.d.	t.b.d.
Rolling friction coefficient (μ_r)	P	t.b.d.	t.b.d.	t.b.d.
	S	t.b.d.	t.b.d.	t.b.d.



(a) (b)

Figure 6.6: Morphological features of pellet and sinter particles: (a) Cumulative particle size distributions and (b) particle shapes.

6.3.2 Design of Experiments

In the DEM simulations, μ_s, μ_r, and e values are allowed to vary between 0 and 1, defining the parameter space for calibration. The Box-Behnken Design (BBD) [10] was employed as an efficient and robust method to explore how the KPIs vary across the parameter space. BBD is particularly advantageous as it enables accurate estimation of linear, interaction, and quadratic effects of parameters (factors) while minimizing the number of experimental runs required [11]. In this design, each factor is assigned three coded levels: -1 (low), 0 (medium), and 1 (high). The factors and their corresponding levels in each model are detailed in Table 6.3. For each model, one center point was used per factor, leading to 45 runs for the pellet and sinter models, and 15 runs for the mixture model. The experimental design diagrams (EDDs) are presented in Appendix D.1. Each run in the EDDs was repeated three times.

6.3.3 Extraction of KPIs

At the end of each simulation, all five KPIs are extracted from simulation data in MATLAB.

1. **Hopper discharge time** (t_d, KPI 1)
   The maximum y-position of particles in the flow is recorded every 0.01 s in the simulations. This data allows for straightforward determination of the hopper discharge time by identifying the time step at which the maximum y-position falls below $y = H$ meters after the discharge valve is opened.

2. **Heap mass** (m_h, KPI 2)
   The positions of individual particles at the final time step are analyzed to identify

Table 6.3: Factors and levels used in the Box-Behnken design. Abbreviations: P = pellet, S = sinter, W = wall, μ_s = sliding friction coefficient, μ_r = rolling friction coefficient, e = restitution coefficient.

Model	Factors (coded)	Factor Levels		
		-1 (low)	*0 (mid)*	*1 (high)*
Pellet model	e^{P-P} (X_1)	0.1	0.5	0.9
	μ_r^{P-P} (X_2)	0.0	0.45	0.9
	μ_s^{P-P} (X_3)	0.1	0.5	0.9
	μ_r^{P-W} (X_4)	0.0	0.45	0.9
	μ_s^{P-W} (X_5)	0.1	0.5	0.9
Sinter model	e^{S-S} (X_6)	0.1	0.5	0.9
	μ_r^{S-S} (X_7)	0.0	0.45	0.9
	μ_s^{S-S} (X_8)	0.1	0.5	0.9
	μ_r^{S-W} (X_9)	0.0	0.45	0.9
	μ_s^{S-W} (X_{10})	0.1	0.5	0.9
Mixture model	e^{P-S} (X_{11})	0.1	0.5	0.9
	μ_r^{P-S} (X_{12})	0.0	0.45	0.9
	μ_s^{P-S} (X_{13})	0.1	0.5	0.9

those within the bench-scale container. Knowing the mass of each particle, the total mass on the bench scale is calculated to obtain the heap mass.

3. **2D heap contour**$^{(*)}$ (KPI 3)
   A front-view snapshot of the simulated heap is captured and processed following the same procedure described in Chapter 5 for extracting the experimental heap shape. The key difference is that no windowpane obstructs the view, allowing the full 0.5 m width of the heap to be captured. Consequently, to convert the contour from pixels to physical dimensions, the x- and y-coordinates are scaled by a factor of $0.5/N_p$, where N_p is the number of pixels along the x-direction.

4. **Heap center height** (H_c, KPI 4)
   After converting the heap contour to meter units, the center height H_c is determined. The center height represents the y-coordinate corresponding to $x = 0.25$ m. Since the heap contour is defined by discrete data points, interpolation is used to estimate the precise height at $x = 0.25$ m.

5. **Heap porosity** (ϕ_h, KPI 5)
   The heap volume is determined by exporting the heap geometry as an STL file at the end of the simulation. This STL file, representing particles as triangular surface meshes, is imported into MATLAB. Using the *alphaShape* tool, a bounding volume is constructed from the triangle vertices (as shown in Figure 6.7). The heap's bulk density is then calculated as

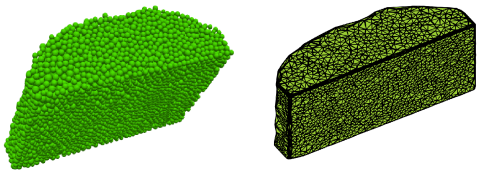


Figure 6.7: Visualization of the STL of a pellet heap (left) and the *alphaShape* created using the STL vertices (right).

$$\rho_h = \frac{m_h}{V_h} \tag{6.1}$$

For simulations with pellet and sinter, the heap porosity is then calculated as

$$\phi_h = 1 - \frac{\rho_h}{\rho_p} \tag{6.2}$$

The simulation results based on the BBD approach are presented in Appendix D.2. The reported response values represent the average of three replications per run.

6.4 Response surface modeling

Response surface modeling is a statistical method used to identify and optimize the relationships between key factors and target responses. In this study, the factors are the interaction parameters μ_s, μ_r, and e, and KPIs 1–5 serve as the calibration targets, which are used as response variables. For the pellet and sinter models, which involve five factors, five response surface models (RSMs) are developed to obtain a set of equations leading to a unique solution. The mixture model, comprising only three factors, requires three RSMs, using KPIs 1–3 as the response variables. Figure 6.8 summarizes the three models to be calibrated, along with their respective factors and responses.

Since responses must be measurable and expressed as numerical values, KPIs 1, 2, 4, and 5 can be directly used as response variables. However, KPI 3 (heap contour) must be transformed into a single numerical value to serve as a response variable. To achieve this, the similarity between the simulated heap contour and the experimental heap contour is quantified as the response variable corresponding to KPI 3. This similarity is calculated using the mean squared error (MSE) between the experimental and simulated heap heights at specific values of x, given by

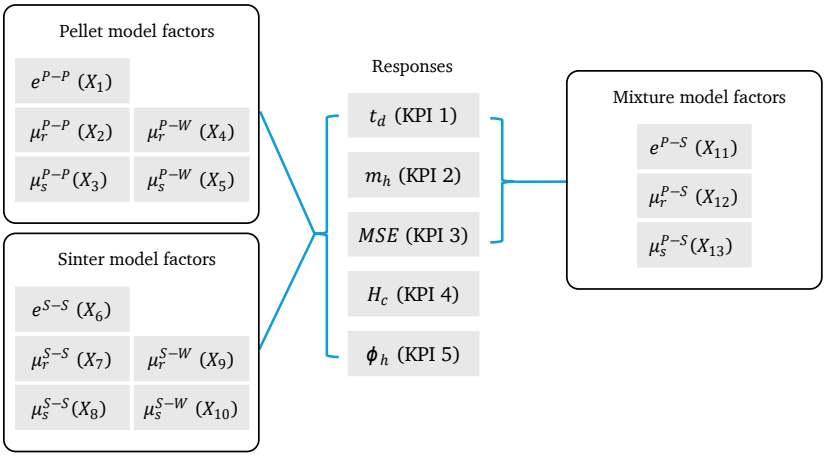


Figure 6.8: Overview of factors $(X_1, \ldots, X_{13})$ and responses (KPIs) for each model.

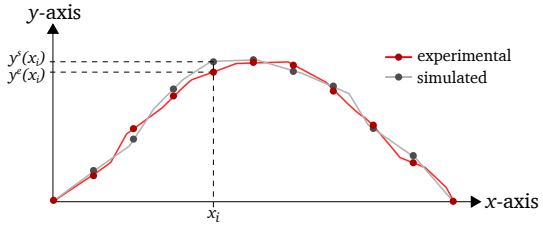


Figure 6.9: Graphical representation of the comparison between simulated and experimental heap contours using $N_{cp} = 11$ contour points.

$$MSE = \frac{1}{N_{cp}} \sum_{i=1}^{N_{cp}} [y^s(x_i) - y^e(x_i)]^2 \tag{6.3}$$

where x_i denotes the horizontal position; $y^s(x_i)$ and $y^e(x_i)$ represent the pile height at position x_i in the simulation and experiment, respectively; and N_{cp} is the total number of heap contour points used for the comparison. Figure 6.9 illustrates this concept with $N_{cp} = 11$, whereas $N_{cp} = 100$ is used in the calculations.

The RSMs are constructed by fitting mathematical equations to the simulation data, thereby establishing relationships between the factors and responses. The fitting process is performed in RSTUDIO. Beginning with a linear model and progressively adding higher-order interactions, the best-fitting regression model for each response variable is identified. The accuracy and reliability of the models are assessed using statistical metrics such as the adjusted R^2 and lack-of-fit (LoF) tests.

Based on the data presented in Tables D3-D5, RSMs are developed for each response variable. The general form of the RSM for pellets, incorporating main effects, interaction effects, and quadratic effects of the factors $(X_1, \dots, X_5)$, is expressed as

$$\begin{aligned} Y^{\alpha} = {} & A + BX_1 + CX_2 + DX_3 + EX_4 + FX_5 \\ & + GX_1X_2 + HX_1X_3 + IX_1X_4 + JX_1X_5 \\ & + KX_2X_3 + LX_2X_4 + MX_2X_5 \\ & + NX_3X_4 + OX_3X_5 \\ & + PX_4X_5 \\ & + QX_1^2 + RX_2^2 + SX_3^2 + TX_4^2 + UX_5^2 \end{aligned} \tag{6.4}$$

where Y represents the response variable. The RSMs for sinter follow the same structure, with the factors $X_1, \dots, X_5$ replaced by $X_6, \dots, X_{10}$, respectively. For the mixture system, which involves three factors (X_{11}, X_{12}, X_{13}), the general form of the RSMs is

$$\begin{aligned} Y^{\alpha} = {} & A + BX_{11} + CX_{12} + DX_{13} \\ & + EX_{11}X_{12} + FX_{11}X_{13} \\ & + GX_{12}X_{13} \\ & + HX_{11}^2 + IX_{12}^2 + JX_{13}^2 \end{aligned} \tag{6.5}$$

The coefficients corresponding to each RSM for pellet, sinter and the mixture are summarized in Table 6.4. As shown in Table 6.5, the models show adequate values of the statistical metrics and therefore capable of describing complex, non-linear relationships between the factors and responses.

Table 6.4: Coefficients for the general response surface model (RSM) equations for pellets, sinter, and the mixture. Equation 6.4 applies to pellets and sinter, where Y represents t_d, m_h, ϕ_h, H_c and MSE. Equation 6.5 applies to the mixture, where Y represents t_d, m_h and MSE.

	Pellet					**Sinter**					**Mixture**		
	t_d	m_h	ϕ_h	H_c	MSE	t_d	m_h	ϕ_h	H_c	MSE	t_d	m_h	MSE
A	4.6381	46.1048	0.4583	0.2008	0.066	4.858	44.364	0.4873	0.221	0.168	4.765	2.732	0.05
B	0	-4.6704	-0.0113	-0.0264	-0.014	0	0	-0.00837	0	-0.002	0	0	0.001
C	0.451	8.795	0.0076	0.0485	0.015	0.263	2.617	0.01197	0.021	0.036	0.18	1.983	0.01
D	0.5658	8.4458	0.0126	0.0518	-0.008	0.708	3.504	0.02938	0.037	-0.023	0.515	4.64	-0.015
E	0.1096	0	0	0	0	0.068	0	0	0	0	0	0	-0.003
F	1.2515	0	0	0	0	1.077	2.147	-0.00417	0.013	0	0	0	-0.002
G	0	-2.9496	-0.0045	-0.021	-0.029	0	0	0	0	-0.005	0.015	0.484	0.017
H	0	-0.2157	-0.0086	-0.0082	-0.024	0	0	-0.00586	0	-0.007	0	0	0
I	0	0	0	0	0	0	0	0	0	0	0	-0.661	-0.001
J	0	0	0	0	0	0	0	-0.0021	0	0	-0.236	-3.934	0.024
K	0	4.8044	0.0037	0.0309	0.022	0	0	0	0	0.044			
L	0	0	0	0	0	0	0	0	0	0			
M	0	0	0	0	0	0	0	0	0	0			
N	0	0	0	0	0	0	0	0	0	0			
O	0	0	0	0	0	0	0	5.21E-05	-0.006	0			
P	0	0	0	0	0	0	0	0	0	0			
Q	0	-3.8128	-0.0041	-0.01969	-0.008	0	0	-0.00239	0	-0.0002			
R	-0.1718	-2.4308	-0.0058	-0.0161	0.017	-0.049	-0.632	-0.00385	-0.005	-0.006			
S	-0.2993	-6.8921	-0.0067	-0.0389	0.015	-0.316	-4.677	0	-0.036	0.025			
T	-0.982	0	0	0	0	-0.007	0	0	0	0			
U	-0.0335	0	0	0	0	-0.275	-0.871	0	-0.005	0			
α	1	1	1	1	0.384	1	1	1	1	0.222	1	1	0.343

Table 6.5: Metrics showing the goodness-of-fit of the developed RSMs.

Material	RSM	LoF p-value[1)]	Adj. R^2
Pellet	t_d	0.47	0.96
	m_h	0.50	0.92
	ϕ_h	0.77	0.90
	H_c	0.40	0.93
	MSE	0.16	0.63
Sinter	t_d	0.68	0.99
	m_h	0.98	0.98
	ϕ_h	0.28	0.99
	H_c	0.26	0.98
	MSE	0.48	0.63
Mixture	t_d	0.54	0.98
	m_h	0.27	0.99
	MSE	0.20	0.88

[1)] Guideline [10]: $p > 0.1$

6.5 Multi-objective optimization

RSMs provide a set of equations that describe how the responses (KPIs) change in relation to the factors (parameter values). For each KPI, the objective is to identify the combination of factors that yields an RSM-predicted value as close as possible to the experimental measurement. As multiple KPIs are involved, the task becomes one of finding the optimal factor combination that satisfies all objectives, which leads to a multi-objective optimization problem. The desirability function approach [12, 13] is widely used for handling such problems, as it converts multiple response objectives into a single composite desirability score. This method assigns a desirability score to each response based on predefined criteria, typically ranging from 0 (undesirable) to 1 (fully desirable). By maximizing the overall desirability function, the optimal factor settings that best satisfy all KPIs can be identified. To identify optimal parameter values, a multi-objective optimization was performed using the desirability function approach. This technique allowed for the simultaneous optimization of multiple responses by assigning weights and combining them into a single desirability score. The parameters that maximized the overall desirability were selected as the optimal calibration parameters for the DEM model.

The steps involved in the desirability function approach are briefly outlined as follows for N factors and M responses. First, a set of sample points (grid) is generated, corresponding to different combinations of the factors $(X_1, \dots, X_N)$. Using the response surface models, the response Y_i^p is then computed for each of these sample points. The relative difference between the predicted response Y_i^p and its experimental counterpart Y_i^e is determined as

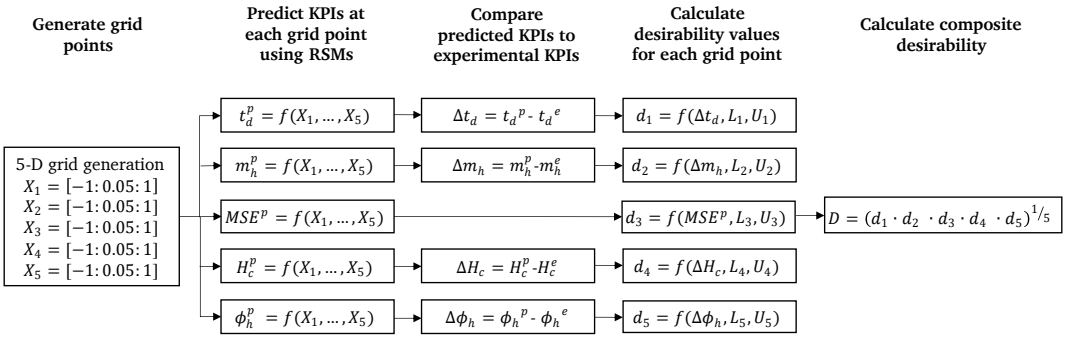


Figure 6.10: Steps involved in calculating the overall desirability from the factors $(X_1, \dots, X_{13})$ and the RSMs.

$$Z_i = \text{abs}\left(Y_i^p - Y_i^e\right)/Y_i^e \tag{6.6}$$

and transform the calculated value into a "desirability" score (d_i) as [13]

$$d_i = \begin{cases} 1, & \text{if } Z_i \leq L, \\ \left(\frac{U-Z_i}{U-L}\right)^s, & \text{if } L < Z_i \leq U, \\ 0, & \text{if } Z_i > U. \end{cases} \tag{6.7}$$

where s is a shape parameter controlling the steepness of the desirability curve and U and L are the upper and lower limits of Z_i, respectively. Note that d_i is an array containing desirability values across all sample points for response i ranging from 0 (undesirable) to 1 (highly desirable). The individual desirability arrays corresponding to each response variable are then aggregated into a single, overall desirability score (D), which is determined by [13]

$$D = \prod_{i=1}^{M} \left(d_i^{w_i}\right)^{1/\sum w_i} \tag{6.8}$$

where w_i is the weight assigned to the i-th response, reflecting its relative importance. Finally, D is maximized to identify the optimal solution across all objectives. In this work, $s = 1$ is used to obtain a linear desirability curve, $w = 1$ to assign equal importance to all responses and use $L = 0.00$ and $U = 0.05$ for each response, indicating that a maximum relative difference of 5% is considered acceptable.

Figure 6.10 illustrates the steps described in applying the desirability function approach. This figure pertains to the calibration of the pellet and sinter models, where five response surface models are used for optimization. The same approach is applied to the

Table 6.6: Calibrated parameter values for pellet, sinter and the pellet–sinter mixture. Abbreviations: p–p = particle–particle, p–w = particle–wall.

Material model	e^{p-p}	μ_r^{p-p}	μ_s^{p-p}	μ_r^{p-w}	μ_s^{p-w}
Pellet	0.1	0.08	0.57	0.15	0.86
Sinter	0.5	0.06	0.49	0.09	0.54
Mixture	0.1	0.28	0.34	N/A	N/A

calibration of the mixture model; however, only three response surface models are utilized, as outlined in Table 6.5.

The multi-objective optimization process was conducted to determine the optimal values of the models' parameters such that there is a maximum deviation of 5% between experimental and RSM-predicted KPI values. The optimal (calibrated) interaction parameter values for all models are summarized in Table 6.6. The overall desirability associated with these solutions for the pellet, sinter and mixture models were 0.51, 0.56 and 0.41, respectively.

6.6 Verification

The parameter values listed in Table 6.6 are applied to the DEM models with a discharge height of $H = 4.665$ m to assess how well the simulated KPIs align with the experimental ones. Table 6.7 presents this comparison, demonstrating that the calibrated parameters enable the models to reproduce the experimental KPIs for pellets, sinter, and the mixture with good accuracy. The relative difference between DEM predictions and experimental values ranges from 0.02% to 5.53%, which is consistent with reported errors in the DEM literature for model calibration using response surface modeling [14–23].

For the heap mass and heap center height, the uncertainties in the simulations are of the same order of magnitude as those observed in the physical experiments. However, the porosity predictions from DEM exhibit much lower uncertainty compared to the laboratory experiments, whereas the opposite trend is seen for discharge time predictions. As discussed in the previous chapter, the high uncertainties in the experimentally measured discharge time for sinter are likely due to the particle shape, particularly the sharp edges of sinter particles that interact with the welds and grooves in the hopper wall. These interactions are not fully captured by our DEM model for two key reasons. First, while the sinter clumps approximate the overall shape of real sinter particles, they do not include sharp edges. Accurately modeling surface roughness would require an impractically high number of small spheres in each clump, which is not feasible with current computational resources. Second, the imperfections in the hopper walls used in the experiments are not completely represented in the DEM geometry, leading to additional particle–wall interactions being omitted. These limitations contribute to the differences observed in

Table 6.7: Comparison of experimental and simulated KPI values after model calibration at H=4.665 m.

KPI (unit)	Material	Exp.	Sim.	Difference
t_d (s)	Pellet	5.24 ± 0.28	4.95 ± 0.02	−5.53%
	Sinter	4.62 ± 1.00	4.65 ± 0.05	+0.65%
	Mixture	4.40 ± 0.31	4.58 ± 0.03	+4.09%
m_h (kg)	Pellet	40.63 ± 0.21	38.63 ± 0.21	−4.92%
	Sinter	42.58 ± 0.63	41.70 ± 0.58	−2.07%
	Mixture	41.96 ± 0.42	41.33 ± 0.41	−1.50%
H_c (cm)	Pellet	16.32 ± 0.41	16.08 ± 0.30	−1.47%
	Sinter	19.88 ± 0.45	19.88 ± 0.50	+0.02%
	Mixture	17.86 ± 0.54	18.48 ± 0.27	+3.47%
ϕ_h (-)	Pellet	0.47 ± 0.01	0.451 ± 0.001	−4.04%
	Sinter	0.47 ± 0.01	0.474 ± 0.004	+0.85%

the discharge time predictions. Nonetheless, the mean sinter discharge time is predicted with high accuracy. The good agreement between the calibrated DEM models and the experimentally observed behavior is further illustrated in Figure 6.11. The plots highlight the overall good match between the simulated and experimentally measured heap contours for pellets, sinter, and the mixture at $H = 4.665$ m. The Concordance Correlation Coefficient (CCC), which quantifies the similarity between the simulated and experimental average heap contours, shows values greater than 0.97 in all cases, indicating a substantial match [24].

To evaluate whether the pellet and sinter models calibrated at high velocity ($\sim$ 9.6 m/s) remain valid at lower flow velocities, the calibrated parameters were tested in simulations at $H = 1$ m and $H = 3$ m, corresponding to estimated velocities of approximately 4.4 m/s and 7.7 m/s, respectively. According to Table 6.8, the relative differences between simulated and experimental KPI values is still in the same order of magnitude as the differences observed at $H = 4.665$ m. Considering the heap shape, Figure 6.12 demonstrates that the simulated and experimental heap contours match well for both pellet and sinter at $H = 1$ m and $H = 3$ m. These results suggest that, for this system and these materials, the calibration outcome is flow invariant.

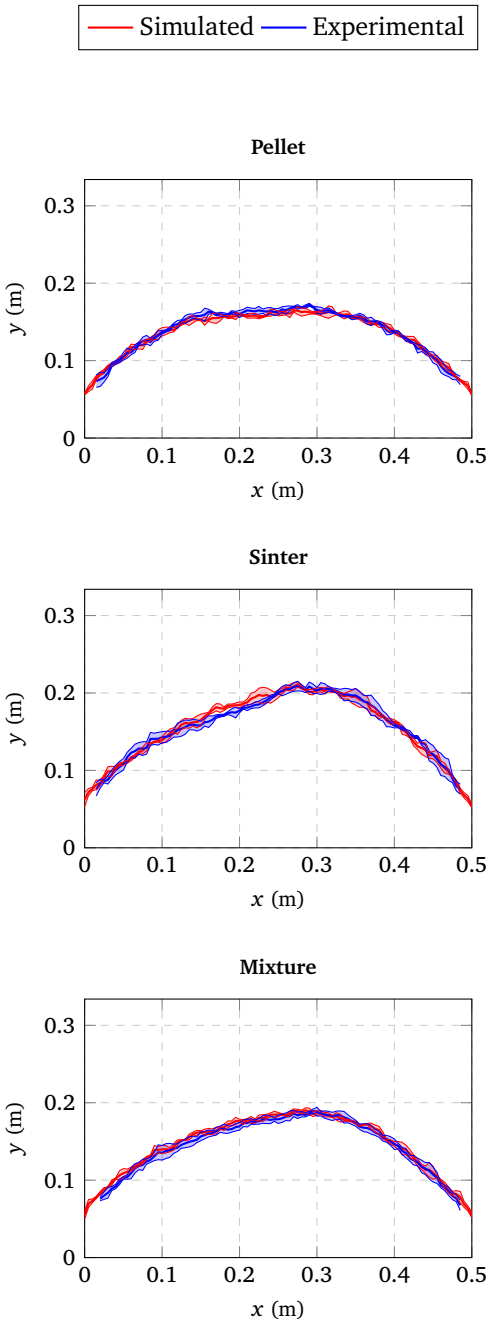


Figure 6.11: Comparison of simulated and experimental heap profiles for different materials at $H = 4.665$ m. Shaded areas represent the standard deviation with $n = 3$ for experiments with pellet and $n = 5$ for experiments with sinter and the mixture.

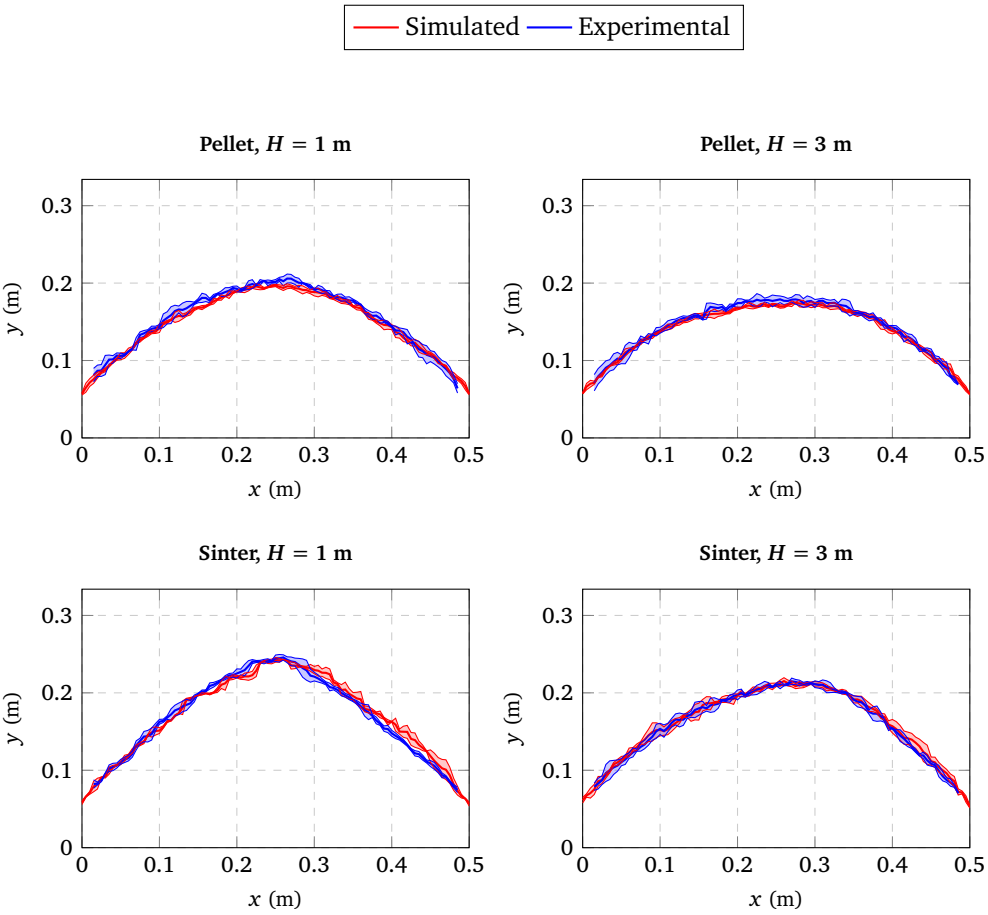


Figure 6.12: Comparison of simulated and experimental heap profiles for different materials at different heights. Shaded areas represent the standard deviation with $n = 3$ for experiments with pellet and $n = 5$ for experiments with sinter and the mixture.

Table 6.8: Comparison of experimental and simulated KPI values for H=1 m and H=3 m after model calibration at H=4.665 m.

KPI (unit)	H	Material	Exp.	Sim.	Difference
m_h (kg)	1 m	Pellet	45.53 ± 0.45	42.92 ± 0.28	−5.73%
		Sinter	45.84 ± 0.45	44.58 ± 0.03	−2.75%
	3 m	Pellet	42.33 ± 0.55	40.10 ± 0.10	−5.27%
		Sinter	43.60 ± 0.25	42.66 ± 0.11	−2.16%
H_c (cm)	1 m	Pellet	20.15 ± 0.31	19.67 ± 0.08	−2.38%
		Sinter	24.26 ± 0.43	24.28 ± 0.27	+0.08%
	3 m	Pellet	17.79 ± 0.58	17.06 ± 0.31	−4.10%
		Sinter	20.88 ± 0.66	21.11 ± 0.24	+1.10%
ϕ_h (-)	1 m	Pellet	0.415±0.020	0.450±0.001	+8.43%
		Sinter	0.483±0.010	0.484±0.001	+0.21%
	3 m	Pellet	0.438±0.023	0.451±0.001	+2.97%
		Sinter	0.466±0.015	0.479±0.002	+2.79%

6.7 Computational cost considerations

The numerical time (Δt) step is a critical parameter that significantly affects the accuracy, stability, and computational time of a DEM simulation. As mentioned in Chapter 3, it is generally recommended to use a value of $\Delta t = [0.2 \dots 0.4] \cdot \Delta t_R$, where Δt_R is the Rayleigh time step. As the value of Δt increases, important interactions, especially collisions and force transmissions, might be poorly captured which can lead to inaccurate simulation results. If Δt is too large, then rapid changes in forces and velocities during collisions can no longer be captured. This results in non-physical behavior such as interpenetrating particles or excessive energy buildup.

In this chapter, the DEM models were calibrated using a conservative time step of $\Delta t = 0.1 \cdot \Delta t_R$. This choice, while smaller than the typical range recommended in the literature, was made to ensure a safe margin for accurately capturing collision dynamics and to avoid any risk of numerical instability. It resulted in simulated KPI values that deviated by no more than 5.5% from experimental measurements. However, such a small time step may lead to unnecessarily long computation times. It is therefore relevant to explore whether Δt can be increased without compromising predictive accuracy. To assess this, simulations of the calibrated *mixture* model were repeated using time steps in the range:

$$\Delta t = [0.1 \quad 0.15 \quad 0.2 \quad 0.25 \quad 0.3 \quad 0.35 \quad 0.4 \quad 0.45 \quad 0.5] \cdot \Delta t_R,$$

with $\Delta t_R = 1.8 \times 10^{-5}$ s. Each case was simulated three times, and KPIs were extracted

using the procedure described in Section 6.3.3. Simulations with $\Delta t = [0.45 \quad 0.5] \cdot \Delta t_R$ were consistently unstable throughout the repeated runs, and simulations with $\Delta t = 0.4 \cdot \Delta t_R$ exhibited occasional instability. These step sizes are therefore too large and results are reported only up to the largest stable time step of $0.35 \cdot \Delta t_R$.

Figures 6.13a–d show the effect of increasing Δt on the predicted KPIs, and Figure 6.13e shows the corresponding decrease in computational time. The predicted KPIs remain stable across the tested time steps, likely due to the conservativeness of the Rayleigh time step, which is dictated by the smallest particle in the clump. These results suggest that the time step can be safely increased to at least $0.3 \cdot \Delta t_R$ without loss of accuracy, enabling significant computational savings. This finding is particularly valuable for larger-scale systems involving many more particles, making it an important step toward feasible industrial scale simulations.

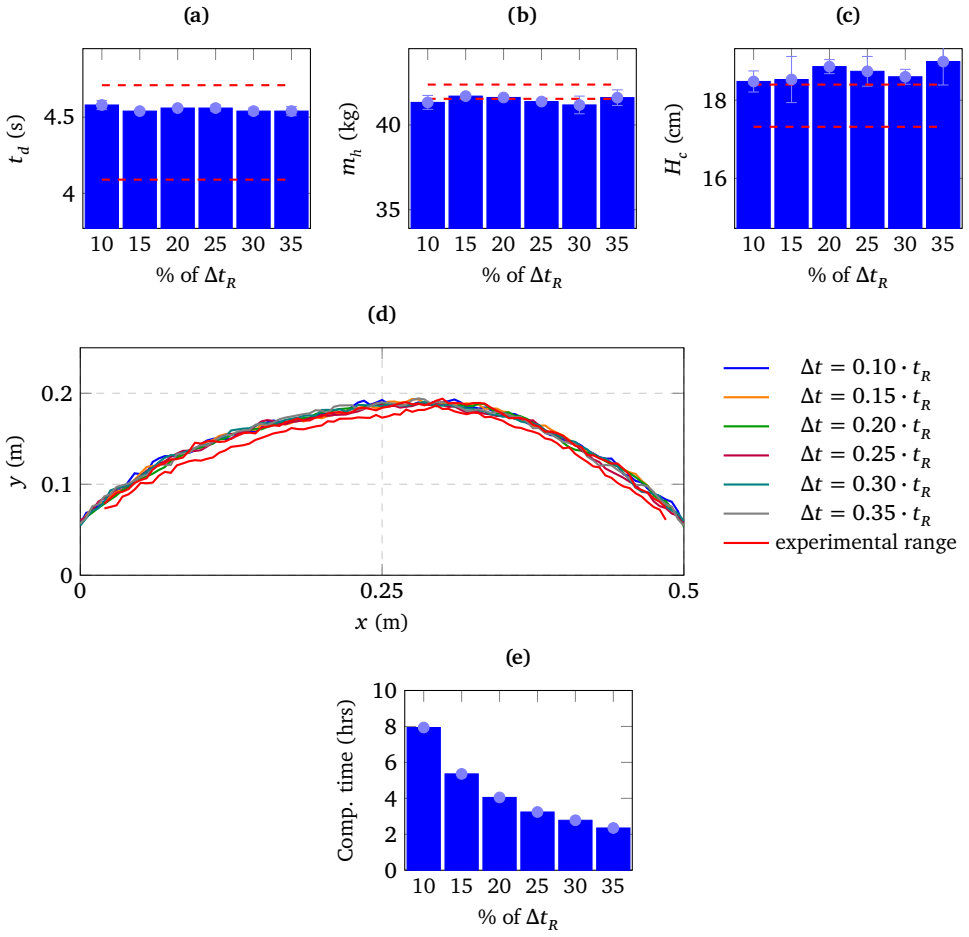


Figure 6.13: Effect of Δt on the predicted KPIs (a-d) and the computational time (e) in the calibration experiment. Error bars indicate the standard deviation based on $n = 3$ repetitions and red dashed lines indicate the upper and lower bounds of the experimentally measured KPI values.

6.8 Conclusions

This chapter developed a *reliable* pellet–sinter mixture model by calibrating model parameters against five key performance indicators (KPIs) under flow conditions representative of blast furnace charging. A step-wise calibration strategy was implemented, initially calibrating the parameters of the individual pellet and sinter models, followed by calibration of the pellet–sinter interaction parameters once the individual models were established. The key conclusions are:

- **The step-wise calibration strategy proved effective.** The calibrated model accurately reproduced the average experimental KPI values at a discharge height of 4.665 m, with a maximum deviation of only 5.5%. This confirms that parameters calibrated for individual materials can be successfully combined in a mixture model, followed by targeted calibration of the inter-component interaction parameters.

- **The model performs well across a range of flow velocities.** Predictions at lower discharge heights also showed good agreement with experimental results, indicating the model's applicability beyond stock surface charging. It can potentially be extended to simulate behavior in upstream charging system segments, such as the stock house, where lower fall heights and velocities occur.

- **Discharge time variability in sinter requires further investigation.** While the sinter model reliably captured average KPI values, it did not replicate the observed variability in sinter discharge times. This highlights the need for future studies to explore the influence of particle shape and other factors on discharge behavior.

- **Larger time steps can reduce computation time without loss of accuracy.** Increasing the DEM simulation time step from 10% to 30% of t_R significantly improved computational efficiency while maintaining predictive accuracy.

Having successfully developed a *reliable* pellet–sinter mixture model at laboratory scale, the next step is to apply the model to an industrial scale blast furnace. Ensuring the model's *feasibility* at this larger scale is the focus of the following chapter.

6.9 Bibliography

[1] R. Roeplal, Y. Pang, A. Adema, J. van der Stel, and D. Schott. "Modelling of phenomena affecting blast furnace burden permeability using the Discrete Element Method (DEM) – A review". In: *Powder Technology* 415 (2023), p. 118161. ISSN: 0032-5910. DOI: 10.1016/j.powtec.2022.118161.

[2] C. Li, T. Honeyands, D. O'Dea, and R. Moreno-Atanasio. "The angle of repose and size segregation of iron ore granules: DEM analysis and experimental investigation". In: *Powder Technology* 320 (2017), pp. 257–272. ISSN: 0032-5910. DOI: 10.1016/j.powtec.2017.07.045.

[3] P. Qiu and T. Pabst. "Waste rock segregation during disposal: Calibration and upscaling of discrete element simulations". In: *Powder Technology* 412 (2022), p. 117981. ISSN: 0032-5910. DOI: 10.1016/j.powtec.2022.117981.

[4] Z. Yan, S. K. Wilkinson, E. H. Stitt, and M. Marigo. "Investigating mixing and segregation using discrete element modelling (DEM) in the Freeman FT4 rheometer". In: *International Journal of Pharmaceutics* 513 (2016), pp. 38–48. ISSN: 0378-5173. DOI: 10.1016/j.ijpharm.2016.08.065.

[5] E. Izard, M. Moreau, and P. Ravier. "Discrete element method simulation of segregation pattern in a sinter cooler charging chute system". In: *Particuology* 59 (2021). Towards Modelling Solids and Multiphase Flow for Large Scale Industrial Systems and Applications, pp. 34–42. ISSN: 1674-2001. DOI: 10.1016/j.partic.2020.08.004.

[6] M. Alizadeh, A. Hassanpour, M. Pasha, M. Ghadiri, and A. Bayly. "The effect of particle shape on predicted segregation in binary powder mixtures". In: *Powder Technology* 319 (2017), pp. 313–322. ISSN: 0032-5910. DOI: 10.1016/j.powtec.2017.06.059.

[7] Delft High Performance Computing Centre (DHPC). *DelftBlue Supercomputer (Phase 2)*. https://www.tudelft.nl/dhpc/ark:/44463/DelftBluePhase2. 2024.

[8] H. Wei, Y. Ge, M. Li, Y. Li, H. Saxén, Z. He, and Y. Yu. "DEM study of the porosity distribution of pellet sandpile formed by ternary size particles". In: *Powder Technology* 360 (2020), pp. 1337–1347. DOI: 10.1016/j.powtec.2019.11.017.

[9] A. Chakrabarty, R. Biswas, S. Basu, and S. Nag. "Characterisation of binary mixtures of pellets and sinter for DEM simulations". In: *Advanced Powder Technology* 33 (2022), p. 103358. ISSN: 0921-8831. DOI: 10.1016/j.apt.2021.11.010.

[10] D. C. Montgomery. *Design and Analysis of Experiments*. 8th. John Wiley {&} Sons, 2013.

[11] D. R. Jensen. “Efficiencies of some small second-order designs”. In: *Statistics {&} Probability Letters* 21 (1994), pp. 255–261. ISSN: 0167-7152. DOI: 10.1016/0167-7152(94)90135-X.

[12] G. Derringer and R. Suich. “Simultaneous Optimization of Several Response Variables”. In: *Journal of Quality Technology* 12 (Oct. 1980), pp. 214–219. ISSN: 0022-4065. DOI: 10.1080/00224065.1980.11980968.

[13] L. V. Candioti, M. M. De Zan, M. S. Cámara, and H. C. Goicoechea. “Experimental design and multiple response optimization. Using the desirability function in analytical methods development”. In: *Talanta* 124 (2014), pp. 123–138. ISSN: 0039-9140. DOI: 10.1016/j.talanta.2014.01.034.

[14] G. Mu, X. Qi, W. Zhang, Z. Lv, T. Zhang, and S. Wang. “Parameter Measurement and Calibration in Discrete Element Simulation of Broken Sweet Potato Seedlings”. In: *American Journal of Biochemistry and Biotechnology* 17 (June 2021), pp. 256–266. DOI: 10.3844/ajbbsp.2021.256.266.

[15] C. Hernández-Vielma, D. Estay, and M. Cruchaga. “Response surface methodology calibration for DEM study of the impact of a spherical bit on a rock”. In: *Simulation Modelling Practice and Theory* 116 (2022), p. 102466. ISSN: 1569-190X. DOI: 10.1016/j.simpat.2021.102466.

[16] W. Jiang, J. Tang, Y. Yin, H. Zhang, T. Jia, J. Qin, H. Wang, and Q. Wei. “Calibration and Experimental Validation of Contact Parameters in a Discrete Element Model for Tobacco Strips”. In: *Processes* 10 (2022). ISSN: 2227-9717. DOI: 10.3390/pr10050998.

[17] G. Shi, J. Li, L. Ding, Z. Zhang, H. Ding, N. Li, and Z. Kan. “Calibration and Tests for the Discrete Element Simulation Parameters of Fallen Jujube Fruit”. In: *Agriculture* 12 (2022). ISSN: 2077-0472. DOI: 10.3390/agriculture12010038.

[18] Y. Yu, S. Ren, J. Li, J. Chang, S. Yu, C. Sun, and T. Chen. “Calibration and Testing of Discrete Element Modeling Parameters for Fresh Goji Berries”. In: *Applied Sciences* 12 (2022). ISSN: 2076-3417. DOI: 10.3390/app122211629.

[19] J. Zhu, M. Zou, Y. Liu, K. Gao, B. Su, and Y. Qi. “Measurement and calibration of DEM parameters of lunar soil simulant”. In: *Acta Astronautica* 191 (2022), pp. 169–177. ISSN: 0094-5765. DOI: 10.1016/j.actaastro.2021.11.009.

[20] X. Wang, W. Wu, and H. Jia. “Calibration of discrete element parameters for simulating wheat crushing”. In: *Food Science {&} Nutrition* 11 (2023), pp. 7751–7764. DOI: 10.1002/fsn3.3693.

[21] B. Xie, J. Bai, J. Yan, S. Zhao, N. Liu, and Q. Zhang. “Calibration of White Rice Simulation Parameters Based on the Discrete Element Method”. In: *INMATEH Agricultural Engineering* 71 (2023), pp. 215–224. DOI: 10.35633/inmateh-71-18.

[22] F. Yuan, H. Yu, L. Wang, Y. Shi, X. Wang, and H. Liu. “Parameter Calibration and Systematic Test of a Discrete Element Model (DEM) for Compound Fertilizer Particles in a Mechanized Variable-Rate Application”. In: *Agronomy* 13 (2023). ISSN: 2073-4395. DOI: 10.3390/agronomy13030706.

[23] Y. Wang, R. He, F. Zhang, R. Yangdao, and P. Li. “Calibration of contact parameters of fresh-eating jujube based on discrete element method: Yuancui jujube in brittle ripe stage”. In: *International Journal of Food Properties* 27 (2024), pp. 1–18. DOI: 10.1080/10942912.2024.2379874.

[24] G. B. McBride. *A proposal for strength-of-agreement criteria for Lin’s Concordance Correlation Coefficient*. NIWA Client Report: HAM2005-062. Accessed May 26, 2025. 2005. URL: https://www.medcalc.org/download/pdf/McBride2005.pdf.

7

Particle Up-Scaling in Industrial Blast Furnace DEM Modeling

The previous chapter demonstrated that DEM can effectively predict the behavior of a pellet–sinter mixture, a computationally intensive system due to the irregular shapes of sinter particles and their broad size distribution, including many fines. Applying this model to industrial blast furnaces, which process several tonnes of ore per layer and billions of particles, presents a significant computational challenge. A common approach to address this is particle up-scaling, where groups of real particles are represented by larger, equivalent "coarse" particles. This reduces the number of simulated particles and allows for larger time steps, making industrial scale simulations computationally feasible. However, the resulting loss in flow resolution may affect the accuracy of particle dynamics. This chapter investigates how up-scaling influences DEM accuracy for blast furnace charging, with the aim of identifying a suitable scaling level for feasible large-scale modeling of the pellet–sinter mixture.

This chapter is based on:
R. Roeplal, A. Hadi, Yusong Pang, Allert Adema, Jan van der Stel, and Dingena Schott. *Improving the burden distribution in blast furnace operations using DEM: industrial scale simulations from stock house to blast furnace* (to be submitted).

7.1 Introduction

Originally developed for modeling flows of mono-sized spherical particles, DEM has since evolved into a sophisticated and widely recognized computational technique for simulating complex granular flows. Advancements such as particle size distributions and clumped-sphere models have greatly improved the realism and accuracy of DEM simulations, enabling their application to practical, real-world processes. Nonetheless, applying DEM at industrial scale remains challenging due to its high computational demands.

When considering a large-scale simulation, assessing memory usage relative to available resources is a critical first step. Memory demands are primarily driven by the number of particles and the data associated with each one, including position, velocity, force, and contact history. As interactions occur, contact data must be stored and updated at each time step –particularly for frictional or cohesive materials that require history-dependent models. Contact detection, often based on neighbor lists or spatial grids, further increases memory usage. These requirements scale with particle count, as more data must be managed throughout the simulation. In addition to particles, walls and boundaries contribute significantly to memory consumption. Tracking interactions with complex wall geometries (often composed of many discrete elements) and integrating them into neighbor searches add further load. While particle data dominates memory use, large and complex wall geometries–frequently encountered in industrial systems–can impose substantial computational demands.

In the previous chapter, a model representing 160 kg of pellet–sinter mixture (approximately 71,800 particles) was successfully simulated using the DelftBlue high-performance computing cluster [1], equipped with GPUs offering up to 32 GB of memory. However, industrial blast furnace operations involve approximately 144 tonnes of material per ore layer –about 900 times the mass previously modeled. Realistic furnace models further amplify memory demands due to complex geometries, such as curved bunkers and chutes. ALTAIR® EDEM™ estimates memory usage at 1–2 kB per particle [2], implying that a 32 GB GPU can accommodate roughly 16 to 32 million particles. Direct estimation from the previous model yields approximately 64.6 million particles ($900 \times 71{,}800$), exceeding this limit by far. Moreover, this estimate is likely conservative, as memory requirements are expected to increase further when accounting for non-spherical particles and wide size distributions, such as in the case of sinter particles, which may consist of up to 45 clumped spheres each. These factors clearly demonstrate that simulating even a single industrial scale ore layer, based on the calibrated model from the previous chapter, remains infeasible with current state-of-the-art hardware.

To address this, particle up-scaling (also referred to as “coarse-graining”) [3] is a commonly used technique, where particles in the simulation are replaced with larger, up-scaled equivalents. This method involves scaling the entire particle size distribution by

a fixed factor, which not only decreases the number of particles per unit volume but also permits the use of larger numerical time steps, thereby enhancing computational efficiency. When employing particle up-scaling in DEM simulations, it is essential to ensure that the dynamic behavior of the up-scaled particles remains representative of the original material. The application of appropriate scaling laws is critical in this context, as contact parameters –such as stiffness, friction, and cohesion– must often be adjusted in relation to particle size to preserve realistic bulk flow behavior. These scaling relationships are inherently dependent on the chosen contact model [4, 5]. Notably, theoretical analyses have shown that the Hertz-Mindlin contact model exhibits scale invariance under the condition that energy density is conserved [6]. Under such circumstances, key energetic quantities –namely potential energy, kinetic energy, energy dissipation, and rotational energy– remain unaffected by particle up-scaling, thereby eliminating the need for parameter scaling.

Given that the model developed in the previous chapter employs the Hertz-Mindlin contact model, the flow behavior is expected to exhibit scale invariance. However, it remains essential to systematically evaluate the validity of particle scaling, as particle–geometry interactions may inherently depend on particle size. The primary concern arises from material-wall interactions occurring during bunker discharge and while flowing over the chute. Literature indicates that increasing the particle size alters bunker discharge behavior due to arching phenomena at the outlet [7]. Regarding the chute, it is important to note that the surface is not smooth, but rather lined with plates of finite thickness. As the material flows over the chute, particles interact with this surface, and it is unclear to what extent increasing the particle size relative to the lining dimensions affects the flow behavior. Consequently, particle up-scaling cannot simply be applied by an arbitrary factor, as has often been done in previous blast furnace modeling studies (see Chapter 3). Instead, a systematic investigation is necessary to assess the validity and limitations of scaling under these conditions.

Hence, the objective of this chapter is to investigate the extent to which particle up-scaling can be applied to the calibrated pellet–sinter mixture model to make industrial scale simulations of an iron ore layer charging feasible. The analysis systematically compares the behavior of the scaled DEM model to that of the unscaled system to evaluate the applicability of this approach without compromising the accuracy of key flow and packing performance indicators. Flow-related indicators include velocity components, mass flow rates, and component segregation as the mixture moves through the charging apparatus. For packing, the assessment is based on the static ore layer after charging, considering the layer profile, component segregation, and porosity distribution.

The contents of this chapter are as follows. Section 7.2 describes the simulation setup for the industrial scale blast furnace, outlining the approaches for modeling the charging process and recording data. The concept of the scaling factor is introduced, alongside

a detailed explanation of how pellet and sinter particles are scaled accordingly. Given that simulating the full-scale ore layer charging with the original, unscaled model is computationally infeasible, a step-wise approach is adopted to investigate the effects of scaling. In Section 7.3, the analysis is limited to the short-term flow behavior on and immediately after the chute. Here, material is generated using dynamic factories in a controlled, reduced volume, allowing simulations with the unscaled model to serve as the "ground truth." The study then examines how the flow behavior deviates from this baseline as the scaling factor is varied. Section 7.4 extends the investigation to full-scale charging starting from the bunkers, replicating realistic conditions. Due to computational demands, these simulations are carried out only for higher scaling factors.

7.2 Ore layer charging: simulation and analysis procedures

7.2.1 Description of layer charging and system representation

The charging system investigated in this work is based on Blast Furnace No. 7 (BF7) at TATA Steel IJmuiden in the Netherlands. An industrial scale furnace is considered, and the associated charging system and furnace throat (the topmost part of the cylindrical furnace) geometry used in the simulation are illustrated in Figure 7.1. The system comprises two top bunkers (each equipped with a rotating discharge valve) arranged in a mirrored configuration, a Y-tube that guides material downward, and a rotating chute that distributes the burden across the furnace throat.

In industrial operation, an ore layer is formed by sequentially discharging two material batches, one from each bunker. Each batch consists of 37.2 tonnes of pellets and 35.2 tonnes of sinter, resulting in 72.4 tonnes of material being discharged from the bunker over a 60-second interval. During this period, the rotating chute operates at a constant angular velocity of 48°/s, completing one full revolution every 7.5 s. After each revolution, the chute inclination is reduced according to a predefined charging program, leading to the deposition of a new concentric ring of material. In total, each batch results in the formation of eight concentric rings. The chute inclination gradually decreases from 47.5° to 11° throughout this process.

7.2.2 Analysis across different scaling factors

To evaluate the effect of particle scaling on the simulation of ore layer charging, a scaling factor s is introduced, with values ranging from 1 to 5, as defined in Section 7.2.4. This range is motivated by previous studies (see Chapter 3), where up-scaling by a factor of up to 4 is common practice. Here, an additional level ($s = 5$) is included to extend the analysis.

As previously noted, simulating the charging of a full ore layer comprising two batches

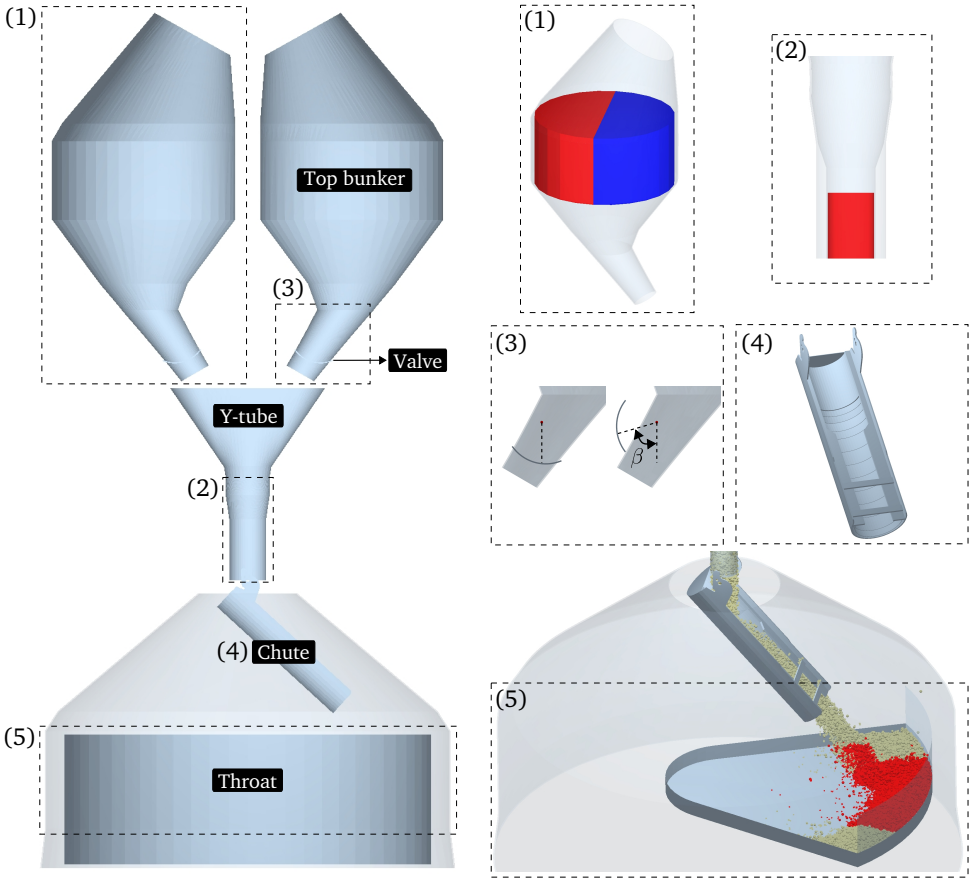


Figure 7.1: Simulation setup and key components. *Left:* overview of the simulation geometry, including the top bunkers with valves (mirrored configurations), the Y-tube, the rotating chute, and the throat. *Right:* zoomed-in views of specific elements – (1) side-by-side semi-cylindrical virtual volumes used for particle generation in the top bunkers; (2) cylindrical virtual volume used for particle generation at the chute inlet; (3) valve opening motion defined by the opening angle β; (4) rotating chute lined with plates; and (5) container in the throat used for collecting particles, with red-colored particles indicating the subset selected for analysis.

involves very high computational cost. To limit this from the outset, the analysis was restricted to a single batch of material (72.4 tonnes discharged from one top bunker). To assess the computational feasibility of simulating single full batch discharged from the bunker (72.4 tonnes), a series of test simulations was conducted using the original, unscaled particle size distribution ($s = 1$). These tests demonstrated that even one quarter of the full-batch mass in the bunker exceeded available GPU capacity. Simulations at $s = 2$ were likewise found to be computationally unfeasible for an ore batch. Based on these results, it was concluded that simulations at $s = 1$ and $s = 2$ are not viable for the full, 8-ring charging analysis when started from the bunkers.

As discussed in the introduction, material–wall interactions in both the bunker and chute regions are expected to play a critical role in how particle scaling affects flow behavior. In particular, particle up-scaling may influence flow due to arching effects during bunker discharge and due to interactions with the non-smooth, lined surface of the chute. To address these concerns, the charging process is examined through two targeted analyses, each focusing on a specific region of the system.

Due to computational constraints, scaling factors $s = 1$ and $s = 2$ can only be applied to small portions of the system over short time periods, where the number of particles remains within feasible limits. Full-scale simulations, including complete batch charging to the throat, are only performed for $s = 3$, $s = 4$, and $s = 5$. While no single simulation captures the entire process across all scales, combining the results provides a systematic evaluation of how particle up-scaling affects key aspects of the charging process. Sections 7.3 and 7.4 synthesize the findings from the two analyses described below.

Note on geometry: Figure 7.1 illustrates the overall geometry used in both analyses, including the partial cylindrical container, the dynamic factory volumes, and the discharge valve rotation mechanism. This figure is referenced throughout this section where relevant.

- **Analysis Part 1: Chute flow and layer formation**
  This analysis focuses on material–wall interactions along the chute, particularly during the formation of the first ring when the chute inclination is steepest and scaling sensitivity is expected to be highest. To enable consistent comparison across all scaling factors, the simulation is run up to $t = 7.5$ s for all cases $s = 1$ to $s = 5$. The mixture is generated using a dynamic particle generation approach, with two overlapping factories assigned to a cylindrical virtual volume (see Figure 7.1). Particles are initialized with a vertical velocity of $v_y = -6$ m/s, approximating the average discharge speed from the bunker. Mass flow rates of 620 kg/s for pellet and 586 kg/s for sinter are applied, matching the theoretical conditions for a 60-second release. For scaling factors $s = 2$ to $s = 5$, the simulation continues beyond 7.5 s until the full layer is formed at $t = 65$ s, covering the deposition of all eight rings. The simulation at $s = 1$ is not extended beyond 7.5 s due to GPU

memory limitations, which make full-layer simulation computationally unfeasible at this resolution.

- **Analysis Part 2: Bunker discharge and layer formation**
  This analysis focuses on material–wall interactions during bunker discharge, where particle scaling may influence flow behavior due to arching effects near the outlet. Full-batch simulations at $s = 1$ and $s = 2$ exceed available memory and are therefore not feasible. As a result, this analysis is conducted at scaling factors $s = 3$, $s = 4$, and $s = 5$, where full-batch charging can be simulated and its impact on layer formation assessed. The bunker is filled using two side-by-side dynamic factories, implemented via semi-cylindrical virtual volumes. Each volume generates one type of material, creating a segregated initial configuration with pellets and sinter arranged side by side. Discharge is initiated by rotating the valve about a fixed point, reaching the desired opening angle β within 0.1 s through angular velocity control.

As illustrated in Figure 7.1, a partial cylindrical container is employed instead of a full 360° geometry. Only particles that land within this domain are retained, while those outside are removed from the simulation. The container is designed to include a 45° "pie slice" analysis domain (see Section 7.2.3). A direct 45° slice-shaped container was avoided to eliminate wall effects that could alter natural layering behavior. Instead, an offset partial cylinder is used, preserving realistic flow around the region of interest. This configuration significantly reduces computational cost: while 72.4 tonnes are initially generated, approximately 23.8 tonnes are retained by the end of each simulation. The approach enables extraction of a representative sample of the ore layer without the computational burden associated with simulating the full 360° geometry.

7.2.3 Analysis domains and recorded data

To monitor and evaluate the system's behavior throughout the simulation, several analysis domains are defined, each designed to track specific data within distinct regions of the geometry. These domains, illustrated in Figure 7.2, provide localized information on particle dynamics, mass distribution, and flow behavior over time:

- Bunker tracker: A rectangular volume that encompasses the entire bunker. Its lower boundary is precisely aligned with the bottom of the bunker, allowing for accurate tracking of the material remaining in the bunker during discharge. The total mass of pellets and sinter within this region is recorded at a time resolution of 0.1 s.

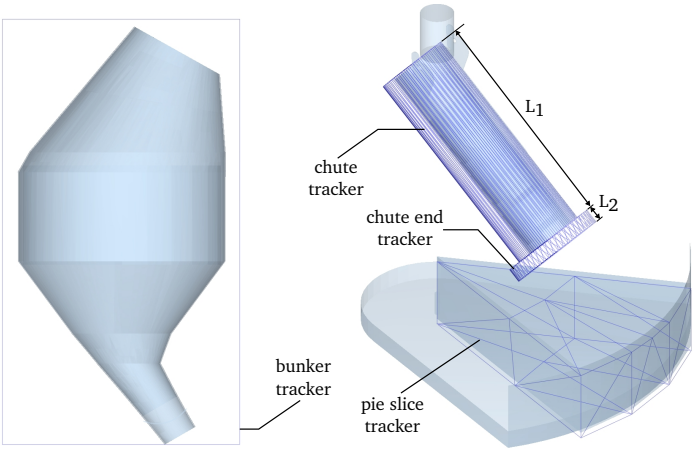


Figure 7.2: Tracker domains used in the simulations for recording local data.

- Chute tracker: A cylindrical volume that encloses the full length of the rotating chute ($L_1 = 4.5$ m). This tracker moves with the chute as it rotates, capturing the positions and velocities of all particles within its bounds. Data from this region are recorded every 7.5 s, corresponding to one full circumferential rotation of the chute.
- Chute-end tracker: Defined to capture the state of the flow immediately after it exits the chute. This region has the same geometry as the chute tracker but with a shorter length of $L_2 = 0.3$ m, positioned directly downstream of the chute outlet.
- Pie slice tracker: Defined at the bottom of the system to analyze the deposited ore layer. This domain represents a 45° sector of the container and is used to record the final positions and masses of all retained particles at the end of each simulation. This region serves as the primary focus for analyzing the layered structure of the charged material.

7.2.4 DEM model parameters

The model parameters –such as particle shapes, size distributions, material properties, and particle–particle and particle–wall interaction parameters– are calibrated values adopted from the previous chapter (see Tables 6.2 and 6.6). When applying particle up-scaling, only the particle size is modified; all other parameters remain unchanged. The particle size is scaled by a factor s, which is varied in this chapter as

$$s = [1 \quad 2 \quad 3 \quad 4 \quad 5]$$

As described in the previous chapter, particle size is defined through particle volume distributions. For pellet particles, which are modeled as spheres, the particle radius is directly scaled by the factor s. Sinter particles, being non-spherical, require a different approach for scaling. It is assumed that the mass ratio of a pellet to a sinter particle remains constant between the original system ("orig") and the up-scaled system ("scaled"). Given that the particle densities remain unchanged, this assumption can be expressed as

$$\left(\frac{V_S}{V_P}\right)_{\text{orig}} = \left(\frac{V_S}{V_P}\right)_{\text{scaled}} \tag{7.1}$$

This relationship can be rearranged to

$$V_{S,\text{scaled}} = V_{S,\text{orig}} \left(\frac{V_{P,\text{scaled}}}{V_{P,\text{orig}}}\right) \tag{7.2}$$

By applying the scaling factor to the pellet radius ($R_{P,\text{scaled}} = sR_{P,\text{orig}}$), the equation becomes

$$V_{S,\text{scaled}} = s^3 \cdot V_{S,\text{orig}} \tag{7.3}$$

Accordingly, the volumes of non-spherical particles are scaled by multiplying the original volume distributions by s^3.

The numerical time step Δt is a model parameter that depends on particle size. In the previous chapter, its value was set to 10% of the Rayleigh time step based on the original particle size distributions, resulting in $\Delta t = 1.8 \times 10^{-6}$ s. Section 6.7 showed that this value can be safely increased by a factor of three without affecting the model's predictive accuracy, while considerably improving computational efficiency. Therefore, the time step for the original system is taken as $\Delta t_{\text{orig}} = 5.4 \times 10^{-6}$ s in this chapter. Since the time step scales linearly with particle size, as given by Eq. 3.16, it increases with the scaling factor s according to

$$\Delta t_{\text{scaled}} = s \cdot \Delta t_{\text{orig}} \tag{7.4}$$

7.3 Effect of scaling on chute flow and resulting burden packing behavior

This section investigates how chute flow varies with different scaling factors and examines the resulting impact on the burden layer in the throat. The chute flow is analyzed in terms

of its velocity components and the deposited burden layer is evaluated based on the layer profile in the throat. The mixture is generated at the chute inlet over a 60-second period, resulting in the accumulation of approximately 23.8 tonnes of material in the container, as described in Section 7.2.1.

The analysis is structured in three parts:

- **Analysis of flow along the chute**: chute flow behavior is examined using data from the chute tracker at $t = 7.5$ s, when the chute completes a full circumferential rotation at its maximum angle of 47.5°. This time step is selected because the flow is considered fully developed; subsequent steps involve a decrease in angle and the charging of a new ring, which disturbs the flow.
- **Analysis of flow at the chute outlet:** material discharge from the chute is analyzed at the same time ($t = 7.5$ s) using data from the chute-end tracker.
- **Analysis of the deposited burden layer**: the layer in the throat is evaluated at $t = 65$ s, after all 8 rings have been deposited, using the pie slice tracker. This analysis is performed for scaling factors $s = [2,\ 3,\ 4,\ 5]$, as the GPU cannot process the full 23.8 tonnes of material at $s = 1$.

7.3.1 Analysis of flow along the chute

Translational velocities along the chute are examined to assess the influence of scaling. Figure 7.3 presents simulation snapshots at $t = 7.5$ s. The snapshots include both top and bottom views of the flow. From the bottom view, the patterned structure of the chute lining is clearly reflected in the velocity distribution. This pattern becomes less distinct as the scaling factor s increases, suggesting that the particles do not adhere to the surface profile at larger scales. Nevertheless, the particle velocities appear to be within the same order of magnitude across all scaling cases.

To enable a more in-depth flow analysis, velocity components are examined in a chute-aligned coordinate system. Particle positions and velocities extracted from EDEM are recorded in the global coordinate system. However, since the chute is inclined and rotates circumferentially, directly analyzing the data in this frame may obscure the stream-wise flow characteristics. Therefore, two coordinate transformations are applied to interpret the motion in a more meaningful way:

1. The first transformation involves moving to a *co-rotating reference frame* to eliminate the rigid-body rotation of the chute. This expresses particle velocities relative to the rotating body while retaining the global orientation:

$$\vec{v}_{\text{corot}} = \vec{v}_{\text{global}} - \vec{\omega} \times \vec{r}_{\text{global}} \tag{7.5}$$

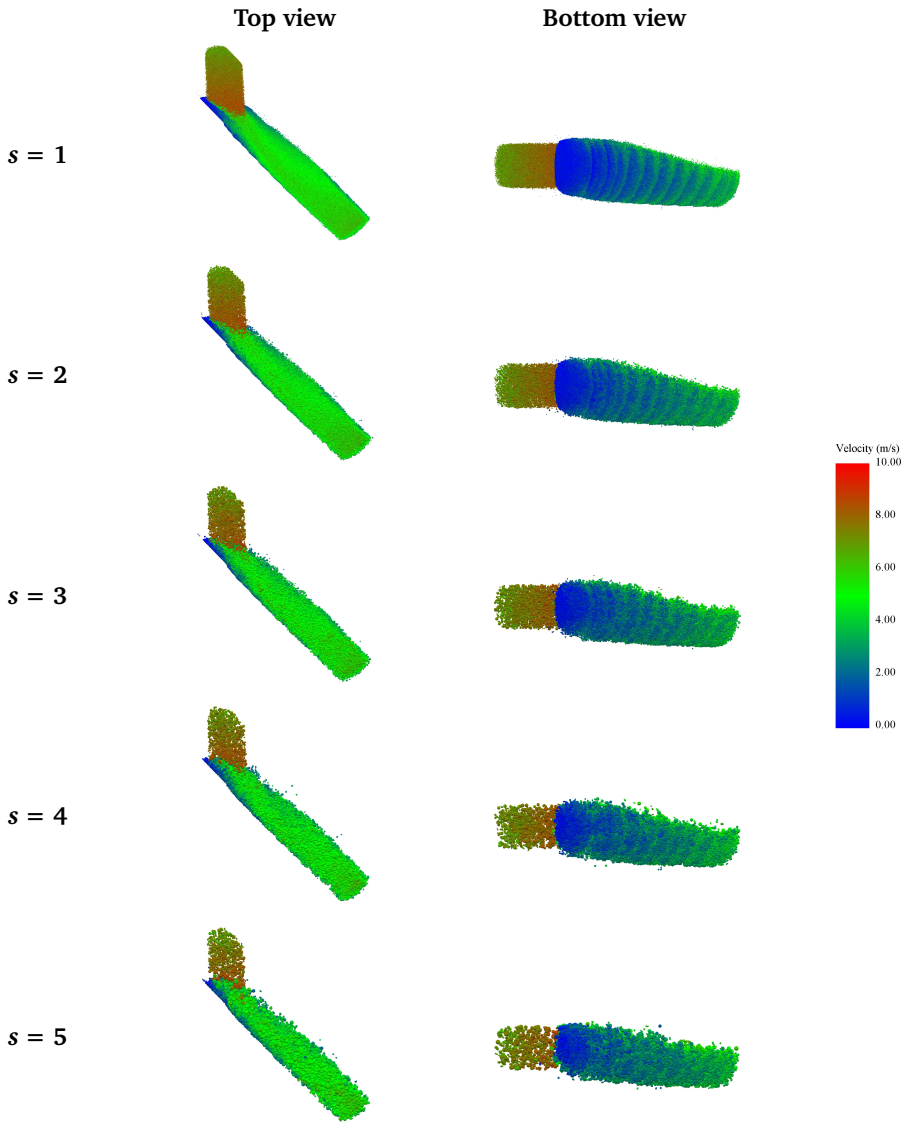


Figure 7.3: Snapshots of the material flow over the chute for different scaling factors s.

where $\vec{v}_{\text{global}}$ is the particle velocity in the inertial (global) frame, $\vec{\omega}$ is the angular velocity vector of the chute, and $\vec{r}_{\text{global}}$ is the particle position vector relative to the rotation axis.

2. Next, a geometric transformation rotates both the particle positions and velocities into a *chute-aligned coordinate system*, in which the stream-wise direction aligns with the local x-axis and the cross-sectional dimensions align with the local y- and z-axes. This reoriented frame provides a clearer interpretation of the flow dynamics. At $t = 7.5$ s, the chute is oriented such that its stream-wise direction aligns with the global x-axis, and the global z-axis intersects the chute symmetrically across its width. The transformation is carried out in two steps. First, a rotation about the global z-axis removes the chute's inclination:

$$\mathrm{R}_{\text{incline}} = \begin{bmatrix} \cos(\phi) & -\sin(\phi) & 0 \\ \sin(\phi) & \cos(\phi) & 0 \\ 0 & 0 & 1 \end{bmatrix} \tag{7.6}$$

where ϕ is the chute's inclination angle (47.5°).

These transformations are applied sequentially to both particle positions and velocities:

$$\vec{r}_{\text{local}} = \mathrm{R}_{\text{incline}} \cdot \vec{r}_{\text{global}}, \quad \vec{v}_{\text{local}} = \mathrm{R}_{\text{incline}} \cdot \vec{v}_{\text{corot}}. \tag{7.7}$$

Together, these transformations yield a local reference frame in which the chute is stationary and aligned with the coordinate axes. This enables a more physically meaningful description of particle motion and facilitates consistent analysis across different scaling factors. The coordinate systems are illustrated in Figure 7.4.

The velocity components are examined along the chute length using spatial bins. This analysis is based on particle data extracted from the chute-end tracker and transformed using the equations above. To ensure consistency across scaling factors, the bin size is chosen based on particle size at the highest scaling level ($s = 5$). Specifically, the bin length is set to $10 \cdot d^{s=5}$, where $d^{s=5} \approx 0.05$ m is the *average* equivalent spherical diameter at $s = 5$. This yields a bin length of 0.5 m and results in nine bins along the chute, as shown in Figure 7.5. The first two bins, located at the chute inlet, are excluded from the analysis as they primarily capture the entry region. The focus is instead on the fully developed flow along the chute surface. Within each bin, the local velocity components ($\vec{v}_x$, $\vec{v}_y$, and $\vec{v}_z$) are computed for all particles. As the same methodology applies to each component, the subscript is omitted in the following expressions. Let N_p represent the

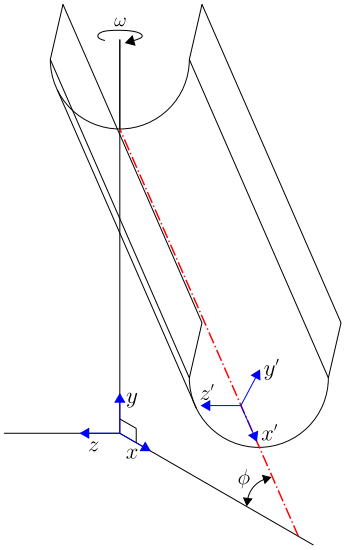


Figure 7.4: Inclined rotating chute with global (x, y, z) and chute-aligned local (x', y', z') coordinate systems. The chute rotates about the global y-axis with angular velocity ω, and the angle ϕ is the inclination angle. The local x'-axis aligns with the stream-wise direction, and z' spans the chute width.

number of particles in bin j; the average velocity in that bin is then calculated as

$$\overline{\vec{v}_j} = \frac{\sum_{i=1}^{N_p} \vec{v}_j^{\,i}}{N_p} \tag{7.8}$$

Figure 7.6a shows the bin-averaged velocity components along the chute at $t = 7.5$ s. The stream-wise velocity component ($\overline{v}_x$) is positive throughout, consistent with the chute being aligned along the positive x'-axis. As expected, $\overline{v}_x$ increases along the chute, reflecting the acceleration of material in the direction of flow. The mean $\overline{v}_y$ is initially negative in the upstream bin (bin 3), which can be attributed to particles entering the chute from above (refer to coordinate system shown in Figure 7.5). As the material progresses along the chute, $\overline{v}_y$ stabilizes near zero, indicating little net motion in the y-direction. The z-component of the velocity, $\overline{v}_z$, is consistently negative along most of the chute. This is explained by Figure 7.6b, which shows that particles tend to drift toward the negative z'-axis as they travel downstream. This lateral motion may result from initial loading asymmetry or interactions with the chute walls. Near the outlet, $\overline{v}_z$ approaches zero, suggesting that some particles begin to shift back toward the positive z-direction, while others continue drifting negatively, leading to a near-zero average.

For all velocity components, the profiles exhibit the same overall trend regardless of

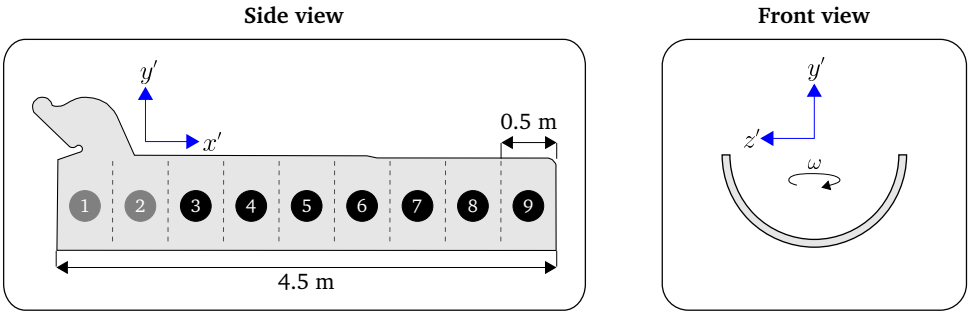


Figure 7.5: Local chute-aligned coordinate system (x', y', z') and binning layout used for velocity analysis. The chute is divided into nine equal-length bins (0.5 m) along the stream-wise x'-axis. Bins 1 and 2, located near the inlet, are excluded from the analysis. The front view shows the cross-sectional orientation of the local axes and the direction of chute rotation.

the scaling factor. For $\bar{v}_x$, a slight dependence on the scaling factor is observed, with the velocity generally decreasing as s increases. This is likely due to subtle changes in the flow dynamics and reduced resolution at higher scaling factors, as fewer particle contacts occur. Nevertheless, the key question is whether this influences the flow immediately after the chute and the formation of the particle layer in the throat. These aspects are addressed in the following sections.

7

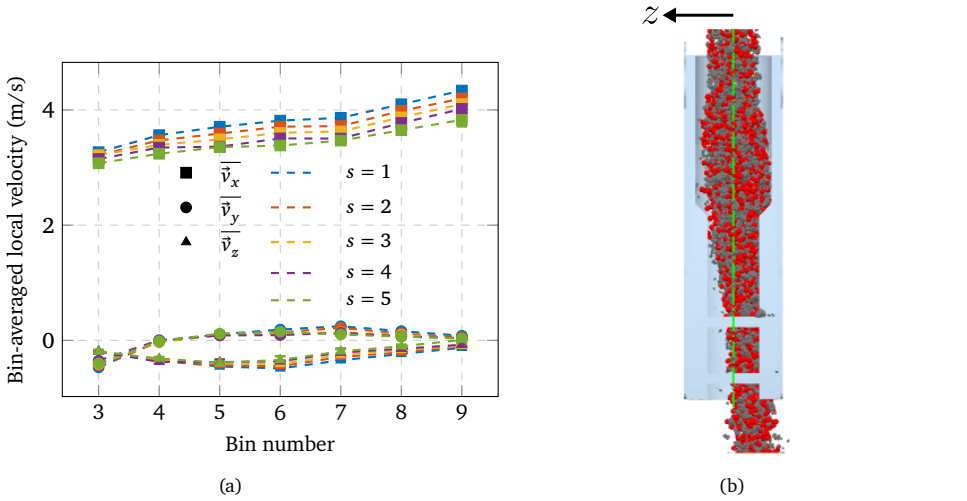
7.3.2 Analysis of flow at the chute outlet

Figure 7.7 shows snapshots of the flow at the chute outlet at $t = 7.5$ s, with particles colored according to their velocities. The average resultant chute velocity ($\vec{v}$) for each case is also indicated and was determined by applying Eq. (7.8) to the particles in the chute outlet tracker. Although the on-chute velocities are clearly influenced by the scaling factor s, as discussed in Section 7.3.1, the flow after the chute appears to be relatively unaffected. The average velocity of the material stream directly after the chute decreases slightly with increasing s. This trend was already suggested by Figure 7.6, and the relative difference between $s = 1$ and $s = 5$ is only 3.7%.

Additionally, the mass flow rate in the chute outlet tracker is considered. The instantaneous mass flow rate is defined as

$$\dot{m} = \frac{\sum_{i=1}^{N_p} \left(m_i \left(v_i \cdot \hat{l} \right) \right)}{l} \tag{7.9}$$

where m_i and v_i are the mass and velocity of particle i in the chute outlet tracker, l is the length of the chute outlet tracker, and $\hat{l}$ is the unit vector along the chute outlet direction. The mass flow rate is extracted from EDEM at intervals of 0.1 s between $t = 6.5$ s and



(a) (b)

Figure 7.6: (a) Bin-averaged local velocity components ($\overline{v}_x$, $\overline{v}_y$, $\overline{v}_z$) plotted along the downstream direction (bin number) for five different scaling factors $s = 1$–5. Marker shapes distinguish velocity components, while colors indicate scaling factor. Error bars denote standard deviations over $n = 3$ repetitions. (b) Top view of the chute during flow, showing instantaneous particle positions with respect to the local chute-aligned coordinate system.

$t = 7.5$ s, and the average value is taken. The resulting mass flow rates are also shown in Figure 7.7, showing that the relative difference between $s = 1$ and $s = 5$ is only 4%. This indicates that the mass flow rate is not significantly affected by the scaling factor, and therefore, the resulting burden layers are also expected to be similar. This expectation is examined in the following analysis.

7.3.3 Analysis of the deposited burden layer

Recall that this analysis was not feasible for the $s = 1$ case due to GPU memory limitations, so the burden layers are only analyzed for $s = [2 \quad 3 \quad 4 \quad 5]$.

The profile of the ore layer is analyzed by extracting a 0.5 m thick slice along the middle of the pie slice analysis domain at $t = 65$ s, as illustrated in Figure 7.8. A front-view screenshot of this slice is taken and processed in MATLAB. The heap contour is extracted (in pixels) by converting the RGB image to a binary format. The pixel coordinates are then converted to meters by scaling the x- and y-coordinates by a factor of $5.2/N$, where N is the number of pixels along the x-direction. Here, 5.2 m corresponds to the length of the pie slice domain, which equals the radius of the furnace throat.

Figure 7.9 shows the resulting layer profiles for scaling factors $s = [2 \quad 3 \quad 4 \quad 5]$. Each profile is represented by an average and a standard deviation based on five repetitions.

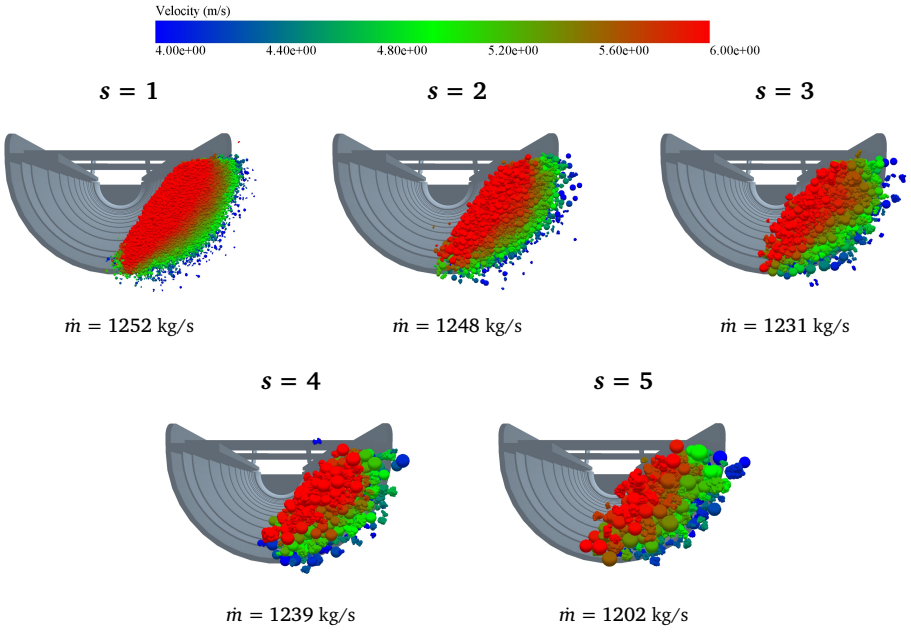


Figure 7.7: Snapshots of the material at the chute outlet at $t = 7.5$ s. Particles are color-coded according to their velocity, with the average velocity $\vec{v}$ in the chute outlet tracker also displayed. The reported mass flow rate $\dot{m}$ is not the instantaneous value at $t = 7.5$ s, but an average taken between $t = 6.5$ s and $t = 7.5$ s at intervals of 0.1 s.

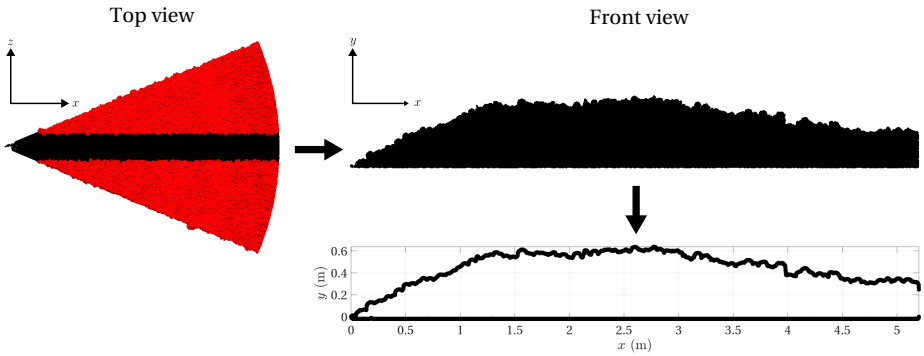


Figure 7.8: Illustration of the slice extraction along the length of the pie slice for analyzing the burden profile.

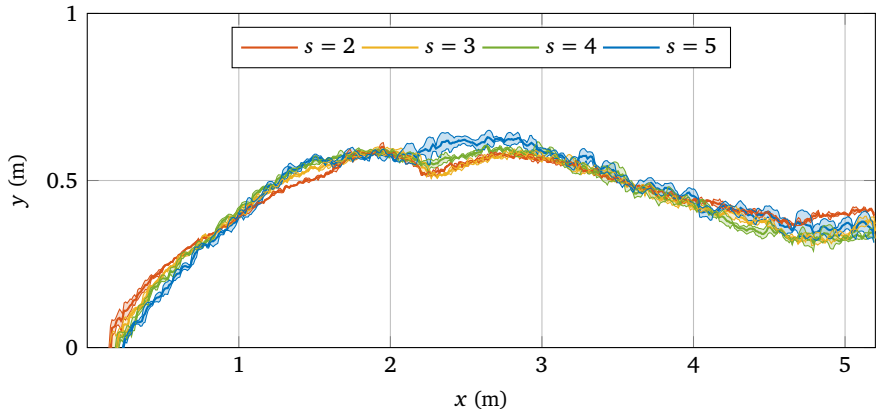


Figure 7.9: Layer profiles at the center of the pie slice for different scaling factors. Shaded areas in the profiles represent the standard deviation with $n = 5$.

Overall, the profiles exhibit good agreement across scaling factors. Minor discrepancies can be observed near the furnace center ($x < 1$ m), the wall ($x > 4$ m), and in the center ($2 < x < 3$ m). Despite these localized differences, the overall layering behavior remains largely consistent across the different scaling cases. Taking the average profile for $s = 2$ as a reference, the Concordance Correlation Coefficient (CCC) [8] was calculated to assess the similarity between the average profiles for $s = [3 \quad 4 \quad 5]$ and the reference, yielding values of CCC $= [0.92 \quad 0.94 \quad 0.97]$. All coefficients exceed 0.9, indicating very good agreement to the average profile for $s = 2$.

7.3.4 Discussion of results

In this study, layer charging was performed in a simplified container, filled with approximately 23.8 tonnes of material, to analyze the flow behavior on the chute, the flow conditions after the chute, and the resulting layering behavior in the throat. Layer formation was achieved for scaling factors $s = [2 \quad 3 \quad 4 \quad 5]$. Table 7.1 summarizes the corresponding number of particles and computational times required to simulate 65 s of ore layer charging. The number of particles, $N_p^{t=65\,\mathrm{s}}$, was extracted at the end of the simulation ($t = 65$ s) to compare the particle count in the deposited layer across different scaling factors. As expected, scaling significantly reduced the computational effort in terms of both particle count and simulation time.

Regarding the results, scaling was found to have a clear influence on the flow within the chute, particularly in terms of particle velocities. However, once the material was discharged from the chute, this effect became negligible, as similar velocities and mass flow rates at the chute outlet and comparable burden profiles at the throat were observed

Table 7.1: Summary of particle count and computational time for different scaling factors during 65 s of ore layer charging using dynamic factories.

Scaling factor s	$N_p^{t=65\,s}$	Computational time
2	1,419,115	$\sim$ 48 hours
3	416,948	$\sim$ 9 hours
4	174,725	$\sim$ 4 hours
5	88,372	$\sim$ 2 hours

across all scaling factors. Since dynamic particle factories were employed at the chute inlet to generate pellet and sinter particles, consistent mass flow rates and particle velocities were achieved across cases to replicate the discharge behavior of a top bunker within 60 s. Hence, it is expected that initiating the process at the bunkers, rather than at the chute inlet using dynamic factories, will yield similar results provided that the flow emerging from the bunker maintains consistent velocities and mass flow rates for different scaling factors. This is investigated in the next section.

7.4 Effect of scaling on bunker discharge and resulting burden packing behavior

This section extends the analysis to the full system by starting from the top bunkers, thereby simulating the actual charging process. The left bunker is filled with 37.2 tonnes of pellets and 35.2 tonnes of sinter in a perfectly segregated arrangement, as described in Section 7.2.1. Once particle generation is complete, the valve is opened at $t = 3$ s and the material is charged into the container.

To ensure the same mass flow conditions at the chute inlet, each bunker must discharge material at a comparable rate across scaling factors. However, literature indicates that the bunker discharge behavior is sensitive to particle size. For example, Zhang *et al.* [7] showed that the instantaneous mass discharge rate from a bunker fluctuates due to the formation and collapse of arches at the outlet. As particle size increases, the number of particles at the outlet decreases, stabilizing these arches and prolonging discharge times. Consequently, when particle up-scaling is applied, the bunker outlet size (β) may need to be enlarged to maintain the target mass flow rate and discharge duration at the chute inlet.

While adjusting the outlet size can help maintain the same mass flow rate at the chute inlet –thereby ensuring comparable flow and packing behavior on the chute and in the throat as observed previously– it is not immediately clear whether such adjustments also preserve the segregation dynamics during discharge. Since the bunkers define the initial conditions of the charging process, any segregation occurring at this stage can influence the degree of segregation in the deposited ore layer and, consequently, affect its porosity

distribution. Therefore, this section addresses two main objectives:

- To determine the extent to which the bunker outlet size must be adjusted for different scaling factors in order to maintain the same mass flow rate in the system.
- To assess whether such adjustments can effectively compensate for scaling effects in the bunker discharge behavior and thereby ensure consistent segregation and porosity distributions in the ore layer across scaling factors.

7.4.1 Determining the outlet size as a function of the scaling factor

Due to GPU memory constraints, simulations for the lower scaling factors $s = 1$ and $s = 2$ could not be performed. Therefore, the analysis is limited to $s = [3 \quad 4 \quad 5]$. For each scaling factor, the outlet opening angle β was varied between 50° and 60° to determine the value required to achieve a discharge time of 60 s, denoted as β_{60}. The following rounded values were obtained: $\beta_{60} = [52^\circ \quad 54^\circ \quad 55^\circ]$ for $s = [3 \quad 4 \quad 5]$, respectively. These results confirm that a larger outlet opening is required to maintain the same discharge time as the scaling factor increases.

7.4.2 Comparison of packing behavior using adjusted bunker outlet size

This investigation addresses the second objective by conducting simulations using the identified β_{60} values and evaluating the extent to which the discharge flow and subsequent packing behavior in the throat remain comparable across different scaling factors.

Component segregation during bunker discharge

Figure 7.10a presents the time evolution of the total mass (M) retained in the bunker for different scaling factors, based on their corresponding β_{60} values. The results confirm that a discharge time of approximately 60 s is achieved in each case, with measured discharge times of $t_d = [60.4 \quad 59.9 \quad 60.6]$ s for $s = [3 \quad 4 \quad 5]$, respectively.

To evaluate component segregation during discharge, the mass fraction of pellets (x_P) within the bunker is monitored over time, calculated as

$$x_P = \frac{m_P}{m_P + m_S} \tag{7.10}$$

where m_P and m_S represent the mass of pellet and sinter particles, respectively, as recorded by the bunker tracker.

Figure 7.10b shows the time evolution of x_P for each case. The curves are similar across all scaling factors, exhibiting a steady decrease in x_P as the bunker empties. This trend indicates that pellets are discharged faster than sinter. This behavior can be understood

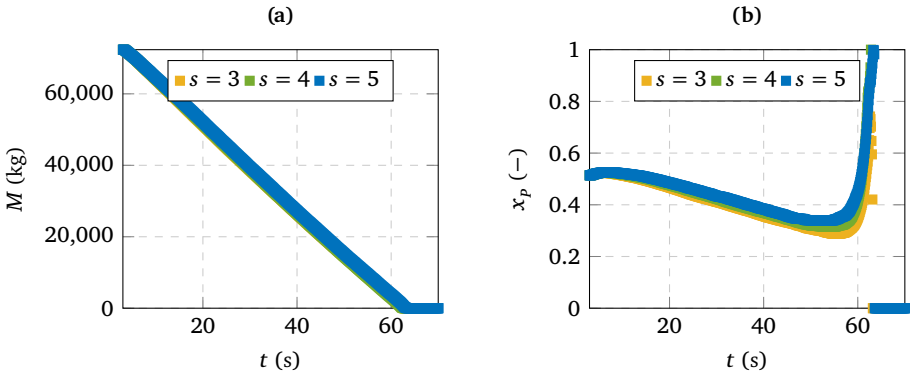


Figure 7.10: Evolution of (a) the total mass and (b) the mass fraction of pellets retained in the bunker during discharge for different scaling factors. The results are based on a single repetition for each case.

by examining the initial particle arrangement illustrated in Figure 7.11, which shows snapshots of the bunker during filling and discharge, with pellets colored red and sinter shown in gray. Due to the combination of the valve opening mechanism and the segregated initial condition, sinter particles are partially obstructed by the valve at the start of the discharge, resulting in a slower discharge rate compared to pellets. As the discharge progresses, the proportion of pellets in the bunker gradually increases, and eventually, all sinter particles are depleted, leaving only pellets in the final stages of the discharge.

This trend is consistently observed across all scaling factors. However, a slight increase in the mass fraction of pellets, x_p, at a given time is noted with increasing scaling factor s. This can be attributed to the fact that a larger scaling factor corresponds to a larger outlet opening (as β_{60} increases with s), which reduces the extent to which sinter particles are retained by the valve. As a result, a greater amount of sinter is discharged per unit time at higher scaling factors, leading to a slightly higher value of x_p as s increases.

Component segregation in the throat

Figure 7.12 shows snapshots of the pie slice tracker at $t = 65$ s for $s = [3 \quad 4 \quad 5]$. To quantify the degree of radial component segregation, the segregation index is computed as described below.

The analysis domain is radially divided into a series of sub-domains (rings) of equal volume, resulting in rings of non-uniform thickness. Five rings are used, labeled R1 to R5, with R1 corresponding to the region nearest the center of the pie slice domain (as shown in Figure 7.13). This configuration ensures that the thinnest ring (R5) has a thickness of approximately 0.5 m, consistent with the earlier criterion of maintaining a bin size at least ten times the average particle diameter at $s = 5$. Introducing more than five rings

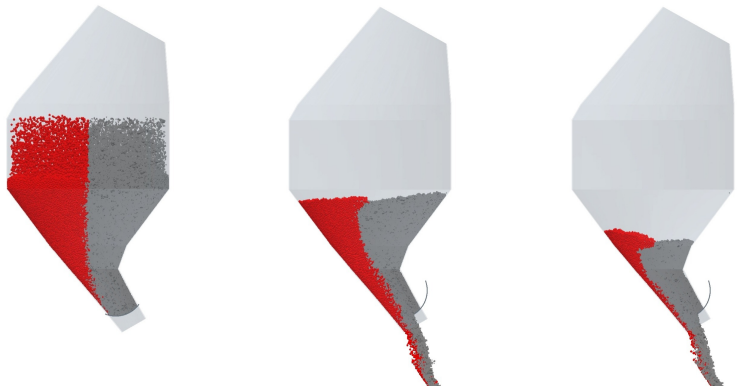


Figure 7.11: Snapshots of (a) the bunker filling process, which generates a segregated initial condition, and (b) and (c) the material discharge from the bunker at $t = 42$ s and $t = 57$ s, respectively. Particles are scaled by a factor $s = 5$, with pellets shown in red and sinter particles in gray.

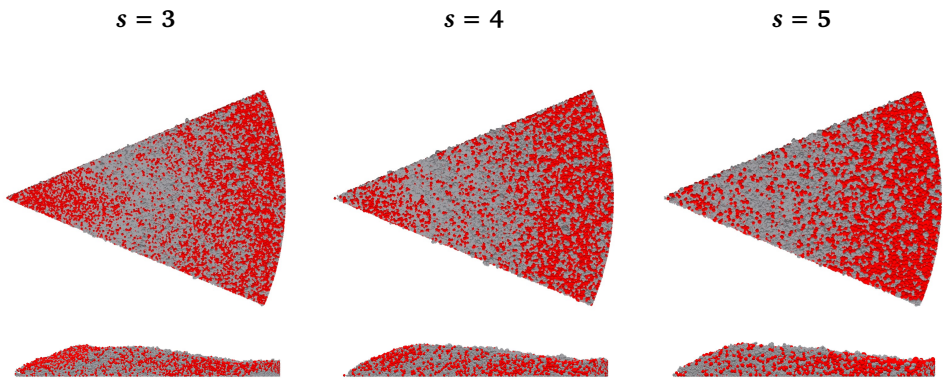


Figure 7.12: Snapshots of the material in the pie slice tracker at $t = 65$ s: top view (top) and front view (bottom). Pellet particles are shown in red, while sinter particles are shown in gray.

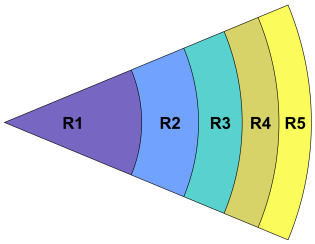


Figure 7.13: Visualization of the radial division of the pie slice domain (top view) into five sub-domains (R1-R5) of equal volume.

would cause the minimum ring thickness to fall below this threshold.

For each ring, the local mass fraction of pellet particles (considered the "tracer") is calculated. The mass fraction of pellets (x_P) is determined for each sub-domain, and the segregation index (SI) is then defined as the relative standard deviation of x_P [9]

$$SI = \frac{\sqrt{\frac{\sum_{i=1}^{N}\left(x_P^i - \overline{x_P}\right)^2}{N-1}}}{\overline{x_P}} \tag{7.11}$$

where N is the number of sub-domains, ($\overline{x_P}$) is the average mass fraction of all domains, determined by

$$\overline{x_P} = \frac{1}{N}\sum_{i=1}^{N} x_P^i \tag{7.12}$$

and x_P^i is the mass fraction of pellets in the i-th cell determined by Eq. 7.10. The value of SI ranges from 0 to 1, where 0 represents a perfectly mixed state and 1 represents a fully segregated state.

Figure 7.14a shows the radial distribution of x_P, demonstrating that the radial pellet distributions are highly similar across the different scaling factors. The corresponding segregation index, SI, values are presented in Figure 7.14b, further confirming this similarity. The difference in SI between $s = 3$ and $s = 5$ is only 0.04, which, considering the full range of SI values (0–1), represents a small difference of 4%.

Porosity distribution in the throat

As with the segregation index, a porosity index (PI) can be used to quantify the uniformity of the radial porosity distribution. To this end, the same previously defined radial divisions, R1–R5, are employed, with the ring height constrained to $h = 0.25$ m, as illustrated in Figure 7.15. The porosity (P) of a ring is calculated as

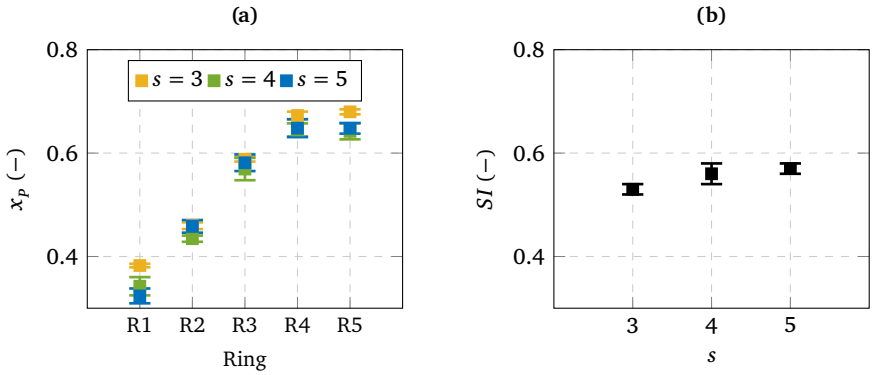


Figure 7.14: Comparison of (a) the mass fraction of pellets (x_p) distribution and (b) the corresponding segregation index (SI) for different scaling factors. Results are shown as averages, with error bars indicating the standard deviation based on three repeated simulations.

$$P = \frac{V_r - V_p}{V_r} \tag{7.13}$$

where V_p is the total volume of all particles within the ring, and V_r is the volume of the ring in the 45° pie slice, given by

$$V_r = \frac{\pi h (R_o^2 - R_i^2)}{8} \tag{7.14}$$

with R_i and R_o denoting the inner and outer radii of the ring, respectively.

The uniformity of the radial porosity distribution is quantified using the porosity index (PI), defined analogously to the segregation index (SI), as

$$PI = \frac{\sqrt{\frac{1}{N_b}\sum_{i=1}^{N_b}(P^i - \overline{P})^2}}{\overline{P}} \tag{7.15}$$

where P^i is the porosity in ring i, calculated using Eq. 8.1, and $\overline{P}$ is the mean porosity across all rings in the pie slice determined by

$$\overline{P} = \frac{1}{N_b}\sum_{i=1}^{N_b} P^i \tag{7.16}$$

A perfectly uniform porosity distribution corresponds to $PI = 0$, and higher PI values indicate increased unevenness in the porosity distribution.

Figures 7.16a and 7.16b present the porosity distribution and corresponding PI values

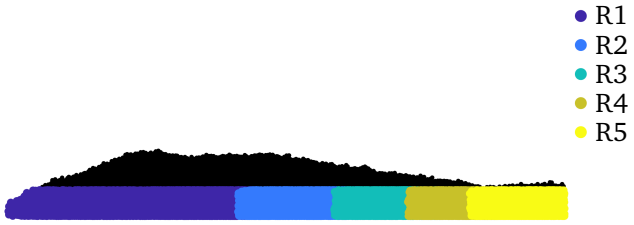


Figure 7.15: Visualization of the bins used for calculating the porosity in each sub-domain.

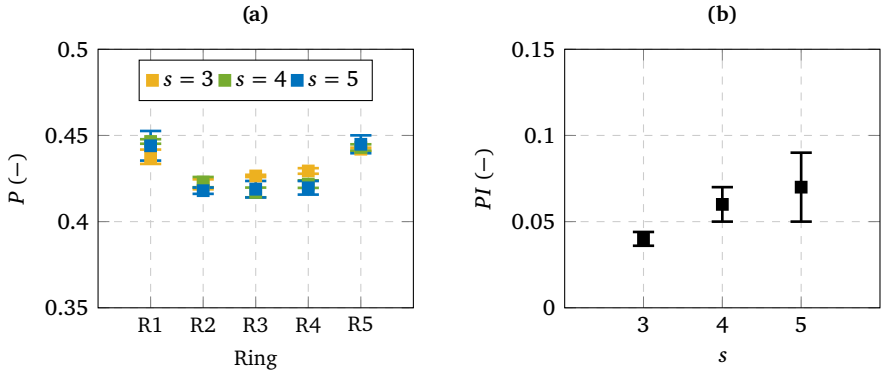


Figure 7.16: Comparison of (a) the porosity (P) distribution and (b) the corresponding porosity index (PI) for different scaling factors. Results are shown as averages, with error bars indicating the standard deviation based on $n = 3$ repetitions.

for the different scaling factors, indicating consistent results across the three cases. The low PI values reflect a nearly uniform porosity distribution considering its full possible range, from 0 to 1.

7.4.3 Discussion of results

In this study, layer charging was simulated by filling the top bunker with a single batch of ore mixture for different particle scaling factors, $s = [3 \quad 4 \quad 5]$. Scaling factors below 3 were found to be computationally infeasible. For each selected scaling factor, the opening size of the bunker valve was calibrated to achieve a consistent discharge time of 60 s. By adjusting the valve opening accordingly, comparable discharge behavior across the different scaling factors was successfully established.

Due to this compensation, the extent of component segregation during bunker discharge was slightly affected. This outcome is attributed to the highly idealized, fully segregated initial configuration of pellets and sinter in the bunker, which represents a

Table 7.2: Summary of particle count and computational time for different scaling factors during 65 s of ore layer charging starting at the top bunker.

Scaling factor s	$N_p^{t=3\,s}$	Computational time
3	1,229,153	$\sim$ 38 hours
4	518,329	$\sim$ 14 hours
5	265,423	$\sim$ 6 hours

worst-case scenario unlikely to occur in real industrial practice. In actual operations, the initial mixture is expected to be more randomized. It is therefore anticipated that better agreement in component segregation across scaling factors would be observed for more realistic, partially mixed initial conditions.

Under the matched discharge conditions, the resulting packing behavior in the furnace throat was found to be very similar across scaling factors. Both the component distribution and the porosity profile in the deposited layers showed a high degree of similarity, confirming the effectiveness of the up-scaling approach.

Table 7.2 provides an overview of the number of particles and the computational time required to simulate 65 s of ore layer charging for each scaling factor. The number of particles, $N_p^{t=3\,s}$, was extracted right before opening the valve ($t = 3$ s) to compare the particle count in the top bunker across different scaling factors. Compared to the configuration where particles are generated at the chute inlet using factories (see Table 7.1), this method requires significantly more computational time. This is expected, as the full batch mass is present at the start of the simulation and gradually exits the system through the throat. In contrast, in simulations using inlet factories, the material enters progressively and does not reach the same total mass. Nonetheless, the current method offers important advantages: it allows for full control over the initial conditions in the bunker –including varying levels of segregation– and thereby enables a more realistic and flexible exploration of operational effects.

7.5 Conclusions

This chapter evaluated the feasibility of industrial scale blast furnace simulations by applying particle up-scaling to the calibrated DEM model. The key conclusions are:

- **Particle up-scaling is essential for industrial scale modeling.** Simulations with scaling factors $s = 1$ and $s = 2$ were found to be computationally unfeasible, confirming the need for up-scaling to enable full-scale simulations.
- **Accurate results can be achieved up to $s = 5$.** For scaling factors $s = 3$, 4, and 5, maintaining consistent mass flow rates at the bunker outlet preserved the key flow dynamics and packing behavior. This confirms that up-scaling up to $s = 5$

is a feasible and reliable approach for modeling the discharge and layering of ore mixtures.

- **Up-scaling enables efficient modeling of full ore layers.** Using $s = 5$, the model can simulate the discharge of a complete ore batch within a practical runtime. Since each furnace layer is formed by two such batches, this approach makes it possible to model full layer formation processes under realistic conditions.

The up-scaled model will be applied in the next chapter to simulate industrial scale charging scenarios, assess burden distribution, and explore potential strategies for improvement.

7.6 Bibliography

[1] Delft High Performance Computing Centre (DHPC). *DelftBlue Supercomputer (Phase 2)*. https://www.tudelft.nl/dhpc/ark:/44463/DelftBluePhase2. 2024.

[2] S. Cole. *How to select a GPU (Graphics Processing Unit) for EDEM*. 2023. URL: https://community.altair.com/discussion/33296/how-to-select-a-gpu-graphics-processing-unit-for-edem.

[3] T. Zhao, B. Zhang, and Y. Huang. "Comparison of Coarse Graining DEM Models Based on Exact Scaling Laws". In: *Computer Modeling in Engineering & Sciences* 127 (2021), pp. 1133–1150. ISSN: 1526-1506. DOI: 10.32604/cmes.2021.016018.

[4] S. C. Thakur, J. Y. Ooi, and H. Ahmadian. "Scaling of discrete element model parameters for cohesionless and cohesive solid". In: *Powder Technology* 293 (2016), pp. 130–137. ISSN: 0032-5910. DOI: 10.1016/j.powtec.2015.05.051.

[5] E. L. Chan and K. Washino. "Coarse grain model for DEM simulation of dense and dynamic particle flow with liquid bridge forces". In: *Chemical Engineering Research and Design* 132 (2018), pp. 1060–1069. ISSN: 0263-8762. DOI: 10.1016/j.cherd.2017.12.033.

[6] S. Lommen, M. J. Mohajeri, G. Lodewijks, and D. Schott. "DEM particle upscaling for large-scale bulk handling equipment and material interaction". In: *Powder Technology* 352 (2019), pp. 273–282. DOI: 10.1016/j.powtec.2019.04.034.

[7] Z. Zhang, Y. Liu, B. Zheng, R. Li, and P. Sun. “Discharge characteristics of binary particles in a rectangular hopper with inclined bottom”. In: *Computational Particle Mechanics* 8 (2021), pp. 315–324. ISSN: 2196-4386. DOI: 10.1007/s40571-020-00332-7.

[8] G. B. McBride. *A proposal for strength-of-agreement criteria for Lin’s Concordance Correlation Coefficient*. NIWA Client Report: HAM2005-062. Accessed May 26, 2025. 2005. URL: https://www.medcalc.org/download/pdf/McBride2005.pdf.

[9] H. Li and J. J. McCarthy. “Cohesive particle mixing and segregation under shear”. In: *Powder Technology* 164 (2006), pp. 58–64. ISSN: 0032-5910. DOI: 10.1016/j.powtec.2005.12.018.

8

Showcasing the Industrial Blast Furnace Charging Model: Insights from Case Studies

Building on the industrial-scale model developed in the previous chapter, this chapter demonstrates its practical application to operational conditions. The up-scaled, calibrated models of the pellet–sinter mixture are employed to gain insights into the ore layer formation after charging, closely replicating industrial practice. A series of case studies are conducted for a blast furnace at TATA Steel IJmuiden in the Netherlands, using the developed DEM mixture model. These case studies, selected in collaboration with process technologists at TATA Steel, focus on key operational aspects relevant to current industrial practice. The findings aim to improve the understanding of burden distribution dynamics and support the development of strategies for improving furnace performance.

8.1 Brief description of ore layer charging

The blast furnace burden contains alternating layers of coke and ore, charged sequentially from the top bunkers. In industrial operation, the top bunkers are filled using skip cars, which transport materials from the stock house via an inclined rail system. Each layer is deposited as a series of concentric rings, formed by varying the chute inclination angle during charging. The chute inclination and its circumferential rotation speed together define the *charging program*, which governs the specific manner in which the material is distributed. Coke and ore are charged according to different charging programs, designed to give each layer a particular profile.

After charging a coke layer, ore layer charging is conducted in two sequential stages:

- Stage 1: A batch of ore mixture is loaded into one of the top bunkers and discharged over a period of 60 seconds according to a predefined charging program (Program 1), resulting in the formation of ore layer 1.
- Stage 2: A subsequent batch of ore mixture is loaded into the second top bunker and discharged using a different charging program (Program 2), also over 60 seconds, forming ore layer 2 atop the first.

In both stages, the weight of the ore mixture is 72,360 kg, consisting of 37,200 kg pellets and 35,160 kg sinter (hence, the pellet mass fraction is 0.51). Together, the two deposits constitute one complete ore layer, after which a new coke layer is charged. This alternating sequence of coke and ore layers continues cyclically throughout the operation.

The blast furnace operates continuously, with the burden descending as molten iron and slag are periodically tapped from the hearth. As a result, the height of the topmost material layer –referred to as the *stock line level*– is continuously monitored. A new charging cycle is triggered when the stock line level drops to a predefined threshold known as the *burden call level*. Ore layer 1 is charged once the coke layer has descended to this level, and ore layer 2 follows only after ore layer 1 reaches the same point.

8.2 Simulation and analysis methods

Simulations were performed using the Hertz-Mindlin no-slip contact model in combination with rolling model C. The software package ALTAIR® EDEM™ (version 2024.1) was used, and simulations were run on the DelftBlue high-performance cluster [1] using a single GPU (NVIDIA Tesla V100S-PCIE-32GB).

8.2.1 Simulation setup

The simulation setup, shown in Figure 8.1, consists of two mirrored top bunkers, a Y-tube, a rotating chute, and a container representing the throat of the blast furnace. The setup

dimensions replicate those of Blast Furnace No. 7 (BF7) at TATA Steel IJmuiden, with the container having a diameter of 10.2 meters. In contrast to the previous chapter, where the ore layer was charged directly into the container (assuming a flat stock surface in the furnace throat), this setup includes a shaped stock surface composed of coke particles, replicating the coke layer in actual furnace conditions. The ore layer is subsequently charged onto this coke layer. The procedures for generating the coke layer and charging the ore layer are described as follows.

Coke layer generation
To ensure a realistic coke layer, actual burden profile records were used to reconstruct the coke layer shape in two dimensions. This 2D profile was then revolved to create a three-dimensional circumferential volume of the coke layer in SolidWorks. The resulting 3D volume was imported into EDEM as a generator volume, positioned above a base that matches the bottom contour of the generator (see Box (1) of Figure 8.1). Coke particles were generated internally within this volume using a dynamic particle factory, allowing them to settle naturally onto the base. As the particles settled, the industrial coke profile shape was effectively recreated.

The coke layer serves as the starting point for the ore charging simulations. To accurately replicate operational conditions, the coke layer is generated at the burden call level. Since the burden surface is not perfectly horizontal, it is necessary to designate a specific reference point on the surface that must reach the burden call level before charging begins. This reference point is indicated by the symbol "×" in Figure 8.2. In blast furnace operation, the maximum charging level is fixed, and the burden call level is measured relative to this maximum. Charging is triggered once the burden has descended to a depth H, measured from point × in Figure 8.2. This depth H defines the burden call level used in both operational practice and the simulation setup.

Ore layer charging
To replicate the two-stage ore charging process (described in section 8.1) from the bunkers to the furnace throat, the same two-stage sequence is implemented in the simulations. As the bunker filling process via skip cars lies outside the scope of this thesis, dynamic particle factories are used to introduce material into the top bunkers in different configurations derived from the work of Hadi *et al.* [2]. The simulation procedure is as follows:

- **Stage 1** begins with the generation of pellet and sinter particles in Top Bunker 1, which takes place from $t = 0$ to $t = 3$ s using dynamic particle factories. At $t = 5$ s, the discharge process is initiated: the bunker valve opens while the chute simultaneously starts rotating from its initial orientation, as shown in Box (2) of Figure 8.1, and continues in the indicated direction. Material begins to flow from

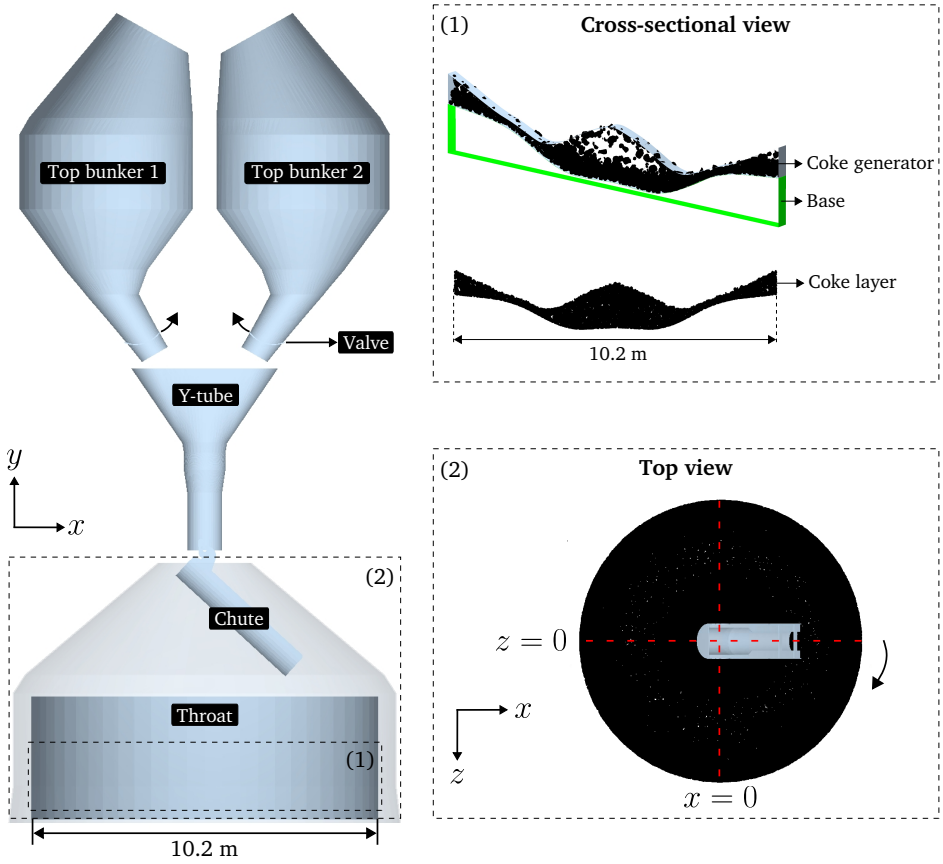


Figure 8.1: Simulation setup of BF7 with key components. The left panel shows the overall configuration, including the top bunkers, Y-tube, rotating chute, and throat region. Box (1) demonstrates the coke layer generation at the base: a cross-sectional view of the coke generation process and the resulting layer profile. Box (2) provides a top view of the throat region, highlighting the chute orientation at the start of its rotation. Curved arrows indicate the direction of chute rotation.

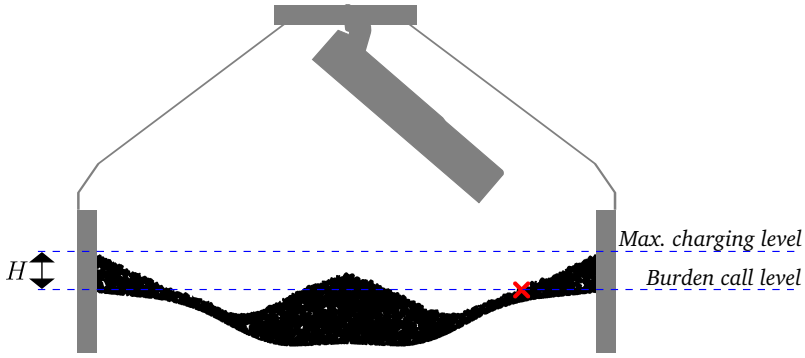


Figure 8.2: Schematic cross-sectional view of a blast furnace, illustrating the maximum charging level and the burden call level, which is located at a distance H below the maximum charging level, measured from the reference point marked "×".

the bunker, passing through the Y-tube and falling onto the rotating chute. The valve follows the same opening mechanism described in the previous chapter, where the target opening angle β is reached within 0.1 s using a constant angular speed calculated to achieve this within the allotted time. Over the next 60 seconds, the contents of the bunker are fully discharged, with the rotating chute distributing the mixture onto the coke layer. The simulation concludes at $t = 65$ s, once all material has been deposited.

- **Layer height adjustment** occurs after the first batch of ore has been deposited onto the coke layer, which initially lies at the burden call level. Under normal operating conditions, further charging would be paused at this point until the burden naturally descends back to the burden call level. To replicate this descent within the simulation, the entire charging system (from the top bunkers to the chute) is translated upward by a distance equal to the height of the deposited ore layer at the point marked '×' relative to the coke layer. This adjustment resets the burden surface to the burden call level before the second batch of ore is charged.

  Stage 2 follows the same procedure as Stage 1, but now utilizes Top Bunker 2. The charging system operates at the adjusted stock line level established after the first deposition, ensuring consistency between the two stages. The chute begins its rotation from the same initial position shown in Box (2) of Figure 8.1.

Figure 8.3 presents an example of the coke layer with an overlying ore layer composed of two sequentially charged batches.



Figure 8.3: Cross-sectional view of the particle bed evolution during the ore layer charging process. The coke layer is first generated, followed by two stages of ore charging. Red and gray particles represent pellet and sinter, respectively, while black particles represent coke.

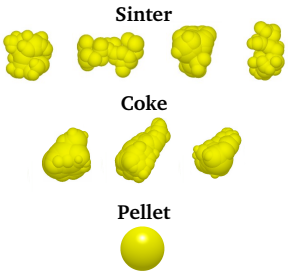


Figure 8.4: Representative particle shapes used in the simulation for different burden materials. Sinter and coke are modeled as non-spherical particles while pellets are represented as spheres.

8.2.2 Model parameters

Table 8.1 summarizes the parameters used in the simulation, which are adopted from the previously calibrated and up-scaled model (scaled by a factor of 5). These include particle size distributions, shapes, material properties, and interaction parameters. Although the pellet mass fraction in the current mixture is 0.51 (compared to 0.50 in the calibrated model), this small difference is not expected to affect material behavior, and the same parameters are applied. The coke model is based on a combination of literature data and direct measurements. Particle density and size distribution were determined using the same procedure as for pellets and sinter, with results presented in Appendix B. The coke size distribution was also scaled by a factor of 5 for consistency. Three coke particles were randomly selected, 3D scanned, and fitted with spheres to generate clump models; the resulting shapes are shown in Figure 8.4. Remaining material properties and interaction parameters were taken from the literature [3, 4]. A numerical time step of 30% of the Rayleigh limit was used, corresponding to $\Delta t = 2.6 \times 10^{-5}$ s.

8.2.3 Extraction of KPIs

At the end of each simulation, the distribution of burden components and the packing structure of the ore layer are analyzed. The coke layer, although present, is excluded from

Table 8.1: Hertz-Mindlin model parameters used in this work. Abbreviations: P = pellet, S = sinter, C = coke, W = wall, PSD = particle size distribution.

Parameter [unit]		Pellet (P)	Sinter (S)	Coke (C)	Steel wall (W)
PSD		App. B	App. B	App. B	N/A
Particle shape		Fig. 8.4	Fig. 8.4	Fig. 8.4	N/A
ρ [kg/m^3]		3602	3449	966	7800
ν		0.25	0.25	0.25	0.3 [5]
E [Pa]		$2.5 \cdot 10^8$	$2.5 \cdot 10^8$	$1 \cdot 10^7$	$5.2 \cdot 10^{11}$
e [-]	P	0.1	0.1	0.34	0.64 [5]
	S	–	0.5	0.31	0.4 [5]
	C	–	–	0.6	0.4 [5]
μ_s [-]	P	0.57	0.34	0.42	0.86
	S	–	0.49	0.79	0.54
	C	–	–	0.55	0.9
μ_r [-]	P	0.08	0.28	0.05	0.15
	S	–	0.06	0.12	0.09
	C	–	–	0.1	0.2

the analysis as it falls outside the scope of this study. Ore particles embedded within the coke are also disregarded, as they are considered separate from the main ore layer. This distinction is important for accurately evaluating the packing structure. Since the starting position of the ore layer varies slightly between different case studies, a consistent radial reference point cannot be defined. To ensure comparability across all scenarios, the first 0.5 m of the bed is excluded from the analysis.

Component segregation

To quantify component segregation within the ore layer, the domain is discretized in both the radial and circumferential directions. Specifically, the layer is divided into eight angular sectors of 45° each, and each sector is further partitioned into four concentric radial rings, resulting in a total of 32 sub-domains, as illustrated in Figure 8.5. The rings, labeled R1 to R4, are defined by the radial boundaries $R = [1, 2, 3, 4, 5.2]$ m, where a particle at radial position r (measured from the furnace center in the horizontal plane) falls within R1 if $1 \leq r < 2$ m, R2 if $2 \leq r < 3$ m, and so on. The central region ($r < 1$ m) is excluded, as it predominantly contains coke rather than ore. Within each cell, the mass fraction of pellets, x_p, is computed. These values are then used to evaluate the segregation index (SI) in accordance with the procedure detailed in Chapter 7, Section 7.4.2.

Packing structure

The porosity is used as an indicator of permeability and is evaluated for sector 1 shown in Figure 8.5. The porosity within each radial ring of the sector is calculated using:

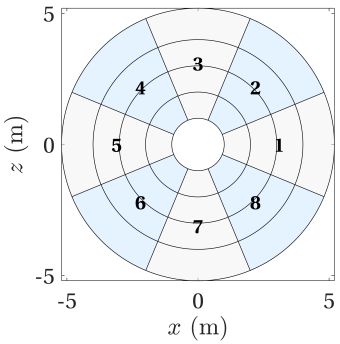


Figure 8.5: Visualization of the sub-domains used in the analysis. The domain is divided into eight sectors of 45° in the circumferential direction, with each sector further subdivided into four radial rings. The coordinate origin ($x = 0, z = 0$) corresponds to the furnace center.

$$P = \frac{V_b - V_p}{V_b} \tag{8.1}$$

where V_p is the total volume of particles located within the ring, and V_b is the bulk volume corresponding to that region. The bulk volume V_b is obtained through a series of steps, as illustrated in Figure 8.6. A slice of the ore layer is first extracted from EDEM along the x-direction, centered at $z = 0$, as shown previously in Figure 7.8. This snapshot is post-processed in MATLAB to isolate the ore layer from the coke layer and to extract the two-dimensional profile of the ore layer. Only the right half of the ore layer's profile is used, corresponding to sector 1.

The extracted profile is imported into SOLIDWORKS, where sector 1 is reconstructed by revolving the profile over an angle of 45°. Radial rings within the sector are then created by slicing the geometry at the specified radii. This allows for direct calculation of the bulk volume V_b for each ring based on the resulting segmented geometry.

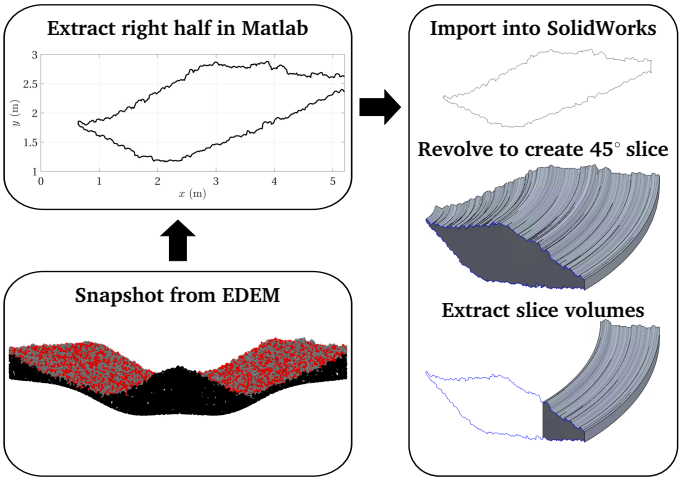


Figure 8.6: Visualization of the method used to quantify radial slice volumes from a packed bed geometry obtained in EDEM.

8.3 Effect of initial mixture configuration in top bunkers

In industrial practice, top bunkers are filled using skip cars that transport raw materials to the blast furnace. This process (see Figure 8.7) begins in the stock house, where skips are loaded by simultaneously discharging the required amounts of pellet and sinter from their respective weighing bunkers. Once filled, the skip ascends to the top of the furnace and tilts to discharge its contents into a funnel, which then directs the material into one of two top bunkers. Recent work by Hadi *et al.* [2] investigated the extent of mixing during the skip filling and subsequent discharging into the top bunkers. Their findings indicated that the material within the skip car remains largely segregated, with this segregation persisting in the top bunkers.

In the stock house, the weighing bunkers are positioned adjacent to each other, providing some flexibility in assigning each bunker to a specific material. Altering this configuration can lead to different initial arrangements of pellet and sinter in the top bunkers, and it is of particular interest to assess how these arrangements influence the resulting burden distribution. In this study, the bunkers are filled using particle factories, resulting in idealized and perfectly segregated initial conditions for pellets and sinter. Three such idealized cases are considered (see Figure 8.8):

- Case 1: Good mixing during skip filling, leading to a fully mixed initial state in the skip. Although unlikely based on the findings of Hadi *et al.*, this case is included for comparison purposes.
- Case 2: Poor mixing during skip filling leads to a segregated initial configuration

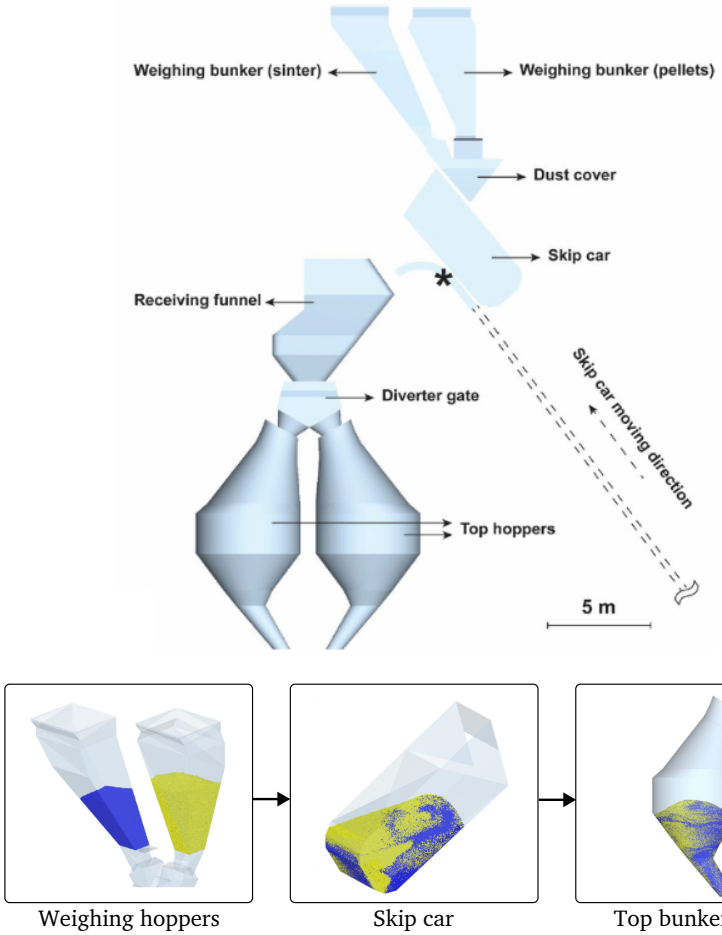


Figure 8.7: Top: Simulation setup from Hadi *et al.* [2], illustrating the charging of the left top bunker through the emptying of a skip car. Bottom: Snapshots showing the distribution of pellets (yellow) and sinter (blue) at various stages of the charging process.

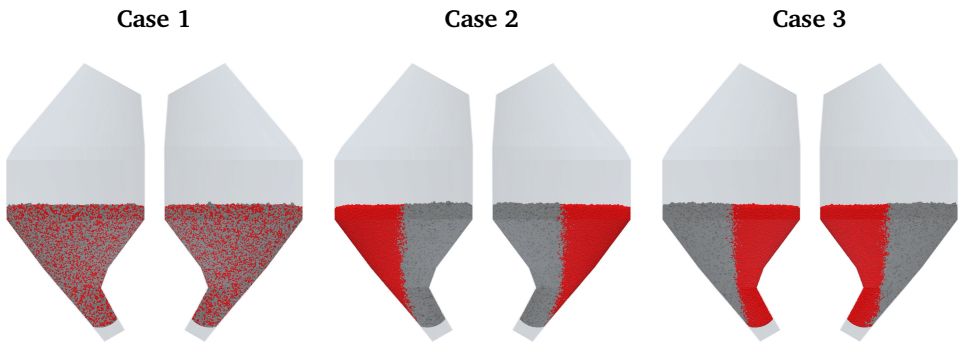


Figure 8.8: Front-view snapshots of the initial filling conditions in the top bunkers for different cases. Particles are color-coded by material type, with red indicating pellets and gray indicating sinter.

in the left bunker referred to as "Pellet–Sinter," where pellets are concentrated on the left side and sinter on the right.

- Case 3: Poor mixing during skip filling results in the opposite configuration in the left bunker, termed "Sinter–Pellet," with sinter concentrated on the left side and pellets on the right.

As shown in Figure 8.8, the right bunker is assumed to mirror the left. The opening angle β required for a 60-second discharge varies slightly across the cases: $\beta = [56.8, 55.9, 57.8]^\circ$ for Cases 1, 2, and 3, respectively. Figure 8.9 presents front-view snapshots of the left bunker with the valve set accordingly. These small differences, not visually distinguishable in Figure 8.9, arise from the variation in particle mobility between pellets and sinter. Pellets, being spherical, have higher mobility than the irregularly shaped sinter particles. In Case 2, the valve obstructs the sinter, allowing the pellets to flow freely. Given their high mobility and unobstructed path, a smaller opening angle is sufficient to maintain the target discharge time. In Case 3, the pellets are obstructed. However, due to their lower mobility, a larger opening angle is required. Case 1, with a well-mixed configuration, results in an intermediate value. These observations highlight the role of particle shape and mobility in governing discharge behavior.

8.3.1 Component distribution

Figure 8.10 presents snapshots of the ore layer in a slice along the x-axis at the end of the simulation for the different cases. These snapshots are obtained by extracting a slice of 0.3 m thickness in the z-direction, with $z = 0$ located at the center of the slice. This provides a view of the pellet distribution in the x-z plane across the full diameter of the furnace. Visual inspection of the snapshots reveals clear differences in the distribution

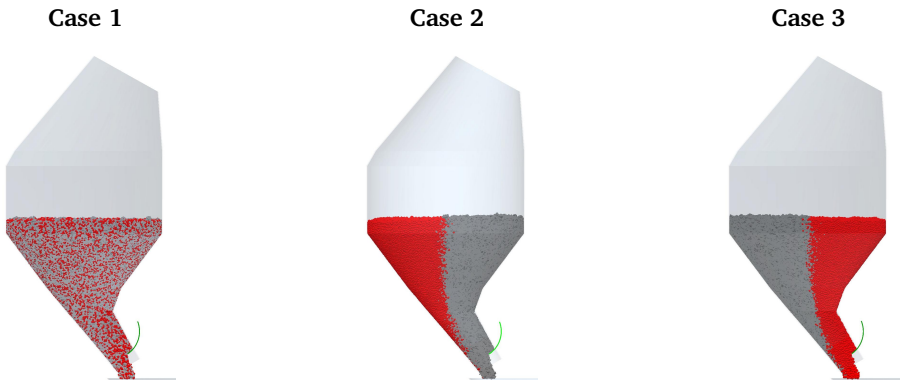


Figure 8.9: Front-view snapshots showing the bunker discharge for different cases. Particles are color-coded by material type, with red representing pellets and gray representing sinter. The bunker valve, colored green, obstructs the outflow of sinter in Case 2 and pellet in Case 3. Although the bunker valve is opened at slightly different angles in the three cases, the variations are minor and not visually distinguishable in the images.



Figure 8.10: Cross-sectional snapshots of the initial filling conditions in the top bunkers for different cases. Particles are color-coded by material type: red represents pellets, and gray represents sinter.

of pellets (colored red) and sinter (colored gray), with the uniformity of the distribution appearing to deteriorate progressively from Case 1 to Case 3.

Figure 8.11 provides a more detailed visual representation of the degree of component segregation across the cases. The mass fraction of pellets (x_p) across the 32 cells is presented using color maps. The corresponding calculated SI value is also indicated for each case. It is evident that component segregation increases progressively from Case 1 to Case 3, which confirms the trend already observed in Figure 8.10. Case 1 exhibits almost no segregation in either the radial or circumferential directions, while Case 2 shows predominantly circumferential segregation, and Case 3 exhibits mainly radial segregation.

The pronounced differences in component distribution between the cases can be explained by the combined effect of three factors: the initial material configuration, the partially opened valve, and the mobility of the pellet and sinter particles. Together, these factors influence the order in which pellet and sinter are discharged. Figure 8.12 and Figure 8.13 show the evolution of the mixture composition in the left top bunker during

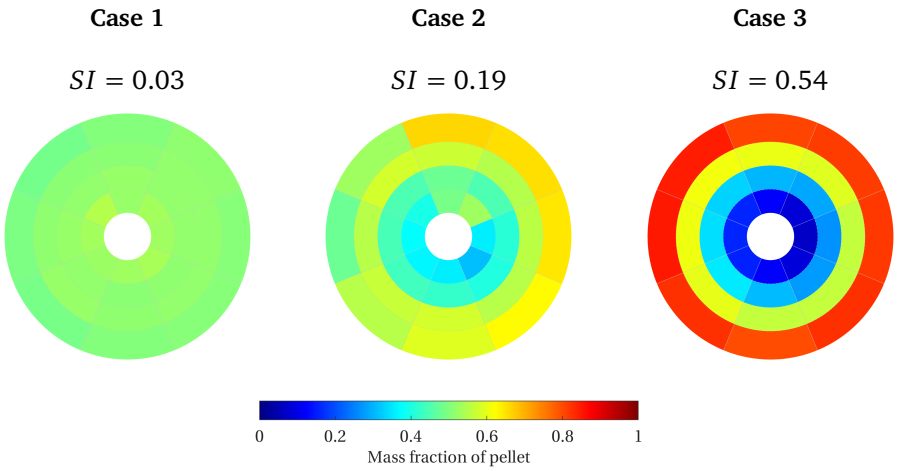


Figure 8.11: Color maps showing the distribution of x_p in the ore layer for different cases. The analysis is based on dividing the layer into eight pie slices, each further subdivided into four concentric rings.

discharge for all three cases. Due to the symmetry of the setup, similar behavior is expected for the right bunker. Together with the visual representation given in Figure 8.13, the plots in Figure 8.12 provide insight into the discharge sequence by indicating how much pellet remains in the bunker over time. As the rotating chute deposits the material, this time-dependent discharge sequence is effectively translated into a spatially segregated surface distribution.

In Case 1, the pellet mass fraction in the bunker remains essentially constant at $x_p = 0.51$, matching the overall mixture composition and indicating that no component segregation occurs during discharge. Both Case 2 and Case 3 begin with a preferential discharge of pellets; likely due to the higher mobility of pellet particles compared to sinter particles due to their spherical shape. This is clearly seen in Figure 8.13: when comparing the images for $t = 5$ s and $t = 15$ s, there is a "dip" in the pellet packing for both cases, showing that pellet discharges faster in both cases regardless of the configuration. In Case 2, the pellet mass fraction gradually decreases, and as discharge continues, a reversal occurs: sinter begins to dominate the flow, resulting in the retention of pellets in the bunker. Eventually, all sinter is discharged, and the remaining pellets exit at the end. Case 3 exhibits a more rapid and continuous decline in pellet mass fraction compared to Case 2, indicating an even stronger initial preference for pellet discharge, despite the obstruction of pellet by the rotating valve. At a later stage, all pellets are discharged, and only sinter remains in the bunker, which is then discharged in the final phase.

Although both Case 2 and Case 3 begin with a preferential discharge of pellets, the

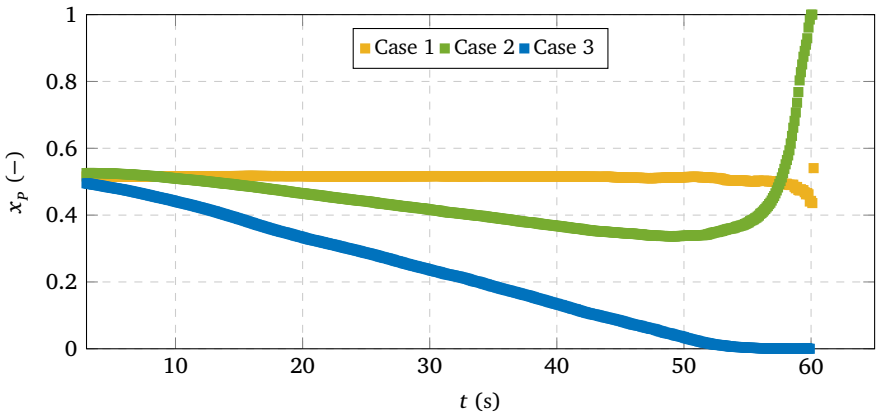


Figure 8.12: Evolution of the mass fraction of pellets (x_p) retained in the left bunker during discharge for different cases.

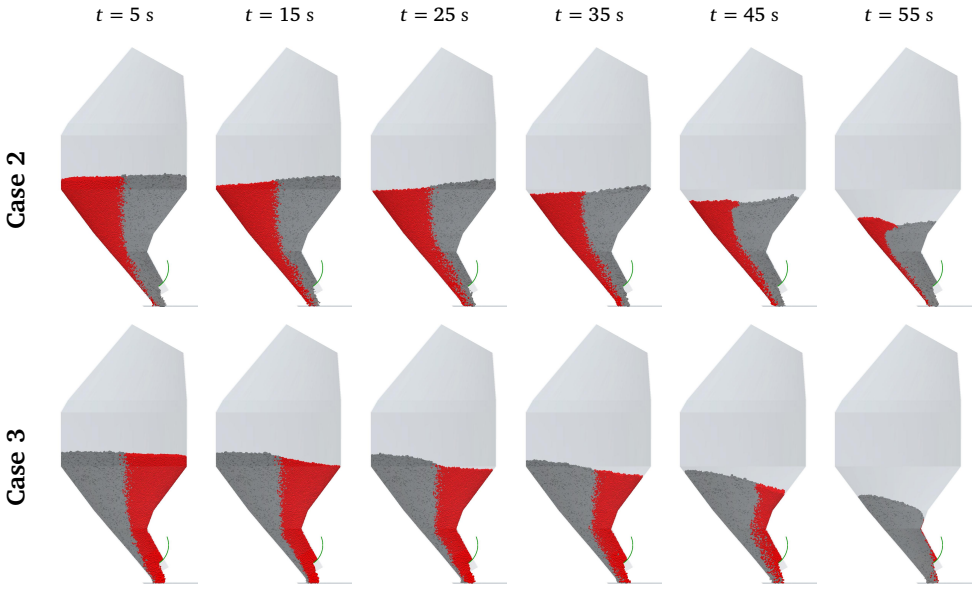


Figure 8.13: Front-view snapshots showing the time evolution of material retained in the left top bunker for Cases 2 and 3.

extent and outcome differ. In Case 2, a shift occurs midway through the discharge, leading to the retention of pellets until the end. This shift in composition contributes to the circumferential inhomogeneity observed in the deposited layer. It is important to recall that in the simulations, the chute begins discharging from the same initial angular position for both bunkers. Consequently, any inhomogeneity introduced during the discharge of the first bunker is reinforced during the discharge of the second. To mitigate this effect, it may be beneficial to reverse the chute rotation direction between the two bunker discharges when the initial condition resembles that of Case 2. In contrast, Case 3 shows a consistent trend in which pellets are discharged early and sinter remains until the end.

Overall, the results demonstrate that the initial condition in the top bunkers significantly influences the component distribution. When pellet and sinter are perfectly mixed in the top bunkers (Case 1), a nearly perfect homogeneous distribution of ore components is achieved in the deposited layer. In other words, no component segregation occurs as the material travels from the top bunkers to the throat region under the current charging program. Therefore, achieving a well-mixed initial condition in the top bunkers should be considered a priority during material delivery from the stock house. The results of Case 2 and Case 3 highlight the importance of carefully assigning the weighing bunkers to pellet and sinter, as the initial arrangement strongly influences the uniformity of the deposited layer. In practice, the degree of segregation is unlikely to be as severe as assumed in Cases 2 and 3; thus, the differences resulting from bunker assignment may be less pronounced. A more comprehensive investigation, involving simulation of the full charging process starting from the weighing bunkers, would be necessary to draw more definitive conclusions. Nevertheless, the current findings clearly demonstrate that the initial mixing condition in the top bunkers plays a critical role in determining the component distribution in the ore layer. Therefore, achieving a well-mixed state in the top bunkers should be regarded as essential in industrial operation.

8.3.2 Packing distribution

Figure 8.14 focuses on the porosity of the radial cells within sector 1 (for definition, see Figure 8.5). The porosity distribution is shown in Figure 8.14a, where it is evident that the distribution for Case 3 deviates significantly from those of Case 1 and Case 2. In the latter two cases, porosity remains relatively uniform across the different rings. This observation is particularly interesting when compared to Figure 8.11, which shows that the component composition across the rings in Case 1 and Case 2 is not as similar as the porosity might suggest.

To further investigate the relationship between local composition and porosity, Figure 8.14b presents the pellet mass fraction plotted against the porosity for each radial ring and case. The plot for Case 1 forms a nearly vertical line around $x_p \approx 0.51$, consistent

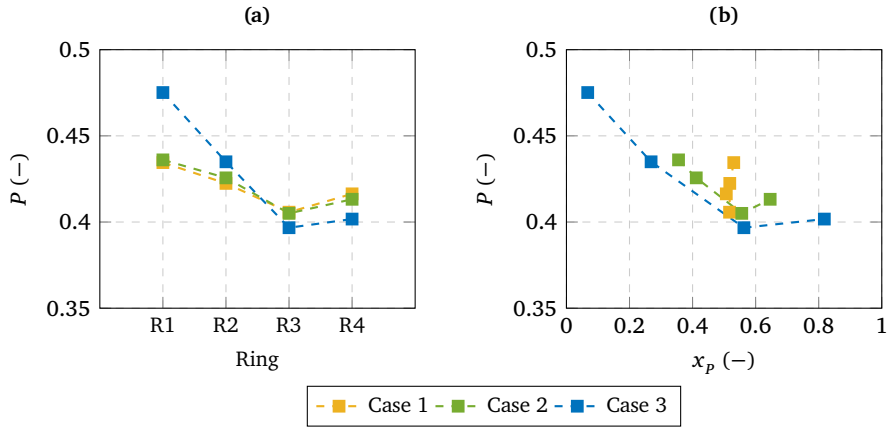


Figure 8.14: Porosity analysis of radial rings in sector 1 for Cases 1–3. (a) Porosity P plotted against ring index (R1-R4, where R1 is closest to the center and R4 is closest to the periphery); (b) Porosity as a function of local pellet mass fraction x_p.

with the minimal component segregation observed in Figure 8.11. The corresponding porosity values range narrowly from approximately 0.41 to 0.43, which is expected: a uniform composition results in a relatively uniform porosity.

The plots for Case 2 and Case 3 reveal similar qualitative trends, though with different values. This behavior is consistent with the trends observed in Figures 8.11 and 8.14a. Specifically, from ring R1 to R3, porosity tends to decrease as the pellet fraction increases, suggesting that local composition influences packing density. However, this trend is interrupted at R4, where porosity increases slightly despite a high pellet concentration. This anomaly is likely due to wall effects, as R4 includes particles located near the furnace periphery.

Another noteworthy observation arises when comparing the porosity of rings R2 and R4 across all three cases. The porosity values for these rings are remarkably similar despite large differences in composition: *e.g.*, $x_p = 0.52$ for Case 1, 0.41 for Case 2, and 0.27 for Case 3 in R2. These compositional differences imply substantial variation in the proportion of spherical versus non-spherical particles between cases in these rings. As particle shape has a strong influence on the connectivity of void spaces, the resulting packing structure (and thus the permeability) is expected to differ significantly. This suggests that porosity alone does not adequately reflect the structure of void networks, which govern bed permeability. Therefore, porosity should not be considered sufficient on its own to characterize the permeability of the granular bed.

Table 8.2: Overview of case studies used to evaluate the influence of the burden call level H on the resulting burden and packing distribution, under different initial bunker filling configurations (Case 1-3). Abbreviations: P=pellet, S=sinter.

	Case A	**Case B**	**Case C**
Case 1	$H = 1$ m, mixed	$H = 1.5$ m, mixed	$H = 2$ m, mixed
Case 2	$H = 1$ m, segregated (P-S)	$H = 1.5$ m, segregated (P-S)	$H = 2$ m, segregated (P-S)
Case 3	$H = 1$ m, segregated (S-P)	$H = 1.5$ m, segregated (S-P)	$H = 2$ m, segregated (S-P)

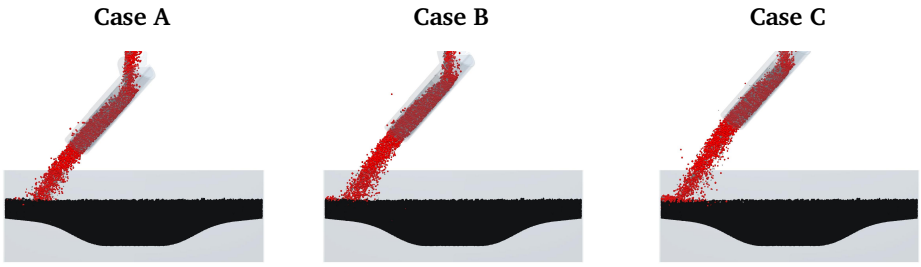


Figure 8.15: Front-view snapshots of burden discharge trajectories at $t = 7.5$ s for Cases A–C, corresponding to burden call levels of $H = 1$, 1.5, and 2 m, respectively. As the burden call level increases, the particles land progressively closer to the furnace wall due to the outward-shifted falling point. Particles are color-coded by material type: red indicates pellets, and gray indicates sinter.

8.4 Effect of burden call level

Referring back to Figure 8.2, the burden call level H is the stock line level at which charging commences, where H is measured as the distance between the point $\times$ and the maximum charging level. Under standard operating conditions, a burden call level of $H = 1$ m is typically used.

Increasing H influences the burden as it reaches the stock surface in two key ways: (i) it increases the impact velocity, and (ii) it shifts the material's landing point outward, increasing the radial distance from the furnace center. In the latter case, material discharged closer to the furnace wall may even scatter upon impact with the wall. These effects are particularly relevant when the initial bunker filling is segregated, as the altered landing behavior may mitigate the component segregation previously observed in the outer regions of the ore layer. Understanding how the burden call level affects the resulting burden distribution is therefore of particular importance. This influence is assessed across different initial bunker configurations, leading to the nine case studies summarized in Table 8.2.

Figure 8.15 presents simulation snapshots at $t = 7.5$ s for different burden call levels.

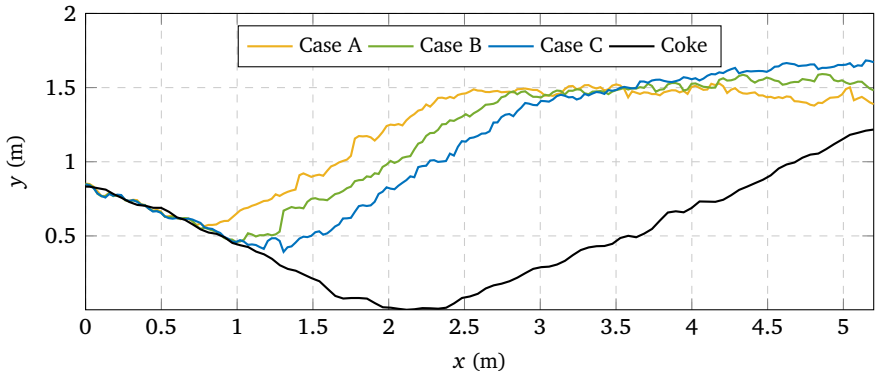


Figure 8.16: Layer profiles in a slice along the x-axis (at $z = 0$) of sector 1 after discharge for different burden call levels. The plots shown correspond to Case 3, although similar trends are observed for Cases 1 and 2.

As the burden call level H increases, the vertical distance between the chute tip and the coke layer becomes larger, causing the material to land farther from the furnace center and closer to the wall. Consequently, the radial deposition of all material rings shifts outward with increasing H. For the outermost ring, particle interaction with the furnace wall upon impact may also induce localized mixing near the periphery. This outward shift is reflected in the layer profiles shown in Figure 8.16, which illustrate how increasing H leads to a progressive reduction in material accumulation at the furnace center. Another noteworthy observation is that the ore layer thickness appears to become more even in radial direction, implying a more even mass distribution in radial direction. Since this is also an important aspect to consider with respect to the permeability (as discussed in Chapter 2), increasing the burden call levels appears to be beneficial in this regard.

8.4.1 Component distribution

Figure 8.17 presents color maps of the final pellet mass fraction in both radial and circumferential directions for the nine scenarios listed in Table 8.2. In all cases, the circumferential distribution remains approximately symmetrical, indicating that variations in the burden call level H have minimal influence on circumferential segregation. This is expected, as only the radial deposition position of the rings is affected by changes in H. However, an increase in overall segregation is observed with increasing H, which can be attributed to the corresponding shift in radial burden distribution.

The color maps reveal improved mixing in the two outer radial rings when comparing Case A to Case B. This is evident from the reduced pellet concentration in these rings, indicating a relative increase in sinter content. Simultaneously, the pellet concentration in

the innermost two rings increases. This trend is consistent with the previously discussed effect of the burden call level: as H increases, the material falls from a greater height and lands farther from the furnace center, resulting in a radial shift in deposition toward the wall. Since the radial rings are defined at fixed positions, this outward shift in material landing point means that a larger fraction of pellets ends up in the outer rings in Cases B and C compared to Case A. Consequently, the color maps reflect this shift in distribution, with the changes in pellet concentration across rings being a direct result of the modified deposition pattern caused by the increased burden call level.

8.4.2 Packing distribution

Figures 8.18a–c show the porosity distribution in sector 1 for different burden call levels H, across Cases 1–3. Interpreting the changes in porosity is not straightforward for this case study, as multiple factors are involved. On the one hand, the local mixture composition within the bins changes with H. As shown in Figure 8.17, the radial position of pellet deposition shifts outward, resulting in a lower pellet concentration near the center and slight mixing near the wall, as indicated by the decreasing pellet fraction in the outer rings with increasing H. On the other hand, the increased falling distance leads to higher impact velocities, which can enhance local compaction. Thus, the observed porosity trends are likely the result of a combined effect of material redistribution and velocity-induced compaction. Comparing subfigures (a), (b), and (c), the porosity distribution remains largely unchanged with increasing H in Cases 1 and 2. However, for Case 3, a noticeable decrease in porosity is observed in R1 as H increases. This may be due to the presence of predominantly sinter in the center, where compaction effects can be more easily interpreted in the absence of material mixing. In such a case, higher impact velocities at larger H values could directly lead to denser packing and reduced porosity. Nonetheless, the overall differences in porosity are relatively small in all the rings, and the current analysis is based on a single simulation per case. To draw more robust conclusions and better identify trends, additional repetitions would be necessary.

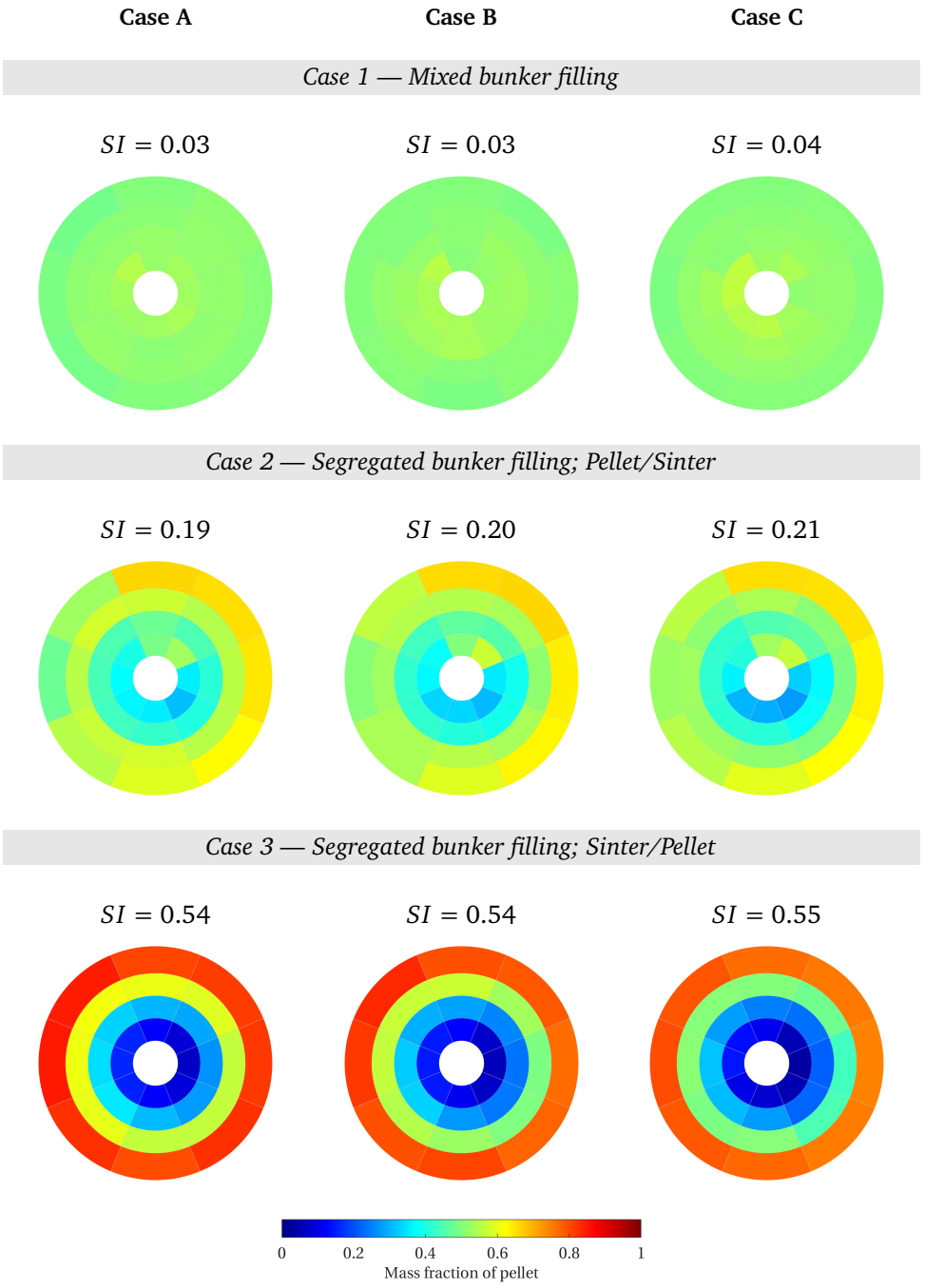


Figure 8.17: Color maps showing the distribution of x_P in the ore layer for different cases. The analysis is based on dividing the layer into eight pie slices, each further subdivided into four concentric rings.



Figure 8.18: Porosity analysis of radial rings in sector 1 for Cases A, B, and C under different initial top bunker conditions: (a) perfectly mixed (Case 1); (b) perfectly segregated with pellets on the left and sinter on the right (P/S, Case 2); and (c) perfectly segregated with sinter on the left and pellets on the right (S/P, Case 3).

8.5 Effect of chute liner condition

In blast furnace operations, wear is an inevitable consequence of the continuous handling of bulk materials, which exposes charging equipment to substantial mechanical stress and degradation. Among the most affected components is the rotating chute, which must endure mass flow rates of approximately 1,250 kg/s and inlet velocities around 7 m/s. As shown previously in Box (2) of Figure 7.1, the chute is lined with wear-resistant plates (together referred to as the chute liner) rather than being a smooth surface. Over time, progressive material loss due to wear reduces the thickness of the liner, and in severe cases, can lead to localized liner removal and even perforations.

Understanding how different wear conditions influence burden distribution is therefore essential for determining when chute replacement is necessary, based on its impact on burden distribution and the corresponding implications for furnace performance. Observations of severely worn chutes at TATA Steel IJmuiden indicate that wear typically initiates in the middle section of the chute and, with continued use, extends to the tip. To capture these representative wear scenarios, three chute liner conditions are analyzed, as shown in Figure 8.19:

- Case D: Chute liner in its original, unworn state.
- Case E: Chute liner exhibiting localized wear in the middle section.
- Case F: Chute liner with extensive wear, combining middle-section damage (as in Case E) with complete erosion at the tip.

The influence of these chute liner conditions is evaluated under varying initial bunker

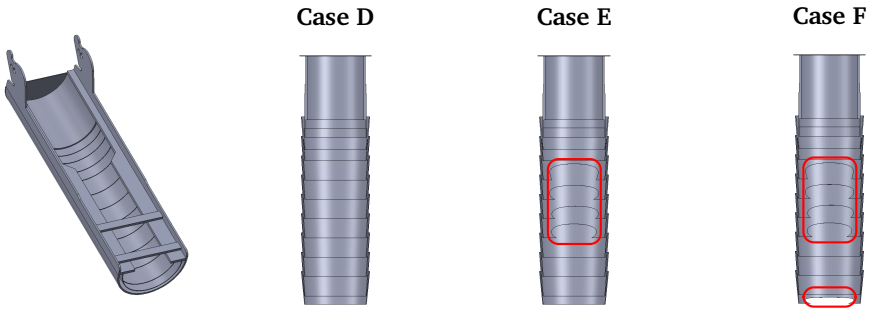


Figure 8.19: Chute geometry and corresponding liner surface conditions. The leftmost figure shows the full chute assembly. The three figures to the right represent different liner wear scenarios: Case D – unworn liner; Case E – localized wear in the middle section (highlighted in red); Case F – extensive wear, including both middle-section damage and complete erosion at the tip (both regions highlighted in red).

Table 8.3: Overview of case studies used to evaluate the influence of the chute liner condition on the resulting burden and packing distribution, under different initial bunker filling configurations (Case 1-3). Abbreviations: P=pellet, S=sinter.

	Case D	**Case E**	**Case F**
Case 1	no wear, mixed	wear: middle, mixed	wear: middle+tip, mixed
Case 2	no wear, segregated (P-S)	wear: middle, segregated (P-S)	wear: middle+tip, segregated (P-S)
Case 3	no wear, segregated (S-P)	wear: middle, segregated (S-P)	wear: middle+tip, segregated (S-P)

filling configurations, resulting in the nine case studies summarized in Table 8.3.

8

8.5.1 Component distribution

Figure 8.20 presents color maps of the final pellet mass fraction in both radial and circumferential directions for the nine scenarios outlined in Table 8.3. The results suggest that the different chute liner conditions do not affect the overall component distribution. This outcome is not entirely unexpected, as the material primarily slides over the chute surface regardless of the specific wear pattern. Based on these results, it can be inferred that the curvature changes introduced by liner wear do not significantly affect particle trajectories or segregation behavior.

8.5.2 Packing distribution

Figures 8.21a–c present the porosity distribution in sector 1 for different chute liner conditions across Cases 1–3. Since the component composition within each ring does not appear to be significantly affected by the chute surface condition, substantial differences in

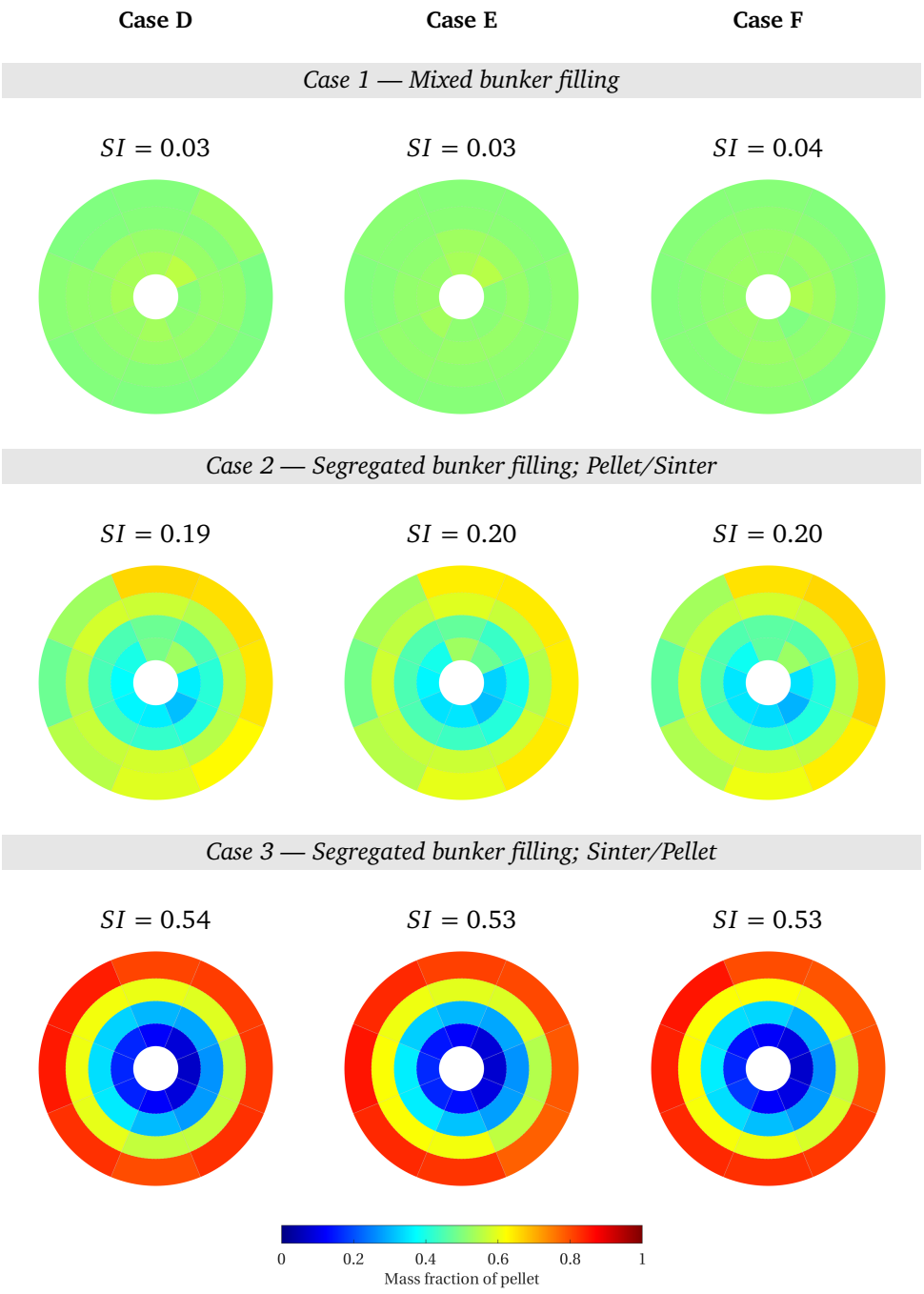


Figure 8.20: Color maps showing the distribution of x_p in the ore layer for different cases. The analysis is based on dividing the layer into eight pie slices, each further subdivided into four concentric rings.

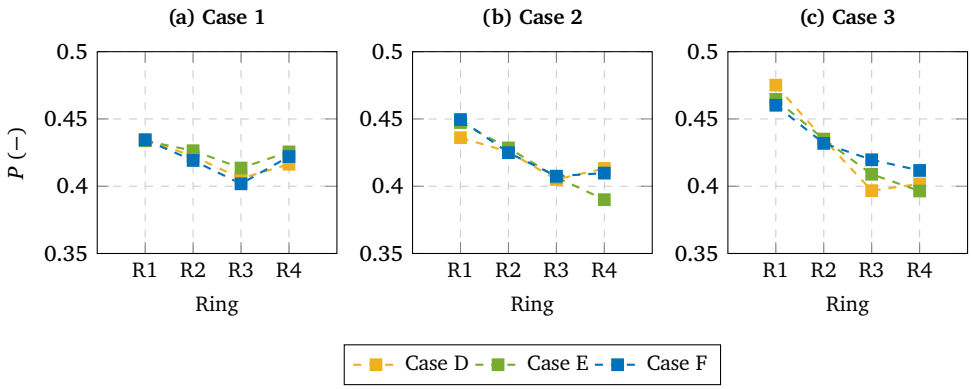


Figure 8.21: Porosity analysis of radial rings in sector 1 for Cases D, E, and F under different initial top bunker conditions: (a) perfectly mixed (Case 1); (b) perfectly segregated with pellets on the left and sinter on the right (P/S, Case 2); and (c) perfectly segregated with sinter on the left and pellets on the right (S/P, Case 3).

ring porosity were not expected. This expectation holds true for Cases 1 and 2, where the porosity remains largely unchanged across the different chute configurations. In Case 3, minor variations in ring porosity are observed depending on the chute surface condition. However, the differences are relatively small, and it remains unclear whether they are the result of meaningful trends or simply simulation variability. Further work would be necessary to determine whether these small deviations reflect a consistent pattern or are due to statistical variability.

8

8.6 Conclusions

This chapter has demonstrated the application of an up-scaled DEM model to simulate the ore charging process in an industrial-scale blast furnace. A series of case studies was conducted to investigate the influence of key operational and design parameters on the resulting component and packing distributions. The following main conclusions can be drawn:

- **Initial bunker configuration is critical.** The arrangement of materials in the top bunkers strongly influences the resulting component distribution in both the radial and circumferential directions. Notably, changing the configuration of the weighing bunkers in the stock has serious implications for the component segregation in the charged ore layer. When the top bunkers are filled with a perfectly mixed ore blend, component segregation in the resulting layer is minimal. This highlights the importance of achieving a well-mixed initial condition, and points to the need for

further investigation into how such mixing can be achieved in practice.

- **Increasing burden call level shifts deposition outward.** Higher burden call levels result in a greater falling distance, causing the material to land closer to the furnace wall. This leads to a shift in the radial deposition pattern, with less material accumulating near the center. At sufficiently high H, particles impact the furnace wall directly, causing local mixing in the outer rings and a slight reduction in segregation there, while segregation in the inner rings becomes more pronounced. The radial mass distribution improves with increasing H, as the ore layer thickness becomes more uniform. Effects on porosity remain small and difficult to interpret due to the combined influence of increased compaction and shifting composition.
- **Chute wear, as modeled here, has minimal impact.** The chute wear patterns considered in this study, primarily involving shape deformation rather than material loss, did not significantly affect either the component distribution or the porosity. It is expected that more severe wear (*e.g.*, perforation of the chute liner) could have a greater influence and warrants further investigation.

These findings demonstrate the model's value for scenario analysis and highlight key areas for future research. Specifically:

- **Top bunker configuration must be known.** Since the initial distribution of materials in the top bunkers plays such a pivotal role, meaningful predictions of burden and packing distributions require knowledge of how materials are delivered to and arranged within the bunkers. Future simulations should therefore be preceded by modeling the skip car delivery process from the stock house to the bunkers.
- **Porosity alone is insufficient to assess packing.** Although porosity is commonly used for packing structure analysis, the results show only minor variation in porosity despite differences in local material composition (*i.e.*, the amount of spherical pellet versus irregular sinter particles present). This suggests that porosity does not fully capture the structure of the void space and may not be a reliable indicator of permeability –the key parameter of interest in the blast furnace context. Permeability depends on the connectivity of voids and governs the ease with which gas can flow through the furnace layers, whereas porosity measures the total void fraction. Accurately assessing void connectivity requires more detailed information about the pore structure than porosity alone can offer. Further research is needed to develop methods for extracting such information from industrial scale DEM data.

8.7 Bibliography

[1] Delft High Performance Computing Centre (DHPC). *DelftBlue Supercomputer (Phase 2)*. https://www.tudelft.nl/dhpc/ark:/44463/DelftBluePhase2. 2024.

[2] A. Hadi, Y. Pang, A. Adema, J. van der Stel, and D. Schott. *Insights into the segregation in the blast furnace charging system: from the stockhouse to top hoppers*. Nov. 2024.

[3] A. Chakrabarty, S. Basu, S. Nag, U. Ghosh, and M. Patra. "Model Study of Centre Coke Charging in Blast Furnace through DEM Simulations". In: *ISIJ International* 61 (Mar. 2021), pp. 782–791. DOI: 10.2355/isijinternational.ISIJINT-2020-498.

[4] M. Kou, W. Zeng, Z. Zhang, X. She, T. Zhang, B. Zhao, X. Ma, and H. Zhou. "Central coke charging and its effect on coke collapse at the throat of blast furnace by DEM simulation". In: *Powder Technology* 408 (2022), p. 117784. ISSN: 0032-5910. DOI: 10.1016/j.powtec.2022.117784.

[5] H. Wei, Y. Ge, M. Li, Y. Li, H. Saxén, Z. He, and Y. Yu. "DEM study of the porosity distribution of pellet sandpile formed by ternary size particles". In: *Powder Technology* 360 (2020), pp. 1337–1347. DOI: 10.1016/j.powtec.2019.11.017.

9

Conclusions and Recommendations

9.1 Conclusions

This thesis demonstrated a systematic approach for developing a reliable and computationally feasible industrial scale DEM model for blast furnace charging with a pellet–sinter mixture. The resulting model can be used to evaluate and optimize operational conditions with the goal of improving bed permeability and, consequently, furnace performance.

The key requirements for achieving good blast furnace bed permeability include uniformity in the packing structure, component distribution, and mass distribution across the layers, and minimizing the presence of fine particles. The extent to which these conditions can be achieved is governed by complex mechanisms such as size and component segregation, particle degradation, flow deviation within the charging system, and the coke-push effect that occurs during ore deposition onto the coke layer. While previous DEM studies have primarily focused on modeling size segregation and flow deviation, component segregation and degradation have received comparatively limited attention, particularly in the context of multi-component mixtures and their influence on permeability. These limitations in the current state of DEM modeling provided the motivation for pursuing a more comprehensive and realistic approach.

Currently available DEM models for blast furnace charging exhibit several shortcomings that undermine their reliability, especially in the case of mixture models which involve a large number of interaction parameters. First, there is a lack of systematic methods to determine these parameters. Many studies rely on parameter values reported in literature, rather than on calibration. Even when calibration is attempted, it often involves adjusting multiple parameters based on a single performance indicator, which can result in non-unique parameter sets. Furthermore, such calibrations are usually conducted under low-velocity conditions that do not represent the high-velocity nature of the flow during

industrial charging. Second, particle up-scaling techniques, used to reduce computational cost, are frequently applied without sufficient evaluation of their impact on segregation and packing behavior. Together, these shortcomings raise concerns regarding the real-world applicability of existing models and call for an approach that combines systematic mixture calibration and up-scaling to capture complex phenomena such as segregation and packing under industrial conditions.

A pre-calibration step involving numerical sensitivity analyses revealed that the interaction parameters between pellet and sinter particles have a significant influence on porosity and component distribution in the mixture model. This indicated that, in addition to calibrating the individual pellet and sinter parameters, the inter-component parameters also needed to be calibrated, making the task particularly challenging given the relatively large set of model parameters. Two essential requirements were identified to ensure model reliability: (i) calibration had to be carried out under flow conditions representative of the high-velocity regime in the blast furnace, and (ii) multiple key performance indicators (KPIs) had to be used to obtain a unique solution for the relatively large parameter set.

A novel laboratory-scale experimental setup was developed to replicate high-velocity charging conditions, enabling the generation of flow velocities comparable to those in industrial scale operations. Systematic piling tests were conducted using pellet, sinter, and their 50/50 mass-based mixture at various discharge heights. Five KPIs were selected to characterize the behavior of the material: hopper discharge time, heap mass, heap contour (shape), heap center height, and heap porosity. Each of these indicators was shown to be sensitive to both flow velocity and material properties, confirming their suitability for calibration. A two-step calibration strategy was developed, involving the separate calibration of the individual material models (pellet and sinter), followed by calibration of the interaction parameters specific to the pellet–sinter mixture. A combination of response surface methodology and the desirability function approach was used, providing a robust means of calibrating the models using the five KPIs to ensure a unique parameter set. The calibrated mixture model was able to accurately reproduce the experimentally observed average KPI values, with a maximum deviation of only 5.5% under the highest flow condition, and showed strong predictive performance across a range of flow velocities, demonstrating its high reliability and applicability.

Simulations conducted with the calibrated mixture model, using particle scaling factors up to 5, showed that key performance characteristics –including burden layering, component segregation, and porosity distribution– were preserved, provided that the mass flow rate was adjusted appropriately. Although higher scaling factors resulted in reduced resolution of local flow details, particularly with respect to velocity variations along the chute, these effects did not significantly affect the final packing structure. This confirmed that particle up-scaling up to a factor of 5 is a viable strategy for making

industrial scale simulations feasible, as long as it is implemented carefully and with appropriate adjustments to preserve realistic flow behavior from the charging system to the stock surface. The up-scaled model demonstrated its value in predicting how different operational conditions influence component distribution and final packing structure.

9.2 Recommendations

The research presented in this thesis led to a reliable and feasible industrial scale model for pellet–sinter mixture charging to a blast furnace. Building on the findings and limitations encountered in this work, several directions for future research are recommended to further improve model accuracy, robustness, and applicability:

- **Investigate the role of particle shape in DEM simulations**
  In line with common practice among many researchers, non-spherical particle shapes were randomly selected for the sinter and pellet–sinter mixture in the DEM model. Calibration involving rolling friction demonstrated that the models accurately captured all average values of the five KPIs. However, this was not the case for the standard deviations. It remains unclear whether this discrepancy can be attributed to the choice of particle shape. Moreover, although the selected shapes performed well during calibration, it is still unknown how particle shape affects segregation and packing structure in the blast furnace layers. Therefore, a systematic and thorough investigation into the influence of particle shape on flow behavior, segregation, and packing structure is recommended. Such a study would clarify to what extent particle shape is relevant for modeling blast furnace permeability and, if so, how to represent it most efficiently in large-scale industrial simulations.

- **Assess model validity across mixture compositions**
  In the experimentation and calibration phase of this work (Chapters 5 and 6), the DEM mixture model was developed based on a 50/50 pellet–sinter composition. In Chapters 7 and 8, this model –calibrated for that specific ratio– was applied to simulate a mixture with a slightly different composition, under the assumption that the calibrated parameter set would remain valid given the relatively small variation. It is recommended that this work be extended by conducting experiments across a broader range of pellet–sinter ratios to assess whether the current DEM model and parameter set can reliably capture the flow and packing behavior under varying compositions. Such an investigation would help validate the underlying assumption and assess the robustness and general applicability of the model, particularly in light of the operational variability in ore blend compositions commonly observed in blast furnace practice.

- **In-depth analysis of packing structure in terms of permeability**
  Component segregation within the ore layer was clearly captured in the DEM simulations of industrial scale charging. However, characterizing the packing structure of the ore layer proved to be considerably more challenging. In this study, porosity was used as an indicator of packing. While it provided some insight into the packing arrangement, porosity alone is insufficient to quantify permeability, which is the key parameter of interest in the blast furnace context. Permeability depends on the connectivity of voids and governs the ease with which gas can flow through the furnace layers, whereas porosity measures the total void fraction. Accurately assessing void connectivity requires more detailed information about the pore structure than porosity alone can offer. Further research is needed to develop methods for extracting such information from industrial scale DEM data.

- **Perform validation against industrial data**
  In this work, the calibrated model demonstrated high reliability at the laboratory scale. To strengthen the credibility and practical relevance of the recommendations presented in Chapter 8, a second step is recommended: validating the industrial scale results against real operational data. Relevant measurements may include burden trajectories after discharge from the chute, stockline profiles, and localized burden layer compositions from operating blast furnaces. Such validation not only confirms the model's predictive capabilities but also helps identify limitations arising from underlying assumptions or simplifications. Establishing this link between simulation and actual operation is essential for building confidence in the model and supporting its application as a tool for process optimization.

A

Supplementary Data for Chapter 4

Effect of sample size on segregation index

Figure A.1a-c show the main effect plots for e^{P-S}, μ_s^{P-S} and μ_r^{P-S} for the reference case using different sample sizes. Each figure shows the plots in radial, vertical and circumferential directions for the reference case. It is clear that the value of SI in radial and circumferential directions are unaffected by the number of samples, while the value in vertical direction decreases as the number of samples increases. Also, slightly different plot trends can be seen when using the smallest sample size. For example, vertical segregation increases with e^{P-S} for high values of e^{P-S} (>0.5) when using 3 layers, while the opposite effect is seen when using 4 or 5 layers. A similar contradiction is seen for the sliding friction coefficient at high values ($\mu_s^{P-S} > 0.5$). For the rolling friction coefficient, a relatively strong effect on vertical segregation in observed for low values of μ_r^{P-S} (<0.5) when using 3 layers, while very little effect is seen for that range when using 4 or 5 layers. Hence, it can be concluded that using 3 layers is in vertical direction is insufficient for the analyses and hence, 4 sub-domains are used in both vertical and radial directions in Chapter 4.

A case is also considered in which the bed is divided into sub-domains in multiple directions. Throughout this section, the term "combined segregation index SI_c" denotes the segregation index determined in this manner. As shown in Figure A.1, segregation in the circumferential direction is negligible compared to the other two directions. Therefore, only the radial and vertical directions are considered to determine SI_c, using equal numbers of rings and layers. Figure A.2 shows the results for the reference case. It can be seen that there is an effect of the sample size in all cases. The most important observation is that the effects of e^{P-S} and μ_r^{P-S} when using the smallest sample size (3 rings and 3 layers) are opposite to the effects observed for larger sample sizes. However, it can also be seen that

A

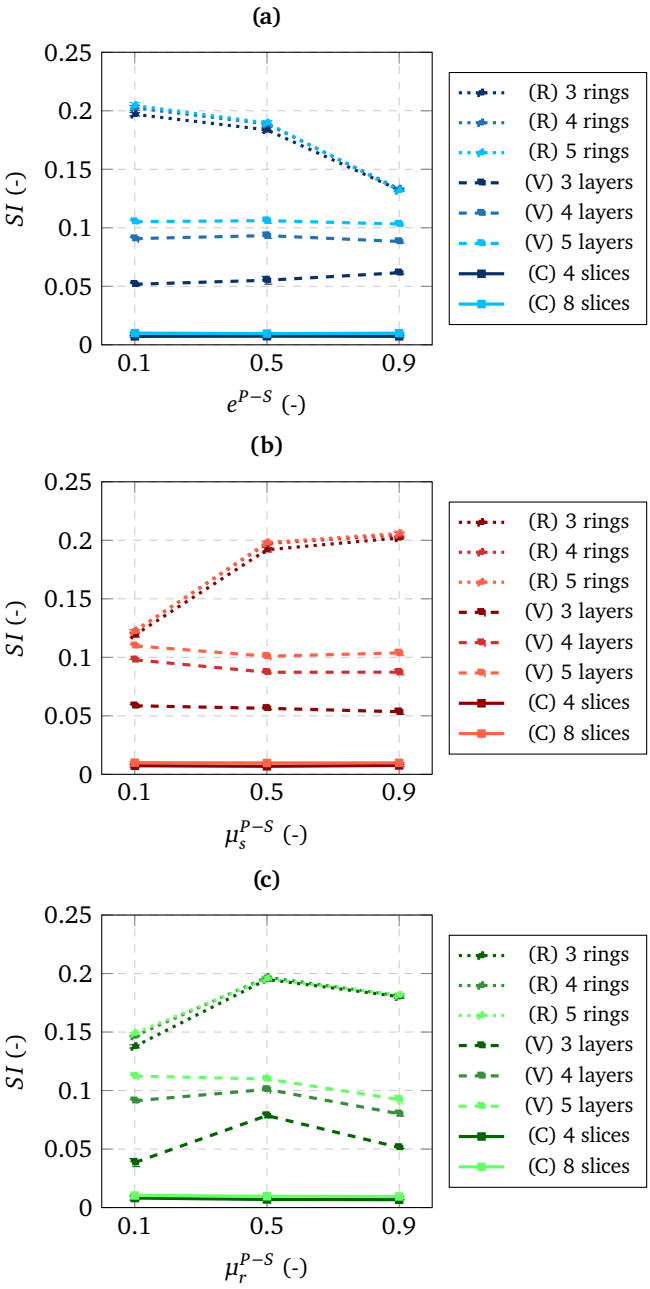


Figure A.1: Effects of (a) e^{P-S}, (b) μ_s^{P-S} and (c) μ_r^{P-S} on segregation in radial (R) and vertical (V) and circumferential (C) directions for $H = 2$ m and $x_P = 0.5$ calculated using different sample sizes. Error bars indicate the standard deviation based on $n = 3$ repetitions. Due to the low variability in the measurements, the error bars are negligible and not discernible in the plotted data.

the SI_c error bars are relatively large when compared to SI error bars in individual radial, vertical and circumferential directions (as seen in Figure A.1). This makes it impossible to confidently interpret the effect plots in Figure A.2. Since the error bars represent the standard deviation, further research is required to scrutinize the number of repetitions which allows the SI_c plots to be interpreted. For the remainder of this work, segregation will be investigated separately in radial and vertical directions.

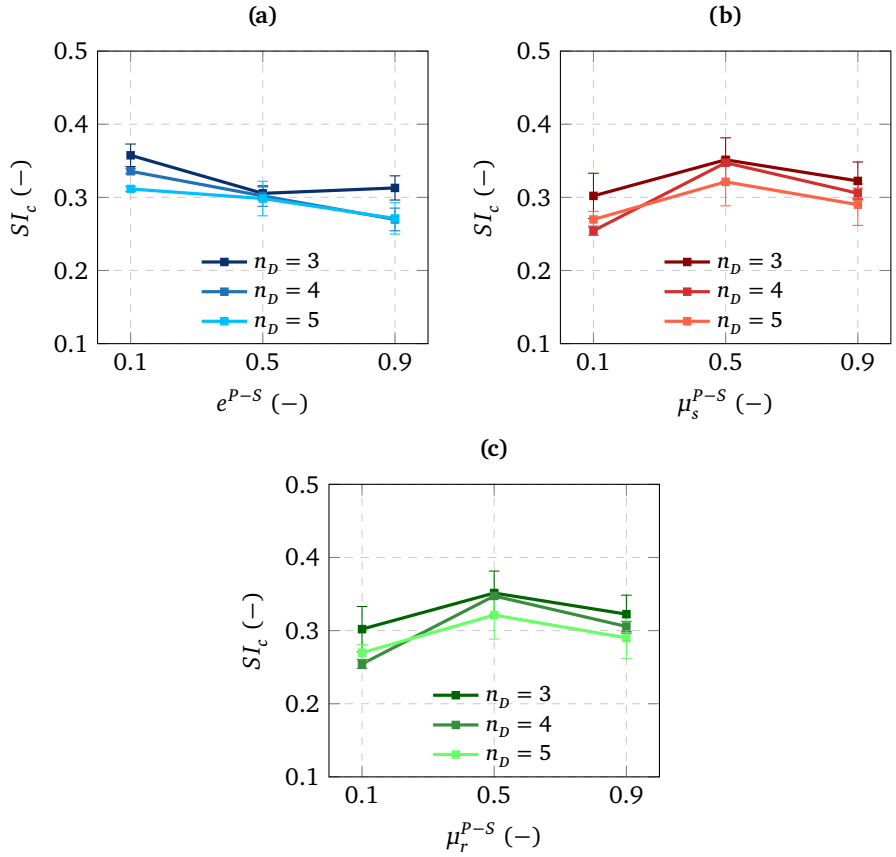


Figure A.2: Effects of (a) e^{P-S}, (b) μ_s^{P-S} and (c) μ_r^{P-S} on segregation in combined radial and vertical directions calculated using different sample sizes. Error bars indicate the standard deviation based on $n = 3$ repetitions

B

Measuring Particle Size Distributions

The particle size distribution of pellet, sinter and coke was determined using a two-step procedure shown in Figure B.1.

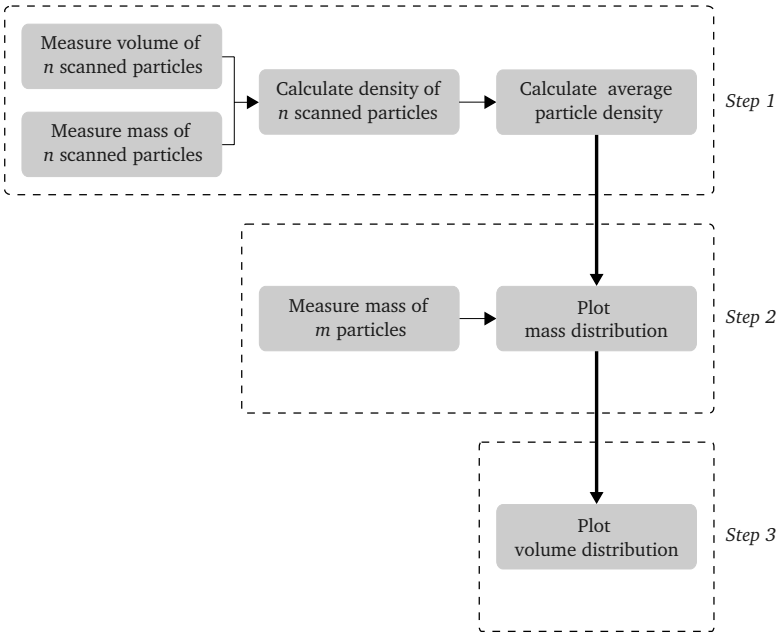


Figure B.1: Step-wise approach to determining the particle volume distributions of pellet, sinter and coke.

B

First, 15 particles of each material were imaged by X-ray computed tomography (CT). The encapsulated volume (*i.e.*, the total volume including the internal pores) of each particle (V_p) was segmented in DRAGONFLY, and the corresponding mass (m_p) was measured on a precision balance. The particle density was then computed as

$$\rho_p = \frac{m_p}{V_p}.$$

and the results are shown in Table B.1.

Table B.1: Calculated densities of pellets, sinter, and coke (in kg/m^3). Values are reported as mean ± standard deviation based on $n = 15$ measurements.

Pellet	Sinter	Coke
3602 ± 62	3449 ± 340	966 ± 88

Next, the particle mass distributions were obtained by sampling each material and measuring the individual particle masses in the sample. These mass distributions were then converted to volume distributions using the corresponding values of ρ_p. Finally, the data were transformed into equivalent spherical diameter (d_{eq}) distributions, shown in Figure B.2.

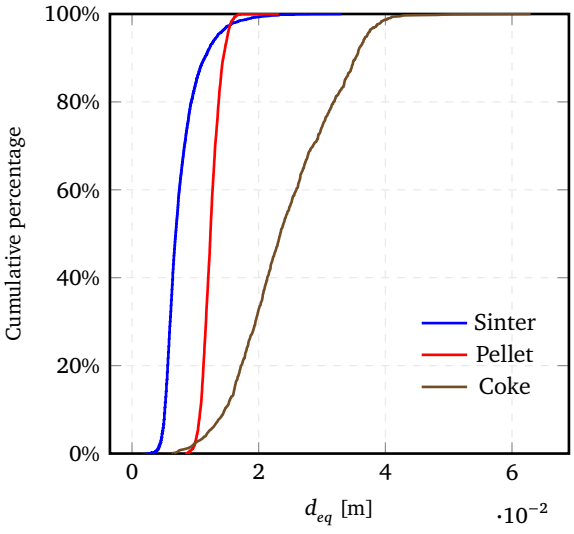


Figure B.2: Cumulative equivalent-diameter distributions based on the following sample sizes: m=2204 for pellet, m=4323 for sinter, and m=976 for coke.

C

Hopper Geometry Imperfections: Observations and Modeling

This appendix provides supplementary data and additional experimental observations and simulations related to Chapters 5 and 6. It focuses on the construction features and imperfections of the hopper used in the experiments, their impact on material flow behavior, and the incorporation of these imperfections into the DEM model. Photographs, descriptions, and supporting simulation results are included to document the hopper design, observed asymmetries in flow patterns, and the efforts to replicate these effects in the DEM simulations.

C.1 Hopper construction imperfections

Figure C.1 shows a photograph of the hopper used in the experiments. The hopper is constructed from three segments that are bolted together to form the complete structure. This modular design was chosen to allow adjustment of the mass flow rate by changing the outlet size. Specifically, removing the bottom segment increases the opening size, thereby enabling a higher mass flow rate.

A drawback of this segmented design is that the hopper could not be manufactured with entirely smooth inner walls. Two main types of manufacturing imperfections were observed:

- **Weld seams:** Figure C.2 shows the interior walls of the hopper, where weld seams and transitions between the segments are visible. Due to time limitations, large welds were ground down as much as possible, but complete removal of all (smaller) welds was not possible. As a result, some weld seams remained, which may interfere with the particle flow.

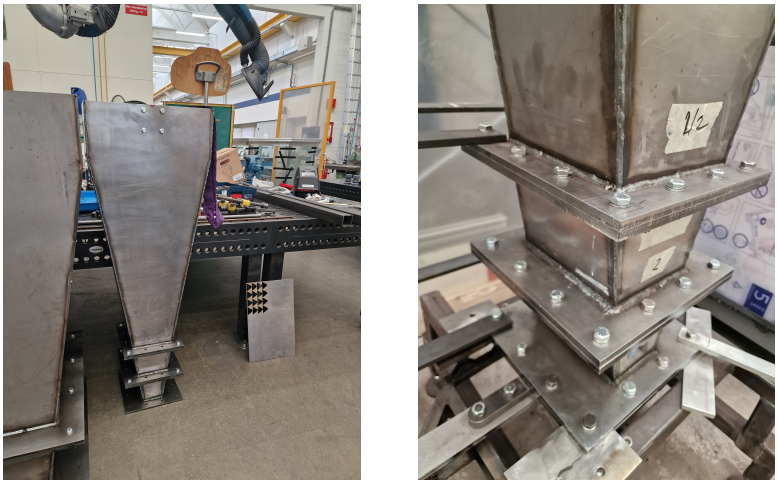


Figure C.1: Photographs of the hopper used in the experiments: (left) full view of the assembled hopper; (right) close-up of the bolted connections between the individual hopper segments.



Figure C.2: Photograph of the interior of the hopper, showing the edges between hopper segments and weld seams.



Figure C.3: Photographs of the edges between the hopper segments.

- **Edges between segments:** Disassembling the hopper revealed several edges inside the hopper caused by imperfect alignment or fitting between the segments, as shown in Figure C.3. Some of these edges protruded by several millimeters and were expected to affect the flow, especially for sinter particles with sharp geometries that can interact with these discontinuities.

C.2 Effect of imperfections on material behavior

During the commissioning phase of the hopper, preliminary tests were conducted using pellet and sinter at a discharge height of $H = 3$ m to verify correct operation. Experiments performed with sinter using the hopper in its original configuration showed that the resulting heap was not symmetrical, in contrast to the more symmetrical heap formed with pellets. Additionally, a significant difference was observed in the mass of material collected at the left and right sides of the hopper. It was hypothesized that this imbalance was caused by interactions between the sinter particles and imperfections in the hopper walls. This hypothesis was based on the observation that the majority of imperfections were located along the left and right interior walls of the hopper, rather than the front and back (refer to Figure C.3). To test this hypothesis, the hopper was rotated 180 degrees, reversing the front and back positions. As shown in Figure C.4, the heap shape and the mass imbalance were also reversed after flipping the hopper, providing further evidence that the observed asymmetry was caused by imperfections in the hopper walls.



Figure C.4: Photographs showing the asymmetry in heap formation after discharging sinter at $H = 1$ m: (left) original hopper orientation; (right) hopper flipped 180 degrees, resulting in reversed heap shapes and mass imbalance in the container.

C.3 Replicating imperfections in hopper geometry

Since the imperfect construction of the hopper appeared to have a clear impact on the heap shape and mass distribution in the container, it was concluded that these imperfections

needed to be incorporated into the geometrical representation of the system in the DEM model. To achieve this, the protruding edges shown in Figure C.3 were measured as accurately as possible using a digital caliper equipped with a depth rod. These measurements were subsequently included in the CAD drawing of the hopper in SolidWorks.

To evaluate whether this virtual representation of the imperfect hopper could capture the heap shape and mass distribution –or at least the general trends– an experiment was designed. Given that the imperfections were located at different sections of the hopper, several test cases were defined, each representing a different combination of section configurations, as illustrated in Figure C.5. In the figure, the circled numbers indicate the wall side: (1) front face and (2) back face. The different combinations (A–G) are obtained by rotating one or more of the three hopper sections so that the section imperfections swap between the front (1) and back (2) sides. The experiments were performed in the laboratory, measuring two KPIs:

1. The total heap mass.
2. The mass ratio in the container, defined as the mass of material on the left side of the heap divided by the mass of material on the right side.

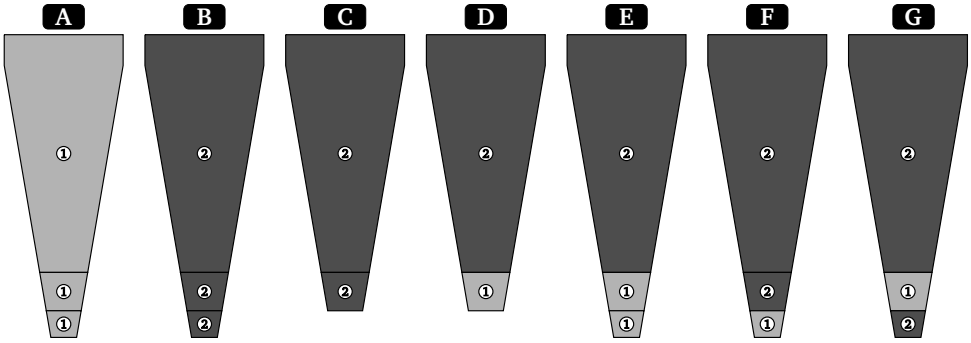


Figure C.5: Overview of the experimental cases. The hopper is assembled from three sections; each case (A–G) rotates one or more sections to relocate the imperfections. Circled numbers indicate wall sides: (1) front face, (2) back face.

The experiments were subsequently replicated in DEM. Since a calibrated DEM model was not yet available, the goal was not to achieve a perfect match between simulations and experiments, but rather to assess whether the model could reproduce the general trends of the mass imbalance.

For the DEM simulations, the calibrated model of Chakrabarty *et al.* [1] previously used

[1] A. Chakrabarty, R. Biswas, S. Basu, S. Nag, *Characterisation of binary mixtures of pellets and sinter for DEM simulations*, Advanced Powder Technology, Volume 33, Issue 1, 2022, 103358, ISSN 0921-8831, https://doi.org/10.1016/j.apt.2021.11.010.

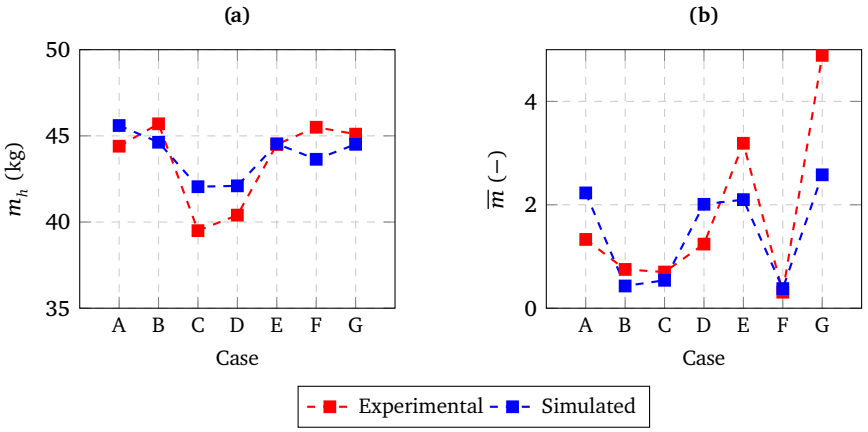


Figure C.6: Results of the case studies, showing the comparison of the total heap mass (left) and the mass ratio in the container (right) between DEM simulations and experiments.

in Chapter 4, was employed. The hopper was filled with 150 kg of sinter and discharged at $H = 3$ m. Figure C.6 shows the results for both the simulations and experiments. Similar trends are observed for both the total mass and the mass ratio. Based on these results, it was concluded that the geometrical imperfections were sufficiently captured in the CAD model, and this imperfect hopper geometry was subsequently used in the simulations presented in Chapter 6 for calibration purposes.

D

Supplementary Data for Chapter 6

This appendix presents supplementary tabular data corresponding to Chapter 6.

D.1 Experimental Design Diagrams

The EDD for the pellet simulations is shown in Table D1. The EDD for the sinter simulations is identical, with X_1-X_5 being replaced by X_6-X_{10}, respectively. The EDD for the mixture simulations is shown in Table D2.

Table D1: Experimental design diagram for establishing a pellet model, detailing the runs and corresponding factor values (X_1–X_5) for each run.

Run	X_1	X_2	X_3	X_4	X_5
1	-1	-1	0	0	0
2	-1	1	0	0	0
3	1	-1	0	0	0
4	1	1	0	0	0
5	-1	0	-1	0	0
6	-1	0	1	0	0
7	1	0	-1	0	0
8	1	0	1	0	0
9	-1	0	0	-1	0
10	-1	0	0	1	0
11	1	0	0	-1	0
12	1	0	0	1	0
13	-1	0	0	0	-1
14	-1	0	0	0	1
15	1	0	0	0	-1

Continued on next page

Continued from previous page

Run	X_1	X_2	X_3	X_4	X_5
16	1	0	0	0	1
17	0	-1	-1	0	0
18	0	-1	1	0	0
19	0	1	-1	0	0
20	0	1	1	0	0
21	0	-1	0	-1	0
22	0	-1	0	1	0
23	0	1	0	-1	0
24	0	1	0	1	0
25	0	-1	0	0	-1
26	0	-1	0	0	1
27	0	1	0	0	-1
28	0	1	0	0	1
29	0	0	-1	-1	0
30	0	0	-1	1	0
31	0	0	1	-1	0
32	0	0	1	1	0
33	0	0	-1	0	-1
34	0	0	-1	0	1
35	0	0	1	0	-1
36	0	0	1	0	1
37	0	0	0	-1	-1
38	0	0	0	-1	1
39	0	0	0	1	-1
40	0	0	0	1	1
41	0	0	0	0	0
42	0	0	0	0	0
43	0	0	0	0	0
44	0	0	0	0	0
45	0	0	0	0	0

Table D2: Experimental design diagram for establishing a mixture model, detailing the runs and corresponding factor values (X_{11}-X_{13}) for each run.

Run	X_{11}	X_{12}	X_{13}
1	-1	-1	0
2	-1	1	0
3	1	-1	0
4	1	1	0
5	-1	0	-1
6	-1	0	1
7	1	0	-1
8	1	0	1
9	0	-1	-1
10	0	-1	1
11	0	1	-1
12	0	1	1
13	0	0	0
14	0	0	0
15	0	0	0

D.2 DEM simulation results

Tables D3 and D4 report the results of simulations using the pellet and sinter EDD (Table D1). Table D5 reports the results of the simulations using the mixture EDD (Table D2). All values are averages over $n = 3$ repetitions for each run.

Table D3: Simulation results for pellets based on the EDD from Table D1.

Run	t_d	m_h	MSE	H_c	ϕ_h
1	4.0100	33.5197	0.0007	0.1251	0.4465
2	5.0967	55.7326	0.0043	0.2595	0.4714
3	4.0633	30.1511	0.0015	0.1145	0.4349
4	4.5267	40.5656	0.0001	0.1647	0.4417
5	3.6300	31.3809	0.0015	0.1071	0.4394
6	5.0167	48.3614	0.0016	0.2210	0.4778
7	3.9033	23.1746	0.0040	0.0809	0.4374
8	4.5400	39.2924	0.0001	0.1618	0.4415
9	4.6433	46.2929	0.0009	0.2068	0.4651
10	4.7400	47.9065	0.0013	0.2121	0.4664
11	4.4433	36.5325	0.0002	0.1495	0.4413
12	4.4267	38.7926	0.0001	0.1554	0.4395
13	3.4233	43.7052	0.0005	0.1878	0.4686
14	6.0500	50.1544	0.0019	0.2310	0.4636
15	3.2833	35.7038	0.0003	0.1451	0.4477
16	5.9567	38.1153	0.0002	0.1557	0.4340

Continued on next page

Continued from previous page

Run	t_d	m_h	MSE	H_c	ϕ_h
17	3.6233	28.2102	0.0023	0.0973	0.4317
18	4.1533	34.1265	0.0005	0.1309	0.4471
19	3.6900	31.0224	0.0015	0.1031	0.4368
20	5.4267	56.1562	0.0047	0.2605	0.4669
21	3.6733	32.9340	0.0007	0.1303	0.4461
22	4.0633	33.8496	0.0007	0.1289	0.4415
23	4.8267	52.7997	0.0027	0.2368	0.4620
24	4.9933	55.0883	0.0036	0.2420	0.4605
25	2.6567	29.1183	0.0020	0.1020	0.4512
26	5.0167	35.7133	0.0003	0.1434	0.4388
27	3.7533	50.4197	0.0019	0.2276	0.4638
28	6.1633	56.5576	0.0041	0.2548	0.4564
29	3.5867	29.7003	0.0017	0.1060	0.4370
30	3.6400	30.7594	0.0015	0.1071	0.4358
31	4.7667	46.9119	0.0011	0.2132	0.4665
32	4.9767	48.8268	0.0014	0.2197	0.4643
33	2.3967	25.7171	0.0034	0.0807	0.4442
34	5.1067	33.6835	0.0007	0.1269	0.4303
35	3.5867	44.3179	0.0006	0.1994	0.4704
36	6.1633	50.7879	0.0020	0.2320	0.4594
37	3.1933	41.6968	0.0003	0.1776	0.4660
38	5.3000	47.4914	0.0011	0.2086	0.4540
39	3.3933	43.5355	0.0004	0.1908	0.4611
40	5.9533	50.2688	0.0016	0.2192	0.4536
41	4.6167	46.9960	0.0009	0.2061	0.4590
42	4.6433	47.6600	0.0010	0.2031	0.4592
43	4.6400	47.0915	0.0010	0.2028	0.4592
44	4.6500	46.5801	0.0008	0.2049	0.4595
45	4.6633	47.1445	0.0010	0.2080	0.4591

Table D4: Simulation results for sinter based on the EDD from Table D1.

Run	t_d	m_h	MSE	H_c	ϕ_h
1	4.5667	41.5630	0.00005	0.1999	0.4774
2	5.1533	46.2120	0.0011	0.2373	0.5038
3	4.5200	40.8297	0.00005	0.1871	0.4591
4	4.9600	46.7408	0.0007	0.2346	0.4857
5	3.8433	37.0293	0.0007	0.1521	0.4408
6	5.3833	42.4819	0.0004	0.2234	0.5116
7	3.8733	34.9315	0.0012	0.1446	0.4350

Continued on next page

Continued from previous page

Run	t_d	m_h	MSE	H_c	ϕ_h
8	5.1133	44.5275	0.0004	0.2229	0.4824
9	4.8367	43.9556	0.0004	0.2240	0.4932
10	4.9200	44.2262	0.0004	0.2263	0.4955
11	4.7800	44.2366	0.0003	0.2140	0.4767
12	4.8300	44.2746	0.0003	0.2218	0.4791
13	3.5433	42.1239	0.0001	0.2100	0.4930
14	5.7433	46.0938	0.0007	0.2313	0.4895
15	3.4733	41.4836	0.0001	0.2017	0.4823
16	5.5667	45.5728	0.0005	0.2247	0.4705
17	3.5800	33.1600	0.0020	0.1300	0.4226
18	4.9633	40.4926	0.00005	0.1962	0.4834
19	3.9800	37.6691	0.0005	0.1619	0.4510
20	5.4933	45.2231	0.0010	0.2380	0.5068
21	4.4767	40.8147	0.00004	0.1908	0.4714
22	4.5667	41.3010	0.00003	0.1958	0.4730
23	4.9433	46.3014	0.0009	0.2355	0.4961
24	5.2167	46.2307	0.0009	0.2392	0.4945
25	3.2233	37.6316	0.0002	0.1805	0.4789
26	5.2767	42.0311	0.0001	0.2026	0.4676
27	3.6833	43.3834	0.0003	0.2182	0.4959
28	5.9500	47.9307	0.0013	0.2471	0.4910
29	3.7533	36.1631	0.0009	0.1509	0.4383
30	3.8900	36.5916	0.0009	0.1520	0.4403
31	5.1900	42.1991	0.0002	0.2174	0.4987
32	5.2800	43.1848	0.0004	0.2223	0.5039
33	2.6200	33.3795	0.0020	0.1147	0.4477
34	4.4733	37.5370	0.0006	0.1596	0.4394
35	3.7600	40.3493	0.0001	0.2063	0.5032
36	6.1533	44.0654	0.0005	0.2282	0.4951
37	3.4567	40.8429	0.0001	0.2041	0.4912
38	5.5467	44.8779	0.0005	0.2253	0.4811
39	3.5400	40.9562	0.0001	0.2015	0.4907
40	5.8267	46.3883	0.0007	0.2341	0.4820
41	4.8467	44.2215	0.0004	0.2221	0.4863
42	4.8700	44.5199	0.0004	0.2159	0.4892
43	4.8567	44.5925	0.0004	0.2236	0.4886
44	4.8600	44.6280	0.0003	0.2183	0.4853
45	4.8700	44.5479	0.0005	0.2231	0.4891

Table D5: Simulation results for the pellet-sinter mixture based on the EDD from Table D2.

Run	t_d	m_h	MSE
1	4.5400	39.8087	0.00003
2	4.9333	44.4751	0.0004
3	4.5733	39.6012	0.0001
4	4.8933	43.8056	0.0003
5	4.0300	34.7813	0.0007
6	5.1433	42.9999	0.0003
7	4.0733	33.5387	0.0009
8	4.9400	43.2776	0.0003
9	3.8100	32.2339	0.0013
10	4.8500	40.8457	0.0001
11	4.1433	34.7597	0.0006
12	5.2433	45.3094	0.0006
13	4.8267	42.8658	0.0002
14	4.8133	42.7009	0.0002
15	4.7733	43.2286	0.0002

Glossary

This glossary provides definitions for technical terms used throughout the thesis, particularly those related to blast furnace operation and DEM modeling. Some definitions contain terms that are themselves defined elsewhere in the glossary. These in-glossary references are marked with a superscript cross "†" to guide the reader to the corresponding entry. In addition, related terms that share a common headword are grouped together.

Burden The raw materials used in blast furnace ironmaking (*e.g.*, "ore burden", "coke burden").

- ***Burden* call level** The stock line level† at which a new charging† cycle is initiated. When the stock surface† descends to this level during operation, it triggers the next batch of material to be charged into the furnace.
- ***Burden* distribution** The spatial arrangement of burden materials.
- ***Burden* layers** The distinct layers of raw materials formed during charging.

Charging The transportation of raw materials from the stock house† to the stock surface† in the blast furnace using dedicated mechanical systems (*e.g.*, belt conveyor, skip car, bell-less top).

Component A material with uniform density and properties, typically referring to a specific burden type such as sinter, pellet, or coke.

- ***Component* distribution** The spatial arrangement of different components within the burden†.
- **Multi-*component* mixture** A mixture composed of two or more components.

Interaction parameter A DEM model parameter that characterizes the mechanical behavior at particle–particle or particle–wall contacts. It defines how contact forces are calculated and typically includes properties such as restitution and friction coefficients.

Intra-component *interaction parameter* An interaction parameter that governs the interactions between particles of the same component[†] (*e.g.*, pellet–pellet or sinter-sinter contacts).

Inter-component *interaction parameter* An interaction parameter that governs the interactions between particles of different component (*e.g.*, pellet–sinter contacts).

Ore Short for "iron ore"; generally refers to iron-bearing burden materials, specifically pellet and sinter in the context of this thesis.

Packing The spatial arrangement of particles within a system, including their positioning, contact network, and overall structure, which affects mechanical stability and permeability.

Permeability A measure of how easily gas can flow through a packed bed of particles, influenced by void connectivity, porosity, and particle arrangement.

Porosity The fraction of total volume in a material that is not occupied by solids; in particulate systems, it quantifies the void space between particles.

Reduction A chemical process in which iron oxides are converted to metallic iron, typically using carbon-based reducing agents.

Direct *reduction* The reduction of iron oxides by solid carbon or CO gas without melting.

Indirect *reduction* The reduction of iron oxides by CO or H_2 gases formed elsewhere in the furnace, typically at lower temperatures.

Segregation Also known as "de-mixing"; a phenomenon where particles separate during flow or discharge based on differences in size, shape, or density.

Skip car A mechanical hoisting container used to transport batches of raw materials along inclined rails to the furnace top for charging.

Stock The raw materials available in storage for blast furnace operation.

***Stock* house** A facility for receiving, storing, and preparing raw materials before they are charged into the furnace.

***Stock* surface** The uppermost level of the charged burden in the furnace, representing the visible top layer of materials.

***Stock*line level** The vertical position of the stock surface, often monitored to regulate the timing of charging cycles.

Acknowledgments

I have never given the pursuit of a PhD much thought. In fact, I started off this journey in 2020 while still figuring out what excites me after finishing my Masters studies, having discovered that company life was not my thrill ride. After all, if you spend eight hours a day doing something, you should at least enjoy it and the company of those you are doing it with. Looking back, it is pretty funny that I chose a PhD in search of something enjoyable. The good news is that I *did* find what excites me, and that I had the best colleagues along the way. It has been a whirlwind from day one, beginning in the COVID pandemic with a plan that blended computational modeling, experiments, and industry, without a clear idea of how to pull it off. I faced challenges early on, and each time I reminded myself to someday thank those who supported, helped, and encouraged me. But to also remember those who brought me joy, because there were many happy moments as well. That day is finally here, and this section is my thank you.

First and foremost, I want to thank my supervisors. Dingena and Yusong, I think that whatever I write here is simply not enough to express my gratitude to you. After five years at the university, and seeing how different things can be, I can confidently say that I am very lucky to have had you as my supervisors. I clearly remember our first meeting in which we discussed expectations, and I mentioned that I would like to meet weekly. I now realize how rare that is and yet, you both came to our weekly meetings with dedication, always being very supportive, encouraging and honest. Dingena, you are a true role model for me. I have learned so much from you in doing research, but even more so in how to be a good leader and supervisor. Your inaugural address was one of the highlights of my time at TU Delft, and perhaps the most inspiring experience I had here. Yusong, I learned a lot from you on how to think about the big picture and connecting the dots in research and writing. You were always so reassuring in our meetings, and all the times you simply said "don't worry, it will be fine" have made such a difference in my experience. Thanks to you both, I will always remember my years at TU Delft as a time marked by steady guidance, trust, and kindness, and by the feeling that I was genuinely supported and able to grow.

The times I spent preparing and executing experiments in the lab were perhaps the most challenging, pushing me out of my comfort zone and requiring patience when so many things went wrong. The technicians at TU Delft were incredibly supportive and worked hard to bring this part of the project over the finish line. Thank you, André, for brainstorming solutions and doing everything you could to speed up construction when

we were staring at months of delay. Huib, thank you for your tireless help during the experiments. At one point we laughingly estimated we had shoveled up to 6 tonnes of iron ore by hand, ending each day with dust in our ears and noses. You always helped as much as possible, even though the work was exhausting and time-consuming. Somehow we still enjoyed our time in the lab, with chats and laughs whenever silly mistakes happened. I am certain I would not have finished the experiments on time without your help and support. Thank you so much.

Being part of the Machines & Materials Interactions section has given me so many happy memories, inspiration, and confidence, and it has frankly set the tone for how I hope to be embraced by colleagues in any future workplace. Thank you, Dingena and Jovana, for leading our group. Your achievements as women in science have always impressed me, and my respect has only grown since completing my PhD. Thanks Javad, Hamid, Marc, Yunpeng, Ahmed, Hao, Marcel, Ana, Aaron, Hesam, Wenhua, Saeed, and Mikhail, for being such great colleagues. I really enjoyed our regular section meetings with coffee, snacks, and a wide range of topics to discuss and learn from, and especially fun activities like *Sinterklaas* celebrations with *kruidnoten* and *cadeautjes*. Some of us even volunteered together in Delft during the summers, which I always considered a unique experience to share with colleagues. Perhaps my most cherished memories are the fun times we shared at conferences in Italy, Scotland and Japan. I am proud to say that even there I often heard our group described as very fun and close knit, and I could only agree. With some of you I spent more time, which left me with many moments of gratitude. Special thanks to Hamid, Javad, and Marc, who supported me a lot in my first year, technically of course, but especially by taking the initiative to check in over coffee, always offering suggestions and inspiration for navigating the PhD journey. Even now, long after you left TU Delft, you still show interest in my path and were eager to attend my defense. Javad, I am so grateful for the time you spent running simulations to provide me with benchmarking data during the months I struggled with debugging software, all while you were wrapping up your PhD and incredibly busy yourself. Thank you, Hao, for your positive and joyful spirit, for always listening with genuine interest and offering highly useful suggestions in our DEM discussions, and for the thesis-cover input that kept it from turning out much duller. I also really enjoyed traveling through Japan together! And Ahmed, looking back, it was a big relief to have you as a colleague working in the same line of research. It was great to have you as a sounding board for both the ideas and the struggles of modeling iron ore mixture charging, and to make that exhausting climb to the top of the blast furnace together back in the winter of 2022!

To all my office mates, the people whose faces I have actually seen the most in the past five years, thank you for being such great company. I am grateful to Yunpeng, the first person I officially met at TU Delft, for welcoming me to the office and helping me settling

in in those very first few weeks. Adrien, although we only met after practically a year at TU Delft due to COVID, it was nice having lunch together and playing board games! Ana, thanks for being there to share struggles, experiences, tips and having me as your paranymph. It was an honor. Sankarshan, you are one of the few people with whom I have had many good conversations about non-PhD related topics, from culture, to traveling and politics. In my quiet times at the office, you would often ask how everything is going, which always lifted my spirits. Thanks for the talk and the laughs! Ethan, although we have only known each other for a short while, I was very happy when you offered to help me clear out my desk on that last day in the office. You have all been very kind and encouraging.

This project was part of a large consortium of academic and industrial partners, alongside fellow PhD researchers working on diverse industrial flow problems. Although our start dates differed, our time as PhDs overlapped, and it was a pleasure to get to know Martijn, Christian, and Sahar. I particularly valued our monthly meetings, where we shared frustrations and celebrated successes. Your work within the consortium was consistently impressive and your presentations inspiring. I wish you all continued success and the very best in your futures. I would also like to express my gratitude to Jan van der Stel, Allert Adema, and Niels van den Burg from TATA Steel for their support throughout the project, their valuable insights, and the engaging discussions that contributed to a meaningful final chapter of this thesis. Special thanks to Allert for reading parts of the work and providing thoughtful feedback.

I feel lucky to have spent so many years in the Netherlands with people who mean so much to me. I am grateful to my family; all my uncles and aunts, for the calls to check in when I was buried in work, and for the game nights and dinners that helped me switch off. Thanks to all my friends, who became more like family in these years. Siroshni and Rayen, thank you for all our adventures together, from kayaking to camping and traveling, the barbecues, and the countless game nights. Chantal and Carlo, we have grown so close these past years. You were there for the big moments: helping us move to Delft, braving the cold winter to find our first car, and now Chantal, standing by my side as a paranymph. To my best friend Rashna, thank you for always being there to talk to and fantasize about our futures with, like we have done together since high school. We have both come such a long way since then, but our bond and excitement for the future remains the same. Of course you are one of my paranymphs as well, and I am so grateful that our timelines in the Netherlands have aligned so that we get to share this moment too.

To my Joël: you have been my biggest support through this whole journey. You are the only non-colleague who can spot “particle segregation” with me in everyday life after hearing me talk about it so much. Thank you for enthusiastically jumping into research chats when I doubted my own logic, and for putting up with my PhD priorities for five

years. You are the only one who has truly seen me at my most stressed, and I am so excited to step into our happiest times together. I am grateful we came to the Netherlands together all those years ago, always sticking side by side and growing so much along the way. The best is yet to come…

This journey would not have been possible without my family back home in Suriname. There was a time when studying abroad felt out of reach, but together, we turned a distant dream into reality. Thank you, mom and dad, for backing me, not just in sending me off to start something better, but for every encouraging word and laugh over the phone when I needed it most. Thanks to my sister Nikita, who started this journey with me back in 2016 when we planned to leave for just two years for our Master's. I'm happy we had each other, sharing the tough moments and celebrating together when we reached our goal. I appreciate the sacrifices of my brother Raoul, who stayed home when his two sisters left, always holding down the fort. We've spent so much time apart these last years, and I can't wait for us all to be together again soon.

So much of what I've achieved comes from the women in my life who have raised me and set examples I live by. Two of them are always with me in spirit: my grandmother and my mom. I often think back to the day I left Suriname to pursue my studies in the Netherlands. I stopped by my grandmother's house to give her a final hug and kiss, promising to meet again soon as I would return after two years of studying. It has been nine years since, and unfortunately I never got to hug my sweet *nani* again. I remember her especially today for the role she played in my upbringing and for instilling a high standard of perseverance. I thank my mom, who has taught me to use that perseverance and always aim high in life. Mom, you have gone above and beyond to make it possible for me to study abroad, sacrificing so much and you were so proud when I told you that I was starting a PhD. I still remember the way you said: "Wow, someday my daughter will be called *doctor*". Mama, we made it!

Raïsa Roeplal
Delft, October 2nd 2025

PhD Portfolio

List of Publications

8. Ahmed Hadi, **Raïsa Roeplal**, Yusong Pang, Allert Adema, Jan van der Stel, Dingena Schott, *Improving the Burden Distribution in Blast Furnace Operations Using DEM: Industrial-Scale Simulations from Stock House to Blast Furnace* (preliminary title), in preparation.

7. **Raïsa Roeplal**, Yusong Pang, Dingena Schott, *Effect of Particle Shape on High-Velocity Flow and Packing Behavior of a Multi-Component Ore Mixture* (preliminary title), in preparation.

6. **Raïsa Roeplal**, Yusong Pang, Dingena Schott, *Towards Realistic DEM Modelling of Blast Furnace Mixture Charging: Calibration and Verification of Model Parameters under High-Velocity Flow Conditions*, Powder Technology, 2025, https://-doi.org/10.1016/j.powtec.2025.121382.

5. **Raïsa Roeplal**, Yusong Pang, Dingena Schott, *The Effect of Particle Properties on Binary Mixture Segregation During Blast Furnace Charging*, VIII International Conference on Particle-Based Methods (PARTICLES 2023), 2024, https://-doi.org/10.23967/c.particles.2023.042

4. **Raïsa Roeplal**, Yusong Pang, Dingena Schott, *Effects of Pellet-Sinter Interaction Parameters on Component Segregation and Bed Porosity Considering Flow Velocity and Mixture Composition: A DEM study*, Advanced Powder Technology, 2024, https://doi.org/10.1016/j.apt.2023.104322

3. Ahmed Hadi[†], **Raïsa Roeplal**[†], Yusong Pang, Dingena Schott, *DEM Modelling of Segregation in Granular Materials: A Review*, KONA Powder and Particle Journal, 2024, https://doi.org/10.14356/kona.2024017

2. Anthony R. Thornton, Timo Plath, Igor Ostanin, Holger Götz, Jan-Willem Bisschop, Mohamed Hassan, **Raïsa Roeplal**, Xiuqi Wang, Sahar Pourandi, Thomas Weinhart, *Recent Advances in MercuryDPM*, Mathematics in Computer Science, 2023, https://doi.org/10.1007/s11786-023-00562-x.

1. **Raïsa Roeplal**, Yusong Pang, Allert Adema, Jan van der Stel, Dingena Schott, *Modelling of Phenomena Affecting Blast Furnace Burden Permeability Using the Discrete Element Method (DEM) – A Review*, Powder Technology, 2023, https://-doi.org/10.1016/j.powtec.2022.118161

Conference Contributions

4. **Raïsa Roeplal**, Ahmed Hadi, Yusong Pang, Allert Adema, Jan van der Stel, Dingena Schott, *Calibration and Application of a Full-Scale Blast Furnace Mixture Charging Model*, 10th International Conference on Discrete Element Methods (DEM10), Himeji (2025), Oral communication.

3. **Raïsa Roeplal**, Yusong Pang, Dingena Schott, *The Effect of Particle Properties on Mixture Segregation During Blast Furnace Charging*, 11th International Conference on Conveying and Handling of Particulate Solids (CHoPS), Edinburgh (2024), Oral communication.

2. **Raïsa Roeplal**, Yusong Pang, Dingena Schott, *The Effect of Particle Properties on Mixture Segregation During Blast Furnace Charging*, PARTICLES2023, Milan (2023), Oral communication.

1. **Raïsa Roeplal**, Yusong Pang, Dingena Schott, *Segregation and Bed Porosity After Charging a Blast Furnace Ore Mixture: Analysis of Sensitivity to Pellet-Sinter Interaction Parameters*, World Congress on Particle Technology (WCPT) 9, Madrid (2022), Poster pitch and presentation.

Other Contributions

3. **Raïsa Roeplal**, Hao Shi, *DEM Simulations for Industrial Granular Flows: Balancing Efficiency and Accuracy*, DelftBlue User Summit, Delft (2024), Oral communication.

2. Hao Shi, **Raïsa Roeplal**, Gert Jan van Selm, Ahmed Hadi, Dingena Schott, *Particle Shape Effects in Granular Processes* Pro2Tech Annual Event, Delft (2024), Poster presentation.

1. **Raïsa Roeplal**, Gert Jan van Selm, Hao Shi, Dingena Schott, *Modelling Non-Spherical Particles in DEM Simulations: Getting into Virtual Shapes*, Pro2Tech Annual Event, Delft (2023), Poster presentation.

Teaching Activities

1. DEM Simulation Course (ME44115), Master Course Mechanical Engineering, 2020-2024.

(Partially) included in this thesis, † Authors contributed equally (joint first authorship).

Supervised Student Projects

6. Sabine van Epen, *Comparison of Calibration Strategies for Mixture Components: A DEM Study of Pellet and Sinter*, MSc. Graduation Project, Delft University of Technology, 2025.MME.9050, 2025.
5. Sabine van Epen, *The Calibration of DEM Parameters in Mixtures with Segregation*, Literature Assignment, Delft University of Technology, 2024.MME.8918, 2024.
4. Siddharth Sasidharan, *Selection & Calibration of Scanners for Bulk Property Measurements*, Research assignment, Delft University of Technology, 2024.MME.8894, 2024.
3. Nilüfer Özhan, *Modelling Particle Degradation in Granular Materials Using Discrete Element Method*, Literature Assignment, Delft University of Technology, 2021.MME.8539, 2021.
2. Diego Burggraaf, *Segregation in Dense Multi-Component Granular Flows: An overview*, Literature Assignment, Delft University of Technology, 2021.MME.8509, 2021.
1. Mitchel Baran, *A Sensitivity Analysis on Bed Permeability and Segregation for Blast Furnaces: A DEM Study*, Research assignment, Delft University of Technology, 2022.MME.8605, 2022.

About the Author



Raïsa Roeplal was born on 19 October 1992 in Paramaribo, Suriname. After obtaining her Bachelor's degree in Mechanical Engineering from the Anton de Kom University of Suriname in 2014, she entered the corporate world and worked on projects from piping engineering and design to oil-tank inspection and repair. While these projects offered great experience, the novelty soon faded and she went looking for tougher, more intricate problems.

In 2016 she moved to the Netherlands to pursue a Master's degree in Mechanical Engineering at the University of Twente, specializing in Thermal & Fluids Engineering. A Multiphase Flows elective left her so intrigued by granular materials that she switched her graduation topic to granular materials: modeling granular flow to mix concrete into a printable paste for 3D concrete printing. That pivot sparked a lasting curiosity about segregation and how to capture it in models and visuals. It satisfied her appetite for complexity, but not for practicality; she still wanted to see models translated into real industrial settings.

In 2020 she joined the GranChaMlab at TU Delft for a PhD with Prof. dr. ir. Dingena Schott and dr. ir. Yusong Pang, studying how pellet–sinter mixtures are charged into blast furnaces and how their packing can be steered. The project delivered on practicality: a central challenge was applying the model at industrial scale. This thesis documents the project and its outcomes, from laboratory experiments to plant-scale models.

Outside the lab she unwinds with strategy board games and long talks around the campfire; inside it, she aims for models that help plants run cleaner and steadier. Looking ahead, she is eager to keep her researcher hat on, developing models that deliver measurable, practical impact across industries.

